PHASE BEHAVIOR OF CARDIOLIPIN

A Dissertation

Presented to the Faculty of the Graduate School

of Cornell University

In Partial Fulfillment of the Requirements for the Degree of

Doctor of Philosophy

by

Yi-Fan Chen

January 2012

PHASE BEHAVIOR OF CARDIOLIPIN

Yi-Fan Chen, Ph. D.

Cornell University 2012

Cardiolipin is a phospholipid with negatively charged headgroups. This lipid is structurally unique in its quadruple-chained configuration and functionally unique in its nearly exclusive involvement in the cellular energy production processes. Whether the structural uniqueness leads to the functional exceptionality has long been an open question. Like other phospholipids, cardiolipin is a liquid crystal and demonstrates polymorphism when it is purified and mixed with water. Many studies have been dedicated to examining the phase behavior of cardiolipin liquid crystals in an effort to understand the driving forces behind phase transitions and to ultimately decipher the structure-function relation. However, few, if any, studies have thus far systematically investigated cardiolipin phase behavior in broad temperature and concentration ranges. In this thesis, small- and wide-angle X-ray scattering techniques were employed to study the phase behavior of cardiolipin-water mixtures. A phase diagram was mapped in lipid concentrations from 32.9 wt% to 85.4 wt% and temperatures from -20 °C to 60 °C. Two striking features were observed in this cardiolipin phase diagram: the presence of a lamellar-lamellar phase separation region and a phase displaying crystalline-like X-ray scattering patterns. Based on the X-ray scattering data underlying the phase diagram, electron density maps of the cardiolipin liquid crystals were reconstructed with two different methods and their structural parameters were derived, both within and across a phase boundary. A relationship between phase behavior and structure was observed from this structural information and utilized to

construct a "structure map". Based on the structure map, an energetics view was provided to explain the observed phase transitions and to explore the nature and origins of the two striking phase behaviors.

BIOGRAPHICAL SKETCH

Yi-Fan Chen has been lucky to attend prestigious educational institutions since high school, which culminated in his studying at Cornell University. He graduated from National Tainan First Senior High School in Taiwan in 1999, received his B.S. in Chemical Engineering from National Taiwan University in 2003 and arrived at Cornell University and the Gruner group in 2005 after a mandatory military service in the R.O.C. Army.

To my parents for their love and supports

ACKNOWLEDGMENTS

This thesis study had been carried out with the assistance, supports and advice from many current and former members of the Gruner group. No word will overstate my particular gratitude and admiration to my thesis advisor, Prof. Sol Gruner. Sol is a very caring and inspiring advisor. I will never forget the words I heard in our conversation: "...I am not doing research for getting famous. I found my responsibility of training the next generation of scientists. Doing researches is a vehicle." Although short, these words have moved me since my first years in the group. They stimulated my aspiration to excelling as a scientist and to be an inspiring mentor as he has been. I thank Dr. Mark Tate for his patient advice and tremendous supports, both technically and intellectually, in my thesis study and other research projects. Without Mark's assistance, this thesis study would have never been completed. However, the same study would have been far more successful and been carried out far more efficiently if having been led by Mark. I also thank Dr. Lucas Koerner and Dr. Suntao Wang. Lucas and Suntao had helped me in numerous experimental setups and data collections at CHESS G1 and F1 stations. Without Lucas's expertise in the computer stuffs, I would have stupidly operated the machine manually and got no chance to sleep in a weeklong data collection at CHESS (simultaneously made tons of mistakes!). Without Suntao, I would even have had no idea about how to shoot X-rays on my samples! The sample box and the sample holder used in this thesis were made by Marty Novak, the most skillful mechanics I have ever known. I am grateful for his help and his wonderful Marty's summer party held every summer.

In my six years in Ithaca, I am very lucky to have friendships from Drs. Nozomi Ando, Buz Barstow, Gil Toombes, Lucas Koerner and Suntao Wang. I sincerely and deeply appreciate Nozomi's support and encouragement in the first years of my

graduate study and in my last years in the group when many difficulties were being encountered. Gil is one of the most knowledgeable people I have ever met (sorry Gil but I have to say that Sol is still superior to you. You should work hard to beat him in the near future!). I thank him for teaching me many experimental skills and science (especially the quantum mechanics!). Buz is an extremely careful experimenter. I thank him for teaching me the right attitude of doing experiments. That will definitely one of the most precious skills I learned here.

I would also like to thank the CHESS staffs, Bill Miller and Scott Smith, for their help in my tricky setup at CHESS F1 station, and Dr. Arthur Wall for his advice and technical support in my experiments at CHESS G1 beamline.

I thank my committee members, Profs. Sol Gruner, Brian Crane and Lois Pollack. Thank you for your advice on the thesis and the very inspiring and constructive questions regarding the study. Those questions encouraged me to think far more deeply into the implications of my study. And also thank you for your patience in my defense. I know it was really exhausting to go through more than one hundred slides!

Finally, I thank my fiancée, Maria Wei-Fang Shen, for all her love, support, encouragement, patience and company in these years. You are on my shoulder now. I will not let you down.

TABLE OF CONTENTS

LIST OF FIGURES

LIST OF TABLES

LIST OF ABBREVIATIONS

↔, →	Lipid phase transition
C18:1	Type of a lipid hydrocarbon chain; the former indicates the number of total carbons and latter for that of total double bonds
2-D	two dimensional
3-D	three dimensional
°C	degrees Celcius
CCD	Charge Coupled Detector
CCP14	Collaborative Computational Project Number 14
CHESS	Cornell High Energy Synchrotron Source
CuK_α	K_α X-rays from Copper (wavelength 1.54 Å)
CuK_β	K_β X-rays from Copper (wavelength 1.39 Å)
CTP	cytidine triphosphate
DDABr	didodecyldimethylammonium bromide
DLVO	The Derjaguin-Landau-Verwey-Overbeek Theory
DOPA	dioleoylphosphatidic acid
DOPC	dioleoylphosphatidylcholine
DOPE	dioleoylphosphatidylethanolamine
DOPG	dioleoylphosphatidylglycerol
DOPS	dioleoylphosphatidylserine
DM-TAP	1,2-dimyristoyl-oxy-3-*N,N,N*-trimethylaminopropane
EDTA	Ethylenediaminetetraacetic acid
FOM	Figure of Merit
FWHM	Full Width at Half Maximum
GeV	Giga-electron volt
HEPES	4-(2-hydroxyethyl)-1-piperazineethanesulfonic acid
K	Kelvin (Temperature)
keV	kilo-electron volt
ILA	Inter-Lamellar Attachment, precursor of the Q_{II} phase in the $L_\alpha \leftrightarrow Q_{II}$ transition
IMI	Inverted Micellar Intermediate for membrane fusion
IPMS	Infinitely Periodic Minimal Surfaces
MAD	Multi-Wavelength Anomalous Diffraction
mA	milliAmpere
mg	milligram
μL	microliter
mm	millimeter
mV	millivolt
nm	nanometer
PA	Phosphatidic Acid
PC	phosphatidylcholine
PE	phosphatidylethanolamine
PS	phosphatidylserine
RNases A	Ribonuclease A
RTD	Resistance Temperature Device

SAXS	Small Angle X-ray Scattering
TC	Tiny Crystals-cluster phase
TLC	Thin-Layer Chromatography
TMC	*trans*-monolayer contact, precursor of the non-lamellar phases in the lamellar-non-lamellar phase transition
SAD	Single-Wavelength Anomalous Diffraction
WAXS	Wide Angle X-ray Scattering
WT%	Weight fraction in percentage e.g., (lipid weight)/(lipid weight + water weight)

LIST OF SYMBOLS

2θ	Scattering angle
A	Lipid-water interfacial surface area
A_i	Amplitude of a cosine function for the electron density profile of a lipid bilayer
A_l	Cross sectional area per lipid molecule
Å	Ångström, 10^{-10} meter
a	Unit cell repeat distance of a lipid phase
$\vec{a}_1, \vec{a}_2, \vec{a}_3$	Lattice vector
B	Bulk compression modulus of a lipid bilayer
C	Monolayer mean curvature
C_0	Monolayer spontaneous curvature
C_L	Lipid concentration
D	Distance between two surfaces
d	d-spacing of a lipid lamellar phase
d_B	Lipid bilayer thickness
d_C	Lipid hydrocarbon chain length
$d_{B,Luzzati}$	Luzzati lipid bilayer thickness
d_{H1}	Distance from the phosphate group to the hydrophobic-hydrophilic interface
d_{obs}	Observed position of an X-ray scattering peak
d_{calc}	Calculated position of an X-ray scattering peak
d_S	Lipid bilayer separation
$d_{S,Luzzati}$	Luzzati lipid bilayer separation
$(da/dT)_C$	Unit cell dimension variation per unit temperature at a constant concentrion
E_{atom}	Electric field of the waves radiated by a group of atoms
$E_{crystal}$	Electric field of the X-rays scattered by a crystal
E_{mol}	Electric field of the X-rays scattered by a molecule
E_{in}	Electric field of the incident X-rays
E_{x0}	Amplitude of the incident X-rays
e	Electron charge
F^{mol}	Structure factor of a molecule
$\left\|F^{mol}\right\|$	Magnitude of the molecular structure factor
f^0	Atomic form factor
f_j^0	Atomic form factor of the j'th atom
f', f''	Anomalous scattering correction terms

G	Monolayer Gaussian curvature
g_{DLVO}	Interaction potential energy per surface area between two surfaces, modeled by the DLVO theory
g_E	Monolayer elastic energy
g_{el}	Electrostatic free energy per unit area between two charged surfaces
g_{el}^{cyl}	Electrostatic free energy per unit area on a charged cylinder
g_{el}^{sphere}	Electrostatic free energy per unit area on a charged sphere
g_p	Lipid hydrocarbon chain packing frustration energy
$< g_p >$	Surface area-averaged hydrocarbon chain packing frustration energy
g_U	Lipid membrane thermal undulation repulsion energy
H	Hamaker constant for the van der Waals force model
H_{II}	Type II (inverted) hexagonal phase
h, k, l	Miller indices
$\hbar\omega$	Photon energy of the incident X-rays
$I(Q)$	Intensity of the scattered X-rays by lipid molecules
$I_{crystal,ideal}$	Theoretical integrated intensity of the scattered X-rays by a crystal
$I_{crystal,real}$	Real integrated intensity of the scattered X-rays by a crystal
K	Monolayer bending modulus
K_B	Boltzmann constant
K^{el}	Electrostatic contribution to the monolayer bending modulus
K_G	Monolayer Gaussian modulus
k	Lipid hydrocarbon chain stretching rigidity
k_0	Wavenumber of the incident X-rays
k_r	Wavenumber of the radiated X-rays by an oscillating electron
k'	Lipid hydrocarbon chain stretching constant defined by Equation 2-3
L_c	Crystalline lamellar phase
L_d	Liquid crystalline lamellar disorder phase
L_o	Liquid crystalline lamellar order phase
L_α	Liquid crystalline lamellar α phase
$L_{\alpha 1}$	Liquid crystalline lamellar α1 phase with larger d-spacings in the phase-phase separation region
$L_{\alpha 2}$	Liquid crystalline lamellar α2 phase with smaller d-spacings in the phase-phase separation region
L_β	Gel lamellar β phase
$L_{\beta'}$	Gel lamellar β' phase
l	Lipid hydrocarbon chain length
l_r	Relaxed equilibrium lipid hydrocarbon chain length
l_{max}	Maximum lipid hydrocarbon chain length
l_{min}	Minimum lipid hydrocarbon chain length
m	Multiplicity factor for X-ray scattering intensity

N	Number of bilayers in the scattering domain
N_u	Scaling constant from the scattered X-ray intensity by lipid molecules
n_1, n_2, n_3	Integer numbers denoting a unit cell within a crystal
n_C^e	Electron umber per lipid molecule of the hydrocarbon chains
n_H^e	Electron umber per lipid molecule of the headgroup
n_W	Inter-bilayer water molecules
P_h	Coefficient of the thermal undulation repulsion energy
Q_{II}	Type II (inverted) cubic phases
Q_{II}^D	Type II (inverted) cubic phase in the IPMS of double diamond
Q_{II}^P	Type II (inverted) cubic phase in the IPMS of plumber's nightmare
Q_{II}^G	Type II (inverted) cubic phase in the IPMS of gyroid
$\vec{Q}$	Momentum transfer of X-ray scattering
$\left\|\vec{Q}\right\|$	Magnitude of the X-ray scattering momentum transfer
R	Distance between an observer and oscillating electrons
R	Cylinder or Sphere radii. In the case of the H_{II} phase, R is the water core radius
R_1, R_2	Monolayer principal curvature
$\vec{R}_n$	Lattice vector of a unit cell within a crystal
$\vec{r}'$	Position from the nucleus of an atom
$\vec{r}_j$	Relative position of the j'th atom.
T	Absolute temperature in Kevin
V_W	Volume of a water molecule
x	Polarization direction of incident X-rays
x	Distance from the midpoint between two charged surfaces
z	Incident X-rays traveling direction
z	Valence of a counterion
z_H	Electron density peak position of the headgroup from a bilayer center
γ	Euler's constant
γ_{phob}	Attraction from hydrophobic-hydrophilic interfacial tension
Δ	Mean square fluctuation of a lipid bilayer
$\Delta E/E$	Energy bandwidth of X-rays
ε	Dielectric constant of water
ε_0	vacuum permitivity
ε_p	Packing factor defined by Equation 2-7
ζ	Distance between midpoints of the hydro-phobic and -philic volumes
ζ_r	ζ when hydrocarbon chains are relaxed
η	Caillé parameter defined by Equation 4-13
κ^{-1}	Debye screen length

λ	Wavelength of the incident X-rays
λ_h	Half decay length of the thermal undulation repulsion energy
Ξ	Coupling parameter for ions distribution near a charged surface
π_{ch}	Repulsion among lipid hydrocarbon chains
π_{hg}	Lateral repulsion among lipid headgroups
$\rho(\vec{r}')$	Electron density at position $\vec{r}'$ from the nucleus of an atom
$\rho(x)$	Counterion number density between two charged surfaces
$\rho(z)$	Electron density along a lipid bilayer surface normal
ρ_{avg}	Average electron density of a lipid bilayer
ρ_∞	Counterion number density in the bulk solution
ρ_0	Counterion number density at the midpoint between two charged surfaces
ρ_a	Electron density of the inter-bilayer water
ρ_C	Electron density peak height of the hydrocarbon chains
ρ_{CH_2}	Electron density of the methylene group on the hydrocarbon chains
ρ_H	Electron density peak height of the headgroup
σ	Surface charge density
σ_C	Gaussian variance of the electron density peak of the hydrocarbon chains
σ_H	Gaussian variance of the electron density peak of the headgroup
ϕ	Phase of the molecular structure factor F^{mol}
ϕ_L	Lipid volume fraction
ψ	Electrostatic potential between charged surfaces

CHAPTER 1

INTRODUCTION

1.1 Overview

Lipids are an important building block of biomembranes. They provide not just a matrix to host proteins and nucleic acids but also an active role in many biological processes (e.g., Wymann and Schneiter, 2008; van Meer et. al., 2008; Valiyaveetil et. al., 2002; Chen et. al., 1997). They are liquid crystals, both *in vivo* and *in vitro*, and usually arranged in a liquid crystalline lamellar structure commonly seen in biomembranes. However, some biologically relevant lipids are capable of self-assembling into a variety of non-lamellar liquid crystalline structures when they are purified and mixed with water, a phenomenon called polymorphism. Understanding the forces driving polymorphism is expected to provide insight on how lipids affect the biomembrane organization and how they interact with proteins (Gruner, 2005). In this thesis study, we chose cardiolipin as our research subject. Cardiolipin is a charged phospholipid. It is structurally unique in its quadruple-chained configuration (other common lipids are double-chained) and functionally unique in its nearly exclusive involvement in the cellular energy production processes (Claypool, 2009; Mileykovskaya et. al., 2005; Haines and Dencher, 2002). Whether and how the structural uniqueness and functional exceptionality are related with each other is still an open question. The goal of this thesis is therefore to provide further understanding of the polymorphic phase behavior of cardiolipin in an effort to shed light on this structure-function relation. Using small- and wide-angle X-ray scattering techniques, we mapped the phase diagram of cardiolipin in lipid concentrations from 32.9 wt% to 85.4 wt% and temperatures from -20 °C to 60 °C, from which two peculiar phase features were observed. A combined energetics and structure perspective was

proposed to explain the mechanisms of the cardiolipin phase behavior. Effects of the cardiolipin headgroup charges were analyzed in terms of two different energetic contributions and found to compete with each other to determine the cardiolipin phase preference.

Our discussion of this topic will begin with a brief review on biological roles (Section 1.2) and polymorphism (Section 1.3) of lipids. The forces driving the lipid phase behavior and their theoretical models will be discussed in Chapter 2. Experimental setup and procedures for this thesis study will be described in Chapter 3. Data on the cardiolipin phase behavior will be presented in Chapter 4, followed by concluding remarks and suggested future studies in Chapter 5.

1.2 Biological Roles of Lipids in Biomembranes

Lipids are a broad group of biomolecules with the common feature of limited water solubility. Natural compounds belonging to this group are as structurally diverse as including fatty acids (e.g., Figure 1.2.1a), fat-soluble vitamins (e.g., Figure 1.2.1b), waxes (e.g., Figure 1.2.1c), steroids (e.g., Figure 1.2.1d), glycerophospholipids (e.g., Figure 1.2.1e) and sphingolipids (e.g., Figure 1.2.1f). Lipid diversity of chemical structures is reflected in their functional versatility. Lipids are major energy storage media in some organisms, attributable to their highly reduced states, and regulate some cell metabolisms by acting as first or second messengers in signal transduction processes (Wymann and Schneiter, 2008). Lipids also affect inter- and intra-molecular organizations and thereby functions of membrane proteins via their specific and/or collective interactions with the proteins (Andersen and Koeppe, 2007). One lipid species has even been suggested to be involved in membrane protein folding

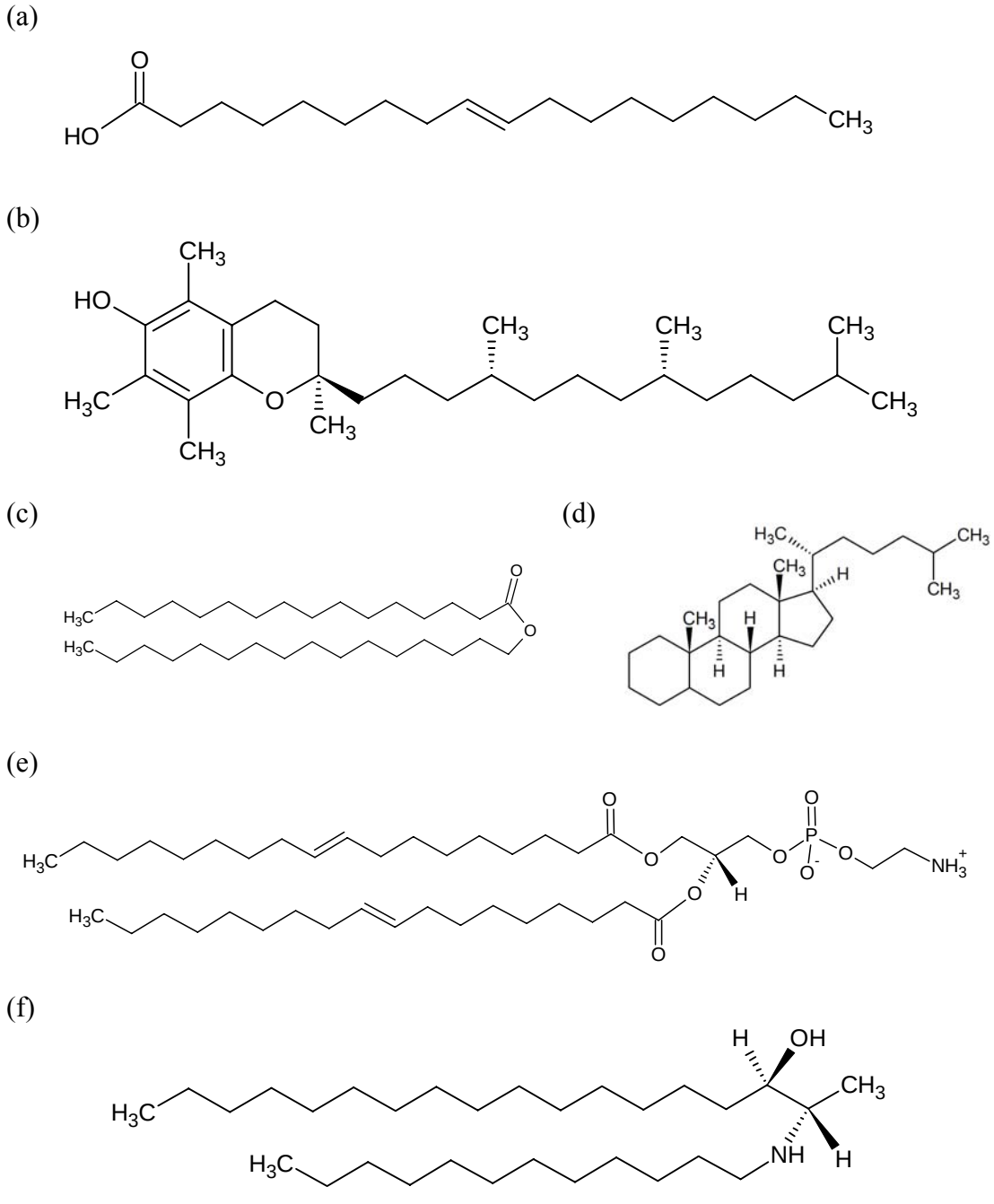

Figure 1.2.1. Chemical structures of different types of lipids: (a) oleic acid; (b) vitamin E; (c) cetyl palmitate; (d) cholesterol; (e) dioleoylphosphatidylethanolamine (DOPE); (f) N-C12-deoxysphinganin.

(Bogdanov and Dowhan, 1998). Among such diverse biological functions, many lipids are most widely known to be a major building block of biomembranes. Many of other lipid functions appear to be the extension of this role.

Biomembranes are mainly composed of lipids and proteins. Although the lipid compositions in biomembranes are extremely complicated, many common biological membranes are primarily constructed with phospholipids (van Meer et. al., 2008). Phospholipids are molecular assemblies of polar headgroups containing phosphates and hydrophobic tails comprising hydrocarbons (Figure 1.2.2a). This combination of hydrophobic and hydrophilic parts renders phospholipids amphipathic characteristics and the ability to self-assemble into various structures against aqueous or oily environments. In ordinary physiological conditions, the most common structures that lipids form are bilayer structures. As the name suggests, bilayer structures are constituted by two layers of lipid molecules, each called a "leaflet", and arranged in such a way that the headgroups form the interfaces with aqueous surroundings and the tails are buried inside (Figure 1.2.2b). The hydrophobic nature of the interior makes biomembranes an efficient barrier against diffusion of ionic and polar compounds into or out of cells and organelles. This property is employed by cells to separate their contents from the environments as well as to compartmentalize cell interiors and form various organelles.

The lateral organization of biomembranes can be modeled as 2-D fluids, or more precisely liquid crystals, which are composed of lipids as the solvents and membrane proteins as the solutes. This viewpoint was historically established by Singer and Nicolson in their fluid mosaic model (Figure 1.2.3; Singer & Nicolson, 1972; Edidin, 2003). In this model, a lipid bilayer acts as a 2-D matrix within which membrane proteins are distributed randomly and diffuse freely in lateral orientations. In other

(a)

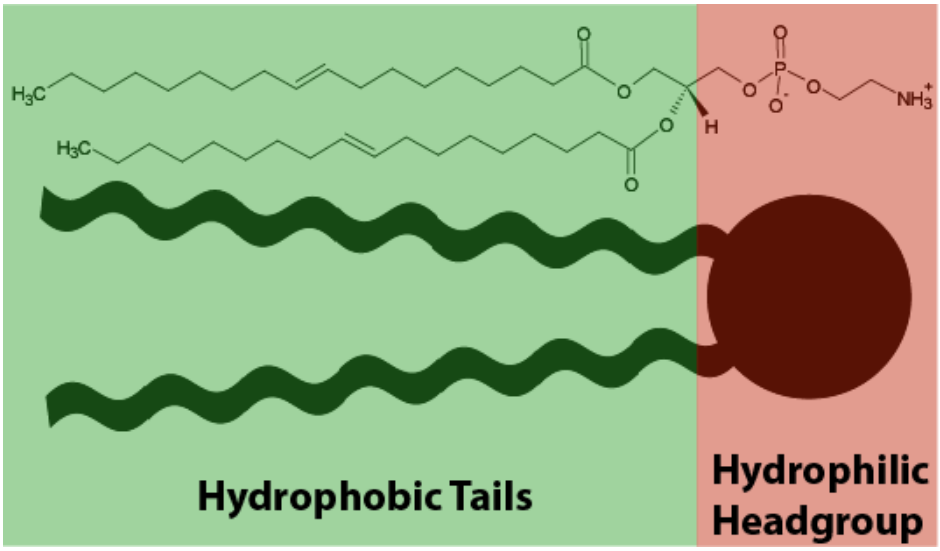

(b)

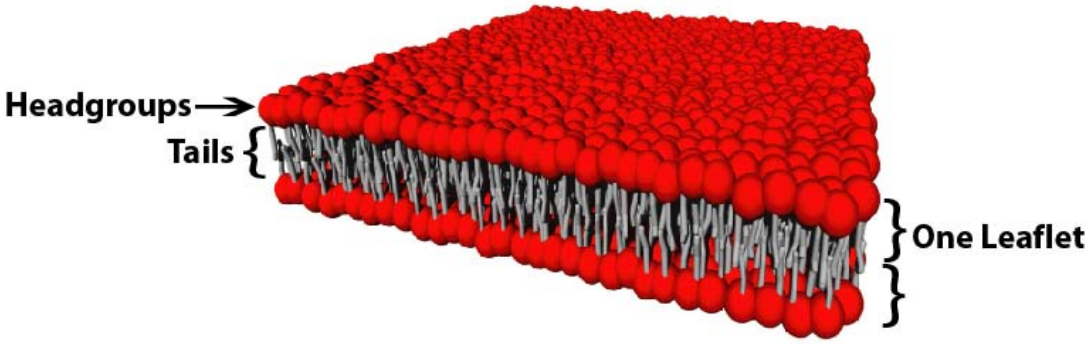

Figure 1.2.2. (a) Chemical structure and schematic representation of a phospholipid molecule. (b) Model of a lipid bilayer structure. ((b) is adapted from Tresset (2009))

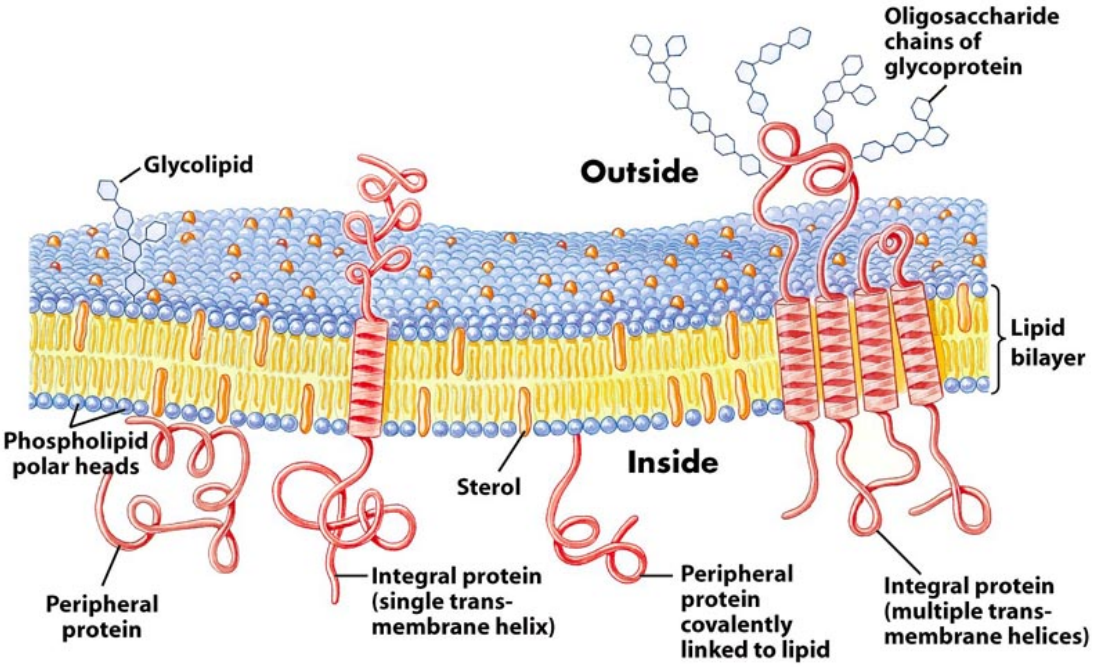

Figure 1.2.3. Fluid mosaic model of cell membranes, proposed by Singer and Nicolson (1972). In this model, lipids form a matrix in which membrane proteins are randomly distributed. This view of biomembranes was later modified considerably. See the text for details. "Outside" and "inside" refer to the compartment bound by the membrane. (The figure is from Nelson and Cox (2005))

words, virtually no long-range order exists within the membrane plane. While basic concepts of the model still hold true today, more recent experimental evidence has implied the need of modifying the model significantly. Rather than distributed evenly, certain lipid and protein species were observed to segregate laterally and form clusters with physical properties distinctive to the bulk of the biomembrane (Simons and Ikonen, 1997; Edidin, 2003). This observation of lateral structure heterogeneity led to proposal of the raft model, which is speculated to be the vehicles employed by biomembranes to fulfill their biological functions. Lipid rafts are postulated as

dynamic nanoscale assemblies of specific lipids and proteins, with the dimension of 10-200 nm and distributed within a bulk lipid matrix (Jacobson et. al., 2007; Pike, 2009; Lingwood and Simons, 2010; van Meer et. al., 2008). The rafts are enriched in two lipid species, sphingolipids and sterols, and the peripheral membrane proteins attached to the rafts via the glycosylphosphotidylinositol linkage. Presumably driven by structural similarity and hydrogen bonding, these raft-forming components possess the potential of assembling with one another and forming small, transient aggregations on biomembrane surfaces. When triggered by biological events such as ligand binding or protein oligomerization, these individual lipid rafts might coalesce to form larger, more stable raft structures through lipid-protein, protein-protein and/or lipid-lipid interactions. This process effectively coordinates and organizes the raft components for specific biological tasks (Lingwood and Simons, 2010). Akin to the presence of organelles within cells, the formation of lipid rafts is equivalent of compartmentalizing biomembranes for a higher biological efficiency. The lipid raft model was initially proposed to explain the observed lipid and protein sorting/trafficking phenomena in the trans-Golgi network of polarized epithelial cells (van Meer et. al., 2008; Simons and van Meer, 1988). Thus far, the model has evolved to be implicated in various biological processes such as signal transduction (Simons and Toomre, 2000), cell apoptosis (Malorni et. al., 2007) and cell migration (Manes et. al., 2003). A salient *in vivo* manifestation of the raft concept is caveolae (Figure 1.2.4), a cholesterol- and glycosphingolipid-rich invagination on the plasma membrane surface, and might be involved in signal transduction, cell cytosis and lipid regulation (Simons and Ikonen, 1997; Parton, 2003; Mouritsen, 2005). However, the identity of caveolae as a type of the rafts is still controversial (Feigenson, personal communication; Simons and Ikonen, 1997; Jacobson et. al., 2007).

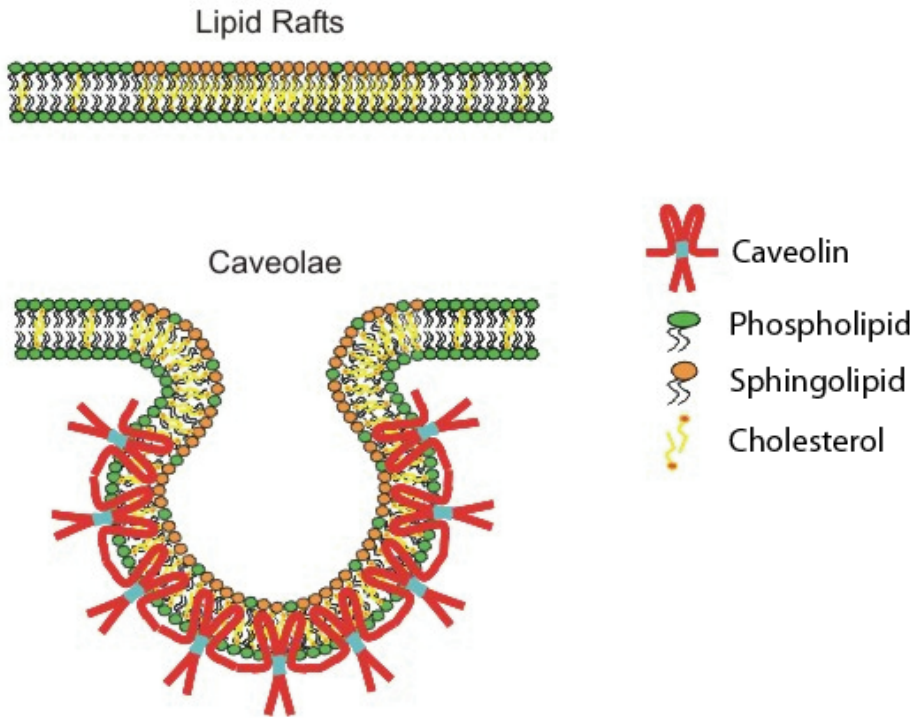

Figure 1.2.4. Model of lipid rafts and schematic representation of caveolae. The two entities share a common feature of the enrichment in sphingolipid and cholesterol. The similarity led some researchers to believe that caveolae is a type of lipid rafts. The protein caveolin is specifically localized in caveolae and may stabilize its curved structure. (The figure is from Razani and Lisanti (2002))

Inquiries into the physical origin and characteristics of lipid rafts have benefited from studies on model membranes (Feigenson, 2009). Contrary to their biological counterparts, model membranes have defined compositions and are usually the ternary mixtures of lipids, which contain cholesterol, a lipid species with high melting point and another lipid species with low melting point. It was observed in model membrane studies that lipids in specific conditions and compositions were capable of phase-separating into two coexisting liquid crystalline phases: the commonly seen liquid-disordered (L_d or L_α) phase and the relatively seldom observed liquid-ordered phase

(L_o). The latter exhibits both characteristics of the liquid crystalline L_d phase by its lateral fluidity and those of the gel L_β phase (see Section 1.3) by its orderly arranged hydrocarbon chains (Figure 1.2.5; Ipsen et. al., 1987; Dietrich et. al., 2001; Veatch and Keller, 2005). This liquid-liquid immiscibility was speculated to be the physical origin of lipid raft formation, with the rafts in the L_o or L_β phases and the bulk lipid matrix in the L_d (L_α) phase (Rietveld and Simons, 1998; Lingwood and Simons, 2010). Nevertheless, while the L_d and L_β phases have been readily observed in cells, the L_o phase and the accompanying phase separation phenomenon seen in model systems have proven to be experimentally elusive in living cells. This fact raised suspicions toward biological relevance of the L_o phase (Kaiser et. al., 2009; Lindwood and Simons, 2010) or even toward the very existence of lipid rafts (Munro, 2003; Jacobson et. al., 2007). Even though growing experimental evidence has favored the existence of lipid rafts, many questions remain to be answered. For example, while membrane shapes and curvatures are believed to affect formation of the rafts as well as their distribution across membranes (Baumgart et. al., 2003; Pencer et. al., 2008; Roux et. al., 2005; Parthasarathy et. al., 2006; Parthasarathy and Groves, 2007; van Meers et. al., 2008; Sorre et. al., 2009; Kurczy et. al., 2010), to our best knowledge the underlying mechanisms are still unclear. Systematic studies are therefore desired to understand whether and how the lipid collective properties, such as the monolayer spontaneous curvature (the curvature adopted by a lipid monolayer if it could be totally relaxed; see Section 2.2.4 for more details), of non-raft lipids affect lipid rafts and their associated membrane proteins. This information may provide insight on the mechanisms behind the influences of membrane shape and curvature on the rafts. This notion is shared with a recent review on the membrane curvature (Parthasarathy and Groves, 2007). It may worth mentioning that the liquid-liquid phase separation phenomenon, speculated as the physical basis of the lipid raft model, appeared to be

(a)

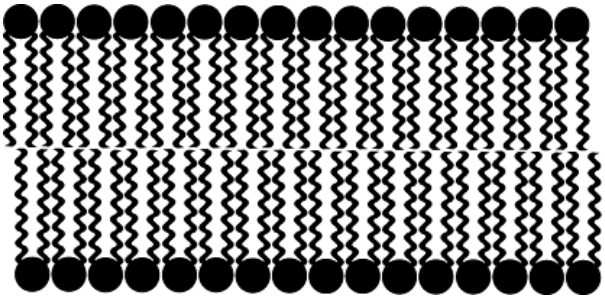

(b)

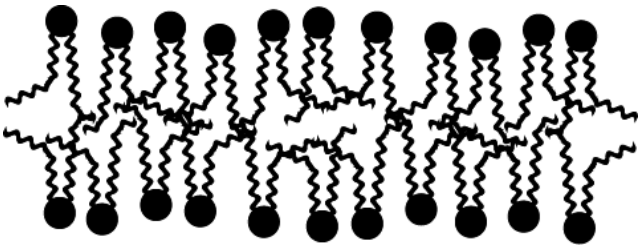

(c)

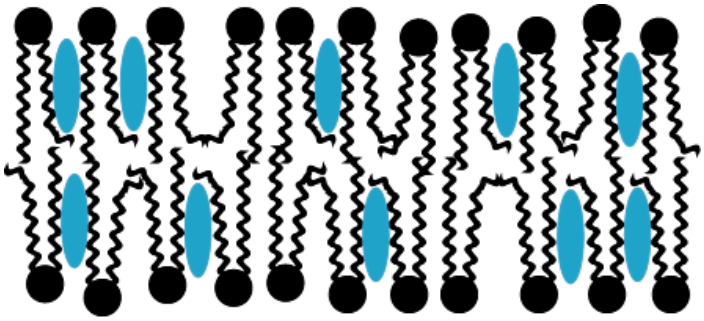

Figure 1.2.5. Models of gel L_β phase (a), liquid crystalline L_d (or L_α) phase (b) and liquid crystalline L_o phase (c). Blue ellipses are cholesterol molecules. The L_o phase possesses hydrocarbon chains with a highly ordered structure while still exhibits fast translational diffusion. In contrast, the other two phases exhibit either a highly ordered structure (the L_β phase) or fast translational diffusion (the L_d phase).

observed in our cardiolipin system. To our best knowledge, this observation is likely to be one of few, if not the only, instances that this phase separation phenomenon is seen in a one-component charged phospholipid system. Whether this observation has any biological implication is out of our scope.

Despite the prominence of bilayer structures, biomembranes are in fact far from being flat at times. Membrane-bound organelles and cells *per se* exhibit rich and complex shape geometries, both spatially and temporally. Examples include some intracellular organelles, such as endoplasmic reticulum and mitochondria, and some specialized cells, such as neurons and some epithelial cells (Figure 1.2.6). These entities display highly curved structures in at least parts of their membranes. Cells frequently produce transient small membrane-bound vesicles, characterized by high curvatures during and after their formation (Figure 1.2.6), to transport molecules among intracellular organelles as well as among intercellular entities. Highly curved membrane structures are also observed in the proximity of the nuclear pores on cell nucleus surfaces. Apparently, maintaining these curved structures is required for proper cell functions and indeed is conserved across species (Voeltz and prinz, 2007). Given the abundance of the proteins surrounding and within biomembranes, protein-lipid interactions are naturally expected to play an important role in this biomembrane deformation. Indeed, facilitating the formation of curved biomembrane structures is an important biological function of proteins and is carried out through their interactions with lipids (McMahon and Gallop, 2005; Parthasarathy and Groves, 2007). Mechanisms of these protein-lipid interactions can be roughly classified into two categories: active force application and surface area modulation. In the former, proteins deform membranes by attaching onto membrane surfaces, say, their banana-shaped domains (BAR domains) as scaffolds

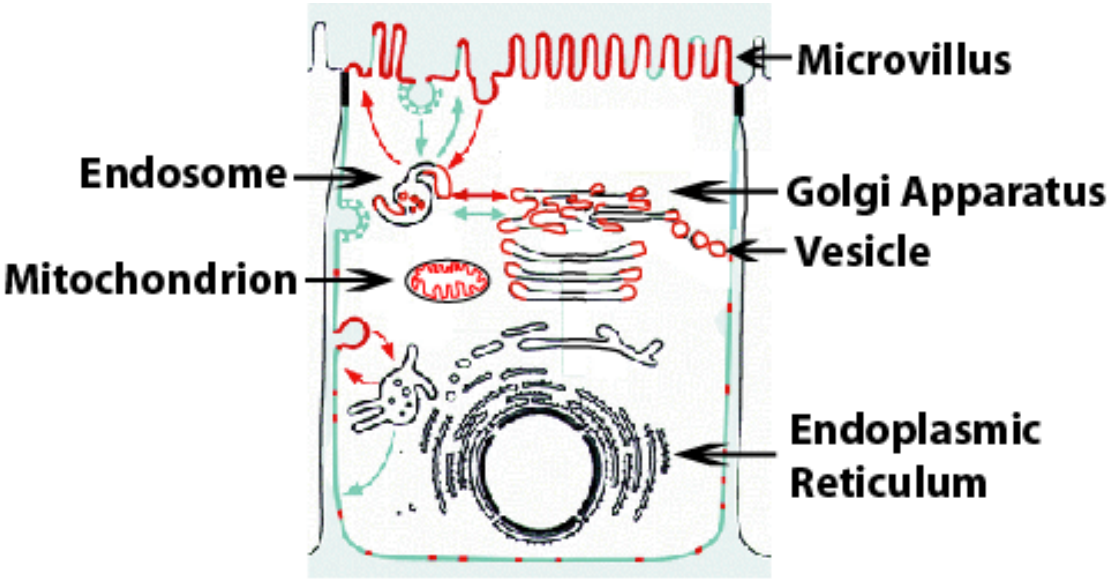

Figure 1.2.6. Illustration of a kidney epithelial cell. Some of the highly curved structures are marked with red. (The figure is adapted from Simons and Ikonen (1997))

(Peter el. al, 2004; McMahon and Gallop, 2005) or by the forces applied by cell cytoskeleton and its motor proteins (Dabora and Sheetz 1988; Yarar et. al., 2005; Zimmerberg and Kozlov, 2005). In the second type, the curvatures are produced by modulating biomembrane surface areas. Presence of wedge-shaped protein domains within biomembranes may modify the surface areas of lipid headgroups relative to that of hydrocarbon chain region and effectively bend the biomembranes toward one side or the other (McMahon and Gallop, 2005; Ford et. al, 2002). Another strategy employed by cells to achieve the surface area modifications is tuning lipid compositions in biomembranes by enzymes. Lipid compositions in biomembranes are complex and diverse, with some species preferring lamellar structures and some favoring curved ones, depending on their molecular shapes (see Section 1.3.3).

Producing and concentrating the lipids with curving tendencies would result in bending of biomembranes from lamellar structures (Kooijman et. al., 2005; McMahon and Gallop, 2005; Parthasarathy and Groves, 2007).

Not only can proteins modify the physical properties of lipid membranes but changes in lipid collective properties would also affect the conformations and functions of proteins (Phillips et. al., 2009; Andersen and Koeppe, 2007). Mechanosensitive channels and voltage-dependent potassium channels are two examples of membrane proteins that are regulated through modulations of the lipid collective properties. Activities of the two proteins were seen to be affected by mechanical stimuli, such as membrane tension (Yoshimura and Sokabe, 2010; Perozo et. al., 2002), and transmembrane electrical potentials (Long et. al., 2005; Jiang et. al., 2003), respectively. The collective properties relevant to lipid-mediated biological activities may include, but are not limited to, the bilayer thickness, the monolayer spontaneous curvature (see Section 2.2.4), the monolayer bending modulus (a constant measuring the stiffness of a lipid membrane) and the transmembrane electrical potential. These factors may not act alone and, as discussed above, can be modulated directly by protein activities or indirectly by enzyme-mediated lipid composition changes. While the former type of modulations implies the potential mechanisms of lipid-mediated protein-protein interactions (Phillips et. al., 2009), the latter reflects a long-standing question in the study of biomembranes: why do cells maintain the curvature-favoring lipids in their flat bilayer membranes even though this inevitably increases the elastic energy stress within the membranes and therefore is energetically costly? One of the leading explanations is that retaining the "non-lamellar" lipids (i.e., the lipids spontaneously forming curved structures if they could be totally relaxed) enables cells to fine-tune the spontaneous curvatures of their membranes within an

optimal range, which may be required for proper protein functions and folding (Gruner, 1985). Indeed, changes in the spontaneous curvature were shown to shift the conductance states of the ion channel alamethicin (Keller et. al., 1993), to regulate the activity of the enzyme CTP:phosphocholine cytidylyltransferase (Attard et. al., 2000), to distort the structure of the key photosynthetic membrane protein bacteriorhodopsin (Kulkarni et. al., 2010), and to shift the equilibrium between two rhodopsin substates (Soubias et. al, 2010). In addition to the spontaneous curvature, other lipid elastic properties such as the bending modulus are generally considered important factors in regulating protein functions (Lundbak et. al., 2010; Lundbak et. al., 2005; Lundbak, 2006). While the collective properties of membranes are the consequence of lipid-lipid interactions and are perturbed by lipid-protein interactions and the immediate environments, the same factors also dictate lipid polymorphic phase behavior (Siegel et. al., 2006; Chavarha et. al., 2010; Haney et. al., 2010). Therefore, understanding the mechanisms behind lipid polymorphism is expected to provide insight on how lipids mediate membrane protein functions, how membrane proteins interact with lipids and how biomembranes adapt to environmental changes among others. This is also what the presented thesis study aspires to do

Due to their compositional simplicity relative to biomembranes, one-, two- or three-component model lipid membranes have long served to elucidate the essentials of their more complex biological counterparts, despite the risk of oversimplification. In the following section, we will briefly review the fundamentals of lipid polymorphism learned from model membranes. Forces driving the lipid polymorphic phase behavior as well as its theoretical models will be further discussed in the next chapter.

1.3 Lipid Liquid Crystals and Gels

1.3.1 Lipid Phases

Biomembranes are liquid crystals. Maintaining a structure rigid enough to confine and regulate the cellular contents while fluidic enough to permit enzymatic reactions carried out near and within the structure is a prerequisite for proper cell functions and even for the very survival of cells (Collings, 2002). Lipids can form various liquid crystalline mesophases, either lamellar or non-lamellar depending on the environmental conditions and lipid identity, when they are dispersed in water as a single- or two-component model lipid membrane (Gruner et. al., 1985). In this way, the liquid crystals formed by lipids are lyotropic liquid crystals, most common of which are mixtures of amphipathic molecules and solvents (Figueiredo Neto and Salinas, 2005; Khoo, 2007). As discussed earlier, lipid bilayers are the most common structures in biomembranes. These structures are designated as lamellar phases. According to states of their hydrocarbon chains, the lamellar phases can be further categorized into L_α (Figure 1.2.5b), L_β (Figure 1.2.5a), $L_{\beta'}$ (Figure 1.3.1a), L_c (Figure 1.3.1b) and other less observed phases, including the L_o phase (Figure 1.2.5c) introduced in Section 1.2 (nevertheless, the L_o phase has thus far only been observed in multi-lipid component membranes). Among them, L_β, $L_{\beta'}$ and L_c are in the "gel" state rather than in the liquid crystalline state. In the L_α phase, hydrocarbon chains are in the fluid state without ordered structures, and lipid molecules exhibit rapid translational diffusion. This phase represents the structures commonly seen for biomembranes *in vivo*. When temperature is depressed or other thermodynamic parameters (such as pressure) are correspondingly changed, the hydrocarbon chains become rigid and lipid self-assembled structures may transform to the L_β phase, with all the hydrocarbon chains perpendicular to the bilayer plane, or to the $L_{\beta'}$ phase, with

(a) (b)

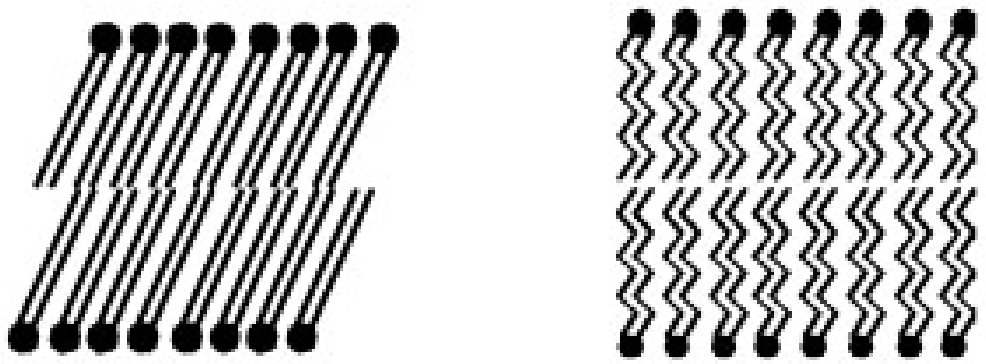

Figure 1.3.1. Illustrations of the tilted lamellar gel $L_{\beta'}$ phase (a) and lamellar crystalline L_c phase (b). (The figure is adapted from Mannock et. al. (2007))

all the chains tilted in some angles relative to the surface normal. This process is conventionally known as the lipid main transition. In these gel phases, the rigid hydrocarbon chains are spatially arranged in lattice-like structures, and lipid molecules are deprived of or considerably lose their translational diffusivity, making lipid membranes display the gel characteristics literally. Compared to the L_α phase, hydrocarbon chains in the gel phases stretch farther due to the ordered structures and lack of flexibility. The extended hydrocarbon chains are experimentally reflected on positions of the X-ray scattering peaks while the ordered hydrocarbon chain structures are revealed by sharp peaks in the wide angle scattering regime, in which only diffuse peaks are observed for hydrocarbon chains of the L_α phase (see Section 3.2.3 for details). If temperature is further depressed, the hydrocarbon chains would obtain orientational orders in additional to translational ones, and the crystalline L_c phase is formed.

On the other hand, if temperature is elevated (or again other thermodynamic parameters are correspondingly changed) beyond the points where the L_α phase are

stable, lipids may display various liquid crystalline phases with distinct non-lamellar structures. The non-lamellar structures formed by lipids are classified into two categories: the normal or type I phase and the inverted or type II phase (Figure 1.3.2). In the normal (type I) phases, lipid self-assembled structures are surrounded by water, with their polar headgroups on the surfaces and their hydrophobic chains buried inside (oil-in-water structures). These structures are readily observed in daily life when drops of cooking oil are dispersed in water. On the other hand, the inverted (type II) phases demonstrate the structures in which water are surrounded by dominating hydrocarbon chains with the headgroups lining the lipid-water interfaces (water-in-oil structure). The lipid preference to the normal or the inverted phases is more or less determined by the level of hydration and lipid molecular shapes (see also the discussion in Section 1.3.3), with higher hydration levels and larger headgroups sizes relative to

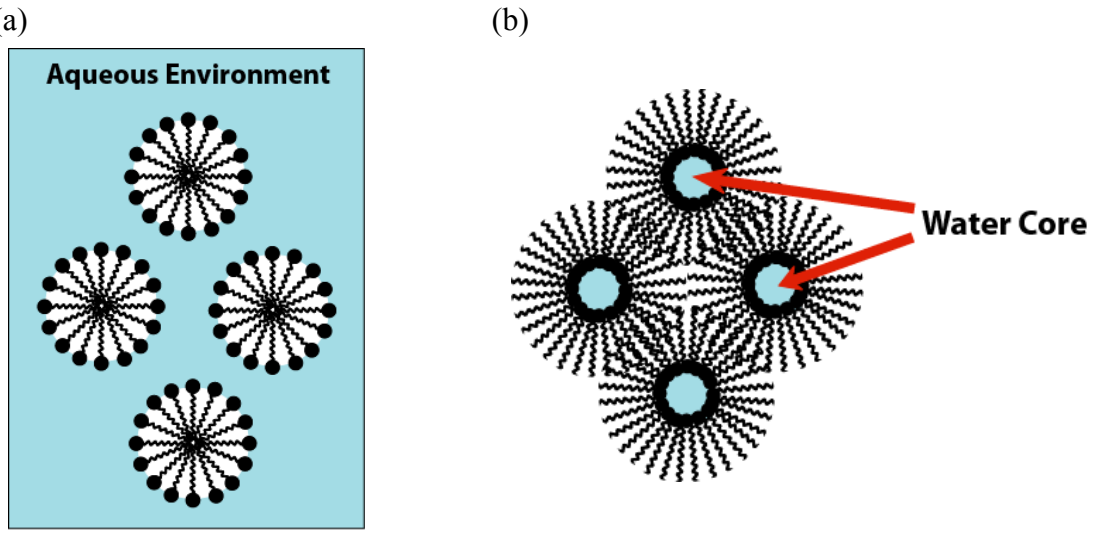

Figure 1.3.2. Illustrations of normal or type I (a) and inverted or type II (b) phases of lipid non-lamellar structures. Blue color denotes the aqueous environment.

hydrocarbon chain regions favoring the normal phases. Therefore, the normal phases are usually observed in lipids like surfactants with relative large headgroups (note "lipid" is broadly defined here. See the beginning of Section 1.2 for the definition) while non-lamellar structures of phospholipids (such as the subject of this thesis study, cardiolipin) are usually the inverted phases. The latter is the focus of our discussion here.

The inverted hexagonal phase, or the H_{II} phase, is probably the most well studied non-lamellar liquid crystalline phase in lipids (Seddon, 1990). In the H_{II} phase, lipids are arranged to form cylinders with water-filled channels in the centers and with the hydrocarbon chains spreading out from the lipid-water interfaces (Figure 1.3.3). These

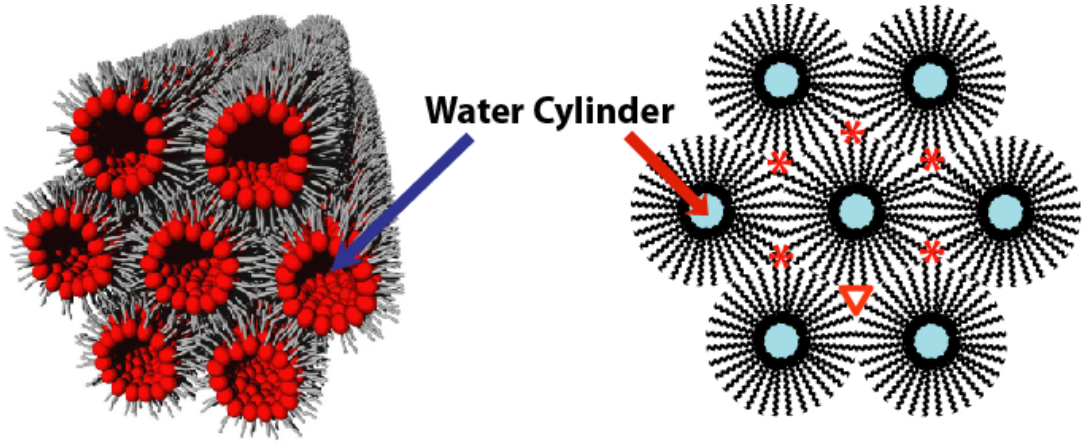

Figure 1.3.3. Structure of the lipid liquid crystalline H_{II} phase viewed from different angles. Red stars mark the positions where the hydrocarbon chain packing constraints arise (see the text). An energetically forbidden vacuum (red triangle) will appear if all the hydrocarbon chains are fixed in an identical length. (The left panel is adapted from Tresset (2009)).

channels are conventionally known as water cores. The H_{II} cylinders are arranged in a 2-D hexagonal lattice when they are viewed in cross-section. As noted in Figure 1.3.3, voids appear between cylinders when they are piled with one another. In order to fill the voids, hydrocarbon chains located in different positions along the water core circumstances have to stretch differentially. This differential stretching results in an energy cost and is one of the competing factors dictating lipid phase preference (see Section 2.2.3 for more details; Kirk and Gruner, 1985; Gruner, 1985).

Another important group of lipid non-lamellar structures are the inverted bicontinuous cubic phases or the Q_{II} phases (Shearman et. al, 2006; Seddon and Templer, 1993; Tate et. al., 1991). These phases have drawn much experimental and theoretical interest not only for their fascinating complex structures but also for their speculated biological roles: understanding of the Q_{II} structures and the transition mechanism from the L_{α} phase is believed to elucidate biomembrane fusion processes (Siegel et. al., 2006; Luzzati, 1997). The Q_{II} phases are also of great use in membrane protein crystallization and act as a substitute of cell membranes in the crystallization process (Caffrey, 2008). Unit cells of the Q_{II} phases exhibit cubic crystallographic symmetries. Within a Q_{II} unit cell, lipid monolayers are modeled as draping on either sides of infinitely periodic minimal surfaces or IPMS (Andersson et. al., 1988; Mariani et. al., 1988), where the minimal surfaces are the surfaces with zero mean curvature at every point on the surfaces (note this does not necessarily mean the surfaces are flat! They can be curved while still having zero mean curvature everywhere on the surfaces. See Figure 2.2.2 and Section 2.2.4 for more details). The imaginary IPMS is in the midplane of a lipid bilayer (Figure 1.3.4) and extends continuously to fill the Q_{II} unit cell. Divided by this continuous lipid bilayer are two separate but intertwined continuous water channels; the structure is therefore called "bicontinuous". The most

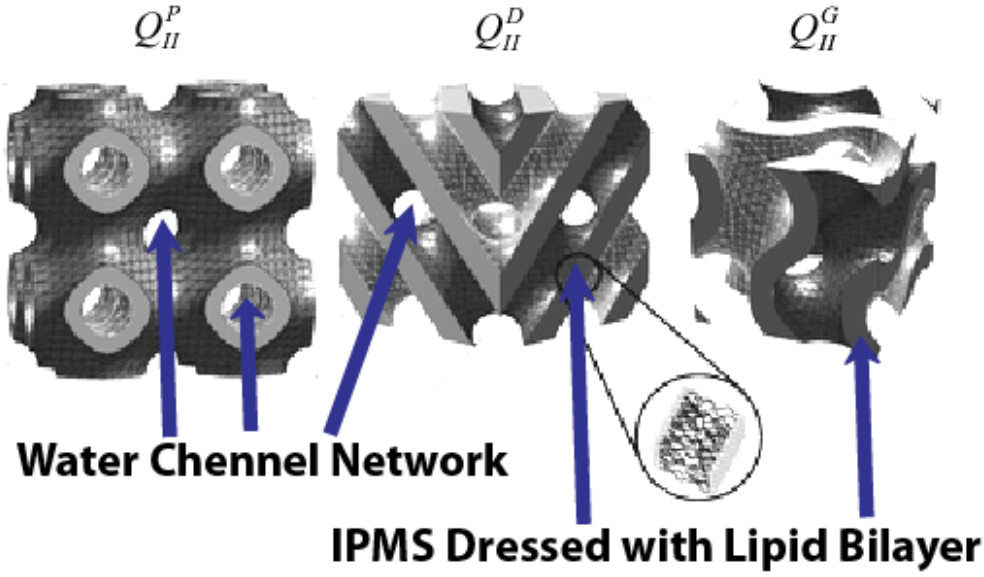

Figure 1.3.4. Unit cells of the lipid liquid crystalline Q_{II} phases with the space groups of *Im3m*, *Pn3m* and *Ia3d* (from left to right). Lipid bilayers wind through the unit cells along the IPMS of Plumber's nightmare, Double diamond and Gyroid (from left to right) and separate the water channels into two independent but intertwined networks. (The figure is adapted from Squires et. al. (2009))

commonly observed lipid Q_{II} structures are those constructed upon the IPMS of Schwartz diamond (denoted as D or the double diamond), Schwartz primitive (P or the plumber's nightmare) and Schoen gyroid (G or the gyroid), which in turn exhibit cubic symmetries with the crystallographic space groups of *Pn3m* (Q_{II}^{D}), *Im3m* (Q_{II}^{P}) and *Ia3d* (Q_{II}^{G}), respectively (Shearman et. al., 2006). There appears to be a universal relationship in the hydration level among these three phases, with the plumber's nightmare structure having the highest water content and the gyroid phase the least (Shearman et. al., 2010).

When the water content is drained, or equivalently the monolayer mean curvature decreases beyond some points, usually where the H_{II} phase is stable and dominating, a

lipid self-assembled structure may transform to one of the inverted periodic micellar phases before becoming an isotropic inverted micellar solution exhibiting no long-range orders (Seddon et. al., 2000; Seddon and Templer, 1995). In contrast to the bicontinuous Q_{II} phases, the micellar phases are "discontinuous" structures in which only the hydrophobic volumes (in the case of type II phases) extend continuously to fill the unit cells, and the hydrophilic volumes are confined in discrete quasi-spherical space and buried inside the hydrophobic volumes (Figure 1.3.5). Unlike its type I counterpart, not many periodic micellar phases were observed in the type II structures. A structure in the space group of *Fd3m* with a cubic symmetry had long been the only

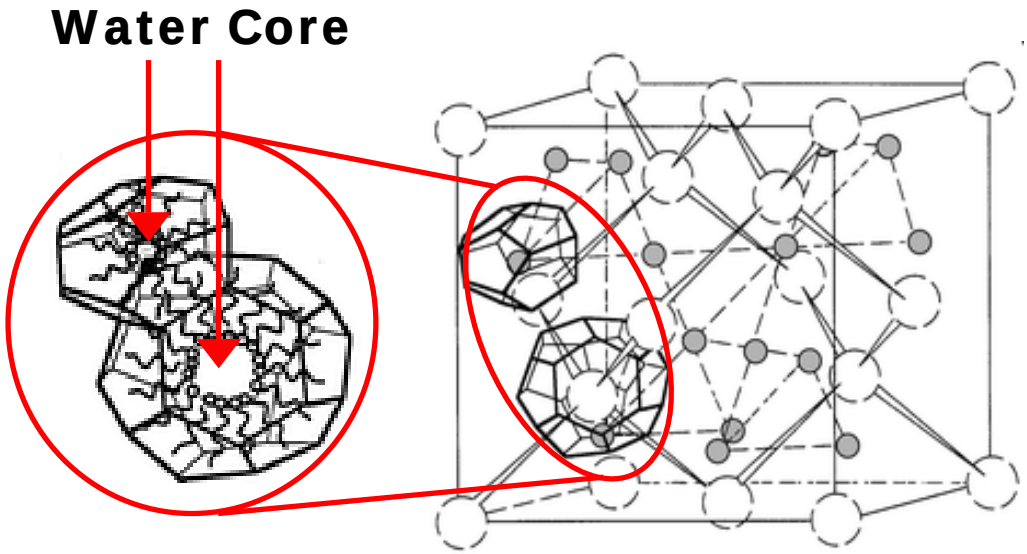

Figure 1.3.5. Unit cell of the inverted micellar cubic phase with the space group of *Fd3m*. The unit cell is comprised of two types of inverted micelles, whose positions are marked with two types of spheres. The enlargement shows the two different micelles, which are in quasi-spherical shapes with water cores buried inside and hydrocarbon chains spreading out from centers. (The figure is adapted from Seddon et. al. (2000))

observed inverted periodic micellar phase until a recent study expanded the list by adding a structure in the space group of $P6_3/mmc$ with a hexagonal symmetry (Shearman et. al., 2009). As will be discussed in Sections 4.2 and 4.5, a phase displaying crystalline-like X-ray scattering patterns was observed in our cardiolipin system. This structure was indexed as in the space group of *P4* with a tetragonal symmetry. Given the low water content in which the phase was observed, the 3-D periodicity appears to imply that the structure was in an inverted micelle configuration. If confirmed, this phase might be a new entry in the thin list of inverted periodic micellar structures.

1.3.2 Phase Sequence

Figure 1.3.6 shows a hypothetical phase diagram of a lipid-water mixture system as a function of the monolayer mean curvature. This diagram demonstrates a phase sequence expected for the liquid crystalline phases introduced in Section 1.3.1 (Seddon et. al., 2000; Seddon and Templer, 1995). The L_α phase is in the middle of the diagram and represents the structure with a nearly zero curvature. Magnitude of the mean curvature increases in either direction from the center. Curvatures of the inverted phases are designated as negative, with the water-lipid interfaces bending toward water, and those of the normal phases as positive. It can be seen that every type II structure has its counterpart in the type I phase. The phases between the L_α and hexagonal phases (regions b and c in Figure 1.3.6) are the bicontinuous cubic structures, and those between the hexagonal phases and isotropic micellar solutions (regions a and d) are the periodic micellar phases. However, lipid liquid crystals do not necessarily follow this sequence exactly in the real world. Indeed, the well-studied DOPE- (dioleoylphosphatidylethanolamine, a lipid with two 18:1 hydrocarbon chains,

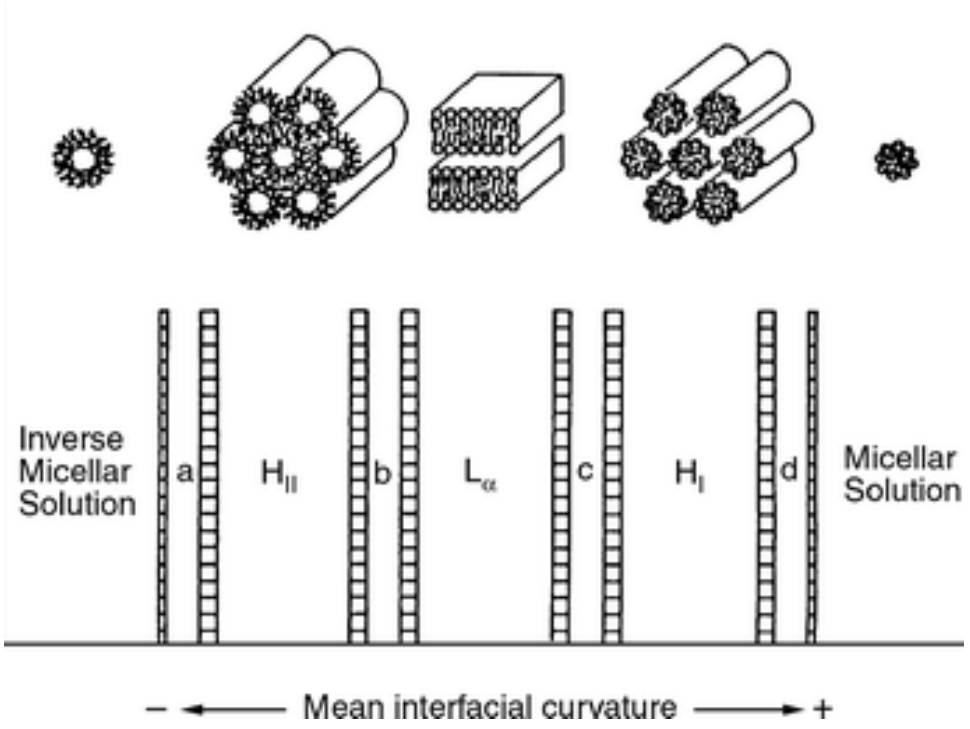

Figure 1.3.6. Hypothetical phase diagram for a lipid-water mixture system as a function of the monolayer mean curvature. The L_α phase is in the middle of the diagram and exhibits a nearly zero curvature. As magnitude of the curvature increases in either direction, the lamellar phase may transform through the cubic phases (regions b, c), the hexagonal phases (regions H_{II}, H_I) and the discontinuous micellar phases (regions a, d) to isotropic micellar solutions. (The figure is from Seddon et. al. (2000))

i.e., 18 carbons and one double bond) water mixture systems never form any of the Q_{II} phases during the $L_\alpha \leftrightarrow H_{II}$ phase transition when they are subjected to a simple temperature variation or pressure perturbation. This is because the kinetic barrier prevents the Q_{II} phases from forming in the experimental time scale; the intermediate Q_{II} phases can only be induced after the DOPE-water systems are incubated at high pressure or under pressure/temperature cycling across the $L_\alpha \leftrightarrow H_{II}$ transition points (So et. al., 1993; Shyamsunder et. al., 1988). Some studies even disputed validity of the

$L_\alpha \leftrightarrow Q_{II} \leftrightarrow H_{II}$ sequence and argued that $L_\alpha \leftrightarrow Q_{II}$ and $L_\alpha \leftrightarrow H_{II}$ actually follow different paths (Siegel, 1999).

1.3.3 Factors Determining the Phase Behavior

Many factors may affect lipid phase preference. Most of these factors involve effects of the monolayer spontaneous curvature. The manifest time-averaged molecular shape of a lipid is one of the characterizations of a polymorphic phase (Figure 1.3.7). It reflects the relative cross-sectional areas of headgroups and hydrocarbon chain region among others. Lipid molecules with nearly zero spontaneous curvatures prefer the L_α phase when they are lumped together. On the other hand, lipids with manifest large headgroups or hydrocarbon chain regions tend to form non-lamellar phases. The most abundant lipid species in biomembranes, phosphatidylcholine (PC), is a typical example of the former type. This may explain the prominence of bilayer structures in biomembranes. However, another common lipid species in biomembranes, phosphatidylethanolamine (PE), is a typical wedge-shape preferring. Its presence imposes the elastic stress within the lamellar biomembranes. Temperature is another important factor that can dictate the assumed, time-averaged molecular shape of a lipid. When temperature is elevated, stronger thermal motions expand the space occupied by hydrocarbon chains and facilitate *trans*- to *gauche*-isomerization of carbon-carbon single bonds of the chains. These phenomena consequently favor the non-lamellar structures. Similarly, electrostatic interactions arising from the headgroups of charged lipids also affect the averaged lipid molecular shapes. The subject of this thesis study, cardiolipin, is a typical example. With its bulky quadruple-chained configuration, cardiolipin is expected to prefer wedged molecular shape and favor the H_{II} phase. However, electrostatic lateral

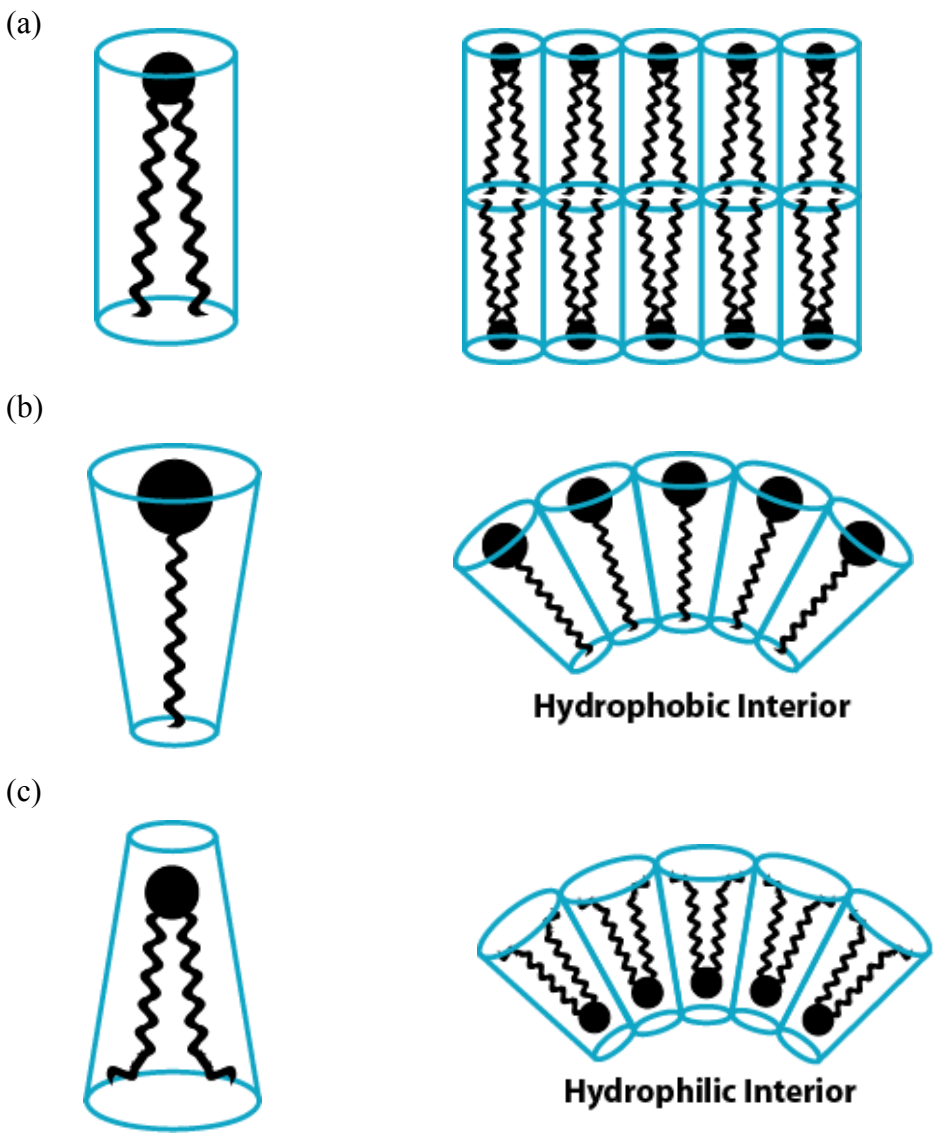

Figure 1.3.7. Lipids with three types of resultant "molecular shapes": molecules with cylindrical shapes are in the lamellar phases (a); molecules with wedged shapes are in the inverted non-lamellar phases (b) or the normal non-lamellar phases (c), depending on the relative sizes of headgroups and hydrocarbon chain region, as well as other interactions.

repulsion among the charged headgroups forces cardiolipin molecules to adopt a cylindrical shape volume and a lamellar structure in the physiological condition. Screening the surface charges by adding counterions (Rand and Sengupta, 1972; Vasilenko et. al., 1982; Loosley-Millman, 1982; Seddon et. al., 1983), by protonation (Seddon et. al., 1983) or by mixing cardiolipin with a cationic lipid (Lewis and McElhaney, 2000) usually restores the average wedged shaped geometry and facilitates formation of the H_{II} phase.

Given the importance of hydrophobic interactions in self-assembly of amphipathic molecules, it is not surprising that hydration plays a significant role in determining the phase behavior of lipid-water mixtures (Rand and Parsegian, 1989). In general, lower hydration levels favor the structures with more negative monolayer mean curvatures, as shown in Figure 1.3.6 (Seddon and Templer, 1995). Sometimes this may simply be the result of a geometrical constraint: water molecules are too few to construct a lamellar phase. Other mechanisms of the hydration contributions will be further discussed in Section 2.2.2.

As discussed in Section 1.2, proteins are capable of modifying biomembrane shapes. This may be carried out through their influence on the lipid phase behavior. The mechanisms include hydrophobic mismatches (the discrepancy in thickness of hydrophobic parts of lipids and proteins) and the monolayer curvature modulations induced by protein shapes (Phillips et. al., 2009; Haney et. al., 2010; Marsh, 2008). Indeed, the $L_{\alpha} \leftrightarrow Q_{II}$ and $L_{\alpha} \leftrightarrow H_{II}$ phases transition temperatures were observed to decrease with increasing concentration of an α-helical transmembrane peptide, WALP. Studying the protein inclusion effects on the lipid phase behavior also provides insight

on functional mechanisms of pulmonary surfactant proteins, SP-B and SP-C, and antimicrobial peptides (Chavarha et. al., 2010; Haney et. al., 2010).

1.4 Cardiolipin and the Phase Transitions

As with DOPS and other anionic phospholipids, charges on the cardiolipin headgroups apply significant influences on its phase behavior, presumably through their effects on the spontaneous curvature (see Section 2.2.5). Removal of the headgroup charges has seen a phase transition to the (single) H_{II} phase from otherwise monotonic lamellar structures. This understanding for cardiolipin was historically established with the observations on the bovine heart cardiolipin (a natural mixture of various cardiolipin species, extracted from the inner mitochondrial membranes of beef hearts). Rand and Sengupta (1972) had found that divalent cations, calcium, magnesium and barium ions, precipitated the bovine heart cardiolipin into the H_{II} structures (the precipitation should indicate the excess water condition of the cardiolipin) from the initial lamellar phase. A later study by Seddon et. al. (1983) supplemented the observation by studying the headgroup charge modification of the bovine heart cardiolipin with a pH control and sodium chloride addition; cardiolipin formed the H_{II} phase at pH < 2.8 or, at pH = 7, in the NaCl concentration > 1.6 M. Comparing the two studies found that at a given temperature the minimum concentration required for the H_{II} phase formation was considerably higher for sodium ions (1.6 M) than for calcium ions (1 mM) and other divalent cations. This may be associated with the two negative charges carried by a cardiolipin molecule. Indeed, it was found that formation of the H_{II} phase induced by mixing tetramyristoyl-cardiolipin (C14:0) with a single-charged cationic lipid, DM-TAP (1,2-dimyristoyl-oxy-3-*N,N,N*-trimethylaminopropane, with the identical type of hydrocarbon chains to that of tetramyristoyl-cardiolipin) occurred at the lowest

observed temperature when the molar ratio of the cardiolipin and DM-TAP was in 1:2; in other words, the transition temperature was at the lowest when the resultant lipid mixtures were electrically neutral. In addition, an important mitochondrial protein, cytochrome C, was seen to induce the H_{II} phase formation within pure cardiolipin membrane or the lipid membranes containing a substantial cardiolipin composition (De Kruijff and Cullis, 1980). This fact may imply the need of the non-lamellar structure-forming ability of cardiolipin for the proper function of a mitochondrion.

The type of hydrocarbon chains is also an important factor in determining the cardiolipin phase preference. A study by Vasilenko et. al. (1982) compared the phase behavior of the bovine heart cardiolipin (containing 88.5% C18:2 cardiolipin) with that of the cardiolipin extracted from the bacterium, *Bacillus subtilis* (containing mostly the cardiolipin with saturated hydrocarbon chains; ~50% C15:0) when the two cardiolipin species were mixed with divalent cations. The authors found that for a given type of counterions the lamellar-H_{II} phase transition temperature was significantly lower in the case of the bovine heart cardiolipin. Indeed, a more controlled experiment carried out for the synthetic cardiolipin revealed that tetraoleoyl-cardiolipin (C18:1, the same cardiolipin species employed in this thesis study) exhibited the $L_{\alpha} \leftrightarrow H_{II}$ phase transition at 25 °C and in the sodium chloride concentrations ≥3.5 M whereas tetramyristoyl cardiolipin remained in the lamellar phases even when the temperature reached 60 °C and the NaCl concentration to 6 M (Sankaram et. al., 1989). Taking together their observations and those from other studies, the authors concluded that higher unsaturation and longer length of hydrocarbon chains lowered the threshold for the H_{II} phase formation.

(a)

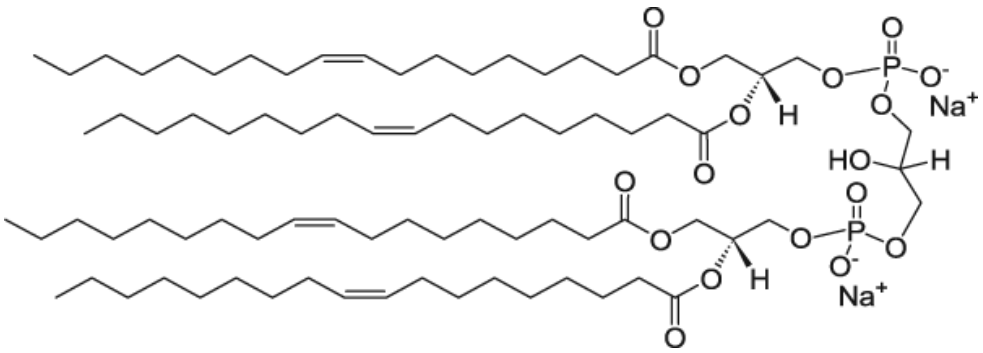

(b)

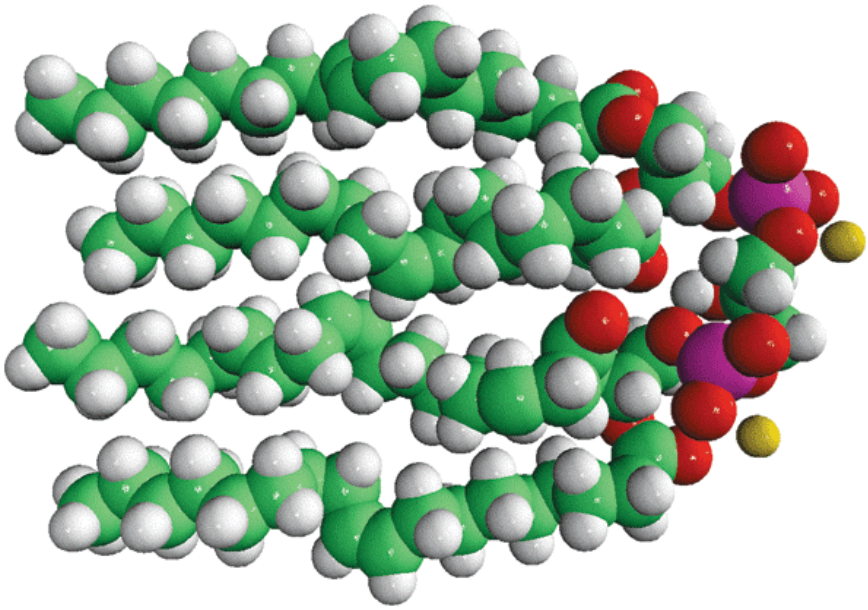

Figure 1.4.1. Chemical structure (a) and space filling model (b) of a cardiolipin molecule. In (b), red spheres are oxygen atoms; pink spheres are phosphorus atoms; dark yellow spheres are sodium ions; green spheres are carbon atoms; white spheres are hydrogen atoms. The models are from our lipid supplier, Avanti Polar Lipids, Inc. (http://www.avantilipids.com).

Given the unique quadruple configuration (Figure 1.4.1), it is not surprising to know that the number of hydrocarbon chains present in a molecule is crucial to the cardiolipin phase behavior. In their nuclear magnetic resonance and X-ray diffraction

study, Powell and Marsh (1985) prepared the cardiolipin molecules with different hydrocarbon chain configurations by acylating or deacylating the bovine heart cardiolipin. The authors found that, with the sodium chloride concentrations up to 3 M, the cardiolipin derivatives with double or triple hydrocarbon chain configurations could only assume the lamellar or micellar phases at room temperature whereas the derivative with five chains were in the H_{II} phase even without counterions present. Only the ordinary cardiolipin molecules exhibited a counterion-induced lamellar-H_{II} phase transition in the same condition. The quadruple hydrocarbon chain configuration of cardiolipin may therefore render cells the ability of controlling the non-lamellar structure-forming propensity by modifying local ions concentrations.

In the next chapter, the factors introduced in Section 1.3.3 will be analyzed in terms of the underlying intermolecular forces relevant to cardiolipin. Theoretical models incorporating these forces to explain the lipid phase behavior will also be reviewed.

CHAPTER 2

LIPID POLYMORPHIC PHASE TRANSITION

2.1 Introduction

Driven by hydrophobic interactions, amphipathic lipids tend to aggregate and self-assemble into various structures when dispersed in water or aqueous solutions. However, hydrophobic interactions alone cannot explain polymorphisms and structural features exhibited by lipids. In this chapter, I will discuss forces and interactions that are commonly observed to affect lipid phase preference and spatial arrangements, and also the theoretic treatments attempting to model the polymorphic phase behaviors based on these forces and interactions.

2.2 Forces and Interactions within Lipid Self-Assembled Structures

2.2.1 van der Waals Force

The van der Waals force is one of the most common molecular interactions and is present between every pair of objects. The interaction arises from spontaneous fluctuations of electric dipole moments of molecules and thus is electrostatic in nature. The interaction can be either attractive or repulsive, depending on the nature of the two interacting objects and the medium in between (Dzyaloshinskii et. al., 1961). For identical or similar molecules, the van der Waals force between two entities is attractive (Leckband and Israelachvili, 2001). Therefore, the attractive van der Waals force is a natural presence between lipid molecules and between their aggregates. The strength of the interaction increases monotonically as two objects approach to each other, and then reaches a maximum when the inter-object distance is the sum of the

respective van der Waals radii. Further shortening the inter-object distance is prohibited due to the Pauli exclusion principle, among others.

In a multi-lamellar configuration of neutral lipids, where multiple lipid bilayers are stacked and separated with inter-bilayer water volumes, van der Waals forces between neutral the lipids compete to determine the inter-bilayer distances. As water content increases, the water volumes expand indefinitely until the attractive van der Waals force counterbalances other repulsive forces (discussed below) and prevents further swelling of the water layers. Excessive water added to the system would then build up outside the multilayer structure and coexists with it. The multi-lamellar structure is therefore in the excess water condition. Similar phenomena are also observed in lipid liquid crystals in the inverted hexagonal (H_{II}) and inverted cubic (Q_{II}) phases. However, presumably due to the permanent electrostatic force, excess water points may never be reached in charged lipids, and the water volumes can expand indefinitely, provided counterions do not fully screen charges on headgroups. Mysteriously as will be presented and discussed in Chapter 4, negatively charged cardiolipin and water mixtures were observed to form a gel phase in the excess water condition even in the absence of external counterions. This observation may imply presence of some peculiar attractive interaction(s).

The van der Waals force plays an important role in lipid phase behavior. The importance of van der Waals forces in the lipid main transition (i.e., $L_\alpha \leftrightarrow$ gel transition) has long been recognized (Tristram-Nagle and Nagle, 2004). To carry out the main transition, lipids in a gel phase must overcome the attractive van der Waals force among their tightly packed hydrocarbon chains to form flexible chains found in the liquid crystalline L_α phase. This energy requirement accounts for more than half of the enthalpy in the melting (Tristram-Nagle and Nagle, 2004). Nevertheless, how the

van der Waals force affects liquid crystalline polymorphic transitions is not so well studied as in the case of the main transition. Systematic studies on how hydrocarbon chain length affects lipid polymorphic phase behavior might shed light on the role of van der Waals force in liquid crystalline phase transitions (Mannock, et. al., 2007; Brito, et. al., 2008). However, the main experimental challenge still lies in distinguishing effect of the van der Waals force from those of others. Indeed, as discussed in Gruner (2005) van der Waals force may determine lipid polymorphic phase behavior indirectly through its influence on the lipid monolayer spontaneous curvature (see Section 2.2.4). Decomposing the effects on the spontaneous curvature into those of van der Waals force and of others (e.g., electrostatic interactions discussed in Section 2.2.5) may pose a significant obstacle for experimenters. Perhaps due to this reason, few, if any, studies addressed the importance of van der Waals force in lipid polymorphic transitions. One of the few theoretic studies is reported by Kozlov et. al. (1994) and involves the DOPE-water system, which displays an unusual $H_{II} \rightarrow L_{\alpha} \rightarrow H_{II}$ phase transition sequence when dehydrated below 22 °C (Gawrisch et. al., 1992). This study explicitly expresses van der Waals force in the total free energy of the L_{α} phase while only implicitly incorporates that interaction into the monolayer spontaneous curvature for the H_{II} phase, another example of the intimacy between van der Waals force and the elastic parameter. This energy model quantitatively agrees with the experiment but even with the van der Waals force neglected, the model can still reproduce the experimental result well. In other words, the van der Waals force appears to be insignificant in the $L_{\alpha} \leftrightarrow H_{II}$ phase transition (Kozlov et. al.,1994). In contrast, another theoretical study by Siegel and Tenchov (2008) found that PE membranes must overcome the attractive van der Waals force to expand the inter-bilayer distances before being able to form a Q_{II} phase. Although the model successfully reproduced qualitative features of the $L_{\alpha} \leftrightarrow Q_{II} \leftrightarrow H_{II}$ transition observed in

experiments, the van der Waals force was still not explicitly formulated in the complex geometries. Nevertheless, these two theoretical contributions have provided a good starting point for quantitatively understanding the role of van der Waals force in lipid polymorphic phase transitions. For our cardiolipin system, the $L_\alpha \leftrightarrow H_{II}$ transition is the only confirmed lamellar-non-lamellar phase transition in the experimental conditions covered here. The van der Waals force may therefore either be contained in the consideration on the spontaneous curvature or be less important to our discussion.

2.2.2 Hydration Interactions

Hydration interactions are an important counterforce against the attractive van der Waals interaction and prevent lipid self-assembled structures from collapsing. It is believed that the hydration repulsion originates from resistance of water molecules orderly arranged on a hydrophilic surface from being disrupted and expelled (Marcelja and Radic, 1976). Some reports claim that hydration interactions may not always be repulsive and, under certain circumstances, may alternate between repulsion and attraction when two interacting objects approach to each other (Leckband and Israelachvili, 2001). For flexible, hydrophilic surfaces, such as lipid bilayers in the L_α phase, hydration interactions are always repulsive. However, hydration interactions behave much differently when the two interacting hydrophilic surfaces are smooth and rigid, features that may characterize lipid bilayers in the L_β phase. In order to further understand the origin and nature of hydration interactions, Israelachvili and Pashley (1983) measured the intermolecular force as a function of separation between two molecularly smooth mica surfaces immersed in 1 mM KCl solution. When the inter-surface distance were greater than 30 Å, potassium ions were partially adsorbed on the mica surfaces in the studied condition, and the measured force versus separation

relation closely followed the prediction of electrical double-layer theory (see Section 2.2.5 and Equation 2-14). Remarkably, the intermolecular force was observed to oscillate dramatically with a mean periodicity of ~2.5±0.3 Å when the inter-surface distance was smaller than 15 Å. While the intermolecular force was still largely repulsive, this repulsive force turned to an attractive one when the two surfaces were at 0, 2.8±0.3 Å or 5.6±0.3 Å apart. These distances, 2.8±0.3 Å and 5.6±0.3 Å, were roughly the thickness of one and two water layers, respectively.

Israelachvili, Wennerstrom and colleagues argued that the oscillatory feature observed in the mica system was a natural consequence of water molecules ordering on polar surfaces (Israelachvili and Pashley, 1983; Israelachvili and Wnnerstrom, 1996; Leckband and Israelachvili, 2001). This is a striking contradiction to the conventional belief regarding hydration interactions, which views the interaction as being repulsive in nature. The researchers also suggested that the exponentially decaying repulsive hydration interactions, commonly observed for flexible surfaces such as lipid bilayers in the L_α phase, are a smearing-out result of the supposedly oscillatory feature. However, this view of hydration interactions is still controversial and demands more theoretical and experimental efforts. Interestingly, the charged surface and rigid structure of cardiolipin bilayers in the gel phase appear to bear a close resemblance to those of the mica system studied in Israelachvili and Pashley (1983). Moreover, separations of two cardiolipin gel bilayers were observed to be far shorter than 15 Å (see Section 4.3.3). It is therefore tempting to apply the oscillatory view of hydration interactions to explaining why the charged cardiolipin bilayers could be in the excess water condition. This speculation will be further discussed in Sections 4.3.3 and 5.1.3.

2.2.3 Hydrocarbon Chain Packing Frustration

Hydrocarbon chain packing frustration arises from the need to differentially stretch hydrocarbon chains to fill the hydrophobic space in curved, inverted configuration of lipids (Kirk et. al., 1984; Kirk and Gruner, 1985; Gruner, 1989; Tate et. al., 1991; Shearman et. al., 2006). The packing stress was proposed, along with the monolayer elastic energy (Section 2.2.4), to model the competing interactions that drive the $L_\alpha \leftrightarrow H_{II}$ phase transition of lipids. In the H_{II} phase, the water-lipid interface along circumstance of a water core is speculated to arrange circularly to reduce the energy cost arising from large local monolayer curvatures inevitable with non-circular shapes. Circular shape of this interface was confirmed experimentally in Turner and Gruner (1992) and Pan et. al. (2006). However, Tuner and Gruner (1992) also found that the water-lipid interface in the H_{II} structure could deviate from a circular shape considerably when repeat distance of its unit cell was greater than ~75 Å. The authors ascribed the observation to the energetic cost of stretching lipid hydrocarbon chains relative to their relaxed lengths, particularly on locations where three unit cells of the H_{II} phase met (Figure 2.2.1). Since the radial distance from center of the unit cell to its corners is longer than to its side, hydrocarbon chains must stretch farther to fill the otherwise energetically unfavorable voids in the corners. This constraint limits the conformations accessible to hydrocarbon chains and thus incurs an entropic cost to the system. When the unit cell dimension expands, the volumes in the corners enlarge and the chains are required to stretch even farther to fill the ever expanding space. To compensate this energetic cost, the water-lipid interface deforms to minimize hydrocarbon chain packing stress. Beyond certain unit cell dimensions, the energetic cost of staying in the H_{II} phase exceeds that of bending monolayers away from their

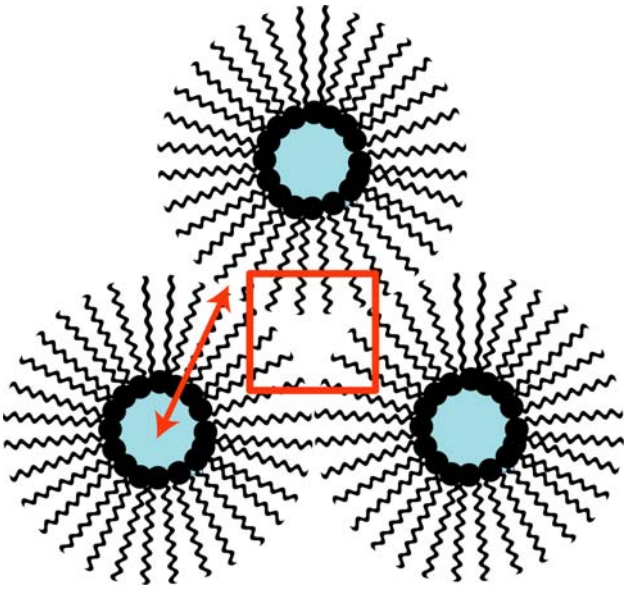

Figure 2.2.1. Unit cell of the H_{II} phase. If the hydrocarbon chains are all in a fixed length, an energetically forbidden void would emerge in the hydrophobic volume, as marked by a square. An arrow illustrates ζ (see the text).

spontaneous curvatures. As a result, lipid molecules transform from the H_{II} phase to the L_α phase. Accordingly, adding free hydrocarbons to lipid-water mixtures is expected to relieve hydrocarbon chain packing stress by filling the voids with the hydrocarbons and shift lipid phase preference to the H_{II} phase (Gruner, 1985). Indeed, Kirk and Gruner (1985) reported that adding 5 % dodecane or tetradecane to a DOPE-water mixture could reduce its L_α-H_{II} phase transition temperature significantly. Tuner and Gruner (1992) also observed the restoration of circular shape in the water-lipid interface when a small amount of alkane was present.

Several theoretical studies have attempted to model hydrocarbon chain packing stress (Kirk, 1984; Tate, 1987; Duesing et. al., 1997). The modeling starts with a Hooke's Law-based formulation to quantify energy costs of stretching or compressing hydrocarbon chains from the relaxed equilibrium length l_r,

$$g_p = k(1 - l_r)^2, \tag{2-1}$$

where k is the stretching rigidity and l is the actual hydrocarbon chain length. Taking into account the upper and lower limits on the hydrocarbon chain length, $l_{\max}$ and $l_{\min}$, Equation 2-1 becomes,

$$g_p = k' \frac{f(l)}{(1 - l_{\min})(1 - l_{\max})}, \tag{2-2}$$

where k' is a stretching constant and $f(l)$ is a function which makes g_p minimal when $l = l_r$. By solving Equation 2-2 for the extreme values, the simplest form of $f(l)$ is found to be $(l - l_r)^2$. Equation 2-1 is therefore only the first term of the Taylor expansion of Equation 2-2 and k is,

$$k = \frac{k'}{(l_r - l_{\min})(l_r - l_{\max})}. \tag{2-3}$$

With the assumption of a constant and homogeneous curvature in the water/lipid interface, the average over the interfacial surface area A of the first term of the Taylor expansion is:

$$< g_p > = k \frac{\int_A (1 - l_r)^2 dA}{\int_A dA} = k \frac{\int_A (\zeta - \zeta_r)^2 dA}{\int_A dA}, \tag{2-4}$$

where ζ is the distance between the midpoints of the hydrophobic and hydrophilic regions of an inverted lipid structure (for example the H_{II} phase see Figure 2.2.1; adopting this framework may allow generalization of the obtained formulation beyond

the H_{II} phase. See Duesing et. al. (1997) for more details), and ζ_r is the corresponding distance when hydrocarbon chains are in their relaxed lengths. Because the averaged packing energy $< g_p >$ is minimal when $\zeta = \zeta_r$, by solving the equation,

$$\frac{d < g_p >}{d\zeta_r} = 2k \frac{\int_A (\zeta_r - \zeta)\, dA}{\int_A dA} = 0\,, \tag{2-5}$$

one can obtain,

$$\zeta_r = \frac{\int_A \zeta dA}{\int_A dA}. \tag{2-6}$$

This indicates that ζ_r is in fact the average of ζ over the entire surface area A. Accordingly, one can finally obtain:

$$\begin{aligned} < g_p > &= k \frac{\int_A (\zeta - \zeta_r)^2 dA}{\int_A dA} = k \left[\frac{\int_A \zeta^2 dA}{\int_A dA} - 2\zeta_r \frac{\int_A \zeta dA}{\int_A dA} + {\zeta_r}^2 \right] \\ &= k \left[\frac{\int_A \left(\zeta / \zeta_r \right)^2 dA}{\int_A dA} - 1 \right] {\zeta_r}^2 = k\, \varepsilon_p\, {\zeta_r}^2 \end{aligned} \tag{2-7}$$

where dimensionless ε_p is denoted as the packing factor in Duesing et. al. (1997). It was noted by the authors that ε_p, the normalized variation of ζ, could be used to quantify how energetically favorable a certain way of packing hydrocarbon chains into hydrophobic space is, with a smaller value representing a lower energetic cost. By their calculations, Duesing et. al. (1997) found that, compared to other possible arrangements, lipids in a structure with a cylindrical lipid-water interface had the

lowest ε_p value of 1.865 x 10^{-3} when those lipid-water cylinders were arranged in a hexagonal lattice (i.e., the experimentally observed arrangement of the H_{II} phase). The consistency with the experimental observation may support validity of this modeling. Also implied in Equation 2-7 is that, for a given lipids spatial arrangement (i.e., a given ε_p value in this context) the packing energy $< g_p >$ of lipids should vary with the monolayer thickness and mean curvature (see Equation 2-8 in the next section) because ζ_r is a function of the thickness and curvature (for the H_{II} phase, $\zeta_r = R + l_r$, where *R* is radius of the water core). This relationship between the packing energy $< g_p >$ and the radius of water core *R* may successfully quantify the expectation that lipids arranged in the H_{II} phase have a higher packing energy cost when their water core radius becomes larger (Gruner, 1985; Gruner, 1989).

2.2.4 Elastic Energy

As discussed in the Section 1.3.3, a lipid molecule exhibits an intrinsic spontaneous curvature according to its chemical structures, and this determines spatial arrangement of lipids when they are dispersed in, say, water. Theoretically, when external constraints (e.g., hydrocarbon packing stress discussed in Section 2.2.3) are absent, lipids should self-assemble into a structure fully reflecting their spontaneous curvature. Since external constraints are inevitable in many cases, particularly *in vivo*, lipids are often forced to adopt a structure different from the optimal one. The energy cost thereby arisen is the origin of the elastic energy. The elastic energy can be conceptualized in the context of the monolayer curvature and lipid elastic properties. Figure 2.2.2 demonstrates definition of the monolayer curvature, in which the lipid-water interface is represented by a thin, curved sheet; the principal curvatures, $1/R_1$ and $1/R_2$, of any given point on the sheet are defined on two perpendicular planes. The

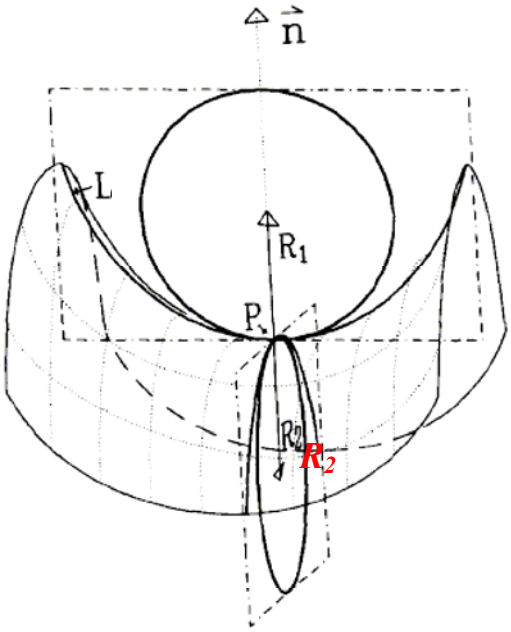

Figure 2.2.2. Definition of the principal curvatures, R_1 and R_2, for a given point P on a curved lipid-water interface. The two principal curvatures are defined individually on two planes that both contain the surface normal on P but are perpendicular to each other. (The figure is adapted from Tate et. al. (1991)).

principal curvatures in turn define the monolayer mean curvature C and the Gaussian curvature G via,

$$\begin{aligned} C &= \frac{1}{2}\left(\frac{1}{R_1}+\frac{1}{R_2}\right) \\ G &= \frac{1}{R_1 R_2} \end{aligned} \quad . \qquad \text{(2-8)}$$

For a cylindrical geometry (like the H_{II} phase), C is reduced to $C = 1/2R$, where R is the water core radius, and G is to zero; for a sphere (like a lipid micellar structure), C is to $C = 1/R$, where R is the sphere radius, and R is to $G = 1/R^2$. Conventionally, curvature of the lipid-water interface bending towards water is denoted as negative

and towards lipid as positive. Therefore, the mean curvature can still equal to zero even when the surface is bent if R_1 and R_2 are in the same value but different signs (such as the case shown in Figure 2.2.1). The mean curvature of a lipid monolayer more or less reflects the desired "molecular shapes" of the constituent lipids and, when in the absence of external constraints, is called the monolayer spontaneous curvature C_0 for that type of lipids in a given conditions (e.g., temperature and pressure). A lipid monolayer with the mean curvature equivalent to the spontaneous curvature is regarded as having minimal elastic energy. However, because of external constraints lipids may assume a structure with the mean curvature deviating from the spontaneous curvature, and an elastic energy penalty g_E arises accordingly,

$$g_E = 2K(C - C_0)^2 + K_G G, \tag{2-9}$$

where K is the bending modulus and K_G is the Gaussian modulus of lipids. These two elastic properties of lipids also vary with environmental conditions (e.g., see the discussion in the next section). The first term of Equation 2-9 quantifies the expectation that an energy penalty will be incurred to the system when a lipid monolayer is bent from its optimal mean curvature. However, physical meaning of the second term is not so straightforward and, given the difficulty in measuring the Gaussian modulus, this term is sometimes neglected in discussing free energies of lipid liquid crystals (Gruner, 1985; Gruner, 1989; Tate et. al., 1991). This omission appears to be legitimate in some cases because the Gaussian curvature vanishes in the geometries of the L_α and the H_{II} phases. However, it has been demonstrated that the Gaussian term is important in determining free energies of the Q_{II} phases and of the hypothetical intermediate structures in the lamellar-non-lamellar phase transitions (see Section 2.3.3; Shearman et. al., 2006; Siegel and Kozlov, 2004; Siegel, 2008). The

latter is important to understanding the lamellar-non-lamellar transition mechanism and may also shed light on how biomembranes proceed in a fusion process. It should be noted that Equation 2-9 only expresses the elastic energy g_E to the quadratic term. It is suggested that the fourth-order term may be required to correctly model free energies of the Q_{II} phases (Siegel, 2010).

A related question in this topic is on what surface should this elastic energy be calculated. This question is solved spontaneously in the lamellar phases but may pose a problem in other geometries. For example, the monolayer mean curvature of a Q_{II} structure determined on the plane of the hydrocarbon chain termini is clearly different from that defined elsewhere because the chain termini locate on IPMS (see Section 1.3.1) and the mean curvature is zero at any point on the plane. A conventional choice for defining the elastic energy is the pivotal surface or the neutral surface. The pivotal surface is a plane where the cross-sectional area of a lipid molecular remains unchanged upon bending; on the neutral surface, bending and stretching deformations are energetically independent (Shearmann et. al., 2006). The two surfaces nearly coincide with each other when the curvature on the lipid-water interface is not large. The elastic energy determined on the pivotal surface and with Equation 2-9 well reproduced the measured energy requirement for bending a DOPC/DOPE monolayer in the H_{II} phase to a given mean curvature (Rand et. al., 1990).

2.2.5 Electrostatic Interactions

Electrostatic interactions are another important factor that contributes to phase preference of charged lipids, such as cardiolipin. Indeed, as discussed in Section 1.3.3, electrostatic repulsion among headgroups overcomes the intrinsic wedged shape of

cardiolipin molecules endowed by the four hydrocarbon chains and favors formation of the L_α phase in physiological conditions. Neutralization of charges on the headgroups by means such as adding counterions or lowering pH often results in phase transitions of cardiolipin to the H_{II} phase (Rand and Sengupta, 1972; Vasilenko, et. al, 1982; Loosley-Millman et. al., 1982; Seddon et. al., 1983). In this thesis study, we may decompose influences of electrostatic interactions on lipid phase preference into two aspects: the contribution to the inter-bilayer potential or the equivalents for other geometries (Kirk et. al., 1984; Cowley et. al., 1978; Anderson et. al., 2010), and the contribution to lipid elastic properties discussed in Section 2.2.4 (Mitchell and Ninham, 1989; Lekkerkerker, 1989; Winterhalter and Helfrich, 1992; Taheri-Araghi and Ha, 2010). For the former, a model based on the electrical double layer theory was proposed for charged surfaces with different geometries (Israelachvili, 1992; Leckband and Israelachvili, 2001). In the double layer model, a charged surface is electrically balanced by layers of ions dispersed in the solution surrounding the surface; the first layer closer and more strongly bound to the charged surface is the Stern layer, and the layer consisting of free counterions and more removed from the surface are known as the diffuse layer. By solving the Poisson-Boltzmann equation,

$$\nabla^2\psi(x) = -(\frac{ze\rho_0}{\varepsilon\varepsilon_0})\exp(-ze\psi / k_B T), \tag{2-10}$$

where $\psi(x)$ is the electrostatic potential; x is the distance with $x = 0$ being halfway between two surfaces; z and ρ_0 are the valence and number density at $x = 0$ of counterions, respectively; e is the electronic charge; ε_0 and ε are the vacuum permittivity and dielectric constant of water, respectively; K_B is the Boltzmann constant; and T is the absolute temperature. With suitable boundary conditions, one

can obtain $\psi(x)$ and $\rho(x)$, and then derive the free energy per unit area g_{el} for the double layer model,

$$g_{el} = \left(\frac{64 k_B T \rho_\infty \gamma^2}{\kappa} \right) \exp(-\kappa D), \tag{2-11}$$

with

$$\gamma = \tanh\left(\frac{ze\psi}{4k_B T} \right), \tag{2-12}$$

and

$$\kappa = \left(\frac{\sum_i \rho_{\infty i} e^2 z_i^{\,2}}{\varepsilon \varepsilon_0 k_B T} \right)^{1/2}, \tag{2-13}$$

where κ^{-1} is the Debye screen length; ρ_∞ is the ion number density in the bulk; and *D* is the distance surfaces. By integrating Equation 2-11 over charged surfaces, Leckband and Israelachvili (2001) obtained the electrostatic interaction energies for different geometries (see Table 3 in the cited report). Functional forms specific for lipid liquid crystals in the lamellar, H_{II} and micelle phases are reported in Kirk et. al. (1984). By combining the electric double layer theory with the attractive van der Waals force, one will obtain the Derjaguin-Landau-Verwey-Overbeek (DLVO) theory, and in the case of two charged spheres the DLVO interaction potential may be written as,

$$g_{DLVO}(D) = \left(\frac{64\pi k_B T R \rho_\infty \gamma^2}{\kappa^2} \right) \exp(-\kappa D) - \frac{HR}{6D}, \tag{2-14}$$

where *R* is the radius of the spheres and *H* is the Hamaker constant for the van der

Waals force. The first term models the electrostatic interactions based on the double layer theory and the second describes the van der Waals force (note lipids forming a sphere with a large radius are equivalent of being arranged in a lamellar configuration as is the case of cell membranes). The theory has successfully reproduced many experimental results (Anderson et. al., 2010; McGuiggan and Pashley, 1988; Pashley et. al., 1986). However, it fails in more complicated cases, for example, when the distance between surfaces is shorter than ~20 Å, presumably due to increasing significance of other interactions (Leckband and Israelachvili, 2001). The DLVO theory may also be inapplicable to the case where counterions interact with charged surfaces strongly because the theory is constructed on the assumption of constant and uniform surface charge density (Taheri-Araghi and Ha, 2010). Further refinements to the DLVO theory are therefore needed to more accurately model the cases for lipid bilayers because the distances between bilayers are sometimes well below 20 Å and strong interactions between lipid and counterions are not rare.

In addition to inter-bilayer repulsion, electrostatic interactions may also modify lipid elastic properties via its lateral repulsion. The relationship between electrostatic interactions and lipid elastic properties was addressed in several theoretical and computational studies. Here, we will focus on those associated with the monolayer bending modulus *K* and spontaneous curvature C_0 (see Equation 2-9), which are directly related with this thesis study. In Lekkerkerker (1989), the Poisson-Boltzmann equation (2-10) was solved for spherical and cylindrical geometries in the limit of thin double layers (again a large sphere may be regarded as being similar to the configuration of cell membranes). The resultant electrical free energies for the two geometries are,

$$g_{el}^{sphere} = \left(\frac{K_B T}{e}\right)^2 \varepsilon\varepsilon_0\kappa \left\{ \begin{array}{l} \left[4\,(p\ln(p+q) - q + 1)\right] - \dfrac{8}{\kappa R}\ln(\dfrac{1}{2}[q+1]) \\ + \dfrac{4}{(\kappa R)^2}\left[\dfrac{(q-1)(q+2)}{(q+1)q} - \displaystyle\int_{z=2/(1+q)}^{z=1} \frac{\ln z}{z-1}\,dz\right] \end{array} \right\}, \tag{2-15}$$

$$g_{el}^{cyl} = \left(\frac{K_B T}{e}\right)^2 \varepsilon\varepsilon_0\kappa \left\{ \begin{array}{l} \left[4\,(p\ln(p+q) - q + 1)\right] - \dfrac{4}{\kappa R}\ln(\dfrac{1}{2}[q+1]) \\ + \dfrac{1}{(\kappa R)^2}\dfrac{(q-1)(q+2)}{(q+1)q} \end{array} \right\}, \tag{2-16}$$

with

$$q = \sqrt{p^2 + 1}\,,$$

$$p = \frac{2\pi Q|\sigma|}{\kappa e}\,,$$

and

$$Q = \frac{e^2}{4\pi\varepsilon\varepsilon_0 k_B T}\,,$$

where K_B is the Boltzmann constant; T is the absolute temperature; e is the electronic charge; ε and ε_0 are the vacuum permitivity and dielectric constant of water, respectively; κ^{-1} is the Debye length defined in Equation 2-13; R is radius of the sphere or cylinder; and σ is charge density of the spherical or cylindrical surface. By comparing Equations 2-15 and 2-16 with Equation 2-9, the author derived the electrostatic contribution to the monolayer bending modulus,

$$K^{el} = \frac{1}{2\pi}\frac{K_B T}{Q\kappa}\frac{(q-1)(q+2)}{(q+1)\,q}\,, \tag{2-17}$$

and, in high surface charge densities and low salt concentrations, as,

$$K^{el} = \frac{1}{2\pi}\frac{K_B T}{Q\kappa}. \tag{2-18}$$

The author noticed that, when using the typical parameters values for lipids, calculated K^{el} was at most barely larger than thermal energy, $1\,K_B T$, and argued that the electrostatic effect on the bending modulus was in many cases negligible as most lipid membranes exhibited much larger bending moduli of 40-60 $K_B T$. Experimental measurements of K^{el} for SOPC protonated at low pH and for ionic SDS surfactant mixtures were consistent with the conclusion (Zhou and Raphael, 2007; Zou et. al., 2007). In the context of our cardiolipin system, this electrostatic contribution needs to be considered only when counterions are present. As will be discussed in the next section, the monolayer bending modulus of cardiolipin is estimated to be ~1 $K_B T$ in this condition.

On the other hand, the influence of electrostatic lateral repulsion on the monolayer spontaneous curvature is strong and obvious. Experimental measurements of the spontaneous curvature C_0 for several charged lipids, DOPS (Fuller et. al., 2003), DOPG (Alley et. al., 2008) and DOPA (Kooijman et. al., 2005), demonstrated dramatic changes in C_0 values when surface charges were screened by counterions or protons. In the case of DOPS, C_0 even changed from an unusually small curvature, +1/144 $Å^{-1}$ to a negative curvature of -1/23 $Å^{-1}$, even larger than that of the typical non-lamellar lipid, DOPE (-1/30 $Å^{-1}$). This change shifted preferred phase of DOPA from a lamellar structure to the H_{II} configuration. It is therefore reasonable to expect that the same effect on C_0 is responsible for the H_{II} structure preference of cardiolipin in low pH or high counterion concentrations (Rand and Sengupta, 1972; Vasilenko et. al, 1982; Loosley-Millman et. al., 1982; Seddon et. al., 1983). Nevertheless, there appears to be few, or even no theoretical treatments explicitly formulating the relation

of electrostatic interactions and the spontaneous curvature as in the case of bending modulus. Even so, electrostatic contribution to the spontaneous curvature is significant and not negligible whether compared with the contribution to bending modulus or in an absolute term. Therefore, we will regard the electrostatic inter-bilayer repulsion (first term of Equation 2-14) and the electrostatic contribution to the spontaneous curvature as the two major effects of headgroup charges on phase preference of cardiolipin in later discussions.

2.2.6 Other Interactions - Thermal Undulation of Bilayers

In addition to the major interactions introduced above, there are some short-range interactions that may often be neglected in some studies. These include but are not limited to thermal undulation of bilayers, steric repulsion among lipid headgroups, and headgroup-headgroup and headgroup-water hydrogen bonding. Since the latter two interactions should be significant only in very short inter-bilayer distances (~3 Å for hydrogen bonding) and specific to chemical structure of a lipid, we will focus our discussion on thermal undulation of bilayer. Thermal undulation of bilayer is repulsive and entropic in nature. When two bilayers approach to each other, shrinking inter-bilayer volumes limit space available for individual bilayers to carry out thermal fluctuations and effectively reduce the conformations accessible to them. Therefore, an entropic penalty is imposed to the system and drives expansion of the inter-bilayer space. In the case applicable to lipid membranes, this thermally activated entropic repulsion g_U can be expressed as (Evans and Needham, 1987),

$$g_U = \left(\frac{\pi k_B T}{16}\right)\left(\frac{P_h}{K\lambda}\right)^{1/2} \exp\left(-\frac{D}{2\lambda_h}\right), \tag{2-19}$$

where T is the absolute temperature; K is the bending modulus; D is the inter-bilayer distance; and P_h and λ_h are the coefficient and half of the decay length for this repulsion, respectively. The latter two parameters were experimentally determined for PCs in Petrache et. al. (1998). Since most lipid bilayers exhibit large bending moduli ($K \approx 40\text{-}60\, K_B T$), contribution of thermal undulation to the total free energy is usually not considered. However, in a recent coarse-grained molecular dynamics simulation, mixing cardiolipin with DOPE or DOPC was found to decrease bending moduli values of the initial DOPE or DOPC membranes considerably when surface charges of cardiolipin were partially neutralized (Dahlberg and Maliniak, 2010). The bending moduli could even be reduced to $\sim 1\, K_B T$ when the cardiolipin ratio in the total lipid composition was near 100%. Although this simulation is inconsistent with some experiments (e.g., the bending moduli of pure DOPE and DOPC membranes are lower that those obtained by experiments), the key observation that the bending modulus decreases with the charge density is still agreeable with experiments (Rowat et. al., 2004). The immediate result observed in this simulation of the bending modulus reduction was that pure cardiolipin membranes exhibited strong thermal undulation when their surface charges were neutralized. Therefore, the energy contribution from thermal undulation appears to be significant enough to be considered when cardiolipin surface charges are partially or completely screened.

2.3 Model of Lipid Liquid Crystal Phase Transitions

2.3.1 Energetics of the Phase Transitions

As discussed in Section 2.2, many forces and interactions contribute to the total free energy of a lipid liquid crystal. In Kirk et. al (1984), four interactions were considered to establish a free energy model for lamellar-non-lamellar phase transitions. These

interactions were hydration interactions, electrostatic interactions, the elastic energy and hydrocarbon chain packing stress. A recent study focusing on the $L_\alpha \leftrightarrow Q_{II}$ phase transitions found the necessity of incorporating an "unbinding energy" term, which arises from van der Waals force, into the free energy model to account for observed metastability of the Q_{II} phases for some lipids (Siegel and Tenchov, 2008). If the interactions discussed in Section 2.2.6 are also taken into consideration, a comprehensive energy description of lipid phase transitions may include at least seven interactions. However, due to lack of a conclusive functional form for some geometry and also due to insignificance in the conditions considered here, some interactions, such as hydrogen bonding and steric repulsions, are either difficult or unnecessary to incorporate into the energetics description here. Moreover, contribution of the hydration interactions may not be as important as those of other interactions in lamellar-non-lamellar phase transitions and may have been reasonably reflected on lipid elastic properties (e.g., the monolayer spontaneous curvature; So, 1992; Kozlov et. al., 1994). Given these reasons and the fact that the $L_\alpha \leftrightarrow H_{II}$ phase transition is the main lamellar-non-lamellar phase transition observed in this thesis study, we will reduce the interactions needed to be considered in our energetics description to hydrocarbon chain packing stress, electrostatic interactions, the elastic energy and thermal undulation. The last interaction may be important only when surface charges of cardiolipin are largely screened by counterions. However, the contribution from hydration interactions will still be invoked when we discuss the lipid main transition for our cardiolipin system.

The elastic energy and hydrocarbon chain packing stress have long been suggested to be the two major competing factors in lipid lamellar-non-lamellar phase transitions, particularly for the $L_\alpha \leftrightarrow H_{II}$ phase transition (Gruner, 1985; Gruner, 1989). The beauty

of this phenomenological model is in two respects. First, unlike other interactions, the same functional form of the elastic energy (Equation 2-9) is applicable to various structural geometries a lipid liquid crystal can assumes, even though additional terms may be needed for some complicated phases. Second, the monolayer spontaneous curvature neatly quantifies the phase preference. This lipid phase preference is reflected in the spontaneous curvatures C_0, with magnitudes of C_0 quantifying lipid tendency of adopting a non-lamellar structure and with its sign denoting direction of bending (toward water or lipid). Moreover, the spontaneous curvature C_0 and other elastic constants, such as the bending modulus *K*, are conceptually akin to coarse-graining, by which details of intermolecular interactions are contained in simple properties without the need of understanding these details when discussion their effects. Indeed, in our discussion in Section 2.2.5 we have seen that part of the free energy contribution from electrostatic interactions is factored into C_0 and *K*. Our other earlier discussions also presented the viewpoint from literature that regards van der Waals force and hydration interactions as having been reflected on the elastic energy. Even effects of environmental conditions such as temperature will be described in the context of the spontaneous curvature and bending modulus in our later discussions. This deliberation further justifies our neglect of some interactions.

2.3.2 Mechanisms of the Phase Transitions

When the monolayer spontaneous curvature C_0 of a lipid is large, no single structural geometry can minimize both the elastic energy and hydrocarbon chain packing stress simultaneously. As a result, frustration exists between these two energy needs: one either satisfies the elastic energy requirement and forms a non-lamellar structure with hydrocarbon chains stretching differentially or minimizes the packing strain but ends

up with a higher elastic energy penalty. This situation was deeply discussed in Anderson et. al. (1988). In this study, the authors first calculated the mean curvature on the lipid-water interface of a $Pn\bar{3}m$ structure with the assumption of constant hydrocarbon chain length throughout the entire unit cell. Then, they calculated the hydrocarbon chain lengths by assuming that the mean curvature was uniform over the unit cell. Their calculations demonstrated that when one of the two parameters, hydrocarbon chain length and mean curvature, was held constant, the other consistently exhibited a spatial variation. In other words, the two energy requirements were never met concomitantly. However, it was also found that compared to the L_α and H_{II} phases this frustration was smaller when lipids were arranged in a Q_{II} phase. This result laid a theoretical foundation for explaining the phase sequence, $L_\alpha \leftrightarrow Q_{II} \leftrightarrow H_{II}$, observed in many experiments (e.g., So et. al., 1993; Gruner et. al., 1988; Shyamsunder et. al., 1988).

Questions relating to this phase transition sequence are how lipids transform between each phase and why some lipids exhibit this sequence while others simply display a facile transition of $L_\alpha \leftrightarrow H_{II}$ without a Q_{II} phase observed. These questions consistently invite research attention because solving these puzzles may shed light on the fusion mechanisms of biomembranes (Milhaud, 2004). Many models have been proposed to describe these fusion mechanisms. According to Siegel (1993), these proposed models can be classified into two categories: one involving an inter-bilayer intermediate structure, "stalk", which connects the monolayers of two apposing bilayers and has a radius comparable to the lipid molecular dimension (Figure 2.3.1a; Markin et. al., 1984), and the other with the inverted micellar intermediate (IMI) as an intermediate structure in fusion (Figure 2.3.1b; Siegel, 1986a,b). Using the energetics model presented in Section 2.3.1, Siegel (1993) calculated free energies of these two

fusion intermediates relative to the L_α phase, and concluded that the stalk model was more energetically favorable than the IMI model. This conclusion was later confirmed by experiments (Siegel et. al, 1994; Yang and Huang, 2002). Subsequent modifications further strengthened validity of the stalk model and established a more complete series of intermediates in lamellar-non-lamellar phase transitions (Siegel and Epand, 1997; Siegel, 1999; Kozlovsky and Kozlov, 2002; Siegel and Kozlov, 2004; Siegel, 2008). Figure 2.3.2 shows results of these theoretical works and illustrates potential mechanisms of the L_α-H_{II} and L_α-Q_{II} phase transitions. Nevertheless, to our best knowledge, there is still no model proposed for mechanisms of the Q_{II}-H_{II} phase transition.

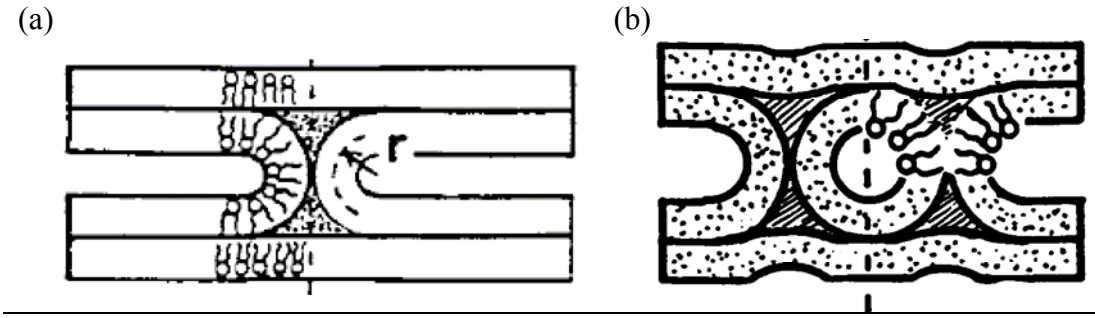

Figure 2.3.1. Schematic representations of the stalk (a) and inverted micellar intermediate (IMI) (b) structures. (The figure is adapted from Siegel (1993) and Siegel (1999)).

Figure 2.3.2. Mechanisms of lamellar-non-lamellar phase transitions based on the modified stalk model. Precursor of the non-lamellar phases is a structure called *trans*-monolayer contact (TMC), which evolves from the stalk structure. This structure may rupture to form an inter-lamellar attachment (ILA) structure. Accumulation of ILA leads to formation of a Q_{II} phase. On the other hand, numerous TMCs can assemble into precursors of the H_{II} phase, which later transform to the phase. (The figure is adapted from Siegel (1997).

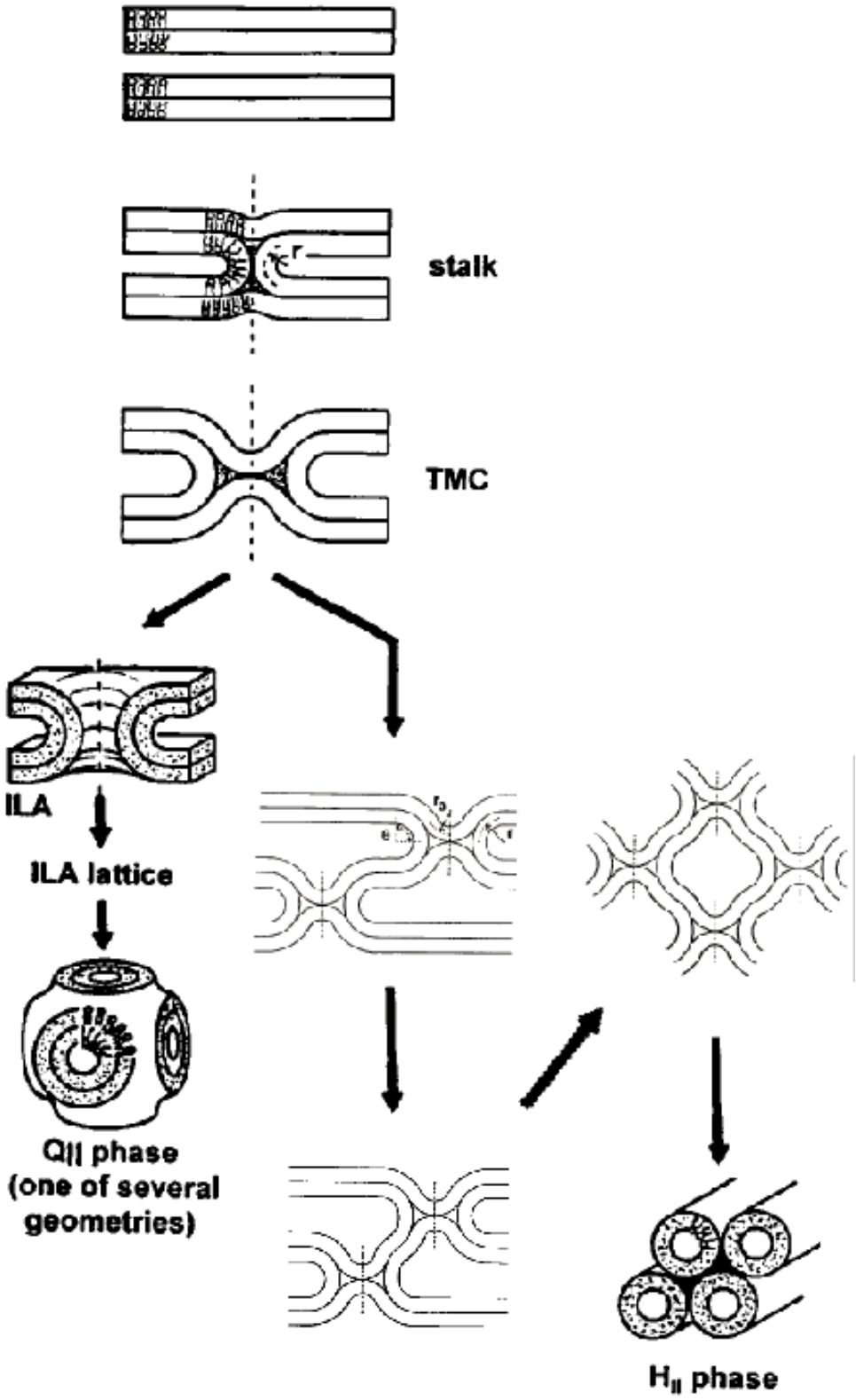
stalk
TMC
ILA
ILA lattice
Q|| phase
(one of several
geometries)
H|| phase

CHAPTER 3

EXPERIMENTAL

3.1 Introduction

This chapter will present the experimental setups and procedures with which this thesis study has been carried out. A brief introduction to the X-ray diffraction theory, based on the standard textbooks (e.g., Als-Nielsen and McMorrow, 2001; Kasai and Kakudo, 2005; Warren, 1969; Drenth, 2007) is also included.

3.2 X-ray Scattering Technique

3.2.1 X-ray Diffraction Theory

X-ray scattering is one of the most widely used experimental methods in the structural studies of biomolecules. The technique provides abundant structural information, from the overall shape of a biomolecule to precise positions of each atom within a biomolecule. In some rare cases, with adoption of special experimental techniques, X-ray scattering can even reveal dynamical properties of a biomolecule (e.g., Rasmussen et. al., 1992; Österberg et. al., 1994; Pollack et. al., 2001; Ihee et. al., 2005).

X-rays mainly interact with the electrons of an atom and effectively map out the electron number densities within a molecule, from which the position of each atom can be derived and thus the structure of the molecule can be determined. Classically, the interactions among X-rays and the electrons are understood in the context of a free electron perturbed by the electrical field of an incident electromagnetic wave. As

illustrated in Figure 3.2.1, the incident X-rays polarized and traveling along x and z directions, respectively, with the electric field E_{in},

$$E_{in} = E_{x0} e^{ik_0 z}, \tag{3-1}$$

where E_{x0} is the amplitude at peak and k_0 is the wavenumber, induces oscillation of a free electron and consequently radiation of spherical electromagnetic waves by the

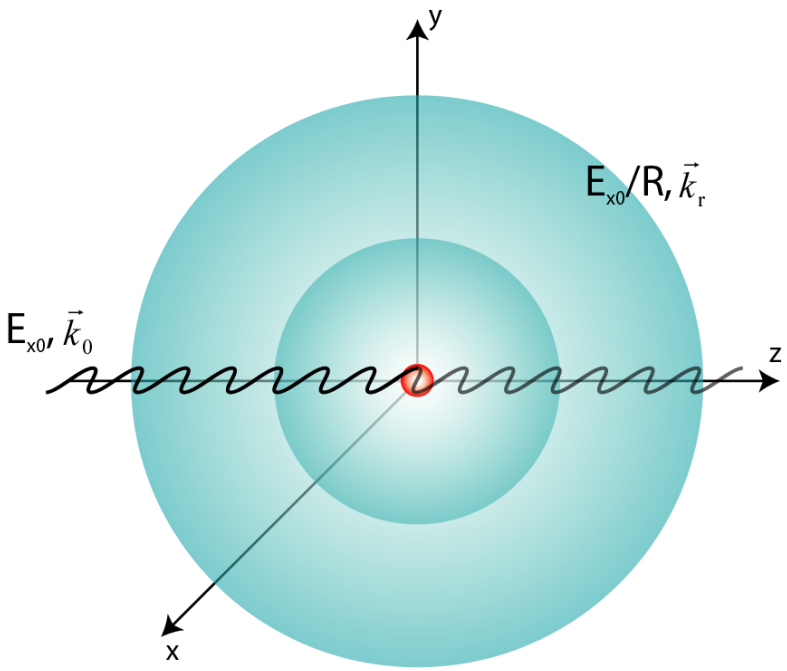

Figure 3.2.1. Classical description of the interaction between incident X-rays (wavy line) and a free electron (red sphere). The incident X-rays, with amplitude E_{x0} and wavevector $\vec{K}_0$, are polarized and travel along x and z directions, respectively. The irradiated free electron emits electromagnetic waves with amplitude E_{x0}/R, where R is the distance from the electron to the observation point, and wavevector $\vec{K}_r$ represented by blue spheres.

electron. In the case of Thomson scattering, the interaction among X-rays and electrons are free of energy loss and the electric field of the radiated spherical wave $E_{e,rad}$, when observed in a distance R from the electron, can be expressed as,

$$E_{e,rad} \propto E_{x0} \frac{e^{ik_r R}}{R}, \tag{3-2}$$

where $k_r = k_0$ is the wavenumber of the radiated wave.

When observed in the limit of R much greater than the electron separations, the radiation from a group of electrons is essentially parallel and identical in wavelength, displaying characteristics of coherence. As the electrons are clustered around nuclei, coherence allows the radiated spherical waves from different atomic electrons to interfere with each other (Figure 3.2.2), reminiscent of the classic double-slit experiment. While many of the spherical wavefronts cancel out with each other due to destructive interference, the amplitude of the composite wave is multiplied in a certain propagation direction where constructive interferences occur. As a result, the atom effectively deflects the incident X-rays from their original direction to the one specified by the momentum transfer vector $\vec{Q}$,

$$\vec{Q} = \vec{k}_r - \vec{k}_0, \tag{3-3}$$

and

$$\left|\vec{Q}\right| = (4\pi / \lambda)\sin\theta, \tag{3-4}$$

where λ is the incident and radiated wavelength, and 2θ is the scattering angle (Figure 3.2.3). The electrical field of the composite waves radiated from the atoms E_{atom} can subsequently be expressed as,

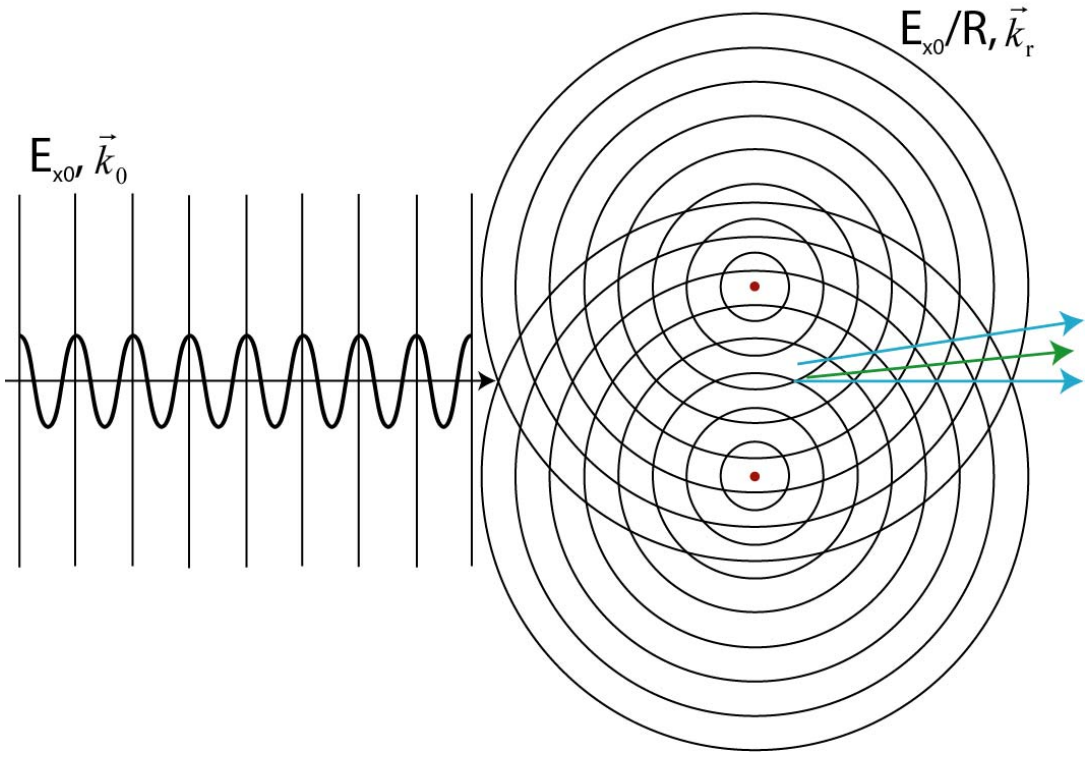

Figure 3.2.2. Interference of spherical waves radiated by two atoms in a close proximity. The straight lines denote peaks of the electromagnetic waves. Constructive interference occurs where peaks from the two waves meet (blue arrow) while coincidence of troughs results in destructive interferences (green arrow).

$$\begin{aligned} E_{atom} &\propto \int \rho(\vec{r}') E_{e,rad} \exp(i\vec{Q}\cdot\vec{r}')\, d\vec{r}' \\ &= E_{e,rad} \int \rho(\vec{r}') \exp(i\vec{Q}\cdot\vec{r}')\, d\vec{r}' \\ &= E_{e,rad} f^0(\vec{Q}) \end{aligned} \tag{3-5}$$

where $\rho(\vec{r}')$ is the electron number density at $\vec{r}'$ with the nucleus at the origin and $f^0(\vec{Q})$ is the atomic form factor with the value of f^0 ($\vec{Q} = 0$) identical to the atomic number of the atom concerned; the exponential term factors in the phase differences of waves arising from the positional shifts of the electrons relative to the origin, i.e., the

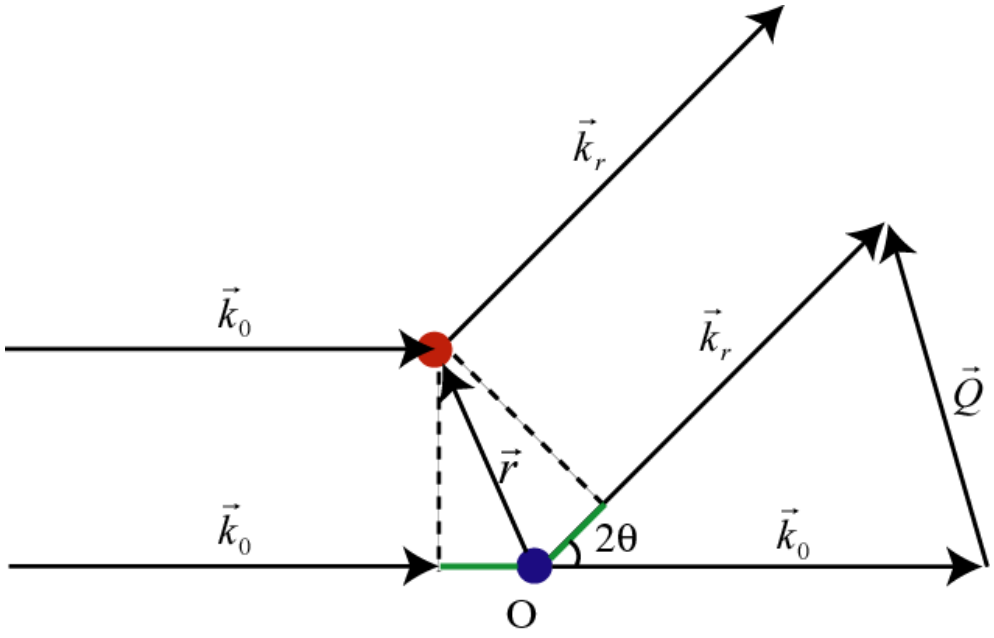

Figure 3.2.3. Geometry of scattering by two objects with separation $\vec{r}$. From the geometry, the difference in traveling path (i.e. the difference in the phase of a wave) between the two scattering events, denoted by green lines, can be expressed as $-\vec{k}_0 \cdot \vec{r} + \vec{k}_r \cdot \vec{r} = \vec{r} \cdot (\vec{k}_r - \vec{k}_0) = \vec{Q} \cdot \vec{r}$, where $\vec{Q}$ is the momentum transfer factor (see the text). The angle between the incident and scattered waves is *2θ*, which, according to the Bragg's law, has the relation of $\lambda = 2d \sin\theta$, where λ is the incident wavelength and *d* is the separation between two neighboring repeat units (see below)

nucleus (Figure 3.2.3). Note that the atomic form factor $f^0(\vec{Q})$ is actually the Fourier transform of the electron density ρ ($\vec{r}$). This important recognition will be further developed below.

In the real world where atomic electrons are bound, additional terms, $f'(\hbar\omega)$ and $if''(\hbar\omega)$ where ħω is the incident photon energy, should be included to correct the scattering power and phase difference when the photon energy is comparable to the binding energies of the electrons (i.e., an adsorption edge of an atom). X-ray scattering

in this condition is called the anomalous scattering and is widely used in macromolecule crystallography to solve the phase problem (see below). Since the photon energies considered in this thesis study are significantly greater than the adsorption edges of the common elements, C, H and O, seen in lipids, anomalous dispersion is neglected and details of the anomalous scattering will not be further discussed here. The reader is encouraged to consult Drenth (2007), Blow (2002) and Als-Nielson and McMorrow (2001) for in-depth discussions of the topic.

As atoms assemble into a molecule, the total X-ray scattering is

$$E_{mol} \propto E_{e,rad} \sum_{\vec{r}_j} f_j^0(\vec{Q}) \exp(i\vec{Q} \cdot \vec{r}_j) = E_{e,rad} F^{mol}(\vec{Q}), \tag{3-6}$$

where $f_j^0(\vec{Q})$ and $\vec{r}_j$ are the atomic form factor and the relative position of the j'th atom within the molecule, respectively. Again, the exponential term denotes the phase difference contributed by the positional shift relative to the origin, which is set arbitrarily within the molecule, and $F^{mol}(\vec{Q})$ is a Fourier series. Alternatively, if the electron density $\rho(\vec{r}')$ is treated as being continuous within a molecule, the total scattering from a molecule can be described as,

$$E_{mol} \propto E_{e,rad} \int_V \rho(\vec{r}) \exp(i\vec{Q} \cdot \vec{r})\, dV = E_{e,rad} F^{mol}(\vec{Q}), \tag{3-7}$$

where $\vec{r}$ is the position vector within the molecular volume V and $F^{mol}(\vec{Q})$ is the Fourier transform of $\rho(\vec{r})$. $F^{mol}(\vec{Q})$ is also known as the structure factor due to its strong relationship with the spatial arrangement of atoms within a molecule.

Although the possibility of determining molecular structures with X-ray scattering from single or a small number of molecules is being intensively explored due to introduction of the next generation photon sources such as X-ray free electron lasers (XFEL) and Energy Recovery Linacs (ERL), crystals are still needed to obtain atomic structures. For a crystal, the X-ray scattering power of each unit cell is added up into the total X-ray scattering of a crystal $E_{crystal}$,

$$E_{crystal} \propto E_{mol} \sum_{\vec{R}_n} \exp(i\vec{Q} \cdot \vec{R}_n), \tag{3-8}$$

where $\vec{R}_n$ is the lattice vector denoting the position of a unit cell within a crystal and the exponential term is the phase factor. It is noticed that due to the large number of unit cells present in a crystal $\vec{Q} \cdot \vec{R}_n$ must be an integer multiple of 2π for the conditions of constructive interference being met so that the scattered X-rays from a crystal are concentrated and can be observed experimentally. Explicitly, when $\vec{R}_n$ is expressed as,

$$\vec{R}_n = n_1\vec{a}_1 + n_2\vec{a}_2 + n_3\vec{a}_3, \tag{3-9}$$

where $\vec{a}_1$, $\vec{a}_2$ and $\vec{a}_3$ are the lattice vectors, and n_1, n_2 and n_3 are integers, the constructive interference conditions is

$$\vec{Q} \cdot \vec{R}_n = n_1(\vec{a}_1 \cdot \vec{Q}) + n_2(\vec{a}_2 \cdot \vec{Q}) + n_3(\vec{a}_3 \cdot \vec{Q}) = 2\pi(hn_1 + kn_2 + ln_3), \tag{3-10}$$

where h, k and l are integers, and $\vec{Q}$ specifies the scattering angle. This condition is known as the Laue condition, which is equivalent to the famous Bragg's law. When

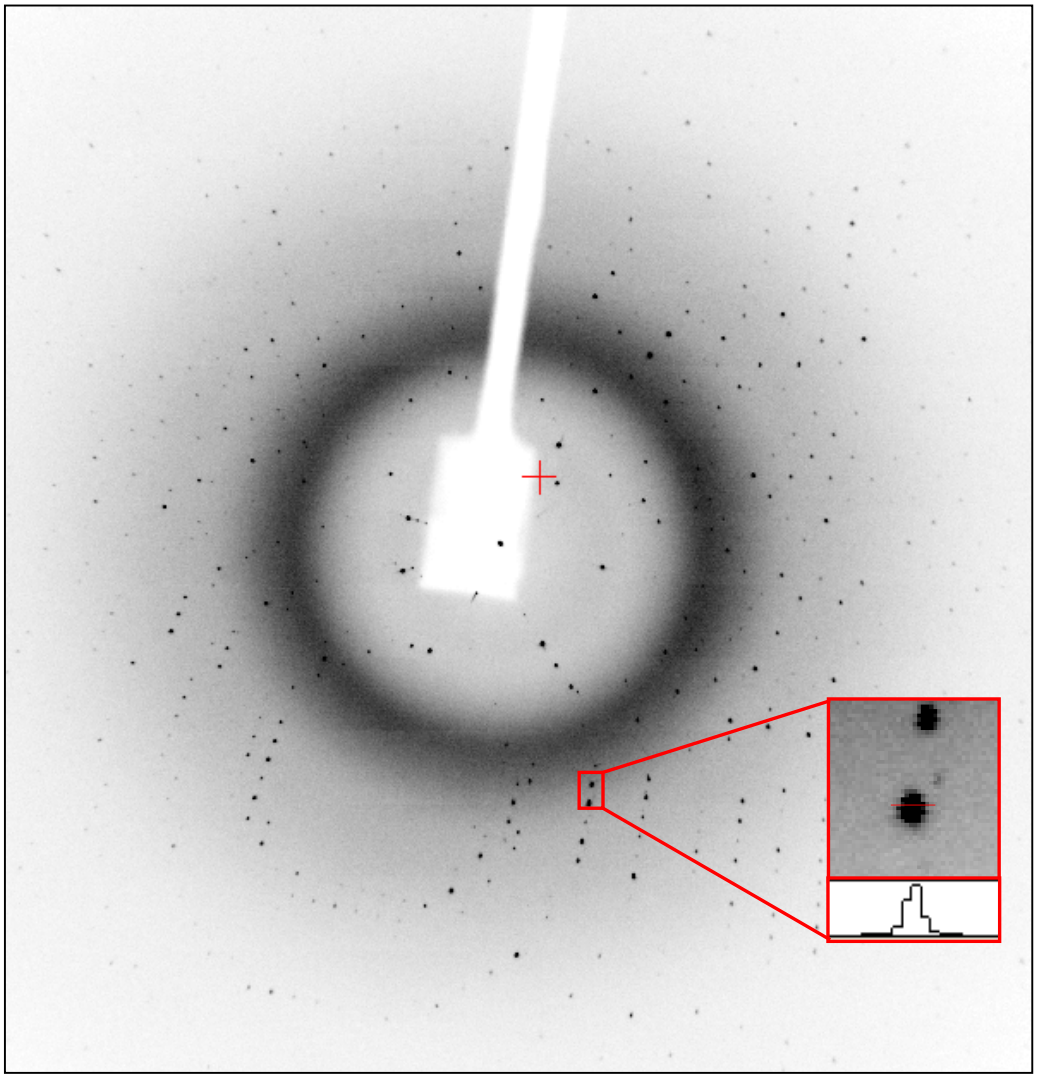

Figure 3.2.4. X-ray diffraction image of a protein *RNase A* single crystal. The inset enlarges two Bragg spots, along with the profile of one of the spots. The profile shows the finite size of the peak (see the text). The shadow arose from a beam stop and the dark diffuse ring came from the oil used to prevent dehydration of the crystal.

the Laue condition is fulfilled, sharp peaks, often called Bragg spots in crystallography, are experimentally observed (Figure 3.2.4) and can be denoted with the Miller indices (h, k, l) in a 3-D lattice or (h, k) in a 2-D lattice.

Theoretically, the diffraction peaks are observable only when the Laue condition is exactly satisfied. However, the incident X-rays are not perfectly collimated and monochromatic. A real, macroscopic crystal is not free of defects, as well. Consequently, the experimentally measurable diffraction peaks are not in the shape of a delta function but are of finite sizes (inset in Figure 3.2.4). Taking these real world constraints into consideration, the Lorentz and polarization factors are introduced and the integrated intensity of the finite size peak $I_{crystal,real}$ is related to the theoretical intensity $I_{crystal,ideal}$ through,

$$I_{crystal,real} \propto \left(\frac{1}{\sin(2\theta)}\right)\left(\frac{1+\cos^2(2\theta)}{2}\right) I_{crystal,ideal}, \tag{3-11}$$

with

$$I_{crystal,ideal} \propto \left|E_{crystal}\right|^2 \propto \left|E_{mol}\right|^2 \propto \left|F^{mol}(\vec{Q})\right|^2, \tag{3-12}$$

where the first term of Equation 3-11 is the Lorentz factor (the readers are referred to Als-Nielsen and McMorrow (2001), and Warren (1969) for the derivation of the factor), and the second term of the same equation is the polarization factor, which is included for unpolarized incident X-rays. Since in this thesis study diffraction data were largely collected in the small scattering angle regime ($2\theta < 0.1$), thus $\cos^2(2\theta) \approx 1$ and the polarization term approaches unity. On the other hand, a similar argument emphasizes the importance of considering the Lorentz factor in the small scattering angle regime. The Lorentz factor was taken into consideration when the electron density map was reconstructed with both the line shape fitting and conventional peak integration methods for the cardiolipin liquid crystals studied here (Section 4.3).

As shown in Equations 3-11 and 3-12, knowledge of the integrated X-ray intensities from an X-ray scattering experiment may ultimately lead to the

understanding of the structure of the experimental subject. Nevertheless, reversing the Fourier transform in Equation 3-7 produces the expression of the electron density $\rho(\vec{r})$ as,

$$\rho(\vec{r}) \propto \sum_{\vec{Q}} F^{mol}(\vec{Q}) \exp(-i\vec{Q}\cdot\vec{r}) = \sum_{\vec{Q}} \left|F^{mol}(\vec{Q})\right| \exp(i\phi(\vec{Q}) - i\vec{Q}\cdot\vec{r}), \tag{3-13}$$

which indicates that the structure factor $F^{mol}(\vec{Q})$ is dependent on both the amplitude, which is proportional to $\left|F^{mol}(\vec{Q})\right|$, and the phase, denoted by $\phi(\vec{Q})$, of the scattered X-rays from a molecule. Apparently, experimental data on integrated intensities can only provide information regarding the amplitude of the structure factor $\left|F^{mol}(\vec{Q})\right|$ through Equations 3-11 and 3-12 while its phase $\phi(\vec{Q})$ cannot be readily derived from an ordinary X-ray diffraction experiment. The difficulty in deducing the phase of the scattered X-rays from diffraction data is the notorious phase problem in crystallography. As noted above, the phenomenon of X-ray anomalous scattering is widely used in solving the phase problem in macromolecule crystallography, methods known as Multiple- and Single-Wavelength Anomalous Diffraction (MAD and SAD). An introductory survey can be found in Drenth (2007).

Since cardiolipin molecules in this thesis study were commonly arranged into centrosymmetric structures of the lamellar and inversed hexagonal lipid phases (see Section 1.3.1), it is worthwhile discussing the phase problem involving centrosymmetric systems. Based on Equation 3-13, the Laue condition of Equation 3-10 and $\vec{r} = x\vec{a}_1 + y\vec{a}_2 + z\vec{a}_3$, the electron density $\rho(\vec{r})$ can be further developed into,

$$\begin{aligned}\rho(\vec{r}) &= \sum_{\vec{Q}} \left|F^{mol}(\vec{Q})\right| \exp(i\phi - i\vec{Q}\cdot\vec{r}) \\ &= \sum_{\vec{Q}} \left|F^{mol}(\vec{Q})\right| [\cos(\phi - \vec{Q}\cdot\vec{r}) + i\sin(\phi - \vec{Q}\cdot\vec{r})] \\ &= \sum_{\vec{Q}} \left|F^{mol}(\vec{Q})\right| [\cos(\phi - 2\pi(hx+ky+lz)) + i\sin(\phi - 2\pi(hx+ky+lz))]\end{aligned} \tag{3-14}$$

For $\rho(\vec{r}) = \rho(-\vec{r})$ i.e. centrosymmetric, the phase of the structure factor $\phi(\vec{Q})$ must be either π or zero such that $\rho(\vec{r})$ is expressed in terms of centrosymmetric cosine functions. As a result, the phase problem in a centrosymmetric system is reduced to determining the sign (plus or minus) of the amplitudes of the structure factor $\left|F^{mol}(\vec{Q})\right|$, simplifying the phase determination process. This characteristic of a centrosymmetric system is used in reconstructing the electron density map with the peak integration method for the cardiolipin liquid crystal studied here (Section 4.3.3).

So far, we have focused on molecules in a single, large crystal. However, instead of forming such single crystals with long-range periodicity, lipid-water and lipid-aqueous solution mixtures, in most cases, exhibit only short-range order with local domains of repeat units randomly oriented. This is similar to the case of powder diffraction in which incident X-rays are scattered by a group of very tiny, unoriented crystals. Although most of the arguments described above still hold true, some need to be slightly modified for powder diffraction. First, while the Laue condition is still a prerequisite for constructive interferences, the scattered X-rays specified by the $\vec{Q}$ fulfilling the Laue condition are not presented as spots in an X-ray detector anymore. Instead, the sheer number of local domains within a preparation may effectively sample all the possible orientations a crystal can assume, and replaces the Bragg spots with diffraction rings (Figure 3.2.5), which may be regarded as being constituted with a vast amount of the spots and can still be denoted with Miller indices. Second, since

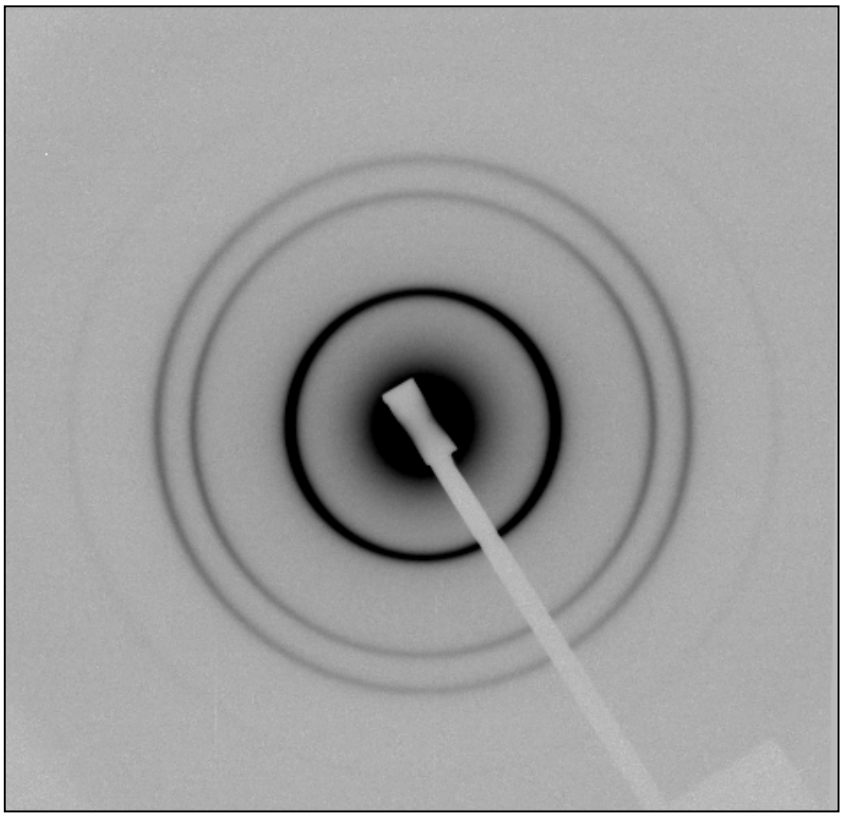

Figure 3.2.5. X-ray diffraction image of a 78.7 wt% cardiolipin-NaCl mixture collected at 40 °C, 1.5 kbar. The Bragg spots demonstrated in Figure 3.2.4 give way to diffraction rings when randomly oriented domains are presented in a huge amount to replace a large single crystal.

the Bragg spots give way to diffraction rings, the observable intensities are now integrated over a ring instead of a spot. In this way, all the scattered X-rays with identical amplitude of the momentum transfer vector $\left|\vec{Q}\right|$, i.e., identical scattering angle, 2θ, contribute equally to the integrated intensity of the same diffraction ring. Therefore, a multiplicity factor, m, must be introduced to take this phenomenon into account. Third, with diffraction rings in place of Bragg spots, the Lorentz factor introduced in Equation 3-11 has to be further modified as over thousands tiny crystals being present simultaneously. Taken together, Equation 3-11 is rewritten as,

$$I_{crystal,real} \propto m\left(\frac{1}{\sin\theta \sin(2\theta)}\right) I_{crystal,ideal}, \tag{3-15}$$

where m is the multiplicity factor, the second term is the Lorentz factor for powder diffraction (for the derivation, refer to Als-Nielsen and McMorrow (2001), and Warren (1969)) and the polarization factor shown in Equation 3-11 is omitted due to the small scattering angle (see above). As reasoned in Turner (1990), the diffraction intensity integration method applied in thesis study, azimuthal integration over a diffraction image recorded on an area detector (Section 3.6), automatically corrects for the factor of $1/\sin\theta$ and, again in the small scattering regime, reduces Equation 3-15 to,

$$I_{crystal,real} \propto \frac{m}{\sin(2\theta)} I_{crystal,ideal} \approx \frac{m}{2\theta} I_{crystal,ideal} \propto \frac{m}{\theta} I_{crystal,ideal}. \tag{3-16}$$

This equation corresponds to Equation 4-15 of Chapter 4 and will be used for the electron density map reconstruction with the peak integration method.

3.2.2 X-ray Apparatus

Setup of a typical X-ray scattering experiment is as illustrated in Figure 3.2.6. X-rays from a source are monochromatized, focused and collimated with X-ray optics before illuminating a sample. The X-rays scattered by the sample are recorded with a detector (either 1-D point detector or 2-D area detector) located in a distance of R from the sample, while the transmitted X-rays are absorbed with a beam stop to prevent the strong direct beam from damaging the detector. The positions of the detector and beam stop depend on the specific type of experiment to be carried out. In a small angle

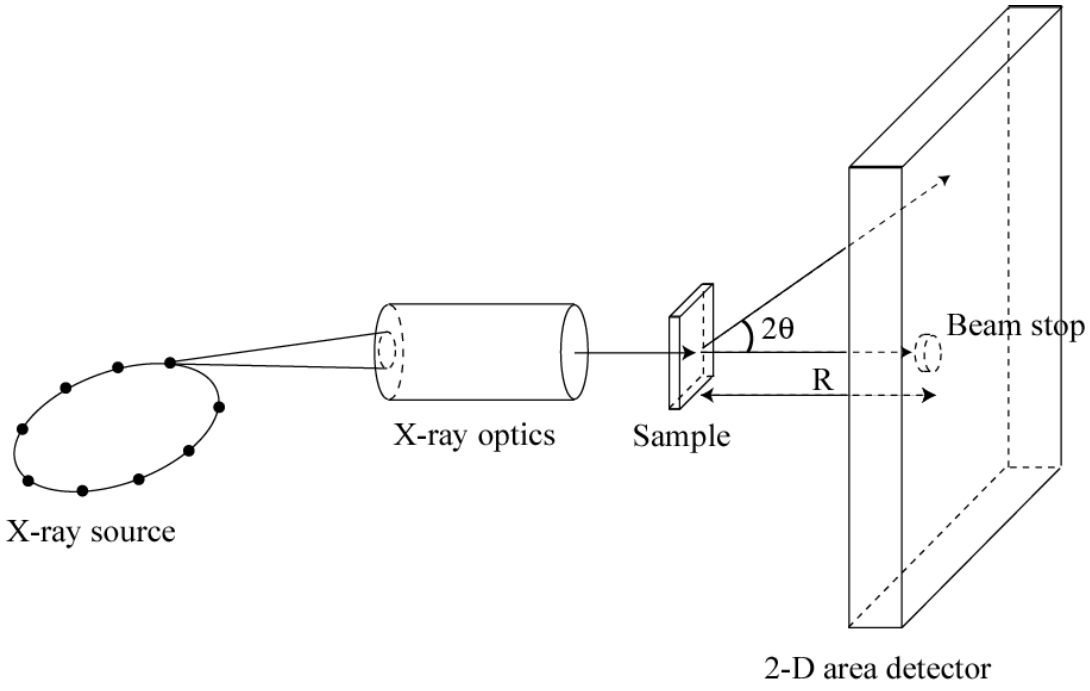

Figure 3.2.6. Setup for a typical X-ray scattering experiment. The X-ray beam is monochromatized, focused and collimated with X-ray optics before illuminating a sample. The scattered X-rays, with the scattering angle 2θ, are recorded with a 2-D area detector placed in a distance R from the sample while the transmitted beam is blocked by a beam stop.

X-ray scattering (SAXS) experiment, the detector is such placed that the scattered X-rays with the scattering angle $2\theta < 0.1$ radians can be clearly resolved, with the beam stop close to the detector to minimize its shadow on the detector. This type of experimental setup entails a long distance between the sample and the detector and, along with the remoteness of the beam stop from the sample, is inevitably accompanied by strong air scattering, which reduces the signal to noise ratio. To counter this, the flight path of the X-ray beam is usually in vacuum or helium gas.

In this thesis study, the X-ray sources were the CuK_α radiation from a Rigaku RU-3HR rotating anode generator in our laboratory and the synchrotron radiation of the G1 beamline at the Cornell High Energy Synchrotron Source (CHESS). The rotating anode generator was operated at 36 kV and a current of 48 mA with a 2mm×0.2mm point focus on the rotating copper anode. At the 6° take-off angle used, this resulted in a 0.2mm×0.2mm focus. The generated X-rays were monochromatized with a 10 μm-thick nickel foil (Goodfellow, PA) to filter out CuK_β radiation, leaving CuK_α of wavelength $\lambda \approx 1.54$ Å, and focused with double Franks mirrors, which also filtered out the Bremsstrahlung radiation. The downstream X-rays were then collimated with a pair of slits perpendicular to each other (horizontal and vertical). The final size of the X-ray beam at the sample was estimated to be <0.5mm×0.5mm and the photon flux be in the order of magnitude of 10^7 photons/sec/mm^2. The flight path of the beam upstream to the slits were purged with helium gas while that of the downstream beam, including through the sample, was under vacuum. The beam stop was placed at the end of a pipe with a fixed length, which holds vacuum for the flight path (Figure 3.2.7). An air gap of <1 cm was left between the beam stop and the detector since the pipe was not attached to the detector for the ease of switching pipes to adjust the sample-to-detector distance. The detector used for the rotating anode source was a home-built 2-D area charge-coupled device (CCD) detector with 1024×1024 pixels and an active input area of 51×51mm^2 (similar to the one reported in Tate et. al. 1995).

For the CHESS G1 beamline, X-rays were radiated from 5.3 GeV positrons winding through a 49-pole wiggler. In this thesis study, the photon energy of the X-ray beam was set to 10.6 or 9.9 keV (equivalent to the wavelength of 1.17 or 1.25 Å). The layout of the beam conditioning for the G1 beamline is shown in Figure 3.2.8. The X-ray beam from the wiggler was pre-filtered with a 0.5 mm-thick graphite filter and

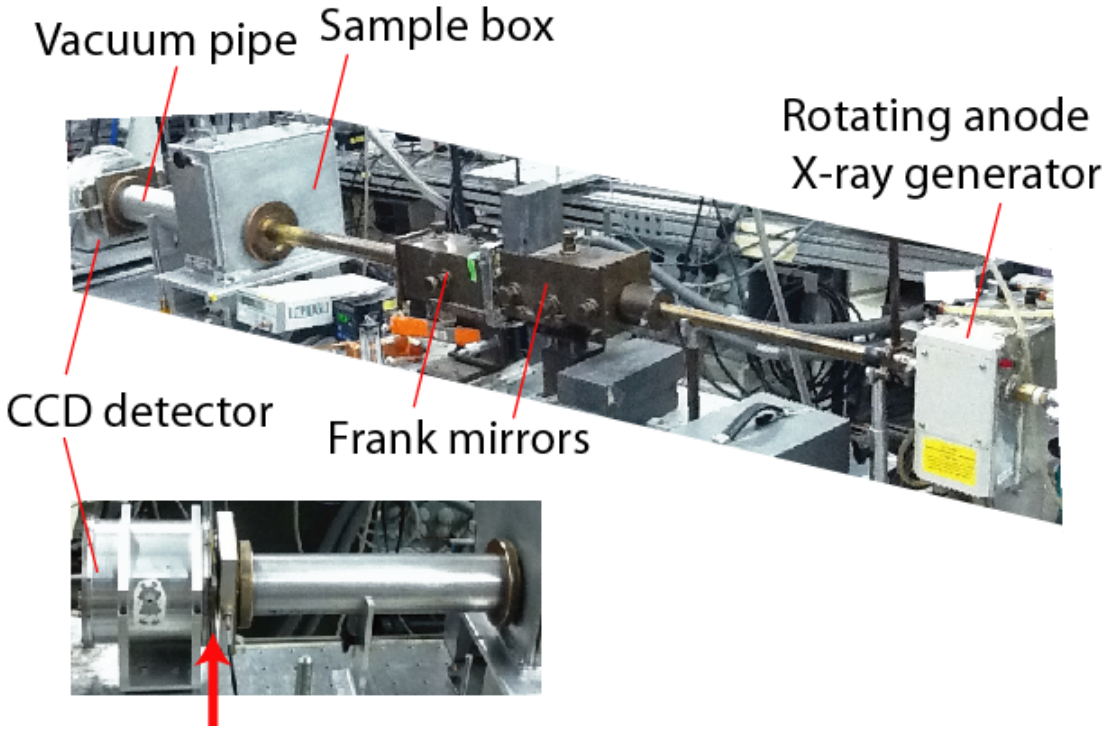

Figure 3.2.7. Setup of the rotation anode X-ray generator beamline. Samples sit inside the vacuum-proof sample box. An air gap (red arrow) exists between the end of the vacuum pipe and the detector. A beam stop is placed on the inner side of the pipe end.

passed through the white-beam mirror made of a rhodium-coated Glidcop substrate to reduce the heat load of the following X-ray optics and to collimate the beam before being monochromatized with multilayers and further focused with a rhodium-coated Si single crystal mirror. The monochromatized X-ray beam had an energy bandwidth $\Delta E/E$ = 1.3% (Kazimirov et. al. 2006). In the G1 hutch, the beam was further collimated with a series of slits, with the final beam size set to 0.5mm×0.5mm and the photon flux in the order of magnitude of 10^{13} photons/sec/mm^2. Compared to the photon flux of 10^7 photons/sec/mm^2 from the rotating anode source, the high photon flux of the synchrotron source significantly reduced the required X-ray exposure time (see below) while still considerably improving the signal-to-noise ratio. Similar to the

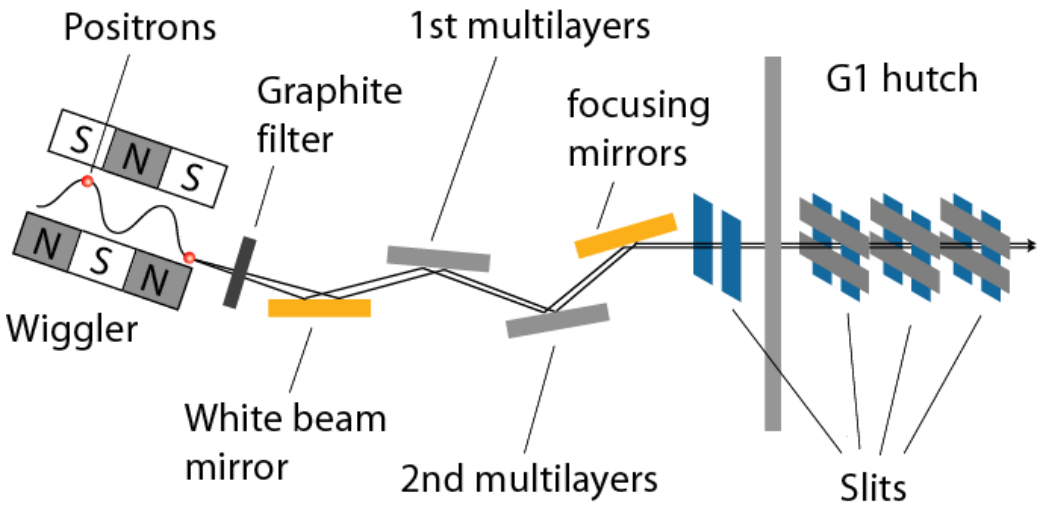

Figure 3.2.8. X-ray optics layout of the G1 beamline at CHESS. X-rays are radiated from positrons winding through the wiggler. See the text for the function of each optics element.

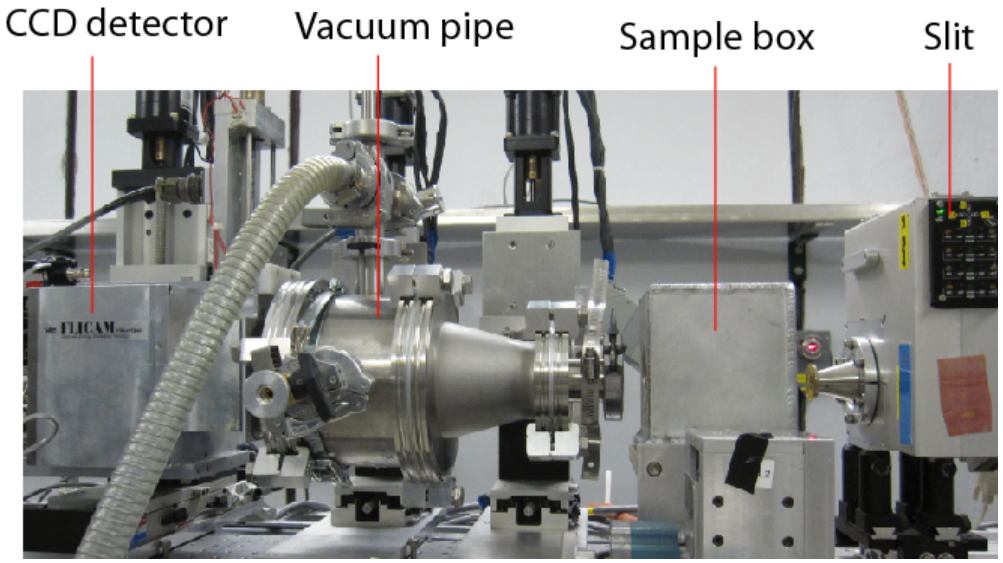

Figure 3.2.9. Setup of the G1 beamline at CHESS. Unlike the setup with the rotating anode, the vacuum pipe and the sample box are within different vacuum circuits.

setup with the rotation anode source, the flight path of the X-ray was purged with helium gas upstream to the sample and placed under vacuum afterwards, with a beam stop at the end of a pipe (Figure 3.2.9). The detector employed for the G1 beamline was a home-built 2-D "Flicam" CCD detector with 1024×1024 pixels and an active area 71.45×71.45 mm^2, again similar to that of Tate et. al. (1995).

3.2.3 Small and Wide Angle Scattering from Lipid Liquid Crystals

In this thesis study, the main X-ray scattering data were collected in the small scattering angle regime with those taken in the wide scattering angle regime serving to verify the lipid phase assignment to a given cardiolipin sample (see below). A typical SAXS experiment concerns X-ray scattering with scattering angles $2\theta < 0.1$ radians and, correspondingly with $\lambda = 1.54$Å, the momentum transfer vector amplitude $|Q|$ within 4 nm^{-1} (Equation 3-4). In these 2θ and $|Q|$ ranges, people study structural orders in a length scale of 2-150 nm. On the other hand, one resorts to the wide angle X-ray scattering (WAXS) to examine orderings in the length scale of <50 Å. This entails an experimental setup focusing on the $|Q| > 0.13$ $Å^{-1}$ and $2\theta > 0.03$ radians.

For the cardiolipin samples studied here, the SAXS data offered information of the distance between two neighboring repeat units, d, of a given lipid phase (see also the caption of the Figure 3.2.3). In the lamellar phases, this distance, conventionally called the d-spacing, comprises the bilayer thickness and width of an inter-bilayer water volume, while in the H_{II} phase d can be regarded as the separation between two closest centers of water cores (Figure 3.2.10). Typical X-ray scattering profiles, in the form of scattering intensity versus the momentum transfer vector amplitude $|Q|$, of lipid liquid crystals in the lamellar and the H_{II} phases are shown in Figure 3.2.11. The diffraction

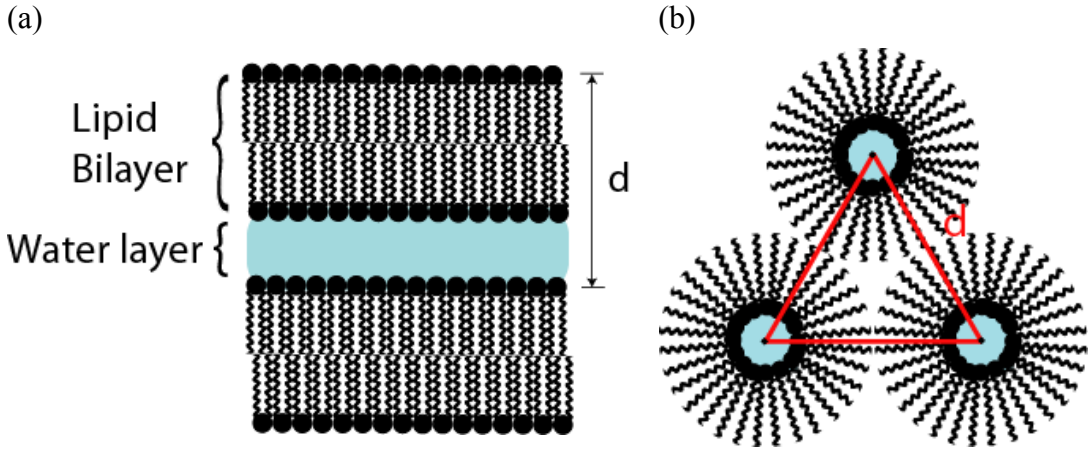

Figure 3.2.10. Illustration of the repeat distances *d* for the lipid liquid crystalline lamellar (a) and H_{II} (b) phases.

peaks of the lamellar phases are spaced with their $|Q|$ in the ratio of *1:2:3:4:...* while those of the H_{II} phase are in the ratio of $1:\sqrt{3}:2:\sqrt{7}:...$ The peaks of the former are customarily designated as the 1st, 2nd, 3rd,... order peaks of the lamellar phases and those of the latter are denoted with the Millar indices (Section 3.2.1) of *(1,0)*, *(1,1)*, *(2,0)*, *(2,1)...* Based on these characteristics of how the diffraction peaks are spaced, one can determine whether a lipid aggregate is arranged in the lamellar phases or in the H_{II} phase. With the relation of $d = 2\pi/|Q|$, one can even derive the repeat distances *d* from $|Q|$ of the 1st order peak of the lamellar phases or of the *(1,0)* peak of the H_{II} phase, although values converted from the latter have to be further multiplied by the factor of $2/\sqrt{3}$ to yield correct values.

Although discontinuity in the d-spacing value (e. g. Figure 3.2.12) can often be conveniently employed to distinguish the L_α phase from a gel phase, which, in our cardiolipin system, consistently displayed a d-spacing of ~58 Å regardless of temperature and lipid composition (Section 4.3.1), lipid phase determination among

(a)

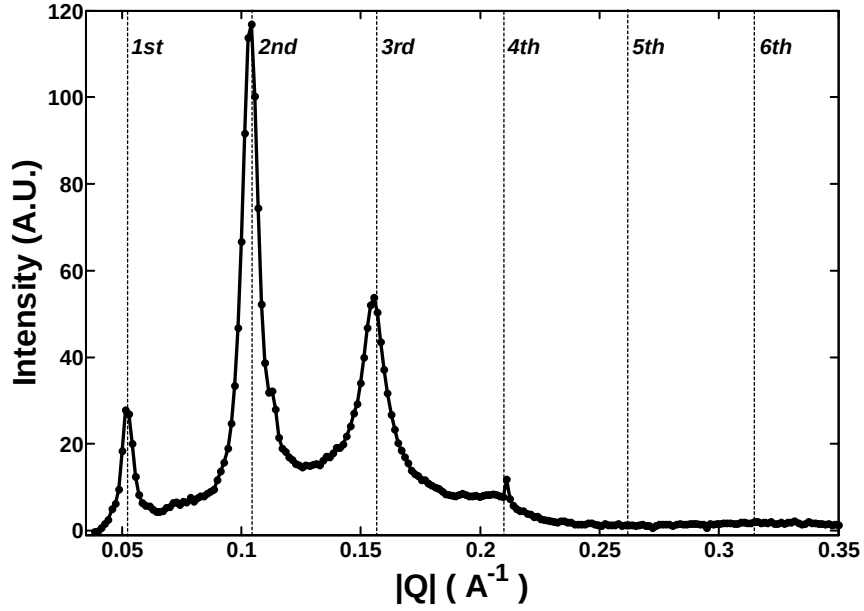

(b)

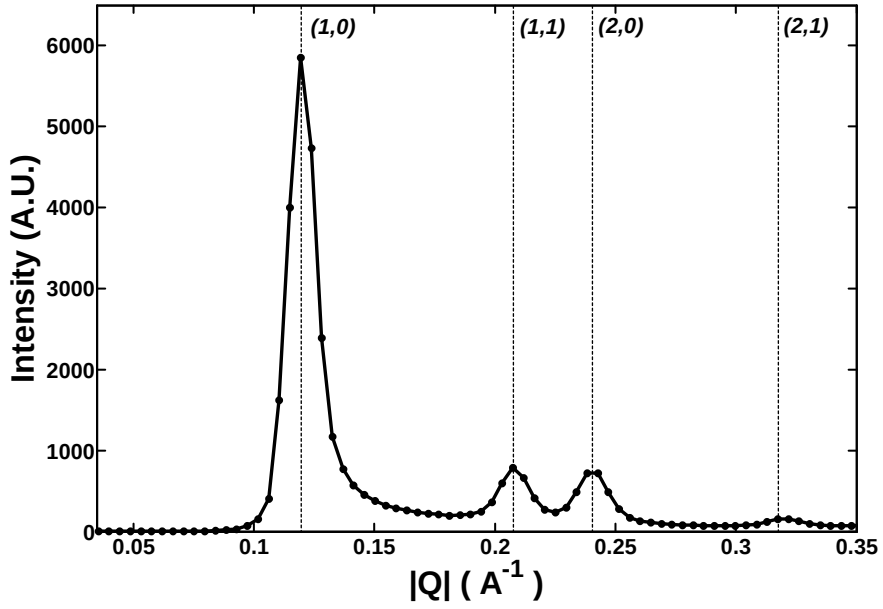

Figure 3.2.11. Typical small angle X-ray scattering profiles of the lipid liquid crystalline L_α phase (a) and H_{II} phase (b), collected from 32.9 wt% cardiolipin-water and 80.2 wt% cardiolipin-$CaCl_2$ mixtures at 20 °C, respectively. Refer to Section 3.3 for the nomenclature of samples. Dashed lines are the expected positions of the peaks.

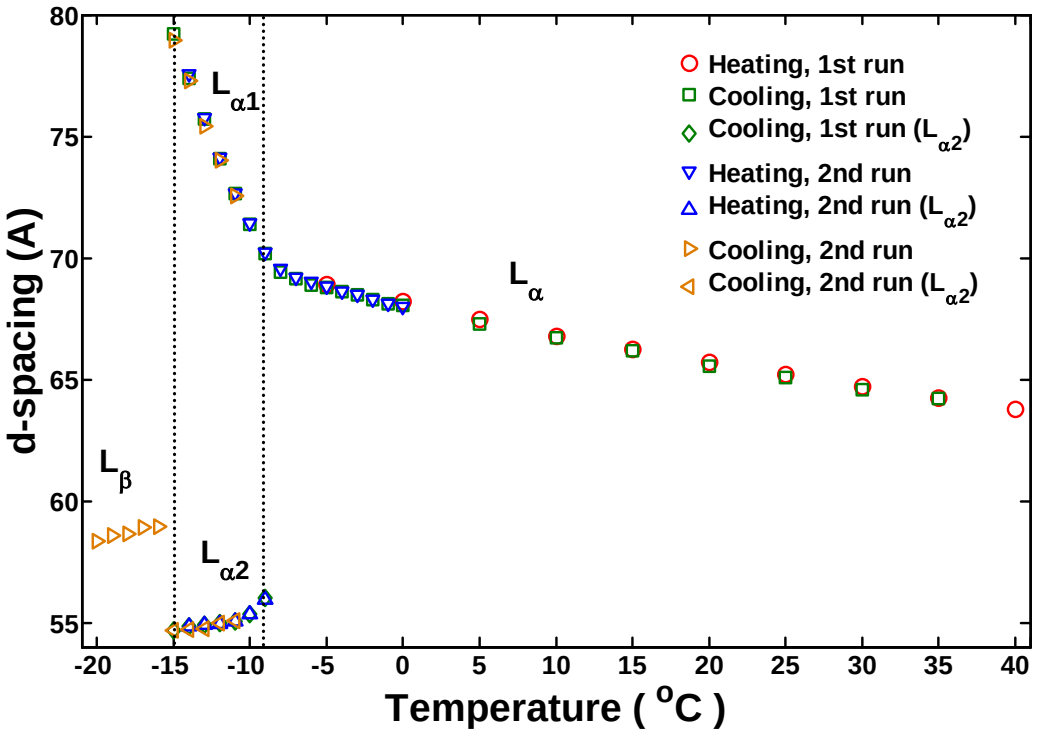

Figure 3.2.12. d-spacings of the lamellar phases as a function of temperature for a 59.8 wt% cardiolipin-water mixture. Discontinuity in the d-spacing is indicative of a phase transition.

the lamellar phases cannot simply rely on how the diffraction peaks are spaced and has to be carried out in a more reliable and determinate way. As discussed in Section 1.3.1, the rigid hydrocarbon chains of a gel phase are arranged in a short range, lattice-like order, in a length scale of ~4.3 Å (or ~1.46 $Å^{-1}$ in $|Q|$) for cardiolipin (Lewis et. al., 2007). This feature of a gel phase is readily observable as a sharp scattering peak in the wide-angle scattering regime (Figure 3.2.13) and can be applied to assigning cardiolipin phases. In addition to the feature resolved with WAXS, the relative X-ray scattering intensities among the diffraction peaks are also of use in assigning the gel L_β phase as this phase typically exhibits a strong 1st order peak, a moderate 4th order peak, and a weak 3rd order peak (Figure 3.2.14; Gruner et. al., 1988). The WAXS data

may further distinguish the gel $L_{\beta'}$ phase (see Section 1.3.1) from the gel L_{β} phase. Unlike the L_{β} phase, the tilted hydrocarbon chains relative to the bilayer surface normal render the $L_{\beta'}$ phase two, rather one, sharp peaks in the WAXS regime of $|Q|$ from 1.3-1.8 $Å^{-1}$ (Tardieu et. al., 1973). The two peaks are centered ~1.37 $Å^{-1}$ and ~1.65 $Å^{-1}$ for cardiolipin (Lewis et. al., 2007). Guided by the WAXS data, we could unambiguously distinguish the L_{α} phase from a gel phase and confirmed the reliability of determining lipid phases with the variation in the d-spacing. Nevertheless, the resolution of our WAXS data was not always high enough to assure a correct lipid phase assignment among the various gel phases. Therefore, we did not further differentiate the gel phases and collectively labeled structures with sharp diffraction peaks in the WAXS regime as the "gel" phase.

Figure 3.2.13. Typical X-ray scattering images (a) and profiles (b) in the WAXS regime. The data compare X-ray scattering from the L_α and a gel phases, and were collected from a 66.1 wt% cardiolipin-water mixture at 5 °C and -16 °C, respectively. The gel phase displays a sharp peak at ~1.4 $Å^{-1}$, which was scattered by its orderly structured hydrocarbon chains (green arrows) whereas only a diffuse scattering peak is observed for the flexible hydrocarbon chains of the L_α phase (red arrows). Numbers index the peaks. Black arrows denote noise because the peaks are not observed in the 2-D diffraction images. Their shapes changed irregularly with the sample temperature.

(a)

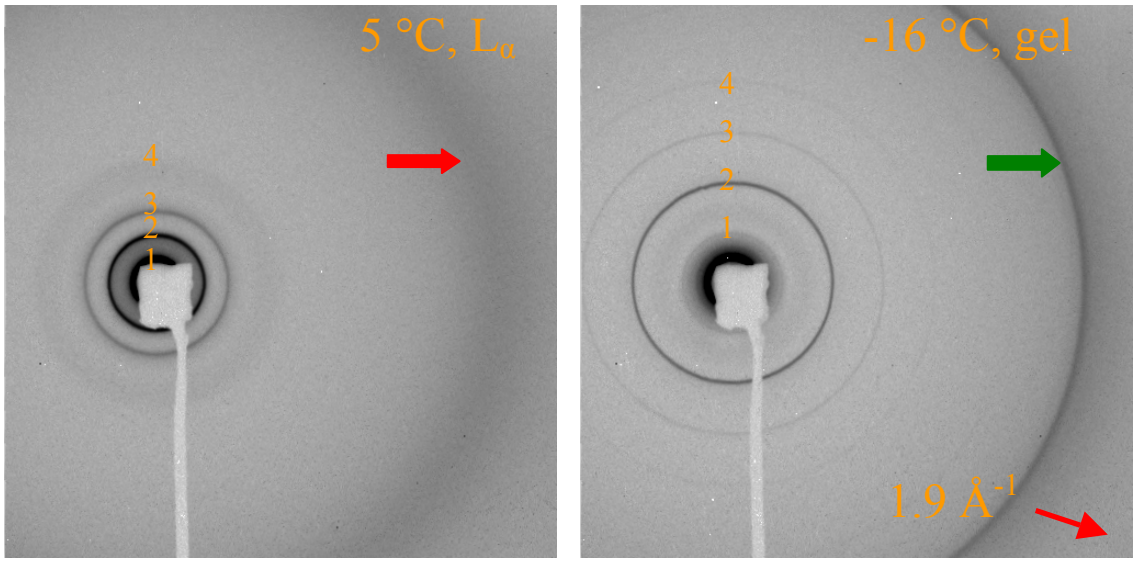
5 °C, L$_\alpha$
4
3
2
1
-16 °C, gel
4
3
2
1
1.9 Å^{-1}

(b)

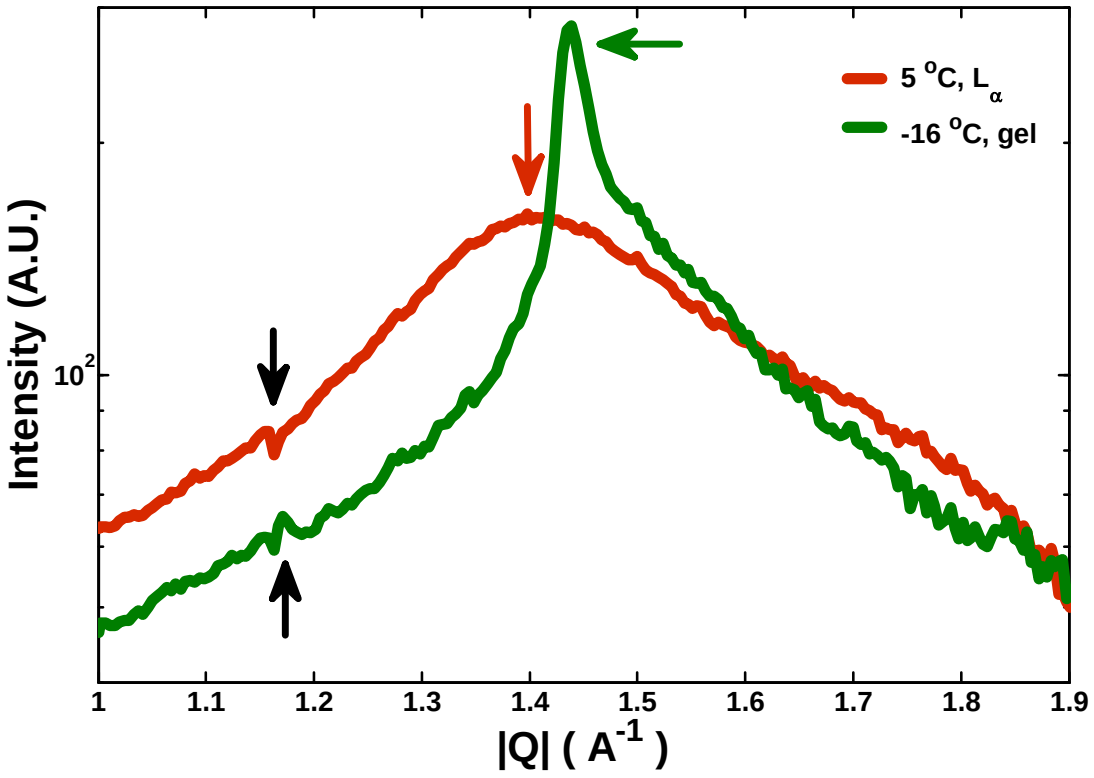
5 °C, L$_\alpha$
-16 °C, gel
Intensity (A.U.)
10^2
1
1.1
1.2
1.3
1.4
1.5
1.6
1.7
1.8
1.9
|Q| (A^{-1})

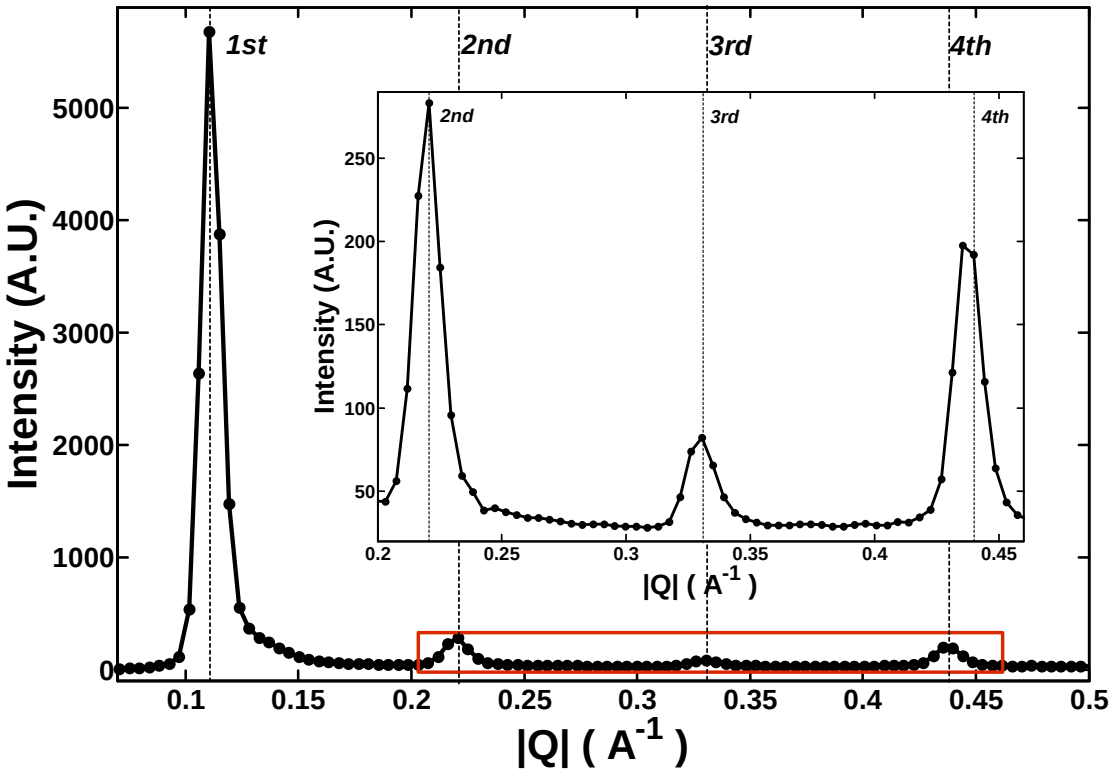

Figure 3.2.14. Small angle X-ray scattering profile of the lipid liquid crystalline L_β phase, collected from a 80.2 wt% cardiolipin-$CaCl_2$ mixture at -20 °C. Inset enlarges the marked region. Dashed lines are the expected peak positions.

3.3 Cardiolipin Lipid Liquid Crystal Sample Preparation

Tetraoleoyl-cardiolipin (C18:1), with the double bond at the C-9 position, was the cardiolipin spices chosen for this thesis study. We chose tetraoleoyl-cardiolipin as our experimental subject, which shares the same hydrocarbon chain as dioleoylphosphatidylethanolamine (DOPE). Moreover, it was found that the proportion of tetraoleoyl-cardiolipin with respect to the total cardiolipin species inside the deep-sea bacterium *photobacterium profundum* increased when the bacterium was cultured at ever elevating pressures (Bartlett, 2002). Studying the phase behavior of

this cardiolipin species, especially at high pressures, may shed light on how piezophilic organisms adapt to high-pressure environments. Tetraoleoyl-cardiolipin is also a dominating cardiolipin species in human lymphoblasts and yeasts (Schlame et. al., 2005).

Tetraoleoyl-cardiolipin sodium salt dissolved in chloroform at a concentration of 25 mg/ml (Cat. no. 710335C) was purchased from Avanti (Alabaster, Alabama) and used without further purification. The cardiolipin chloroform solution was stored at -90 °C before sample preparation. The sample preparation process involves two major steps: lyophilizing the cardiolipin salt and mixing the resultant powder with water or salt solutions. When lyophilizing the cardiolipin salt, 160-200 μl stock solution, containing 4-5 mg the cardiolipin salt, was placed in a glass cone-bottomed centrifuge tube pre-rinsed with ACS-grade chloroform (Cat. no. 4440-04, Mallinckrodt Chemicals, Phillipsburg, NJ). Chloroform in the lipid solution was evaporated under Ar gas, followed by an overnight incubation under vacuum (<50 mbar). The resultant chloroform-free cardiolipin film was dissolved in 50-60 μl ACS-grade cyclohexane (Cat. no. 9206-22, Mallinckrodt Chemicals, Phillipsburg, NJ) and then transferred to an X-ray glass capillary with O.D. 0.9 mm (Cat. no. 09-SG, Charles Supper, Natick, MA), which was cleaned with the mixture of hydrochloric and nitric acids in advance to remove contaminants. After freezing at -90 °C for at least 30 minutes, the cardiolipin cyclohexane solution was freeze-dried in an ice-water bath while under vacuum (~70 mbar). The resultant cardiolipin powder was left under vacuum for over 1.5 hours to evaporate residual cyclohexane. Ambient pressure was restored to the cardiolipin powder by filling in Ar gas after the powder had been warmed to room temperature under vacuum for additional 30 minutes. The cardiolipin powder was

either used immediately for the next step of mixing or stored in an Ar gas-filled tube at -90 °C before further use.

To prepare a cardiolipin-water and cardiolipin-salt solution mixture, one of the following solutions was mixed with the cardiolipin powder accordingly: 1mM EDTA, 5 mM HEPES in pH = 6.76; 1mM EDTA, 3M NaCl, 5mM HEPES, in pH = 6.35; 1M $CaCl_2$, 5mM HEPES in pH = 6.94; 1mM EDTA, 0.5 M $LaCl_3$, 5mM HEPES in pH = 6.51. The concentrations of the salts were such chosen that the ionic strength of each of the salt solutions was identical. Except for the calcium salt solution, EDTA was added to sequester residual calcium ions in the other solutions. The mixtures of the cardiolipin powder with the above solutions were designated as "cardiolipin-water", "cardiolipin-NaCl", "cardiolipin-$CaCl_2$" and "cardiolipin-$LaCl_3$" mixtures, respectively (or collectively called cardiolipin-salt solution mixtures for the latter three), and concentrations (in wt%) prefixing the designations referred to the cardiolipin fraction of the total contents. In preparing the mixtures with a needed lipid concentration, a given amount of the cardiolipin powder, measured with an electro-balance (Model no. C-29, Cahn Instruments, Cerritos, CA) with a precision down to 1 μg, was mixed with a certain amount of water or salt solution. The glass capillary containing the mixture was then flame-sealed immediately after purging with Ar gas to prevent lipid degradation (see the next section), and the final lipid concentration (named "nominal concentration" here; see Section 3.6) was determined by comparing the weight of the capillary before and after adding water or salt solutions (weight of an empty capillary had been measured in advance). The mixture was subsequently centrifuged alternately against both ends of the capillary for 15-20 times such that the mixture could flow back and forth within the capillary to be homogenized. After centrifugation, the mixture was subjected to ten freeze-thaw cycles between -90 °C

and room temperature by alternately placing the mixture in and out of a deep-freezer to further improve homogeneity. For cardiolipin-salt solution mixtures, an additional homogenizing process was employed. This process entailed a scheme named "spinning-while-thawing", in which the same centrifugation procedure used above was performed again but only when the sample was freshly retrieved and thawed from -90 °C. Two such spinning-while-thawing processes were carried out for a cardiolipin-salt solution mixture with an intervening overnight incubation at 4 °C. For cardiolipin-water mixtures, the well-mixed samples were then used immediately for X-ray scattering experiments while the cardiolipin-salt solution mixtures were usually stored at 4 °C for another 5-8 days to further improve homogenization. A scheme for examining sample homogenization was performed before a data collection and will be described in the Section 3.5. Immediately before being used in an X-ray scattering experiment at ambient pressure, the capillary containing the cardiolipin sample were shortened with flame to < 1".

In addition to the regular cardiolipin-water mixtures, cardiolipin-water mixtures containing dodecane were also prepared. In preparing the samples, spectro-grade dodecane (Cat. no. 13089, Eastman Kodak, Rochester, NY) was pipetted to the cardiolipin powder before water. The capillary was weighed with the electro-balance after the addition to determine the amount of dodecane added. Fractions of dodecane with respect to the total organic contents (i.e. dodecane plus cardiolipin) were controlled to 5-10 wt%. The same sample preparation steps described above were followed after this point. It was not particularly difficult to homogenize water with the mixture of cardiolipin and dodecane. Again, the concentration prefixing a sample designation still referred to cardiolipin fraction with respect to the total content of the whole mixture.

3.4 Thin-Layer Chromatography of the Cardiolipin Samples

To examine the integrity of the cardiolipin molecules, thin-layer chromatography (TLC) was carried out for the cardiolipin samples after each step of the sample preparation and an X-ray scattering data collection. Depending on the sample preparation stage at which a cardiolipin sample was retrieved, different procedures were followed in performing the chromatography. The first step was invariantly to dissolve a cardiolipin sample back into chloroform, and the resultant solution could be directly used for the next step if the sample preparation stage was prior to mixing with water or salt solutions. However, if a sample had been mixed with water or salt solutions inside a glass capillary, more steps had to be carried out before proceeding to the next step. In this case, the capillary was cut to preserve only the sample-loaded portion and then placed into chloroform. Vigorous vortexing was followed to dissolve the cardiolipin-water or -salt solution mixtures and to retrieve them from within the capillary. The chloroform solution was then purged with Ar gas to evaporate most of the chloroform before incubated under vacuum (<50 mbar) for ~20 minutes to remove the remaining chloroform and water or salt solutions. Note that the purging step cannot be bypassed since placing the chloroform solution directly under vacuum would result in sudden boiling and loss of sample. The liquid-free cardiolipin sample could now be dissolved in chloroform again and used for the next step.

Three aliquots in 1-3 μl of the cardiolipin chloroform solution were dropped onto a silica gel 60 TLC plate along a line 25 mm from one end. The chloroform was evaporated in a fume hood before the plate was placed into an enclosed glass bottle containing a solvent mixture of chloroform, methanol and water in the ratio of 65:25:4. The amount of the solvent mixture was sufficient to cover the bottom 5 mm

of a TLC plate. The solvent mixture was allowed to carry and spread the cardiolipin sample across the plate for twenty minutes. After drying, molybdenum blue spray reagent (Cat. no. M1942, Sigma-Aldrich, St. Louis, MO) was sprayed onto the plate to spot the migrating cardiolipin sample.

The TLC results for cardiolipin samples at different sample preparation stages were shown in Figure 3.4.1. It was found that cardiolipin molecules remained intact until they were mixed with water. Upon that sample preparation stage, an additional spots, indicating the presence of degraded cardiolipin molecules (presumably with one or more of the double bonds oxidized), emerged even before a data collection was taken (Figure 3.4.1b). Lipid degradation could further develop to generate five spots after leaving a 55 wt% cardiolipin-water mixture at room temperature for two weeks (Figure 3.4.1c). Fortunately, the lipid degradation arising from water addition did not appreciably increase after a rapidly applied data collection at different temperatures up to 40 °C (Figure 3.4.1d; see the next section for the data collection scheme applied in this thesis study). This "free of further degradation" observation was still valid even after a data collection was performed up to 60 °C (Figure 3.4.1e). Even though TLC was not carried out for a cardiolipin sample after a data collection to higher temperatures, reversibility of the thermal phase behavior indicated that 60 °C might be the highest temperatures without inducing thermal lipid degradation in the time scale sufficient for a complete data collection (see below).

Since lipid degradation appeared to be inevitable for a cardiolipin-water mixture, we thus established two criteria to determine the reliability of a data set. For a data set to be accepted, the sample must both demonstrate reversible phase behavior, reflected in X-ray scattering patterns, through at least two temperature scans (either heating or heating and cooling), since irreversibility was indicative of lipid degradation, and TLC

result for the sample must display no additional spots to the two which had already been present after water addition. Previous experience indicated that phase behavior of a cardiolipin sample became irreversible following two temperature scans up to 90 °C while reversibility was still preserved after multiple temperature scans were conducted through 60 °C (e.g., Figure 3.4.2). We therefore limited our temperature scan to this temperature to avoid further lipid degradation. In addition, we also estimated the extent of degradation by comparing the TLC results of a given cardiolipin sample before and after dilution (Figure 3.4.1e). If darkness of the secondary TLC spots, representative of the degraded cardiolipin molecules, of a given sample were comparable to or weaker than that of the primary spots after the sample was, say, twenty times diluted, the degraded molecules were said to be in the fraction of ~5 mol%. The cardiolipin samples prepared in this thesis study were estimated to have <2 mol% degraded cardiolipin molecules.

Figure 3.4.1. Thin-layer chromatography results from the cardiolipin samples in different sample preparation stages: (a) the cardiolipin sample retrieved after an overnight incubation under vacuum (<50 mbar); (b) the cardiolipin sample retrieved after water addition and the homogenization process; (c) the cardiolipin sample after the standard preparation process, a data collection and 2-week storage at ambient condition; (d) the cardiolipin sample after the standard preparation process and a data collection up to 40 °C; (e) after the standard preparation process and a data collection. Note that various cardiolipin samples were used to produce these results. Lanes of each plate were deposited with different amounts of the cardiolipin solutions (1 or 1.5, 2 and 3 μl; distinguishable from the size of a spot). Note that the lane showing only one visible spot in (e) was deposited with the same solution as used in the other lanes but with one hundred times dilution. The drop sizes deposited on the lanes were 3, 3 and 1 μl from left to right.

(a)

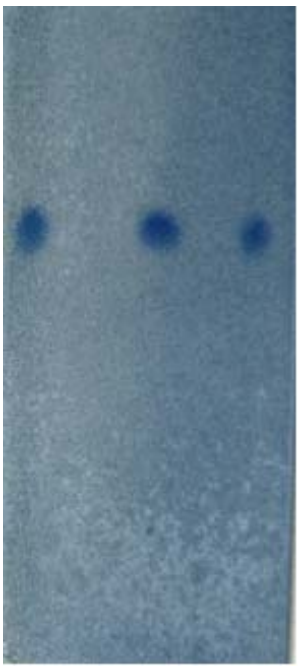

(b)

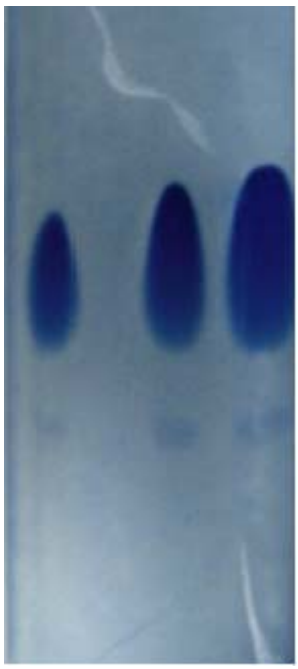

(c)

(d)

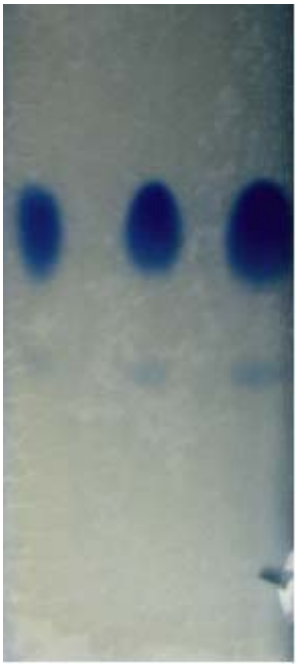

(e)

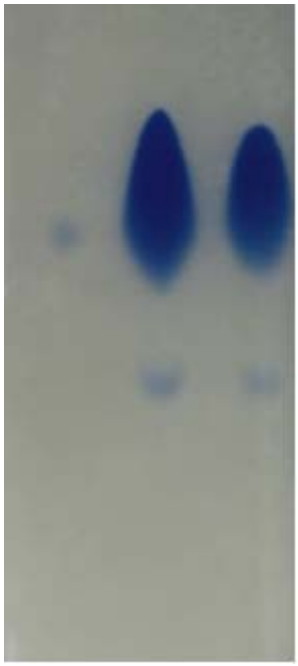

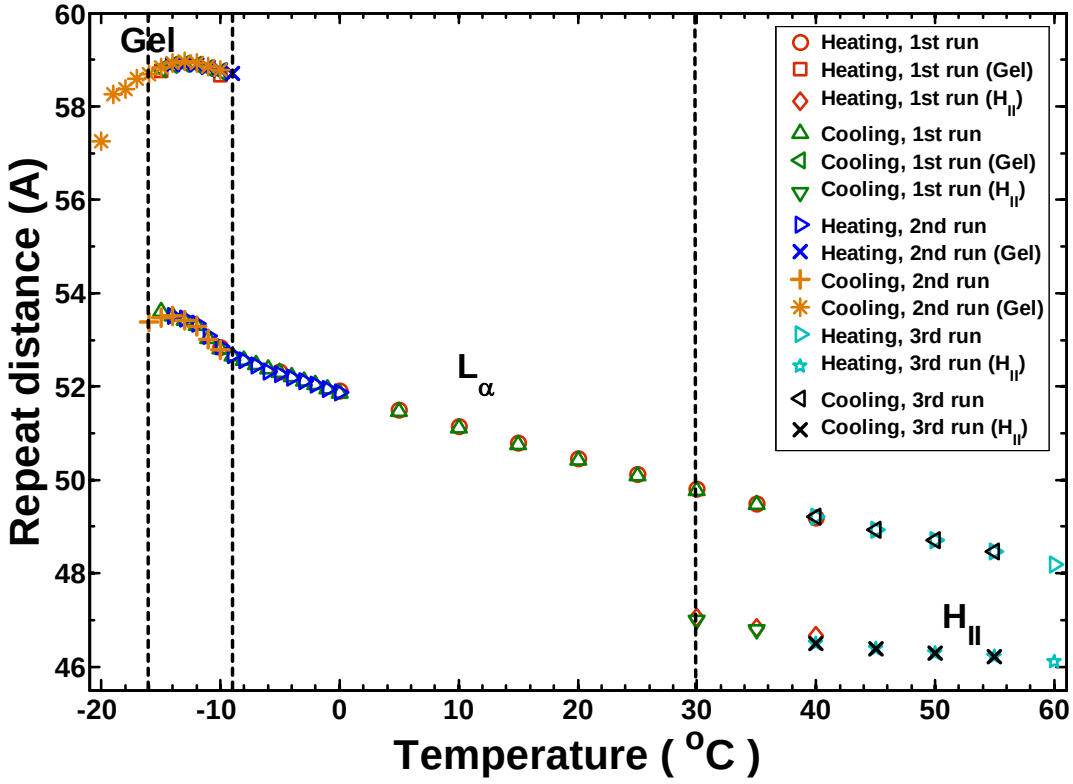

Figure 3.4.2. Repeat distance of the lamellar and the H_{II} phases as a function of temperature for an 80.6 wt% cardiolipin-water mixture. Phase behavior and the repeat distances were found to be reversible even after multiple temperature scans through 60 °C.

3.5 X-ray Scattering Data Collection

In an X-ray scattering experiment conducted at ambient pressure, a cardiolipin sample-loaded capillary was placed in a copper sample holder shown in Figure 3.5.1 during a data collection with the rotating anode X-ray beamline. The sample holder was located inside the vacuum sample box shown in Figure 3.2.7. Behind the sample holder were two Peltier coolers in series (Model. no. 9500/071/085B, Ferrotec, Santa Clara, CA) which were powered by a temperature controller (MTCA series, Melcor,

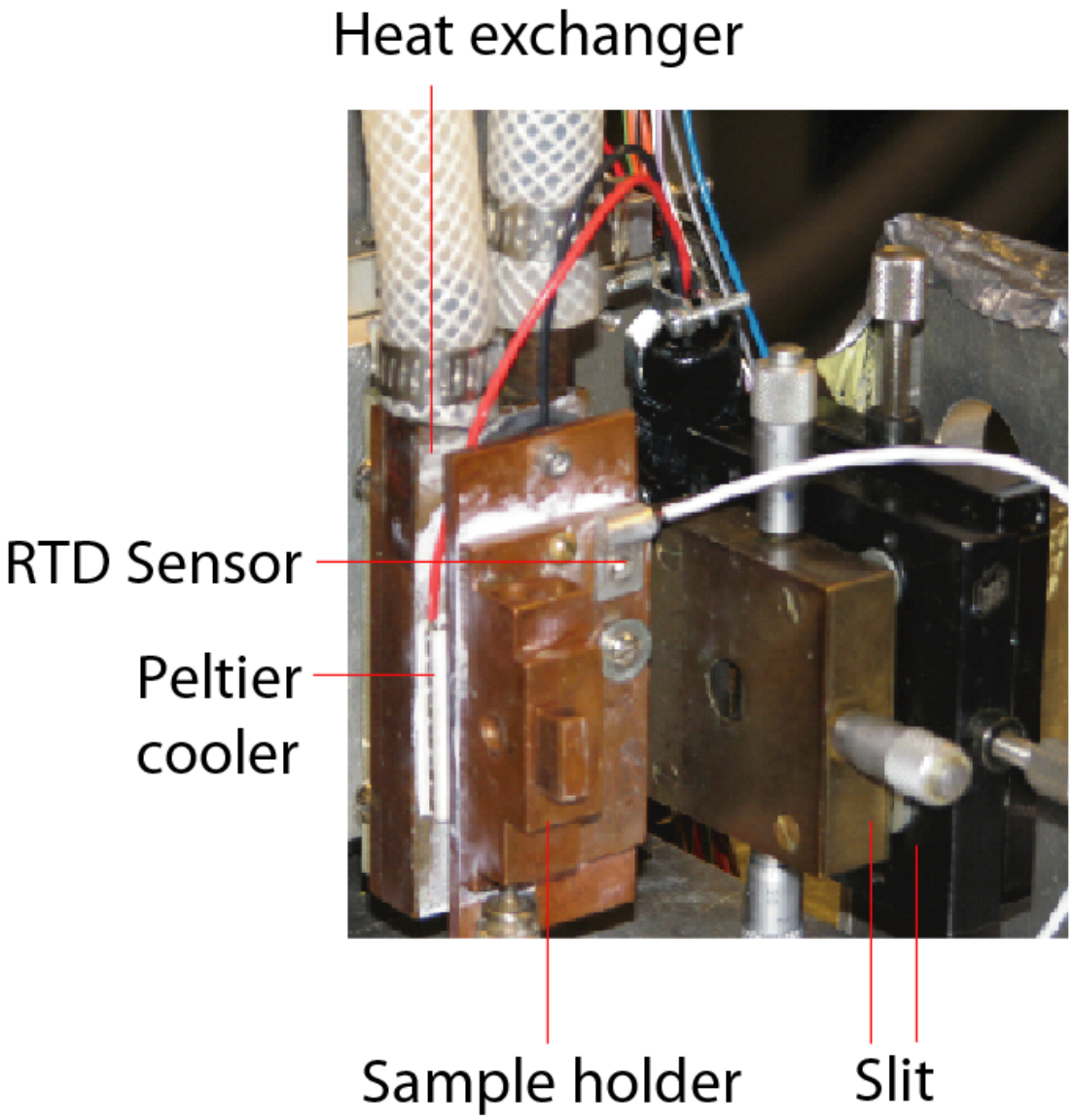

Figure 3.5.1. Interior of the sample box shown in Figure 3.2.7 for the rotating anode X-ray beamline. The sample box is vacuum when a data collection is underway. The sample holder is removable and can be replaced with the Be cell holder shown in Figure 3.5.2 to carry out a high pressure X-ray scattering experiment.

Trenton, NJ) connected to a personal computer, and cooled by a home-made heat exchanger circulated with water at 15 °C. An RTD temperature sensor (Part no. RTD-830, Omega Engineering, Stamford, CT) was attached to the sample holder and also connected to the temperature controller mentioned above. The same sample holder was also used for a data collection in the G1 beamline at CHESS though a new sample box needed to be built to house the sample holder (Figures 3.2.9 and 3.5.2). Design of the new sample box is depicted in Figures 3.5.3 to 3.5.7 and is similar to that of the original sample box in layout and function of the components and the ability to hold vacuum: a Peltier cooler with its power supplied by the same temperature controller and its heat dissipated by another home-made heat exchanger; all the cables and tubing connect to the box interior through vacuum-proof adapters. This new sample box is also capable of housing high-pressure equipment to carry out a high pressure X-ray scattering experiment (Figures 3.5.2 and 3.5.8). See the caption of Figures 3.5.3 to 3.5.7 for the detailed description of each component. Unlike the original sample box, only one Peltier cooler is incorporated into the new box. The temperature range achievable with the new box is therefore relatively limited but still covers all the temperatures employed here. As mentioned in the caption of Figure 3.2.9, the vacuum circuit of the new sample box is independent of that of the vacuum pipe. Two air gaps were present on both sides of the sample box to ease the loading of a sample. The temperature of the sample holder within both of the boxes was controlled with a home-developed program *TVX* (version 7.2) at the rotating anode beamline and with the software package *SPEC* (Certified Scientific Software, Cambridge, MA) at the G1 beamline. The two programs were also used to control the data collection.

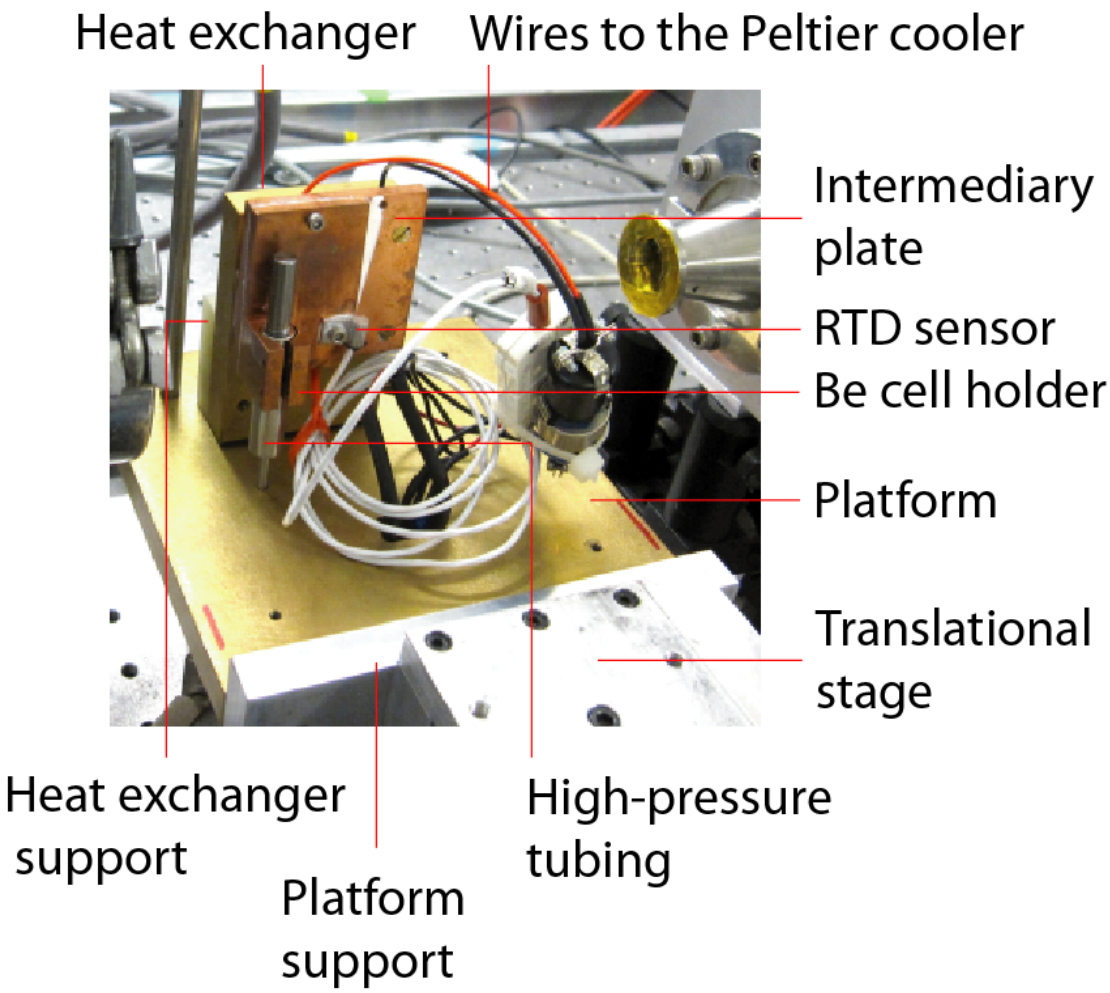

Figure 3.5.2. Sample box used in the G1 beamline. The cover with two X-ray transparent kapton windows was lifted to show the interior of the box, which was in the setting for high-pressure X-ray scattering experiments. See Figure 3.2.9 for the sample box with the cover in place and Figures 3.5.3 to 3.5.7 for the description of each component.

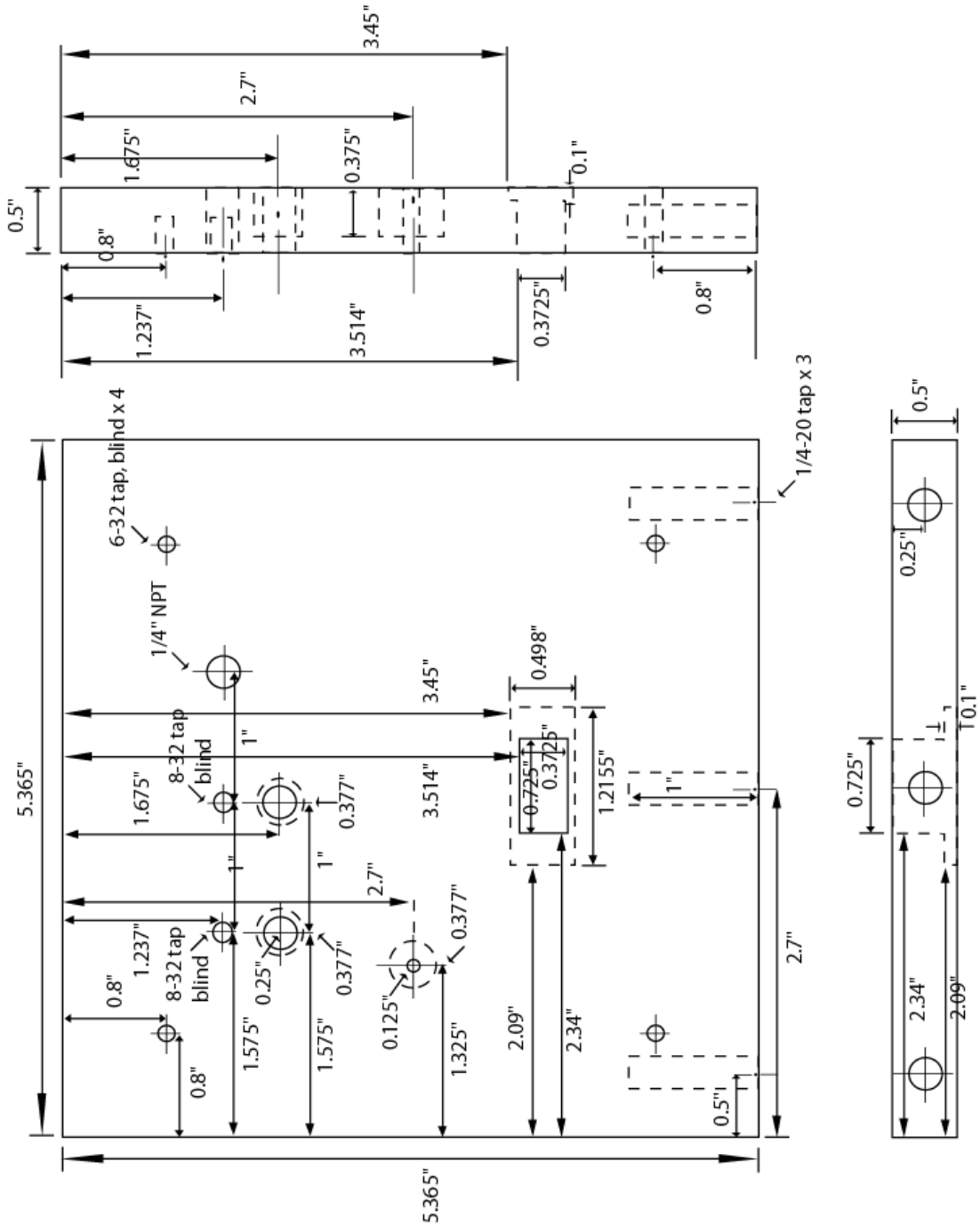

Figure 3.5.3. Brass-made platform of the sample box shown in Figure 3.5.2. The platform is used to house the other components.

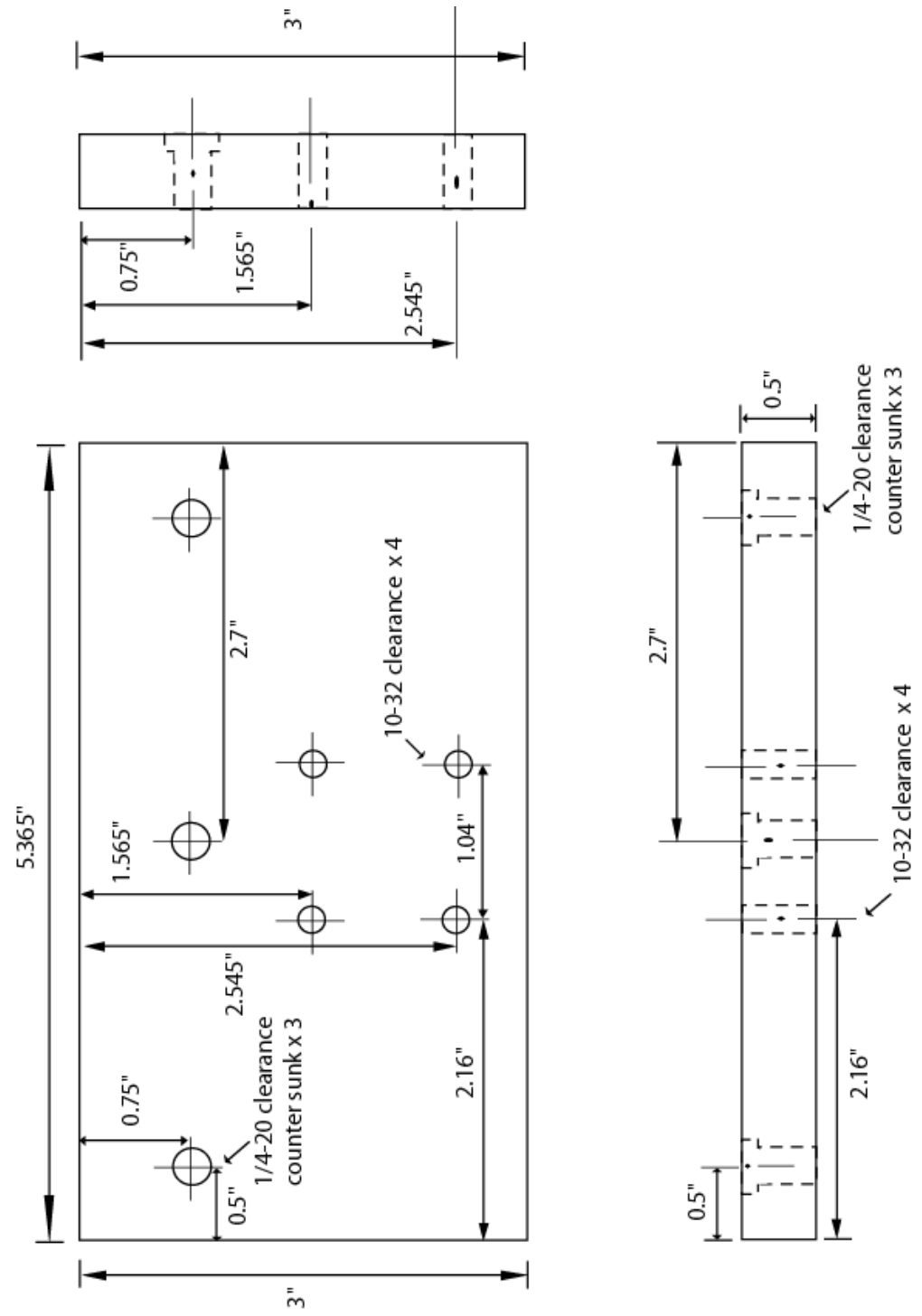

Figure 3.5.4. Aluminum platform support of the sample box shown in Figure 3.5.2. The support holds the platform to the translational stage in the G1 hutch.

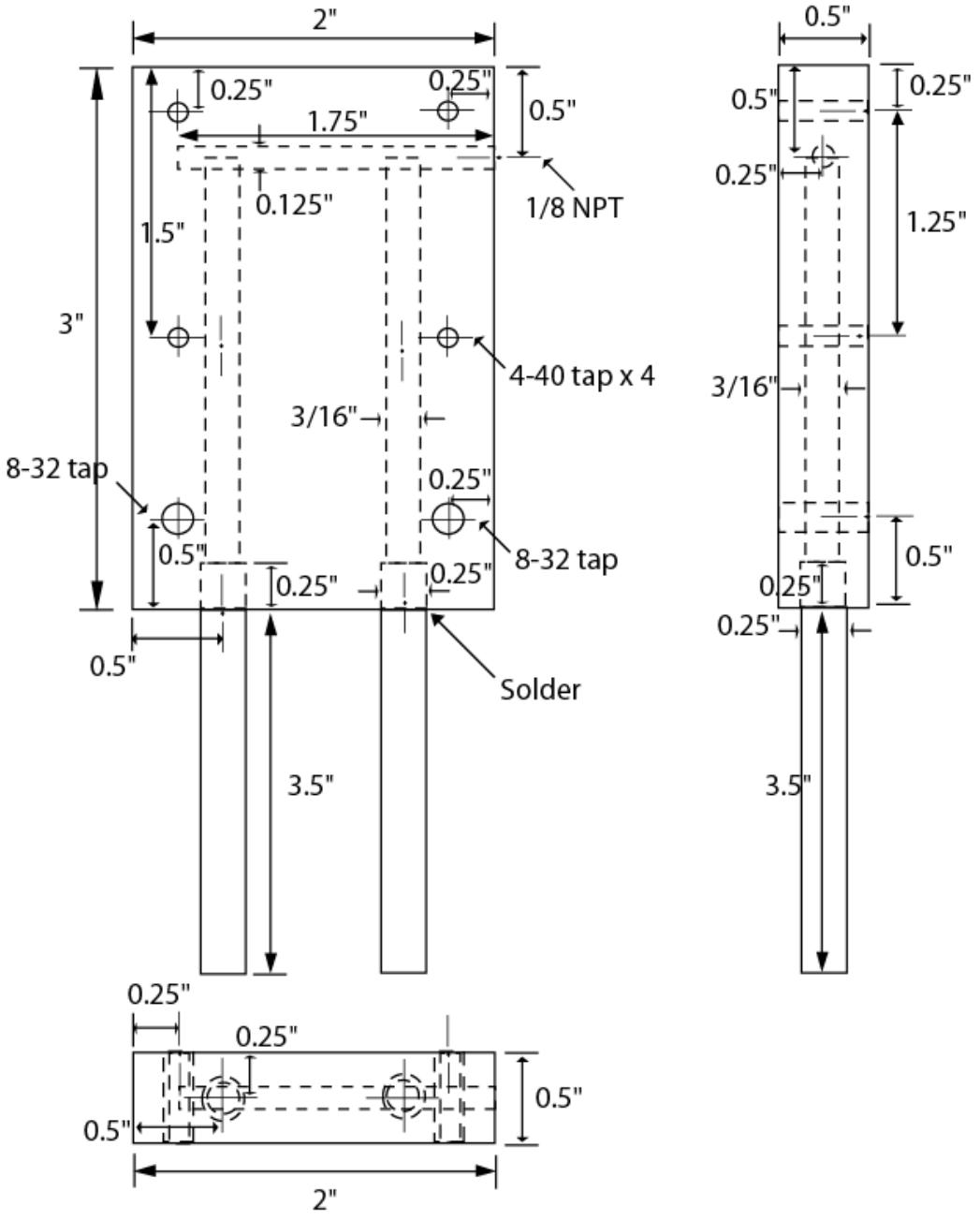

Figure 3.5.5. Brass-made heat exchanger of the sample box shown in Figure 3.5.2. The heat exchanger is circulated with 15 °C water and used to dissipate heat generated by the Petlier cooler.

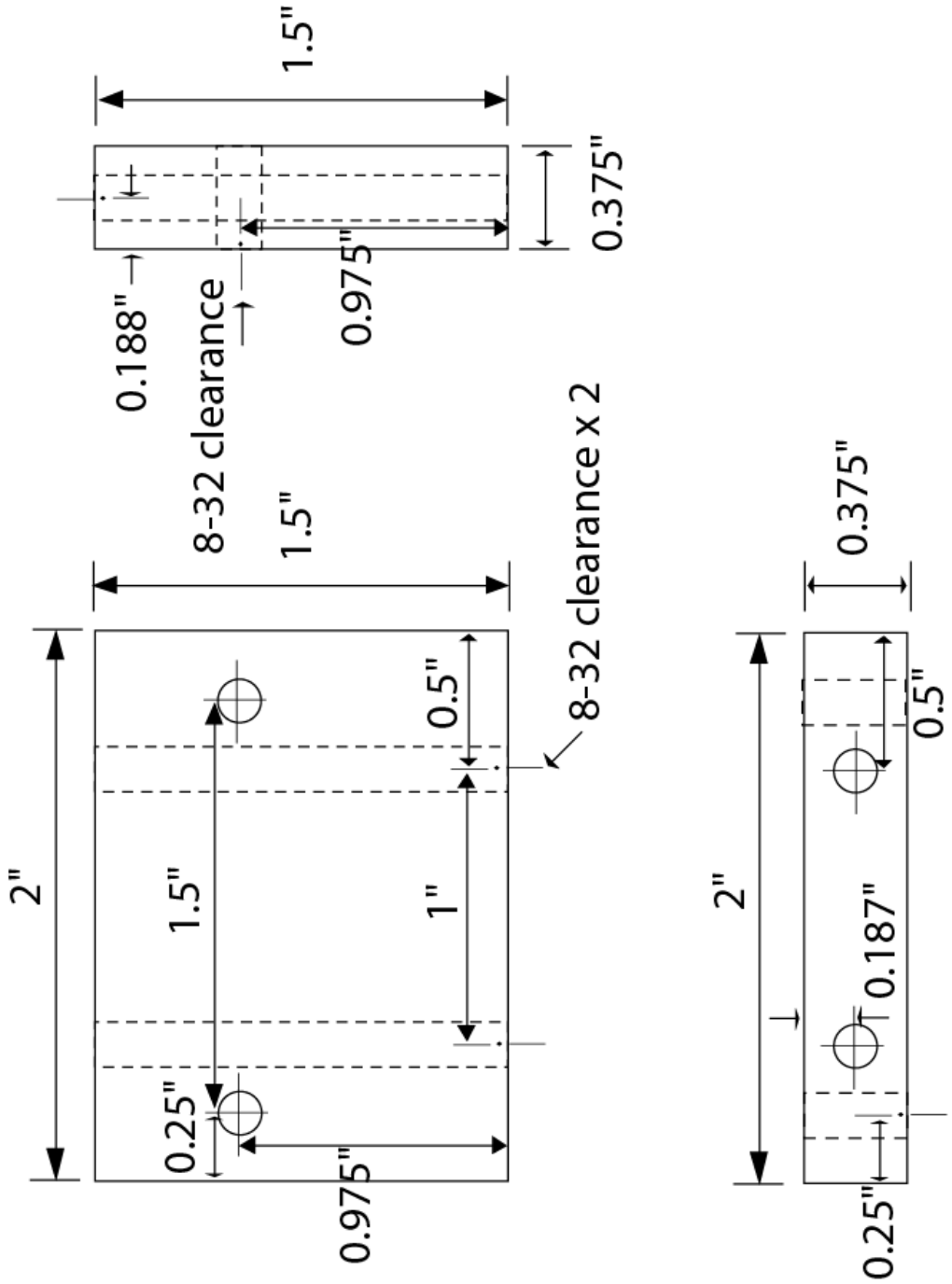

Figure 3.5.6. Heat exchanger support of the sample box shown in Figure 3.5.2. The support is made of G10 fiberglass laminated epoxy resin and used to stabilize the heat exchanger.

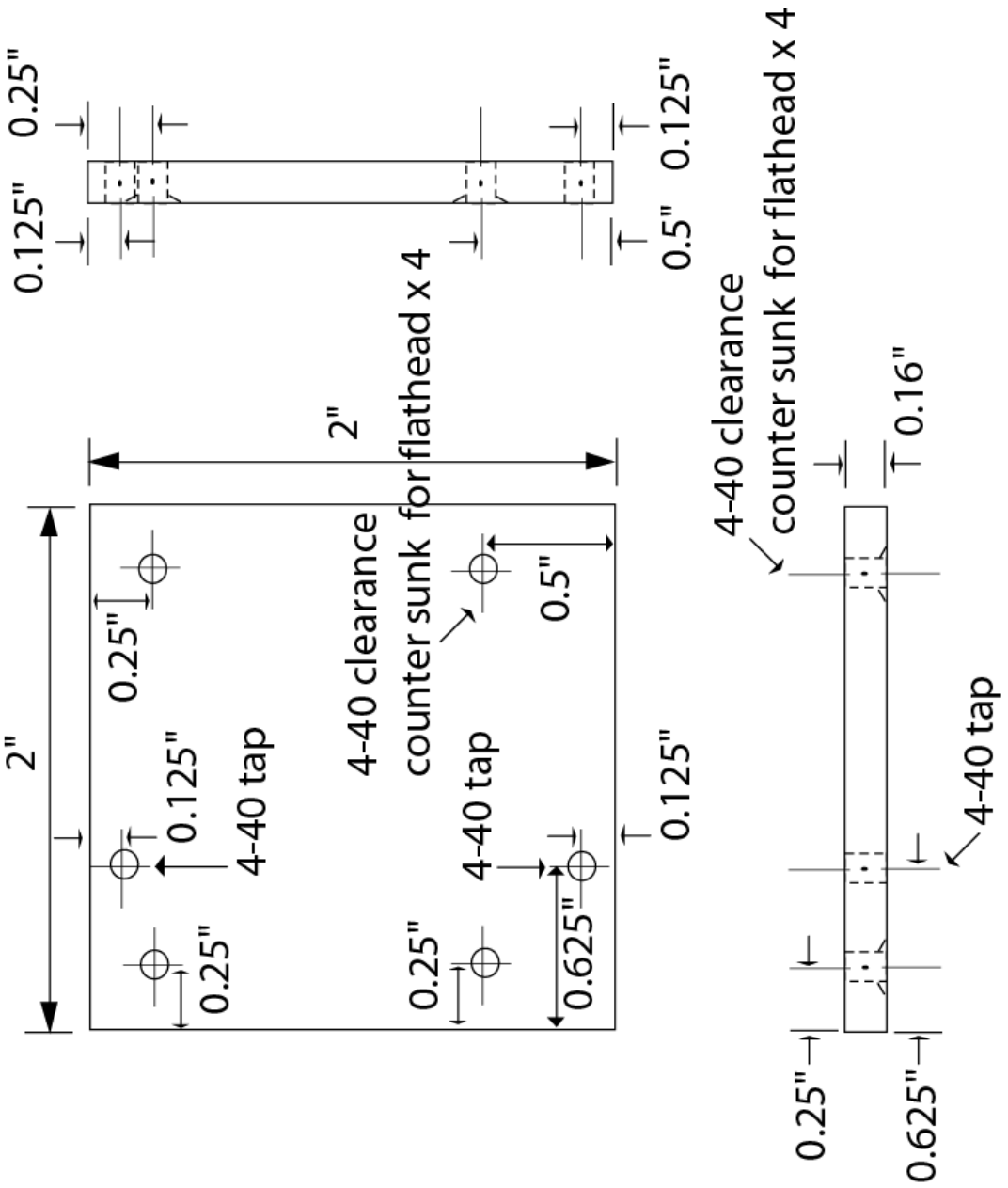

Figure 3.5.7. Copper intermediary plate of the sample box shown in Figure 3.5.2. The plate clamps the Peltier cooler onto the heat exchanger and holds the sample holder shown in Figure 3.5.1 in place.

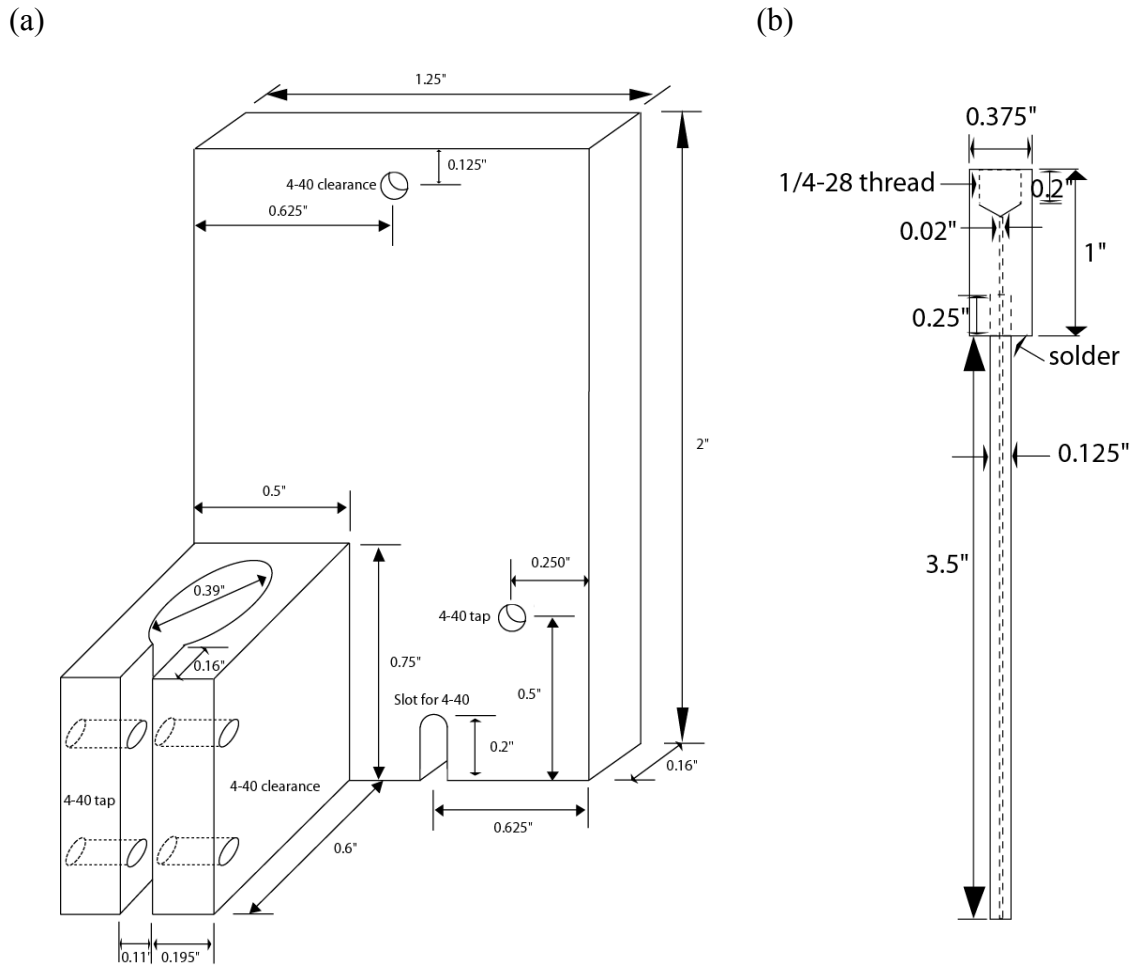

Figure 3.5.8. (a) Copper Beryllium cell holder as shown in Figure 3.5.2. The holder is attached to the intermediary plate shown in Figure 3.5.7 and used to house and conduct heat to/from the Beryllium high pressure cell, which can accommodate a sample-loaded glass capillary and hold pressure up to 2.4 kbar. Refer to Urayama (2001) for the details of the cell. The holder can also be used in the setup with the rotating anode beamline. The schematic is not drawn in scale. (b) High pressure tubing as shown in Figure 3.5.2. The tubing penetrates the platform shown in Figure 3.5.3 through a vacuum-proof adapter and connects to the Be cell in the top end and to a high-pressure pump at the other end. In an ordinary setup, the top end of this tubing may be the actual component clamped by (a).

The X-ray apparatus used for the data collections has already been described in Section 3.2.2. Vacuum pipes with various lengths were chosen according to the needed sample-to-detector distances, which were calibrated with silver behenate powder (Blanton et. al., 1995) in advance. Prior to each data collection, homogeneity of a cardiolipin sample was examined by measuring |Q| of the first order peak of the L_α phase or the *(1,0)* peak of the H_{II} phase as the X-ray beam was translated along the long axis of the capillary at ambient pressure and 20 °C. Diffraction images and the relative integrated intensities of peaks in each phase were also compared. Data collection would be stopped if diffraction images taken for a sample homogeneity test had displayed an observable discrepancy (e.g., Figure 3.5.9) when compared to one another. The vast majority of the samples used for the data collections demonstrated <0.1 Å variations in d-spacing or in *(1,0)* peak position, and the relative peak intensities were essentially unchanged (e.g., Figure 3.5.10) when results from different parts of a sample were compared. A minor exception was the cardiolipin-NaCl mixtures, which exhibited ~1 Å variations in average. The larger discrepancy in d-spacing might be ascribed to the high NaCl concentration (3 M) employed for these samples.

X-ray scattering data for this thesis study were collected at various sample temperatures. Different temperature schemes were followed, depending on the anticipated phase transition temperatures for a given condition. In general, a cardiolipin sample was first cooled from 20 °C where a homogeneity test was carried out to a lower temperature, usually subzero ones, with the rate of 2 °Cmin^{-1}. At each temperature point, a sample was allowed to equilibrate for 15 minutes (or 20 minutes for samples within a Be cell, due to reduced thermal conduction efficacy) before exposed to X-rays. Temperature was changed with the rate of 2 °Cmin^{-1} and

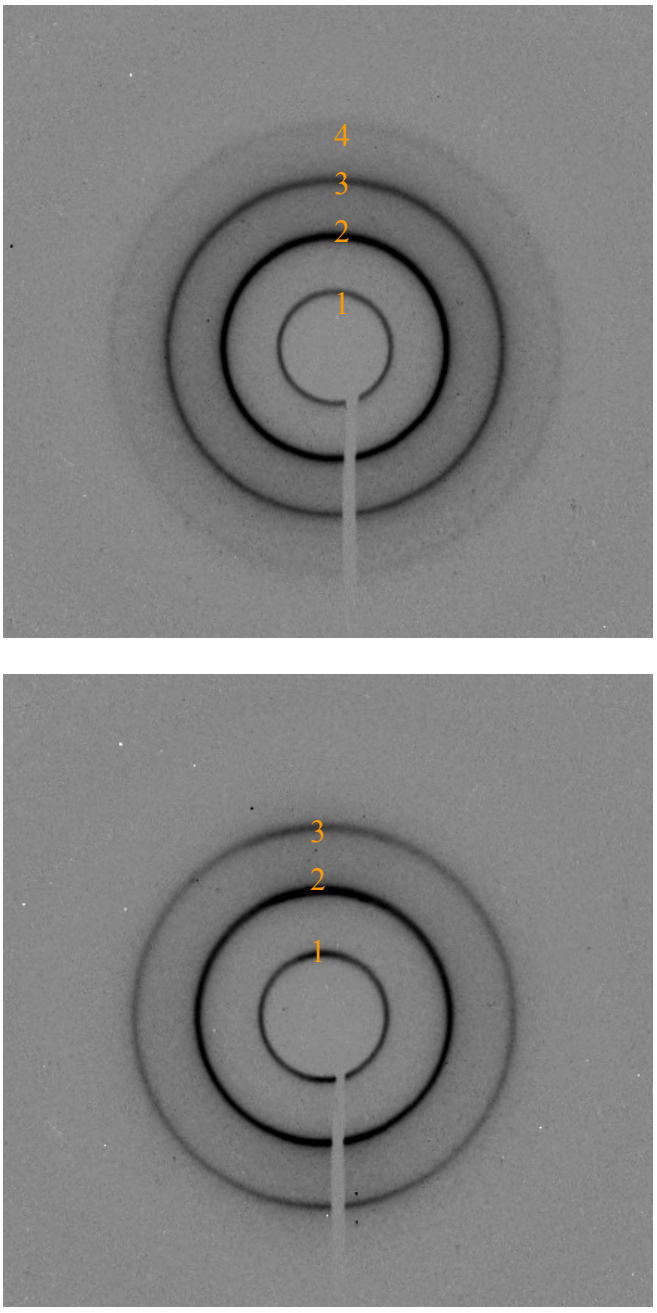

Figure 3.5.9. Example of a sample with poor homogeneity. The homogeneity test was carried out for a 40 wt% cardiolipin-water mixture, with the X-ray images taken at two separate parts of the sample. The two images display outstanding differences in positions and quantity of the resolvable peaks. Numbers index the peaks.

(a)

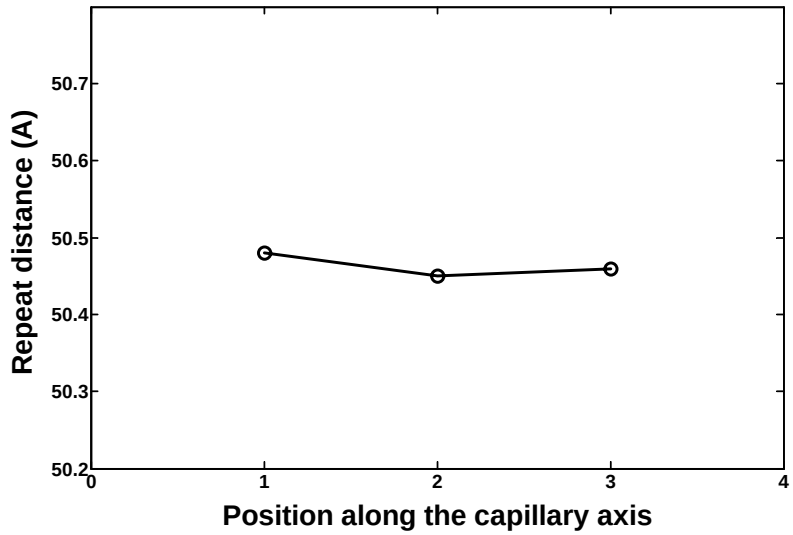

(b)

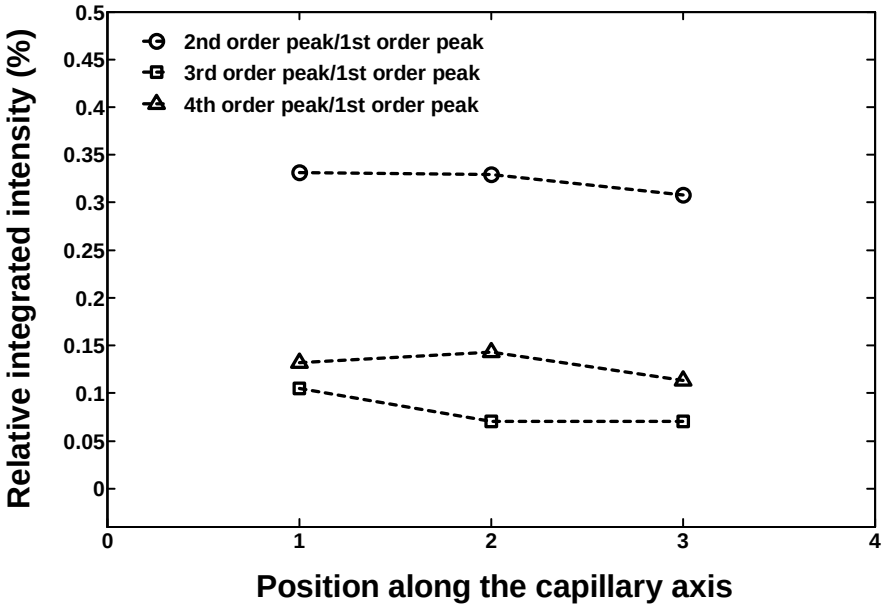

Figure 3.5.10. Example of a sample with acceptable homogeneity. The homogeneity test result of an 81.3 wt% cardiolipin-water mixture shows repeat distances of the L_α phase (a) and integrated intensities of the higher order peaks relative to that of the first order peak (b) at different sample positions. X-rays were illuminated on positions equally spaced across the sample along the capillary axis.

temperature points were 5 °C apart (in some cases, such as shown in Figure 3.5.2, the interval was down to 1 °C to confirm the observation of the phase separation phenomenon discussed in Section 4.4). In this thesis study, we limited upper and lower bounds of temperatures to 60 °C and -20 °C, respectively. Total X-ray exposure times were set to either 100 seconds (adopted for the homogeneity tests), 300 seconds or 600 seconds with the rotating anode beamline and 0.8 seconds with the G1 beamline. For each temperature point, two X-ray images were taken consecutively to split the aforementioned total exposure time evenly for the zinger removal purpose (see the next section).

In addition to the regular data, dark images with the X-ray shutter closed were collected for each data set to record the thermally- and defect-induced dark currents of the CCD detectors for the data processing purpose (see the next section). Background noise arising from air scatter (which was very week, due to the vacuum condition), the glass capillaries and kapton windows were also recorded by exposing empty capillaries to X-rays for the electron density map reconstruction with the line-shape fitting method (Section 4.3.2). For the same purpose, the shapes of X-ray beam were registered by recording the attenuated X-rays without a beam stop and a sample. The same exposure times were applied to these subsidiary data collections.

3.6 X-ray Scattering Data Processing and Analysis

Image correction procedures were carried out for raw X-ray scattering data. A more detailed description of the process can be found in Barna et. al. (1999). An ordinary X-ray scattering image, in addition to wanted signals originating from samples, also includes bright, spatially confined, random signals from cosmic rays,

decaying radioactive isotopes in the environment or other sources. These unwanted signals are called zingers. Since zingers are randomly located over a detector active area, they can be revealed by comparing two or more scattering images taken in essentially identical conditions. Any statistically significant difference between these images is presumed to arise from zingers and should be removed, or *de-zingered*, to improve data quality. As noted in the last section, two nominally identical X-ray images were collected for a given experimental condition (i.e. sample identity and temperature) for the de-zingering process. At the rotating anode beamline, the de-zingering process was carried out manually with the program *TVX* after a data collection was completed. In the G1 beamline, the program *SPEC* was set to de-zinger the two images automatically after the X-ray exposures. As expected, longer X-ray exposure times are inevitably accompanied by more zingers. We therefore limited the maximum exposure time to 300 seconds for each image with the rotating anode beamline. If the needed total exposure time exceeded 600 seconds, more than two images would be taken consecutively to split the exposure time. The short exposure time employed in the G1 beamline did not require a similar limitation.

A de-zingered image then underwent a dark current subtraction with a de-zingered dark image. Again, *TVX* was used to manually carry out the process in the rotating anode beamline while dark currents were automatically subtracted in the G1 beamline. Finally, the images were corrected for the image distortions intrinsic to CCD detectors using a distortion correction map. The method of producing a distortion correction map is described in Barna et. al. (1999). *TVX* and *SPEC* were respectively used to perform the distortion correction for the rotating anode and G1 data. The image correction process is summarized in Figure 3.6.1.

Corrected images were then azimuthally integrated to generate X-ray scattering profiles (e.g., Figure 3.2.11). The azimuthal integration involves integrating the scattering intensities along a circumference with a specific radius. This process carries on with an ever increasing radius until the image edges are reached. All the data, collected both with the rotating anode and G1 beamline, were integrated with *TVX*, in which the radius range could be set to exclude the beam stop shadow. The resultant X-ray scattering profiles, expressed as scattering intensity versus radial distance from the center (in pixel number), provided information of the repeat distances and lipid phases of the cardiolipin samples, from which the electron density maps were reconstructed (Section 4.3). The repeat distances were determined with *TVX* by evaluating peaks positions in $|Q|$ while lipid phase assignments were performed according to the principles outlined in Section 3.2.3. The vast majority of the lipid phase determinations were straightforward and unambiguous. However, assigning lipid phases to X-ray images displaying crystalline-like patterns and phase separation phenomenon was more complicated. For those two types of data, more effort was dedicated to determining the lipid phases and will be detailed in Sections 4.4 and 4.5.

The nominal lipid concentrations also needed to be calibrated. Ideally, the nominal concentration was supposed to reflect the real sample concentrations. However, many experimental errors could be introduced in determining the sample concentrations with a gravimetric method. It was noticed that d-spacing of the lipid liquid crystalline L_α phase invariantly demonstrated a power law relationship with the lipid concentration (Figure 3.6.2 and also Section 4.3.1). Due to the higher accuracy in the d-spacing measurement, the lipid concentration derived from d-spacings and the power law relation was expected to be more reliable and closer to the real sample concentration. We therefore calibrated the sample concentrations accordingly by first fitting the d-

spacing against nominal concentration curves with power laws and then fed the d-spacings back to the obtained equations to yield the calibrated sample concentrations. X-ray scattering data collected at 20 °C and ambient pressure, including those from the homogeneity tests, were used for this calibration process. The result of the calibration is shown in Table 3.6.1. Due to the limited amounts of the samples, this calibration process was not carried out on the cardiolipin-salt solution mixtures.

Figure 3.6.1. Summary of the X-ray image correction process. The raw images (top), with strong zingers such as that highlighted, are de-zingered to generate a zinger-free image (middle). Dark currents are then subtracted from this de-zingered image using a dark image collected for this data set (bottom left). The distortion correction process follows to produce the final image (bottom right). The circles in the bottom images compare ellipticity of the scattering rings before and after the distortion correction.

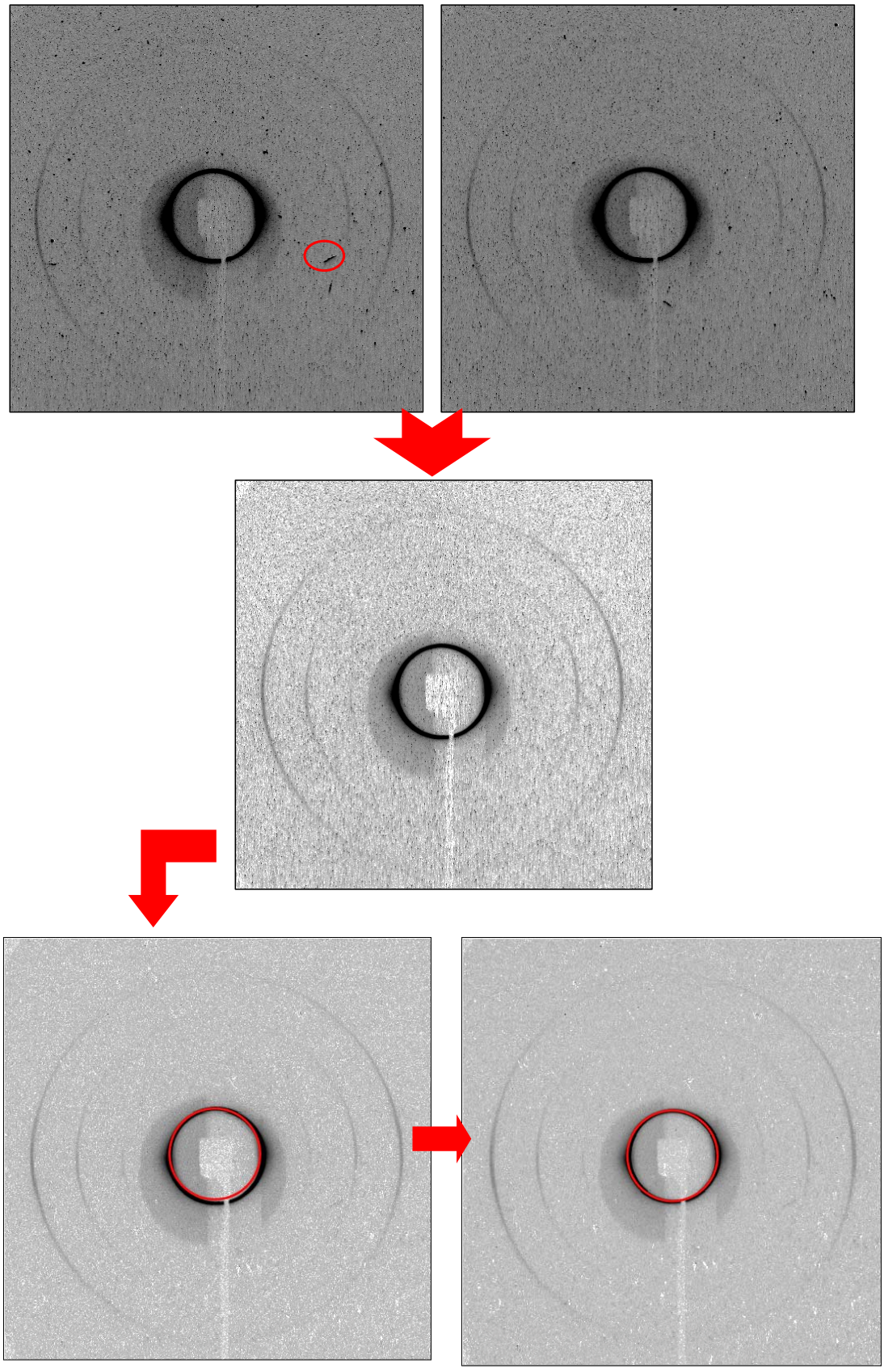

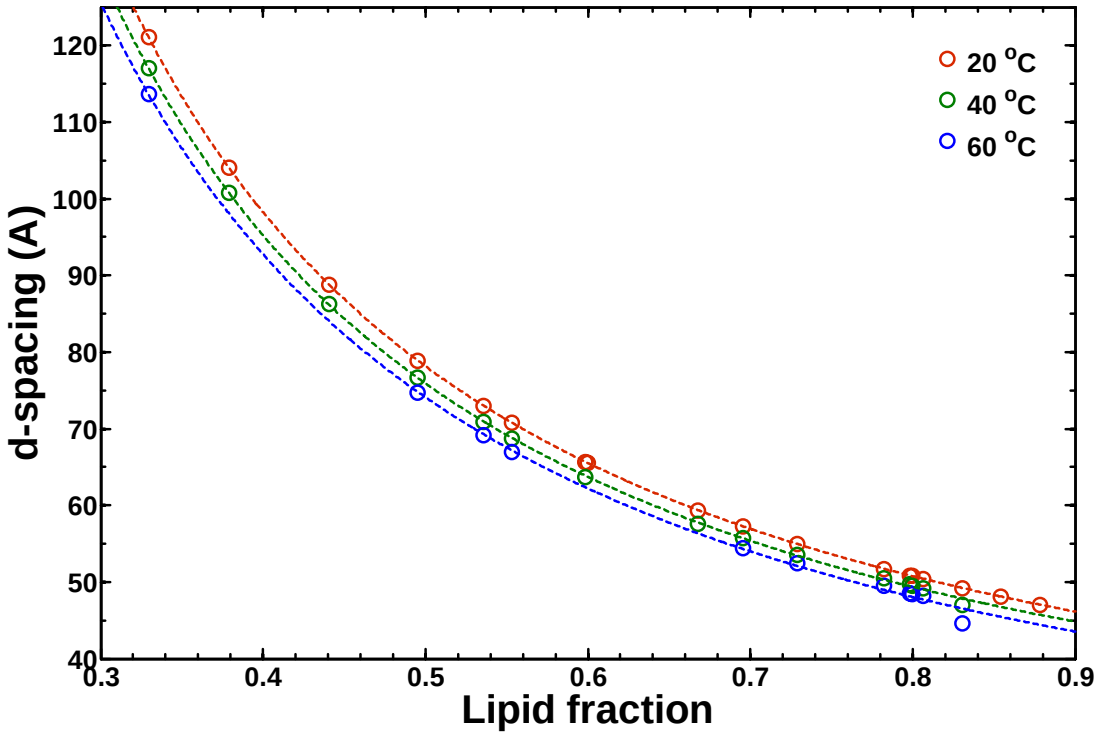

Figure 3.6.2. d-spacing as a function of lipid fraction for the cardiolipin-water mixtures at different temperatures. The data points were seen to follow parallel power law relations, which can be utilized to calibrate the sample concentrations (see the text). The power laws fitted to the data are $y = ax^b+c$ with $a = 24.56$, $b = -1.292$, $c = 18.01$ for 20 °C; $a = 24.72$, $b = -1.263$, $c = 16.59$ for 40 °C; $a = 25.81$, $b = -1.215$, $c = 14.21$ for 60 °C.

Table 3.6.1. Nominal and calibrated sample concentrations of the cardiolipin-water mixtures used in this thesis study.

Nominal concentration (wt %)	Calibrated concentration (wt %)
32.9	32.9
38.0	37.9
44.2	44.0
49.1	49.5
53.9	53.6
55.1	55.3
55.6	55.3
60.0	59.8
60.2	60.0
66.5	66.8
68.5	69.5
72.5	72.9
77.1	78.2
79.8	79.8
80.7	79.9
82.1	80.6
85.1	83.0
86.3	85.4
86.7	87.8

CHAPTER 4

PHASE BEHAVIOR OF CARDIOLIPIN LIQUID CRYSTALS

4.1 Introduction

In this chapter, I present the experimental results of this thesis study. These results can be summarized in a temperature-composition phase diagram of the cardiolipin-water mixtures, which covers the lipid concentrations from 32.9 wt% to 85.4 wt% in the temperature range of -20 °C to 60 °C and will be discussed in Section 4.2. Based on the underlying data of the phase diagram, electron density maps of the cardiolipin-water mixtures were reconstructed and presented in Section 4.3, to provide a structural explanation to the observed phase boundaries. Two striking features were also observed in the phase diagram: the presence of a lamellar-lamellar phase separation region and a phase displaying crystalline-like X-ray scattering patterns at the high concentration limits. Two dedicated sections, 4.4 and 4.5, will explore the nature and origins of these two phases. The results for the cardiolipin-alkane-water mixtures are presented in Section 4.6.

4.2 Temperature-Composition Phase Diagram

Previous studies have established that, upon mixing with sodium, calcium or other cation salts, cardiolipin can spatially arrange into the liquid crystalline H_{II} phase (Seddon et. al., 1983; Rand and Sengupta, 1972). This phenomenon was ascribed to the reduction of electrostatic repulsion among the charged headgroups, which enhanced the wedged molecular shape contributed by the bulky hydrocarbon chain region of the lipid (see Sections 1.3 and 2.3). It is therefore predictable to observe, within the temperature and concentration ranges examined in this thesis study, that

cardiolipin predominantly assumed the L_α phase when suspended in pure water without the presence of counterions (Figure 4.2.1). Moreover, presumably due to the absence of counterions, the d-spacing of the L_α phase expanded indefinitely with increasing water amount and never coexisted with bulk water as zwitterionic lipid-water systems do (see Section 4.3.1 for detailed discussion). Nevertheless, a variety of phase transitions, including the one to the H_{II} phase, still occurred even without counterions when the cardiolipin-water mixtures were at high concentration.

At low temperatures, approximately <-15 °C, the main transition occurred, in which the liquid crystalline L_α phase transformed to a gel phase. Unlike the L_α phase, d-spacing of the phase was observed to assume an essentially fixed value of 58.0±0.5 Å at -20 °C regardless of the sample concentration. The gel phase was thus inferred to coexist with bulk water, i.e., being in the excess water condition (refer to Section 4.3.1 and Figure 4.3.1a for details). The origin of this excess water condition is not very clear since electrostatic interactions arising from the charged headgroup are presumed to overwhelm any inter-bilayer van der Waals attraction needed for the excess water condition to occur (see also Section 2.2.1). However, we speculated it to be involved with oscillatory hydration interactions, which might result in net inter-bilayer attraction even in the presence of surface charges (Section 2.2.2). This will be further discussed in Section 4.3.3. In the concentration range of 55.3 wt% to 72.9 wt% or beyond, peculiar phase behavior was observed before formation of the gel phase at lower temperatures (the "$L_{\alpha 1}$+ $L_{\alpha 2}$" region of Figure 4.2.1). The upper boundary of this phase region shifted toward higher temperatures with increasing sample concentration and was speculated to drop dramatically as the sample concentration approached 78.2 wt% (the dashed line in the "$L_{\alpha 1}$+ $L_{\alpha 2}$" of Figure 4.2.1). As illustrated in Figure 4.2.2, the scattering peaks arising from the L_α phase in this concentration range apparently

Figure 4.2.1. Temperature-composition phase diagram of cardiolipin-water mixtures. Data points of each concentration were backed by a separate sample. The dashed lines are the speculated phase boundaries. The phase displaying crystalline-like diffraction patterns is designated as the "tiny crystals-cluster (TC)" phase. Red upward triangles represent the L_α phase; Green diamonds the lamellar-lamellar phase separation region; blue downward triangles the L_β phase; orange right-pointing triangles the L_α-L_β phase coexistence region; downward triangles the L_α-TC phase coexistence region; left-pointing triangles the H_{II}-TC phase coexistence region; crosses the L_α-H_{II} phase coexistence region. Straight-line boundaries are, obviously, simplifications and approximations.

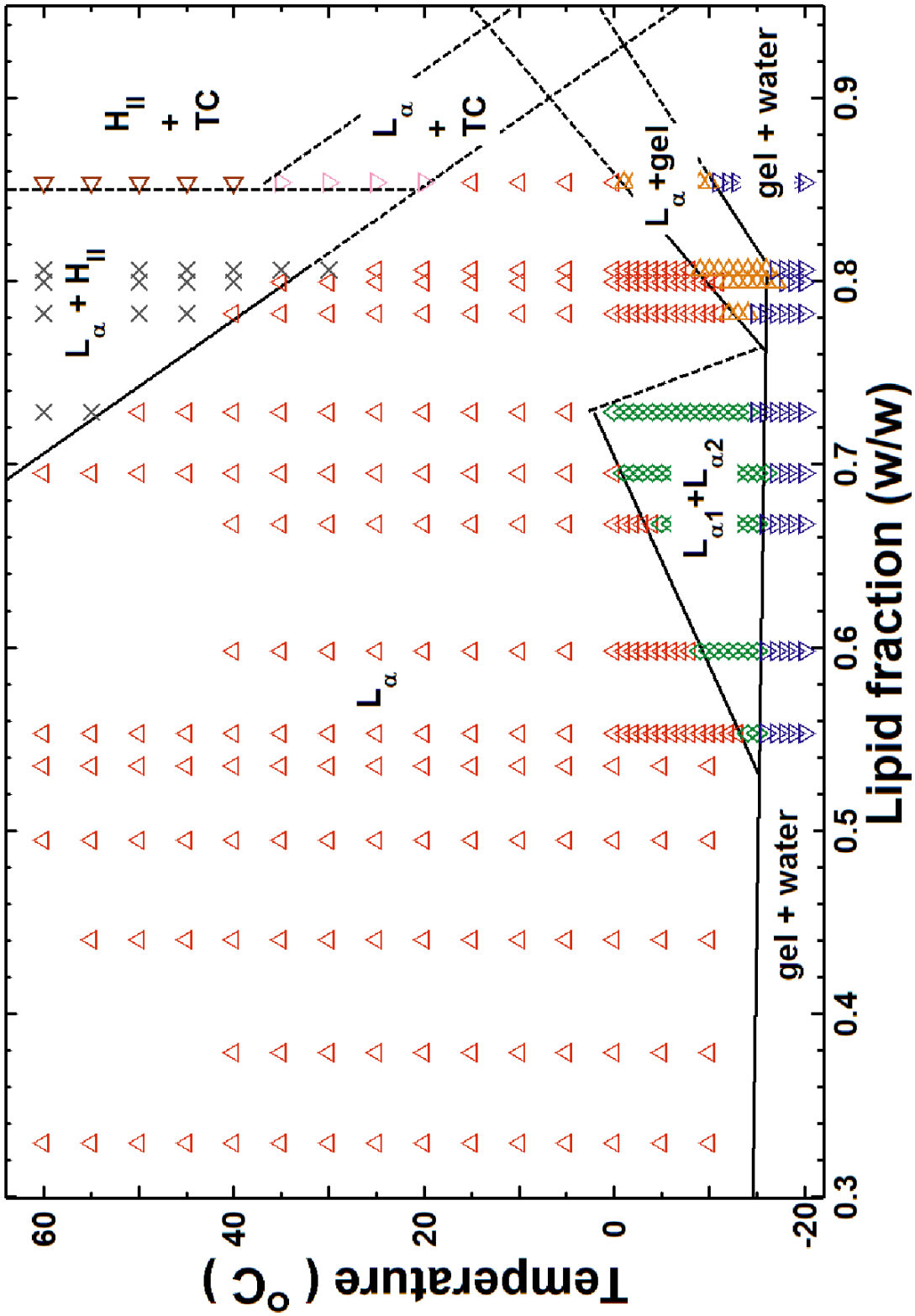
Temperature (°C)
Lipid fraction (w/w)
60
40
20
0
-20
0.3
0.4
0.5
0.6
0.7
0.8
0.9
H_II + TC
L_α + TC
L_α + H_II
L_α
L_α +gel
gel + water
L_α1 +L_α2
L_α
gel + water

(a)

(b)

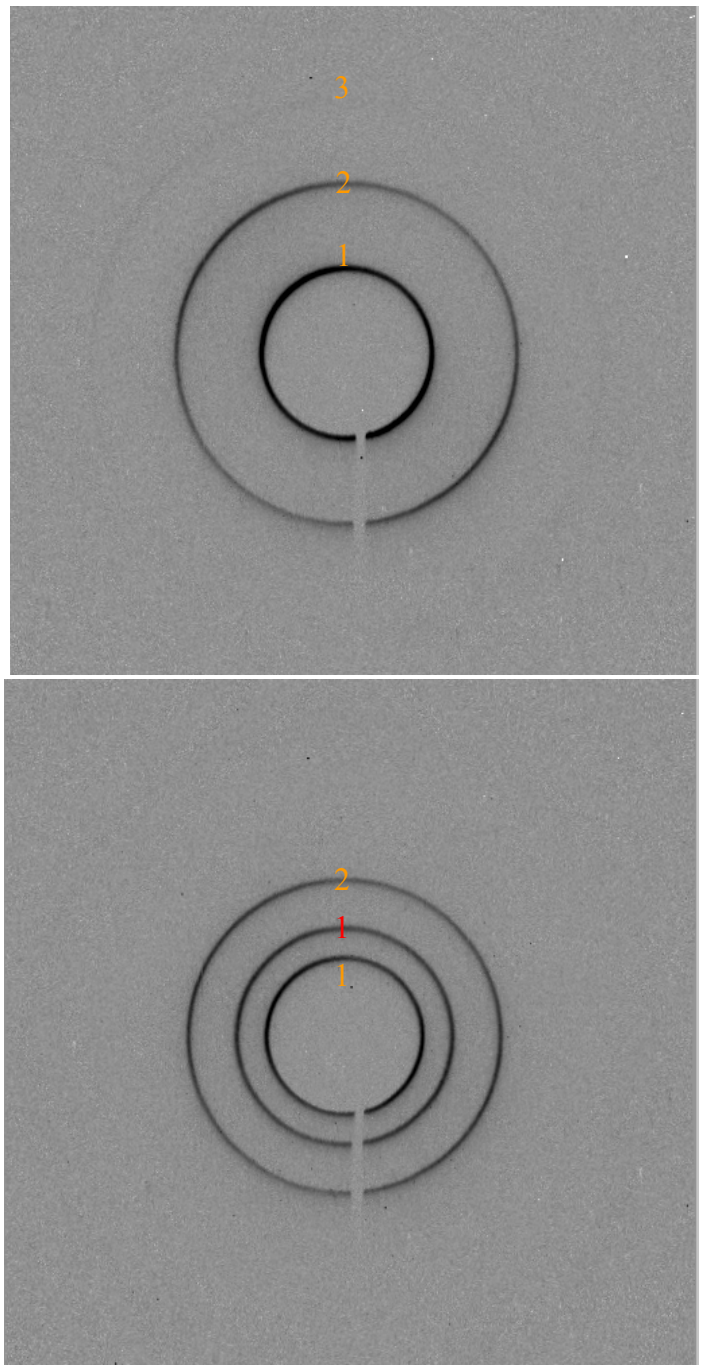

Figure 4.2.2. X-ray diffraction images of a 59.8 wt% cardiolipin-water mixture at -5 °C (a), showing diffraction peaks from a single lamellar phase, and at -13 °C (b), displaying an additional diffraction peak presumably from another lamellar phase. Numbers index the peaks, with different colors for the two different phases.

split into two sets of peaks when temperature was depressed. The two sets of peaks changed their positions with temperature differently and could not be collectively indexed as a single phase. This fact may indicate that the peaks arose from two coexisting phases. Indeed, the Gibbs phase rule, *(degree of freedom) = (number of chemical components) - (number of coexisting phases) + 2*, allows two phases to coexist within a lipid-water system when it is in the limited water condition (this fact applies to the other coexisting regions observed in the phase diagram of Figure 4.2.1). The WAXS data confirmed the melted state of the hydrocarbon chains and the liquid crystalline nature of the two coexisting phases (Figure 4.2.3). However, as will be discussed in Section 4.4, only three scattering peaks at most could be resolved unambiguously for each of the two phases. In some cases, the scattering peaks from the two phases even overlapped (e.g., Figure 4.2.3b). These two constraints limited certainty of the phase assignment. Many of the X-ray scattering profiles could unambiguously reveal the nature of one of the coexisting phases but comparison with other profiles collected at different temperatures for the same sample was necessary for indexing the other phase. For example, in Figure 4.2.3b the set of scattering peaks with smaller d-spacing (or higher $|Q|$ values) were clearly from a phase in the lamellar configuration because the four peaks were equally spaced even though one of them was overlapped. Nevertheless, the peak overlap reduced the total unambiguous peaks of the other phase and incurred uncertainty to phase assigning. By comparing this diffraction profile with that collected at a slightly higher temperature (Figure 4.2.3b inset), we might, with decent certainty, determine that the set of peaks with larger d-spacing was also from a lamellar phase, even though the higher temperature profile still exhibited the peak overlap problem. We therefore labeled this region as the "lamellar-lamellar phase separation" region. However, this region may still need to be understood as a "phase region consistent with two lamellar phases coexistence" in the

Figure 4.2.3. WAXS scattering image (a) and azimuthally integrated profile (b) collected in the lamellar-lamellar phase separation region (see the text for the labeling) from a 66.1 wt% cardiolipin-water mixture at -10 °C. Black and red dashed lines in (b) are the expected peak position for the $L\alpha_1$ and $L\alpha_2$ phases (see the text for the phase assignment), respectively. The diffuse scattering peak indicated by black arrows was from the melted hydrocarbon chains. No sharp peak arising from the hydrocarbon chains of a gel phase was observed. A red arrow in (b) denotes an artifact. The inset in (b) highlights the SAXS regime and compares the diffraction profile collected at this temperature (-10 °C) with that at -5 °C. Black and red arrows in the inset denote the peaks from the $L\alpha_1$ phases at -10 °C and -5 °C, respectively. The first and second order peaks of the $L\alpha_1$ phase were unambiguously resolved at -10 °C whereas the resolvable peaks for the $L\alpha_1$ phase were the second and third orders at -5 °C. The first order peaks of the $L\alpha_1$ and $L\alpha_2$ phases overlapped at -5 °C (green arrow).

(a)

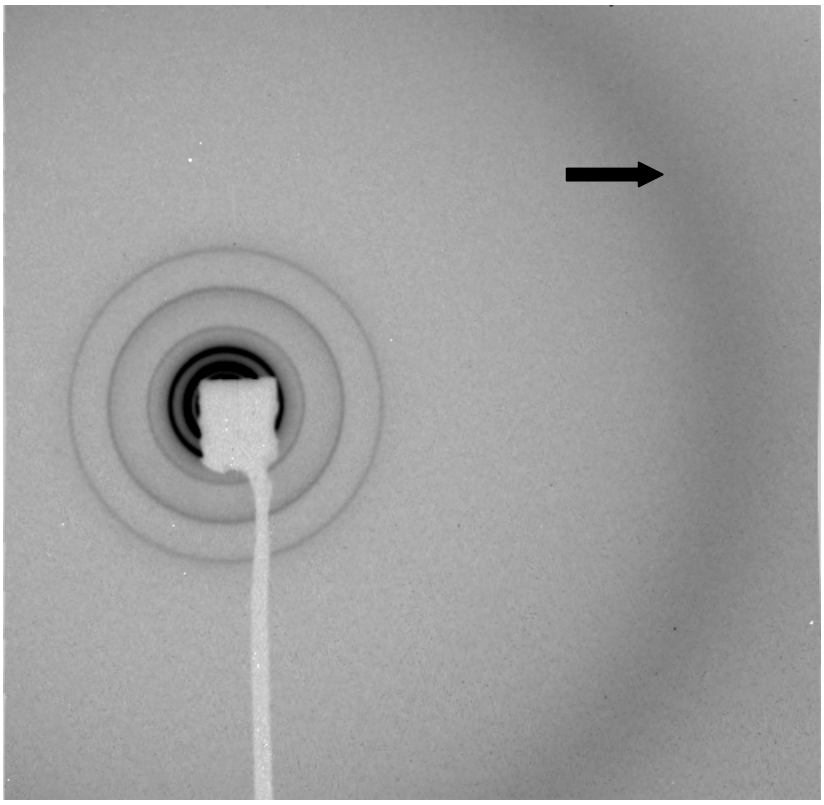

(b)

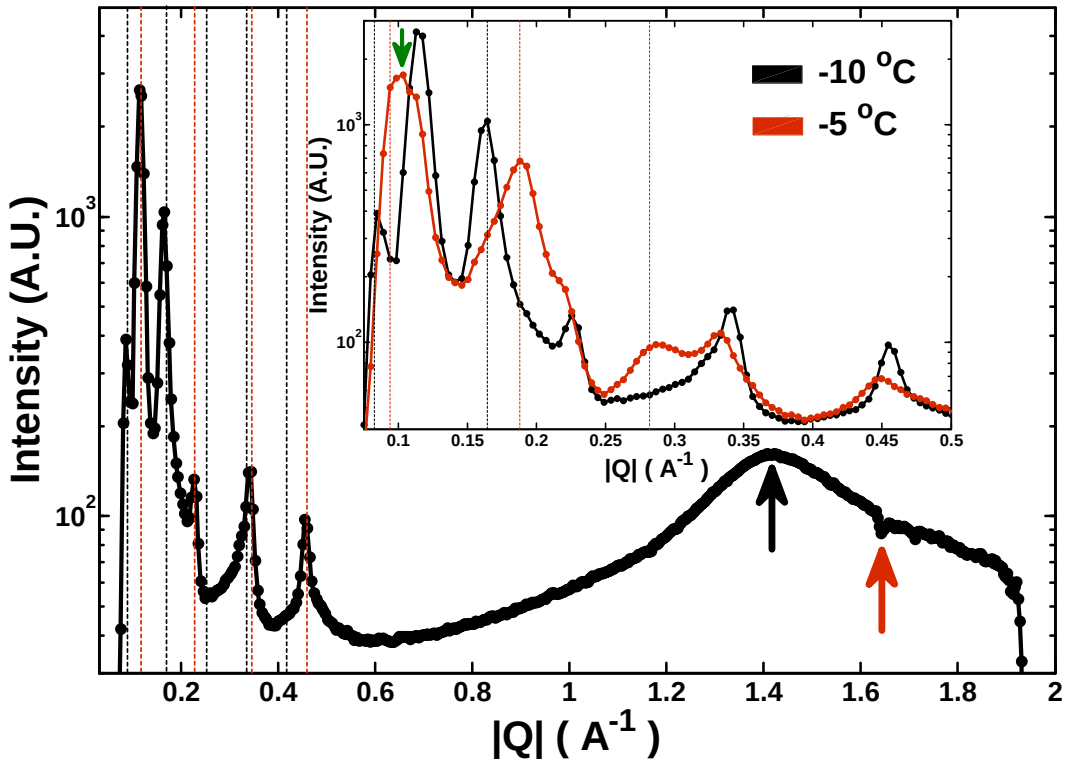
Intensity (A.U.)
10^3
10^2
0.2
0.4
0.6
0.8
1
1.2
1.4
1.6
1.8
2
|Q| (A^-1)
-10 °C
-5 °C
Intensity (A.U.)
10^3
10^2
0.1
0.15
0.2
0.25
0.3
0.35
0.4
0.45
0.5
|Q| (A^-1)

most rigorous sense. These two coexisting lamellar phases exhibited remarkably distinct d-spacings and rates of d-spacing variation with temperature (e.g., Figure 4.2.4). We designated the lamellar phase with the larger d-spacings as the $L_{\alpha 1}$ phase and the other as the $L_{\alpha 2}$ phase. Moreover, repeated temperature scans (e.g., Figure 4.2.4) attest that the two liquid crystalline lamellar phases were thermodynamically stable phases. Whether these two phases arose from a differential water distribution or other physical effects will be discussed in Section 4.4.

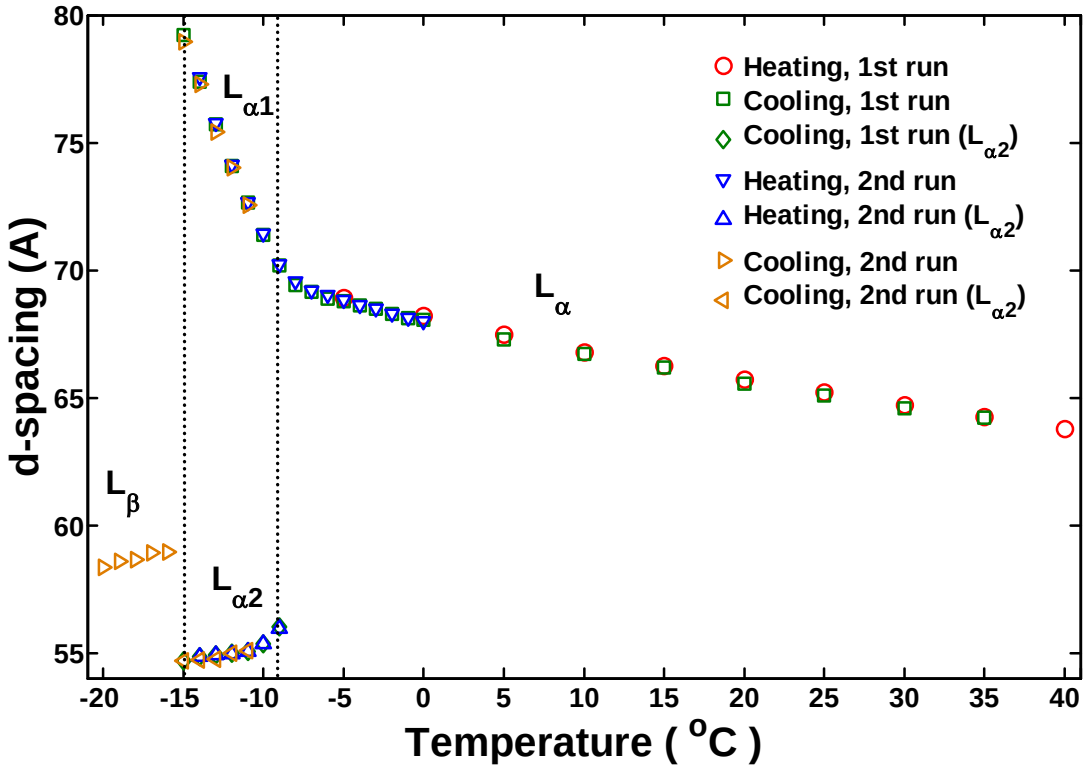

Figure 4.2.4. d-spacings of the lamellar phases as a function of temperature for a 59.8 wt% cardiolipin-water mixture. Between the two dashed lines is the lamellar-lamellar phase-separation region.

When the sample concentration increased, the main transition temperature in the lamellar-lamellar phase separation region remained at -15.5±0.7 °C until the concentration reached 78.2 wt%. Beyond this concentration, the phase boundary between the L_α and the gel phases became obscure and another two-phase coexistence region emerged. The WAXS data demonstrated the frozen state of the hydrocarbon chains and, based on the d-spacings exhibited by the two phases (58.3 Å and 52.7 Å at 5 °C), we determined that this was a L_α-gel phase coexistence region (Figure 4.2.5). Both the upper and lower boundaries of this phase coexistence region moved to higher temperatures when the sample concentration increased. A plausible explanation to this observation might be as follows: In the lateral stress profile of a lipid monolayer, three interactions must be balanced with one another. They are repulsions among headgroups, π_{hg}, and hydrocarbon chains, π_{ch}, and attraction arising from hydrophobic-hydrophilic interfacial tension, γ_{phob} (Shearman et. al., 2006; Marsh, 2008). That is to say, the equation $\pi_{hg} + \pi_{ch} = \gamma_{phob}$ must be satisfied. As reported in Luzzati and Husson (1962), the average surface area per headgroup of a lipid shrank when the sample concentration increased, even in the cases of charged lipids. Accordingly, the cardiolipin headgroups are expected to become closer to one another when the water content is lower, which results in stronger π_{hg} due to the enhancing electrostatic and/or steric interactions (refer to Chapter 2 for a theoretical description). Since γ_{phob} is likely not much unchanged in this situation, the hydrocarbon chain repulsion, $\pi_{ch} = \gamma_{phob} - \pi_{hg}$, would decrease accordingly, allowing the chains to pack more tightly. Stronger thermal motions are thus needed to break the tighter packing, leading to higher main transition temperatures.

In the higher temperature regime, the liquid crystalline H_{II} phase gradually emerged when the sample concentration was over 72.9 wt% (Figure 4.2.1). However,

Figure 4.2.5. WAXS scattering image (a) and azimuthally integrated profile (b) collected in the L_{α}-gel phase coexistence region from a 85.8 wt% cardiolipin-water mixture at -5 °C. Black and red dashed lines in (b) are the expected peak positions for the lamellar gel (d-spacing = 58.3 Å) and Lα (d-spacing = 52.7 Å) phases, respectively. A sharp diffraction peak (black arrows) arose from the frozen, structured hydrocarbon chains of a gel phase and is flanked by two shoulders (green arrows). The presence of the two shoulders may imply formation of the $L_{\beta'}$ phase. However, we refrained from further differentiating the gel phases due to data quality. A red arrow denotes an artifact.

(a)

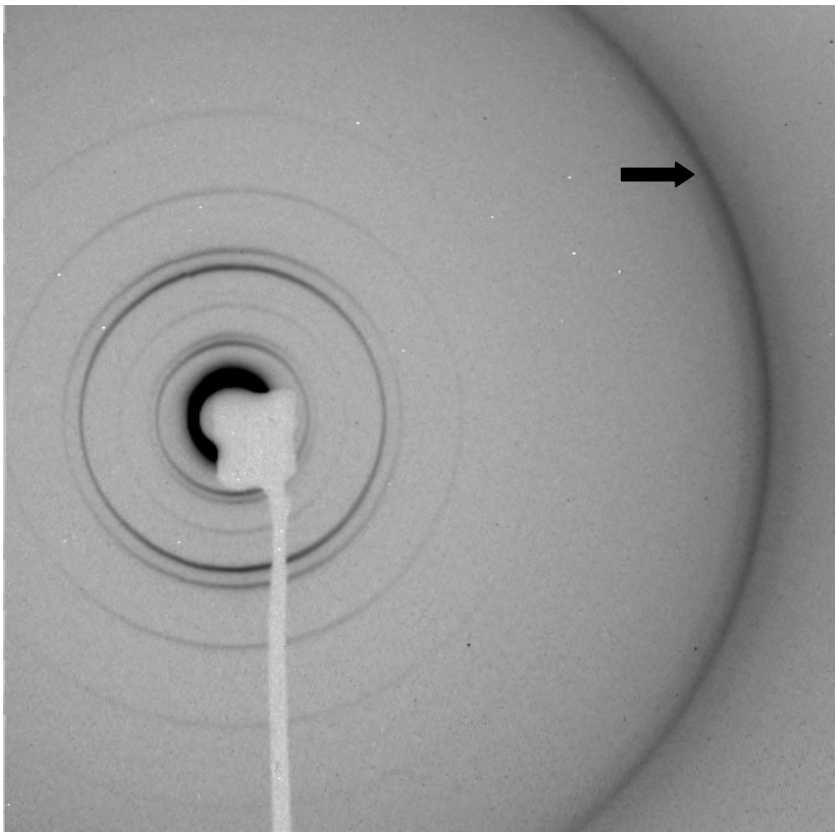

(b)

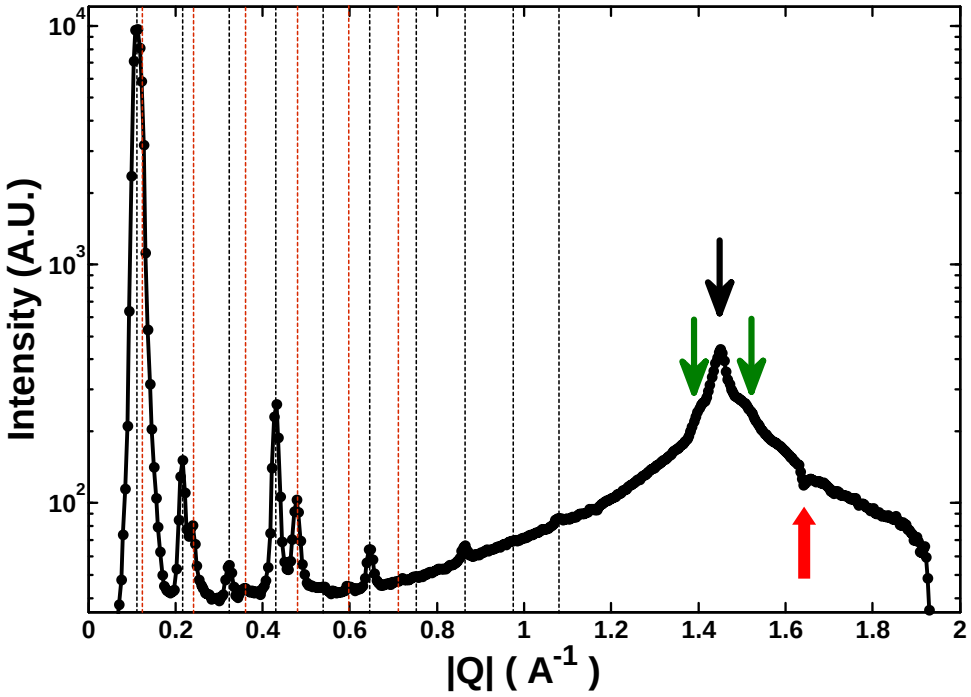

the non-lamellar phase never appeared alone and always coexisted with the L_α phase in the absence of counterions and the experimental conditions studied here. The $L_\alpha \leftrightarrow L_\alpha + H_{II}$ phase transition temperature was seen to decrease with increasing lipid concentration. This was because removal of water diminished surface areas of the headgroups (see the above discussion and refer to Luzzati and Husson (1962)) and thus enhanced the propensity for the cardiolipin monolayers to bend toward water (equivalent to increasing the monolayer curvature). As discussed in Section 2.2.3, the H_{II} structure with a larger water core radius is under higher hydrocarbon chain packing stress due to the geometrical constraint (Gruner, 1985). On the other hand, when the water content decreases, the potential water core dimension of the H_{II} phase should shrink and the packing strain would diminish accordingly. This might constitute another factor favoring formation of the H_{II} phase at higher sample concentrations, as observed. The importance of the hydrocarbon chain packing stress in the $L_\alpha \leftrightarrow L_\alpha + H_{II}$ phase transition is further emphasized by the experimental result obtained from the cardiolipin-alkane-water mixtures. It was shown that adding alkane into the cardiolipin-water mixtures dramatically lowered the temperatures and concentrations required for the $L_\alpha \leftrightarrow L_\alpha + H_{II}$ phase transition to occur (Section 4.6). Despite the higher (negative) spontaneous curvature and weaker packing stress, in the absence of counterions, the H_{II} phase only coexisted with the L_α phase and was never seen as a single phase however high the sample concentration was. This suggests that combination of the two driving factors was still unable to overcome the dominance of the electrostatic interactions arising from the charged headgroups. Other interactions that might have contributed to the cardiolipin phase preferences include hydration interactions (Section 2.2.2) and bilayer thermal undulations (Section 2.2.6). Nevertheless, with the usual functional forms, the hydration interactions contributions are indistinguishable from those of the monolayer elastic energy (Tuner, 1990).

Therefore, it is unclear whether the hydration interactions favor the H_{II} phase or the L_{α} phase. In contrast, Equation 2-19 suggests stronger thermal undulation repulsion for bilayers at higher temperatures and with thinner water layers. This trend might further amplify the energetic penalty for the cardiolipin liquid crystals to remain in the L_{α} phase when temperature and the sample concentration were all increased.

As the lipid concentration increased beyond ~86 wt%, an unexpected phase was observed at temperatures >20 °C (denoted as NC in Figure 4.2.1). This phase displayed X-ray scattering patterns that were reminiscent of the scattering from a cluster of tiny crystals (e.g. Figure 4.2.6a), and coexisted with the L_{α} phase and the H_{II} phase at lower and higher temperatures, respectively (e.g. Figure 4.2.7). The scattering pattern of this phase evolved with time at an incubation temperature of 30 °C or 40 °C, to typical X-ray powder diffraction patterns (e.g., Figure 4.2.6b). This temporal evolution of the scattering pattern was shown to be the result of lipid degradation upon prolonged high temperature incubation. An attempt to index the diffraction peaks and discussion regarding the nature of the phase will be presented in Section 4.5.

Comparing the phase diagram of our cardiolipin system (Figure 4.2.1) with those of other charged phospholipids is not easy, due to the scarcity of the temperature-composition phase diagrams reported for other charged phospholipids with the C18:1 hydrocarbon chains. Koynova and Caffrey (2002) compiled an index listing all the available temperature-composition phase diagrams reported until July, 2001. Within the list, we found the phase diagrams of the charged phospholipids, DOPA (C18:1) and DMPS (C14:0); the latter was the only available phosphatidylserine species with its temperature-composition phase diagram mapped. Compared to DOPA, our cardiolipin system lacked a single H_{II} phase region seen in the DOPA-water mixtures with sample concentrations >65 wt% (Figure 4.2.8a; Lindblom et. al., 1991). This

(a)

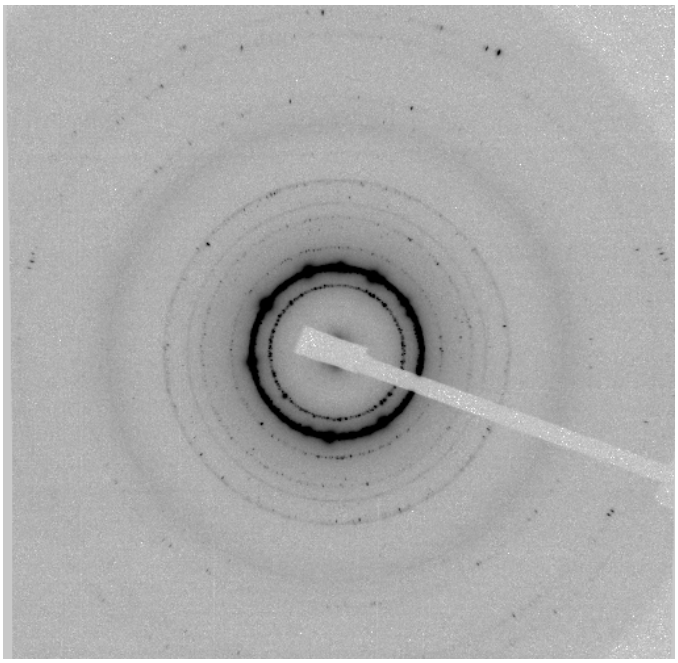

(b)

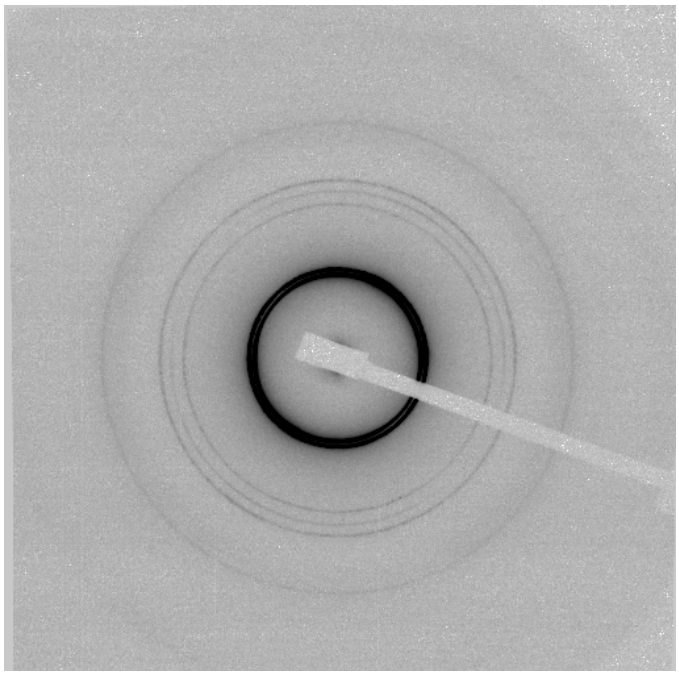

Figure 4.2.6. X-ray diffraction images of an 86.6 wt% cardiolipin-water mixture after incubation at 40 °C for 4 hours (a), in which a crystalline-like diffraction pattern is shown, and for 22 hours (b), in which the crystalline-like pattern transformed to one indicative of smaller crystalline regions.

Figure 4.2.7. Azimuthally integrated X-ray scattering profiles of an 87.8 wt% cardiolipin-water mixture collected at 15 °C (a) and 45 °C (b). Black and red dashed lines denote the diffraction peaks from the L_α (a) or H_{II} (b) phase and the TC phase, respectively. Arrows denote artifacts because the peaks are not observed in the 2-D diffraction image. Their shapes changed with the area that was integrated, and their positions were independent of the sample temperature.

(a)

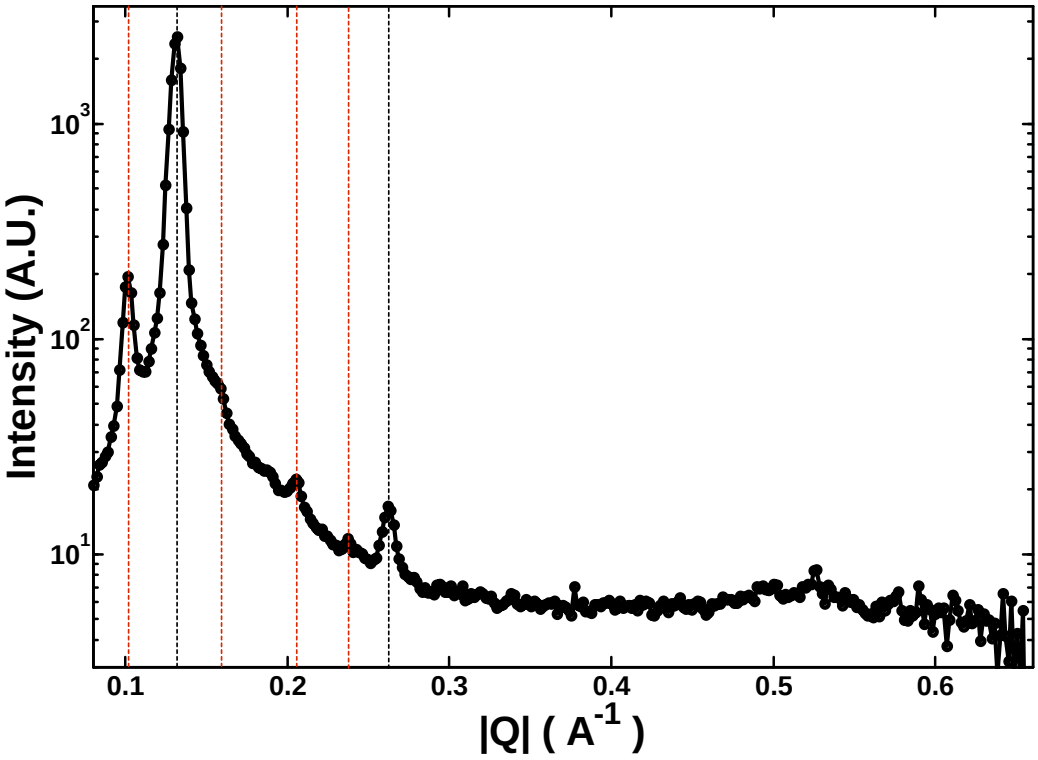
Intensity (A.U.)
10^3
10^2
10^1
0.1
0.2
0.3
0.4
0.5
0.6
|Q| (A^-1)

(b)

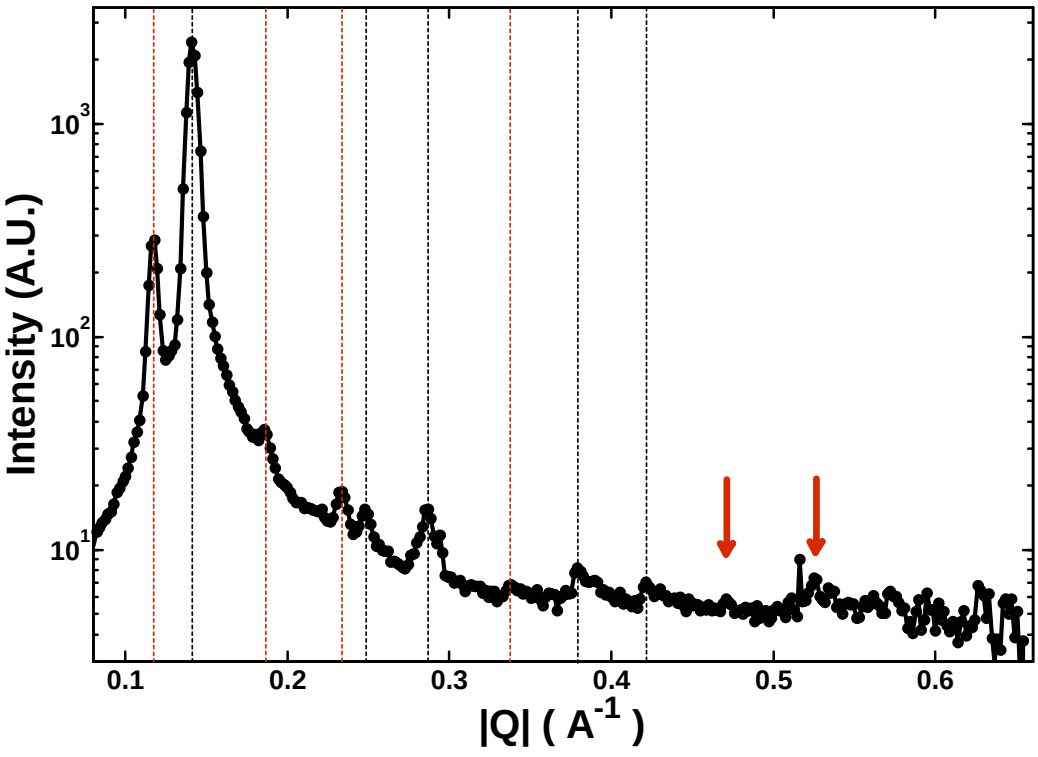
Intensity (A.U.)
10^3
10^2
10^1
0.1
0.2
0.3
0.4
0.5
0.6
|Q| (A^-1)

discrepancy is expected to arise from the difference in the charge densities per molecule of the two lipids. With two negative charges carried by a molecule, the spontaneous curvature of cardiolipin is speculated to be smaller than that of single-charged DOPA, even though the bulky quadruple chain configuration should increase the spontaneous curvature. Indeed, studies have shown that DOPA could form the single H_{II} phase at pH $\leq$ 3.7 whereas only the L_{α}+H_{II} phase coexistence was observed for the bovine heart cardiolipin (>88% C18:2 cardiolipin) even when pH was as low as 2.8 (Farren et. al., 1983; Seddon et. al, 1983). This understanding re-emphasizes the importance of the electrostatic lateral repulsion in determining the spontaneous curvature (see Section 2.2.5) and thus the phase preference of cardiolipin.

On the other hand, our cardiolipin system demonstrated richer phase behavior when compared with DMPS at above-zero temperatures and comparable concentrations (Figure 4.2.8b; Hauser et. al., 1982). In the lipid concentrations from 0 wt% to 100 wt%, only the main transition ($L_{\beta'} \leftrightarrow L_{\alpha}$) was observed for DMPS. Since both the headgroup type and hydrocarbon chain species in DMPS are different from those of our cardiolipin system, we are unable to ascribe the discrepancy in phase behavior to any of the factors unambiguously. As mentioned in Section 2.2.5, DOPS (C18:1) exhibited the spontaneous curvature of +1/144 $Å^{-1}$ when counterions were absent (Fuller et. al., 2003). This already unusually small spontaneous curvature might be further reduced as the shorter hydrocarbon chain length and lower chain saturation of DMPS (C14:0) are expected to diminish the hydrocarbon chain splaying. This might explain why only the main transition was observed in the DMPS system even in the extremely low water contents.

The above comparisons are consistent with the observed non-lamellar structure-forming tendency of PA > Cardiolipin > PS, reported in Lewis and McElhaney (2000).

(a)

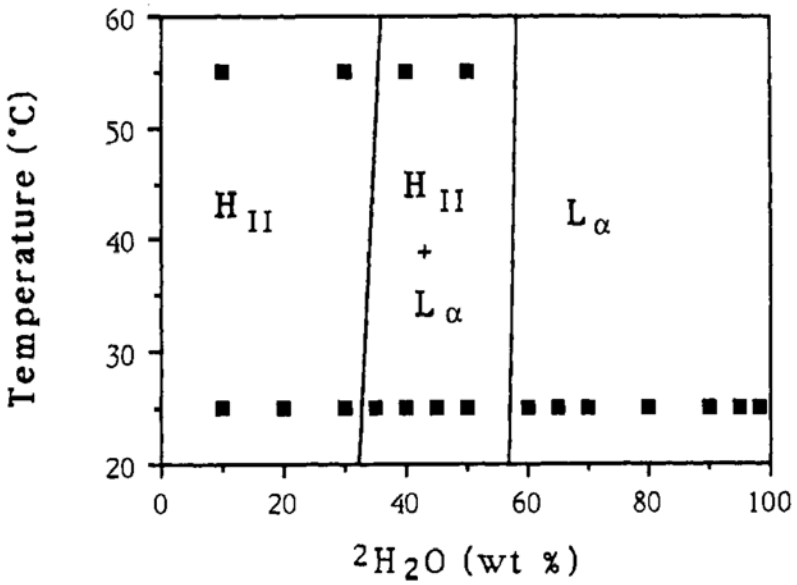

(b)

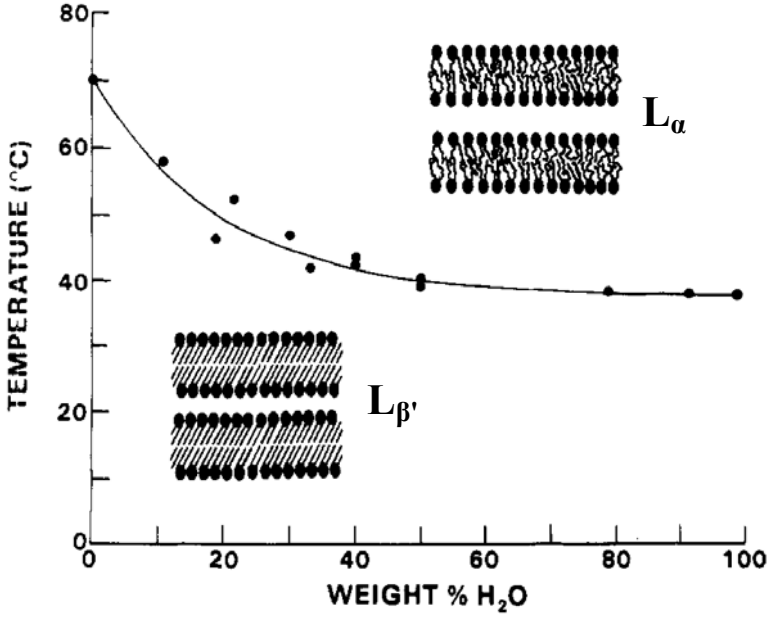

Figure 4.2.8. Temperature-composition phase diagrams of the charged phospholipids, DOPA (a) and DMPS (b). Squares in (a) denote the collected data points. See the text for their comparisons with the cardiolipin system reported here. (a) is from Lindblom et. al. (1991); (b) is from Hauser et. al. (1982).

Quantitatively, this should indicate that the spontaneous curvature of our cardiolipin system without counterions was in the range from -1/130 $Å^{-1}$ (for DOPA; Kooijman et. al., 2005) to +1/144 $Å^{-1}$ (for DOPS; Fuller et. al., 2003). One may accordingly speculate that the doubly charged headgroups of cardiolipin result in a spontaneous curvature smaller than that of single-charged DOPA whereas the bulky quadruple chain configuration of cardiolipin leads to a larger (and perhaps negative) spontaneous curvature when compared with DOPS, which possesses bulkier headgroups. This intermediate spontaneous curvature might also have contributed to formation of the TC phase. It should be noted that the phase diagram of DOPA does not cover any sub-zero temperature (Figure 4.2.8a). It is therefore not clear whether DOPA will display the lamellar-lamellar phase separation phenomenon observed here when temperature is depressed. Also, both of the compared phase diagrams are supported by very few data points. Doubts are therefore cast on the reliability of the phase diagrams, which further exacerbates the scarcity of the available phase diagrams for charged phospholipids. This is one of the reasons that we decided to systematically study our chosen charged phospholipid in wide temperature and concentration ranges.

In the next section, we shall discuss the structural parameters of the phases observed in the phase diagram of Figure 4.2.1. These structural parameters varied both when the cardiolipin-water mixtures were within and across the phase boundaries. We begin with the discussion on how the unit cell dimension of each phase changed with temperature and concentration and then proceed to the individual structural parameters by reconstructing the electron density map of each phase. The structural information is expected to shed light on the mechanisms behind the phase transitions.

4.3 Electron Density Map Reconstruction and Structural Parameter Analysis

4.3.1 General Trend of the Unit Cell Dimension

In this section, we will examine the general trend of the unit cell dimension variation induced by changes in temperature and concentration. Reconstruction of the electron density maps will follow to extract the individual structural parameters and to understand the mechanisms behind the unit cell dimension variations. Figure 4.3.1a and Table 4.3.1 shows the d-spacings of the L_α and gel phases as a function of the sample concentration at representative temperatures. The apparent insensitivity to the sample concentration of the gel phase unit cell dimension led to the conclusion that the gel phase was in the excess water condition over the entire concentration range covered here. On the other hand, the d-spacing of the L_α phase decreased monotonically with the water content and appeared to follow a power law trend as shown in Figure 4.3.1b. It can also be seen in Figure 4.3.1b that a temperature change simply shifted the curve in parallel to lower d-spacing values without distorting its overall shape. As detailed in Section 3.6, these features were exploited to calibrate lipid concentration of the cardiolipin-water mixtures because measurements with the X-ray scattering were more reliable than the gravimetrical measurements for the nominal sample concentrations. A peculiar feature was observed with the -10 °C curve of Figure 4.3.1a, in which two d-spacing values emerged simultaneously in the sample concentrations from 55.3 wt% to 72.9 wt%, corresponding to the lamellar-lamellar phase separation region of Figure 4.2.1. The two distinct d-spacings were ascribed to the scattering from the $L_{\alpha 1}$ and $L_{\alpha 2}$ phases, respectively, as noted in Section 4.2. Interestingly, while d-spacing of the $L_{\alpha 2}$ phase remained constant with respect to the sample concentration, unit cell dimension of the $L_{\alpha 1}$ phase expanded with increasing lipid fraction. This behavior of the $L_{\alpha 1}$ phase is opposite to the general trend of the unit

Figure 4.3.1. (a) d-spacing as a function of lipid fraction for the cardiolipin-water mixtures in the lamellar phases. The curves were compiled from many data collections, with each concentration backed by a separate sample. Error bars of the data points are smaller than the mark size and were estimated based on the sample homogeneity tests (see Section 3.5). See the text for the discussion on the peculiar feature of the -10 °C curve. (b) Power law fits to the relationship between d-spacing and the lipid fraction for the L_α phase at 20 °C, 40 °C and 60 °C. The power laws fitted to the data are $y = ax^b + c$ with a = 24.56, b = -1.292, c = 18.01 for 20 °C; a = 24.72, b = -1.263, c = 16.59 for 40 °C; a = 25.81, b = -1.215, c = 14.21 for 60 °C.

(a)

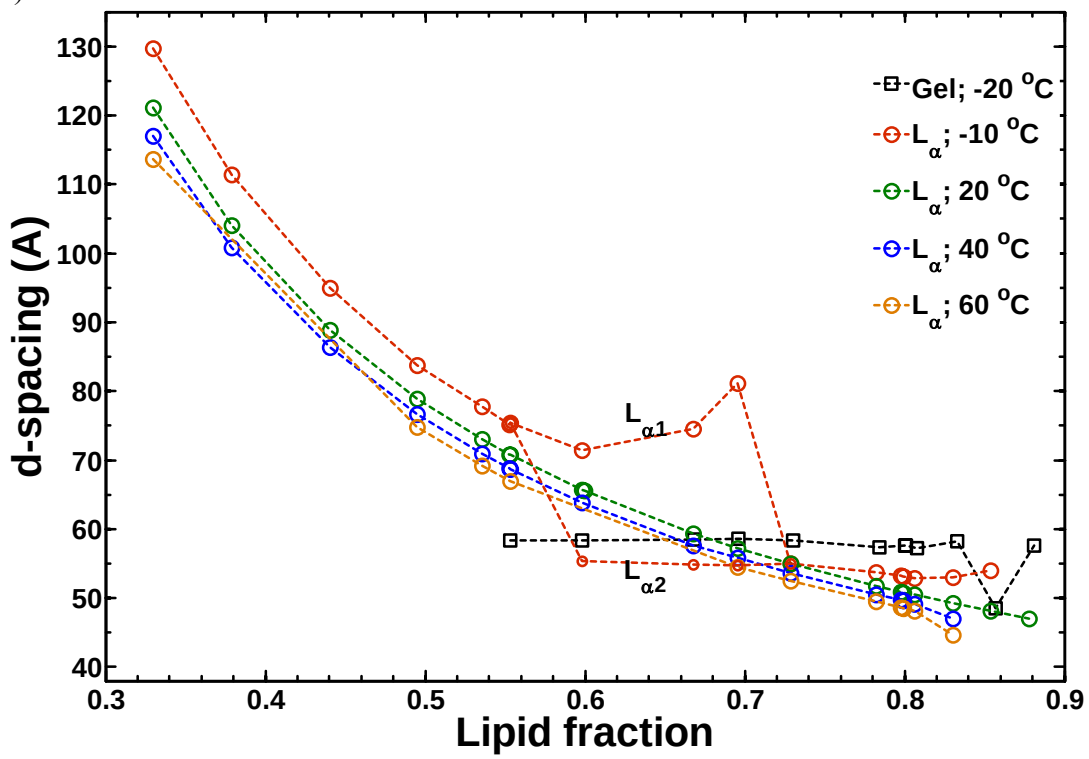
d-spacing (A)
Lipid fraction
Gel; -20 °C
Lα; -10 °C
Lα; 20 °C
Lα; 40 °C
Lα; 60 °C
Lα1
Lα2

(b)

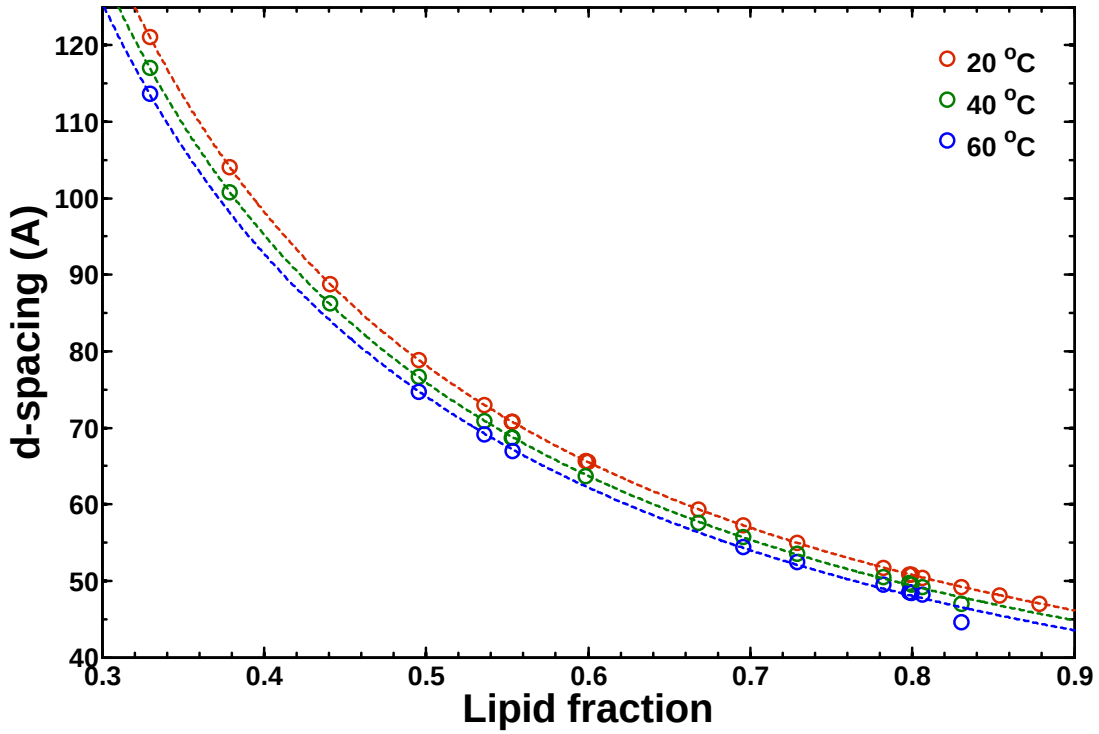
d-spacing (A)
Lipid fraction
20 °C
40 °C
60 °C

Table 4.3.1. d-spacings of the cardiolipin-water mixtures in the lamellar phases observed in this thesis study (see also Figure 4.3.1). *d* is the d-spacing in Å; C_L is the lipid fraction.

60 °C		40 °C		20 °C		-10 °C		-20 °C	
C_L	*d*	C_L	*d*	C_L	*d*	C_L	*d*	C_L	*d*
0.329	113.6	0.329	117.0	0.329	121.1	0.329	129.7	0.553	58.4
0.495	74.8	0.379	100.8	0.379	104.1	0.379	111.4	0.598	58.4
0.536	69.2	0.440	86.3	0.440	88.9	0.440	95.0	0.668	58.5
0.553	67.0	0.495	76.7	0.495	78.9	0.495	83.8	0.695	58.6
0.695	54.5	0.536	71.0	0.536	73.1	0.536	77.8	0.729	58.4
0.729	52.5	0.553	68.8	0.553	70.8	0.553	75.2	0.782	57.3
0.782	49.5	0.553	68.8	0.553	70.8	0.553	75.4	0.798	57.6
0.798	48.6	0.598	63.8	0.598	65.7	0.598	71.4/55.5	0.799	57.6
0.799	48.5	0.668	57.7	0.600	65.5	0.668	74.6/54.8	0.806	57.3
0.806	48.2	0.695	55.8	0.668	59.4	0.695	81.1/54.8	0.830	58.3
0.830	44.7	0.729	53.6	0.695	57.3	0.729	55.0	0.854	48.5
		0.782	50.6	0.729	55.0	0.782	53.8	0.878	57.6
		0.798	49.7	0.782	51.86	0.798	53.3		
		0.799	49.6	0.798	50.9	0.799	53.1		
		0.806	49.2	0.799	50.8	0.806	52.9		
		0.830	47.1	0.806	50.5	0.830	53.0		
				0.830	49.3	0.854	54.0		
				0.854	48.1				
				0.878	47.1				

cell dimension variations observed for the cardiolipin-water mixtures in other experimental conditions. We will rely on the individual structural parameters extracted from the electron density map reconstruction to explore the nature of these two coexisting lamellar phases and the reason behind this peculiar behavior (Section 4.4). Unit cell dimension variation per unit temperature was also scrutinized for the L_α phase over the entire sample concentration range. The values of the parameter were

determined by the slopes of the linear fits to the d-spacing versus temperature relations in the single L_α phase regions (e.g., the region to the right of the area defined by two dashed lines in Figure 4.2.3); the error bars were the 95% confidence bounds of the fitted slopes (Figure 4.3.2 and Table 4.3.2). Temperature sensitivity of the L_α unit cell dimension was seen to diminish with increasing sample concentration initially. At the lipid concentration of ~80 wt%, temperature dependence of the unit cell dimension reached a turning point and intensified thereafter with increasing lipid fraction. Again, understanding the mechanism behind this observation suggested a need to decompose the unit cell dimensions into individual structure parameters by reconstructing electron

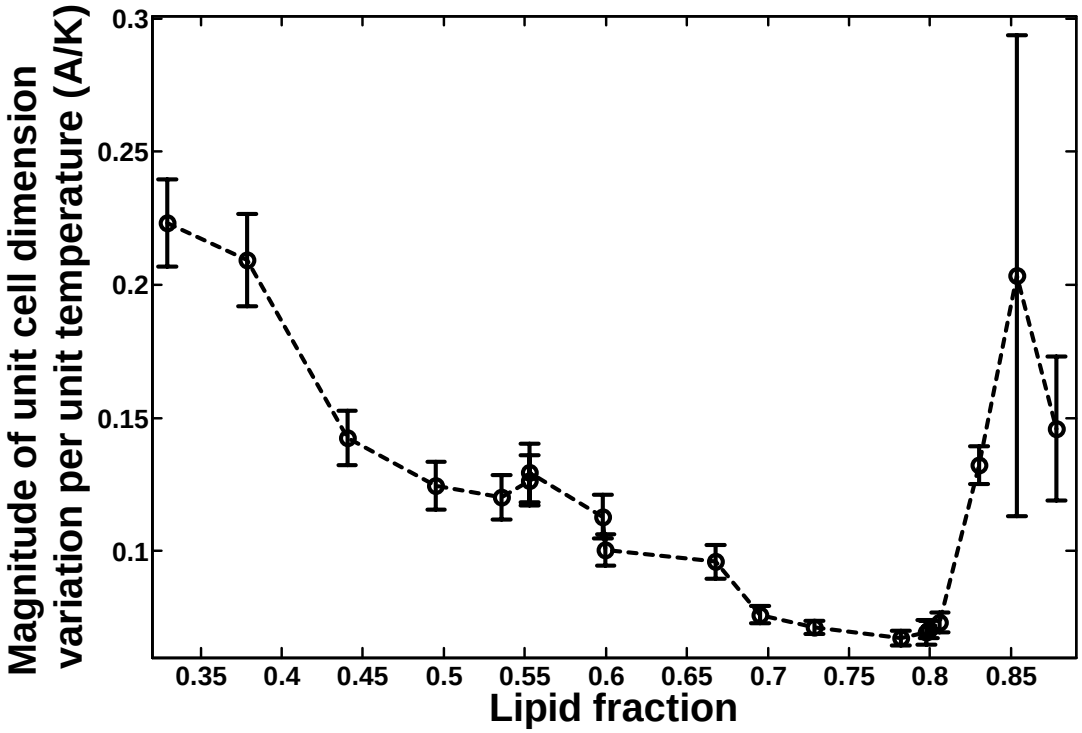

Figure 4.3.2. Magnitude of the unit cell dimension variation per unit temperature as a function of lipid fraction for the cardiolipin-water mixtures in the L_α phases. The curve was compiled from 19 samples, with each concentration backed by a separate sample. See the text for the discussion.

Table 4.3.2. Temperature dependence of unit cell dimension variation for the cardiolipin-water mixtures in the L_α phase. $(da/dT)_{C_L}$ is the unit cell dimension variation per unit temperature for a given sample concentration in Å/K; a is the unit cell dimension in Å; T is temperature in K; C_L is the lipid fraction. The errors for some samples are not shown because their values are smaller than the distance resolution of the SAXS experiments.

C_L	$(da/dT)_{C_L}$
0.329	-0.22±0.02
0.379	-0.21±0.02
0.440	-0.14±0.01
0.495	-0.12±0.01
0.536	-0.12±0.01
0.553	-0.13±0.01
0.553	-0.13±0.01
0.598	-0.11±0.01
0.600	-0.10±0.01
0.668	-0.10±0.01
0.695	-0.08
0.729	-0.07
0.782	-0.07
0.798	-0.08
0.799	-0.07
0.806	-0.07
0.830	-0.13
0.854	-0.20±0.09
0.878	-0.15±0.03

density map. Data presented in Section 4.3.3 suggests that the initial decline in the temperature dependence of the L_α phase was the result of thinner water layers and thicker lipid bilayers at denser sample concentrations. See that section for details.

Obtaining the unit cell dimension-lipid fraction relationship for the H_{II} phase is not as straightforward as for the lamellar phases. The H_{II} phase consistently coexisted with the L_α phase in the absence of counterions and water might thus not distribute evenly between the two phases. As a result, reconstructing electron density maps appears to be the only way to study structural parameters of the H_{II} phase. Nevertheless, due to the great overlap of the L_α 1st order peak and the H_{II} *(1,0)* peak, integrated peak intensities could not be determined unambiguously. This problem was exacerbated by the weak *(1,1)* and *(2,0)* peaks of the H_{II} phase. We were therefore unable to reconstruct the electron density maps for the H_{II} phase reliably and, within this chapter, limit our discussion to the lamellar phases.

4.3.2 Electron Density Map Reconstruction

Detailed structural information of a lipid liquid crystalline phase can be extracted from its electron density map. An electron density map spatially shows electron number densities within a molecule or a group of molecules and is the Fourier transform of intensities and phases of the X-rays scattered by an object (see Section 3.2.1 for the theory background). A typical electron density profile of a phospholipid liquid crystal in the bilayer structure is shown in Figure 4.3.3, in which three Gaussian functions are used to model the spatial configuration of two lipid molecules forming the bilayer. The electron-thick, phosphorus-containing regions of the lipid headgroups are represented by two Gaussian peaks, and the electron-thin region of hydrocarbon

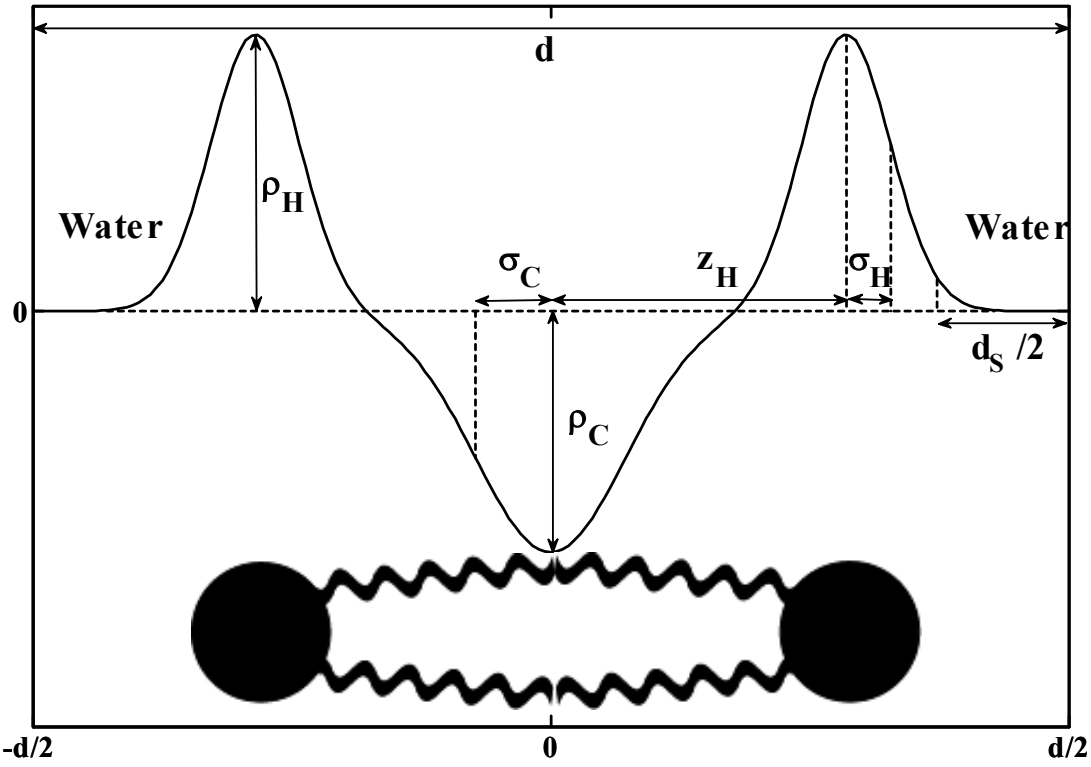

Figure 4.3.3. Typical electron density profile of a phospholipid liquid crystal in the bilayer structure. The abscissa is the distance from the bilayer center along the bilayer normal. The peaks and the trough correspond to the lipid molecules shown below.

chains is by the other inverted Gaussian. The inter-bilayer water volume is conveniently assumed to bear zero electron density. The electron density profile $\rho(z)$ of a lipid molecule is therefore formulated as (Pabst et. al., 2003a),

$$\rho(z) = \exp\left[\frac{-(z-z_H)^2}{2\sigma_H^2}\right] + \exp\left[\frac{-(z+z_H)^2}{2\sigma_H^2}\right] - \rho_r \exp\left(\frac{-z^2}{2\sigma_C^2}\right) \tag{4-1}$$

$$\rho_r = \frac{\rho_C - \rho_a}{\rho_H - \rho_a},$$

where the Gaussian variances, σ_H *and* $\sigma_C = FWHM / 2\sqrt{2\ln 2}$ (FWHM is the full

width at half maximum of the respective peaks), and the definitions of z_H, ρ_C and ρ_H are as illustrated in Figure 4.3.3. We define $\rho_a = 0$ as the electron density of the inter-bilayer water since the profile can always have an arbitrary additional constant. Based on these parameters, one can decompose the unit cell dimension *d* to the bilayer thickness d_B and the bilayer separation d_S with the following relations,

$$d_B = 2\left(z_H + 2\sigma_H\right) \tag{4-2}$$

and

$$d_S = d - d_B . \tag{4-3}$$

The bilayer thickness d_B defined here is different from the traditional Luzzati bilayer thickness determined with the lipid volume fraction ϕ_L (Luzzati and Husson, 1962; Nagle and Tristram-Nagle, 2000),

$$d_{B,Luzzati} = \phi_L \, d \, , \tag{4-4}$$

and employed widely in the field (e.g., Gruner et. al., 1988 and Harper et. al., 2001). Because the volumetric information for our cardiolipin system was not readily available, we could not conveniently apply Equation 4-4 to decompose unit cell dimensions of the L_α phase and had to rely on the electron density profile reconstruction for the same purpose. In the context of the electron density profile, the Luzzati bilayer thickness corresponds to the distance between the two phosphate peaks (i.e., $2z_H$) in the profile and does not explicitly take into account the blurred interfacial boundary between lipid and water (Rappolt et. al., 2003). This discrepancy in definition deserves a special caution especially in comparing the results obtained here with the literature data.

In principal, other structural parameters such as the hydrocarbon chain length d_C, the cross sectional area per lipid molecule A_l and the number of the inter-bilayer water molecules per lipid n_W can also be derived from the electron density map through (Pabst et. al., 2000; Pabst et. al., 2003b),

$$d_C = z_H - d_{H1}, \tag{4-5}$$

$$A_l = \frac{1}{\rho_{CH_2}(\rho_r - 1)}\left(\frac{\rho_r n_C^e}{d_C} - \frac{n_H^e}{d_H}\right), \tag{4-6}$$

and

$$n_W = \frac{A_l(d/2 - z_H)}{V_W}, \tag{4-7}$$

where d_{H1} is the distance from the phosphate group to the hydrophobic-hydrophilic interface, ρ_{CH_2} is the electron density of the methylene group on the hydrocarbon chains, V_W is the volume of a water molecule, and n_C^e and n_H^e are numbers of electrons per lipid molecule of the hydrocarbon chains and headgroup, respectively. In calculating d_C, a fixed value of 4 Å was adopted by Lewis et. al. (2007) and Pabst et. al. (2003) for d_{H1}. Obviously, this value is only an approximation since d_C is expected to change with factors including water content and temperature, as will be discussed in Section 4.3.3. We therefore will not further decompose the bilayer thickness into the headgroup dimension and the hydrocarbon chain length. The difference between the bilayer thickness and the hydrocarbon chain length will be a constant and have no effect on our analysis here even if the approximation holds true. In addition, Equations 4-6 and 4-7 are of no use here unless volumetric information of our cardiolipin system is available to calculate n_C^e and n_H^e (Nagle and Tristram-Nagle, 2000; Petrache et. al., 1998). As a result, we only extracted the bilayer thickness and

inter-bilayer distance from the electron density profiles reconstructed in this thesis study. Nevertheless, the two structural parameters still provide valuable insight in structurally explaining phase behavior of the cardiolipin-water mixtures.

Conventionally, to reconstruct electron density maps one has to accurately measure the intensities and determine the phases of the scattered X-rays (Turner and Gruner, 1992; Harper et. al., 2001). This conventional method also entails that at least four and five X-ray scattering peaks are resolved for the L_α and H_{II} phases respectively to produce electron density maps with decent precision (Rappolt et. al., 2003; Nagle and Tristram-Nagle, 2000; Pabst et. al., 2000). However, most of the X-ray scattering data collected for this thesis study could at best provide three resolvable Bragg peaks. We therefore had to employ another method described in Pabst et. al. (2000, 2003a and 2006), based on reasonable *a priori* assumption, to reconstruct electron density maps from our data. This method is referred as the line-shape fitting method in this thesis study and is elaborated below.

Intensities, *I(Q)*, of the X-rays scattered by lipid molecules arranged in an unoriented multilayer structure (i.e., stacks of bilayer structures as seen in this thesis study) can be expressed as,

$$I(Q) = \frac{S(Q)\left|F(Q)\right|^2}{Q^2}, \tag{4-8}$$

where Q is the momentum transfer vector (refer to Section 3.2.1), *S(Q)* is the lattice structure factor describing the 1-D lattice order of the multilayer structure, and *F(Q)* is the structure factor derived from the Fourier transform of electron density profile of two lipid molecules arranged in the bilayer structure (Equation 4-1 and Figure 4.3.3).

Since positionally uncorrelated bilayers, behaving like unilamellar vesicles, may be also present along with the multilayer structures, an additional term is included to account for the diffuse scattering arising from these bilayers,

$$I(Q) = \frac{S(Q)\left|F(Q)\right|^2}{Q^2} + N_u \frac{\left|F(Q)\right|^2}{Q^2}, \tag{4-9}$$

where N_u is a scaling constant. In formulating the lattice structure factor *S(Q)*, the spatial arrangement of a lipid bilayer can be modeled as,

$$S(Q) = N + 2\sum_{k=1}^{N-1}(N-k)\cos(kQd), \tag{4-10}$$

where *N* is the number of bilayers in the scattering domain, if the bilayers are perfectly flat and separated with a consistent distance *d* (i.e., repeat distance or d-spacing). Since lipid bilayers are not perfectly flat and stacked flawlessly, the thermal perturbations and lattice disorders must be taken into consideration in the real world and are addressed with the paracrystalline theory (Guiner, 1963) and the modified Caillé theory (Zhang et. al., 1994) in different circumstances. In the paracrystalline theory, individual bilayers are still treated as flat surfaces but with lattice disorders and thermal fluctuations about the equilibrium positions. The structure factor is thereby modified to,

$$S_{PT}(Q) = N + 2\sum_{k=1}^{N-1}(N-k)\cos(kQd)\exp(\frac{-k^2Q^2\Delta^2}{2}), \tag{4-11}$$

where Δ is the mean square fluctuation of the bilayer. The bilayers modeled by the

paracrystalline theory are a close approximation of the lipid gel structure, which is rigid and flat compared to the L_α phase. Therefore, the paracrystalline model was applied our data in reconstructing electron density profiles of cardiolipin-water mixtures in the gel phase. On the other hand, the assumption of a flat surface is invalidated by thermal undulations of the flexible lipid liquid crystalline L_α structure (Section 2.2.6). The structure factor has therefore to be further modified to,

$$S_{MCT}(Q) = N + 2\sum_{k=1}^{N-1}(N-k)\cos(kQd)\exp\left\{-(d/2\pi)^2 Q^2 \eta\left[\gamma + \ln(\pi k)\right]\right\}, \qquad (4\text{-}12)$$

where γ is Euler's constant and the Caillé parameter η is,

$$\eta = \frac{\pi k_B T}{2d^2\sqrt{BK}}, \qquad (4\text{-}13)$$

with B being the bulk compression modulus and K the bending modulus of the bilayer. The Caillé parameter also offers the valuable information regarding the bilayer flexibility, which may be important in understanding the origin and property of the coexisting lamellar liquid crystalline phases in the lamellar-lamellar phase separation region (see Section 4.4). Taken together, fitting data with Equations 4-9 to 4-13 and Equation 4-1 allows one to utilize entire data sets of collected X-ray scattering intensities, including shapes and amplitudes of the Bragg peaks and of diffuse scattering in between, and to retrieve electron density profiles even with a scarcity of the Bragg peaks. Given the significance of the line shape in this reconstruction method, influences of the beam geometry and background scattering were also taken into consideration here in processing the raw data prior to the electron density profile reconstruction. See Sections 3.5 and 3.6 for data collection and processing.

4.3.3 Electron Density Profile and Structural Parameters

Typical diffraction profiles fitted with Equations 4-9 to 4-13 and Equation 4-1 are presented in Figure 4.3.4. It can be seen from the figure that the fits are in reasonable agreement with the data of lower lipid concentrations. As the lipid concentration increases, however, disagreements between the fits and data are larger. This phenomenon presumably arises from the inadequateness of modeling the bilayers with three Gaussians in high lipid concentrations as the bilayers may have actually been deformed in these conditions. Nevertheless, the electron density profiles were still reconstructed with this method (Figure 4.3.5) since the profiles are still able to provide some structural information with decent precision, such as the bilayer thickness.

A temperature series of electron density profiles, from 5 °C to 60 °C, were first reconstructed for the cardiolipin samples in the concentration of 32.9 wt% and in the single L_α phase. The extracted structural parameters are presented in Table 4.3.3 and Figure 4.3.6 compares temperature variations of d-spacing, (Luzzati) bilayer thickness and (Luzzati) bilayer separation of the 32.9 wt% sample. It is seen in this comparison that the decrease in d-spacing of the L_α phase, as shown in Figure 4.3.1, is the combination of variations in the bilayer thickness and in bilayer separation. This is consistent with the observations from fully hydrated lipid liquid crystal systems, such as PEs with various hydrocarbon chain lengths (Rappolt et. al., 2003; Harper et. al., 2001) and DOPC (Pan et. al., 2008), even though the cardiolipin system studied here was in the limited water condition. Due to lack of the volumetric information, data on the effective surface area of a lipid headgroup are inaccessible for our cardiolipin-water system. However, it is still speculated that this surface area per headgroup increased when temperature went up, as demonstrated by other lipid-water systems

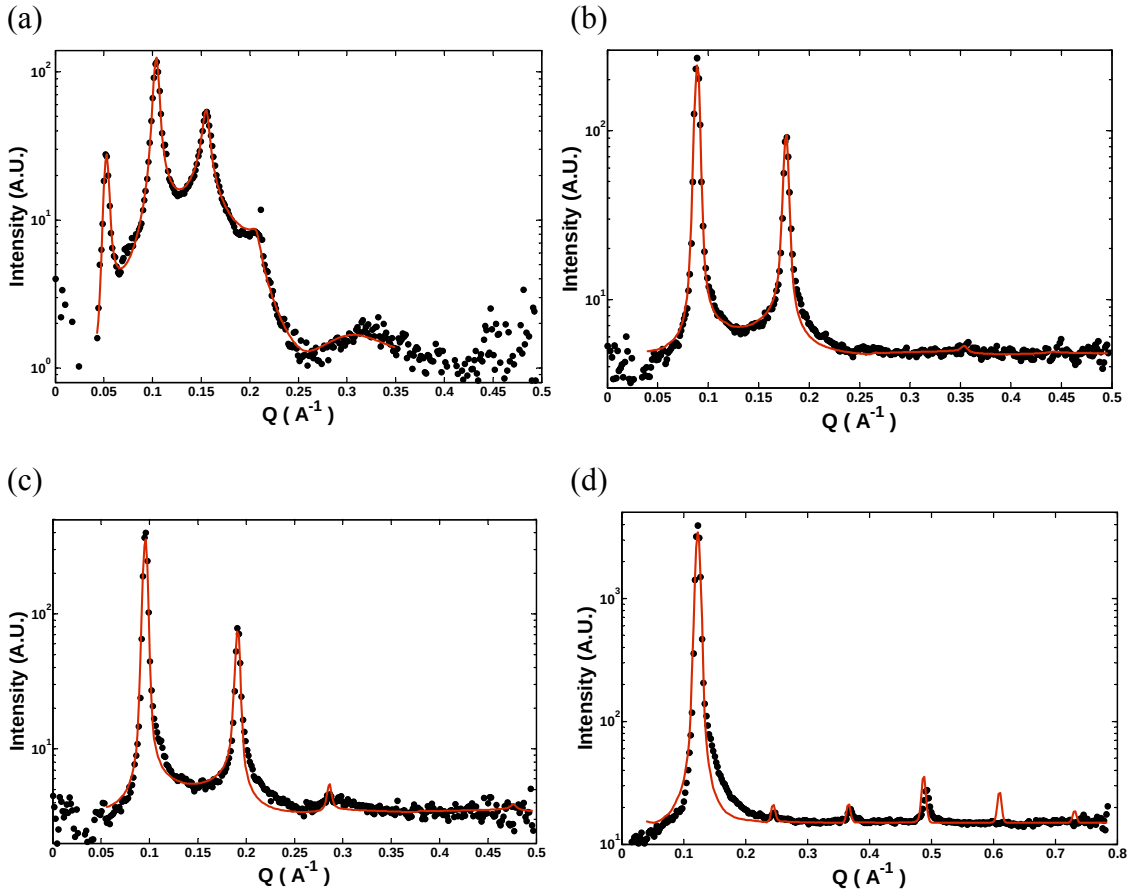

Figure 4.3.4. Representative azimuthally integrated X-ray scattering profiles fitted with Equations 4-9 to 4-12 and Equation 4-1 for the cardiolipin-water mixtures in the concentrations of 32.9 wt% (a), 55.3 wt% (b), 60.0 wt% (c) and 79.9 wt% (d). All datasets were collected at 20 °C. Deviation of the fits from the data became obvious when the lipid concentration increased. The fitted parameters are z_H = 20.2 Å, σ_H = 3 Å, ρ_r = -0.98, σ_C = 4.5 Å, N_u = 0, N = 9.67, d = 121.9 Å, η = 0.06982 for (a); z_H = 19.7 Å, σ_H = 3 Å, ρ_r = -0.98, σ_C = 6.2 Å, N_u = 0.01, N = 34.71, d = 71.2 Å, η = 0.03433 for (b); z_H = 19.5 Å, σ_H = 3 Å, ρ_r = -0.95, σ_C = 6.2 Å, N_u = 0.4, N = 49.36, d = 65.7 Å, η = 0.04114 for (c); z_H = 21.2 Å, σ_H = 3 Å, ρ_r = -0.67, σ_C = 4.7 Å, N_u = 0.1, N = 85.62, d = 51.6 Å, η = 0.00021 for (d).

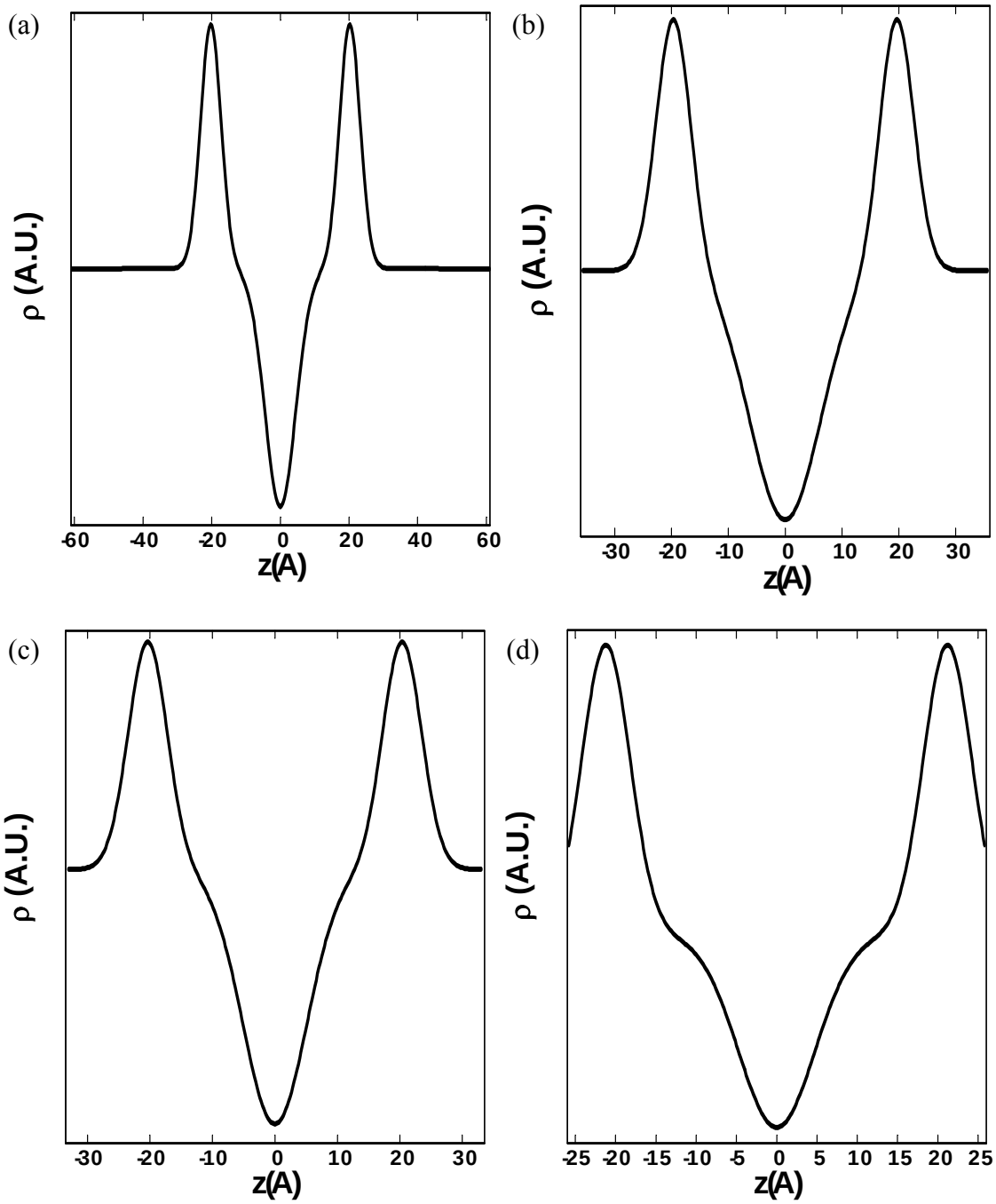

Figure 4.3.5. Typical electron density profiles of the cardiolipin-water mixtures constructed with the line-shape fitting method. The samples correspond to those in Figure 4.3.4.

(Harper et. al., 2001; Rappolt et. al., 2003; Pan et. al., 2008). Therefore, the decrease in the bilayer separation might result from higher inter-lamellar water penetration into surroundings of headgroups, which drove the lipid-water interface further towards the hydrophobic region (recall that the lipid-water interface does not exactly lies on the phosphorus of the headgroup, as discussed earlier). On the other hand, a decrease in the bilayer thickness was the consequence of stronger thermally induced splaying of the hydrocarbon chains (see Section 1.3.3). According to the decreasing rate (slope of the curve in Figure 4.3.6), shrinkage in the bilayer separation appears to play a bigger role in variation of the overall repeat distance. Moreover, this decreasing rate of the bilayer separation is also significantly larger than those observed in Harper et. al. (2001) for PEs and in Pan et. al. (2008) for DOPC. The discrepancy is speculatively due to the unique quadruple-chain configuration of cardiolipin because, in lamellar structures, bulky hydrocarbon tails must be accompanied by a larger headgroup surface area to fulfill the geometry requirement. Charges on the headgroups might also play its role in enhancing this discrepancy, since expansion of the surface areas might have otherwise been limited by the van der Waals attraction among headgroups, as in neutral lipids. Nevertheless, the relative magnitudes of the decreasing rates for the bilayer thickness and bilayer separation might have been reversed in high lipid concentrations. It is noted that the unit cell dimension variation per unit temperature, $(da/dT)_{C_L}$, for the L_α phase was depressed to values in the range of -0.07 Å/K to -0.08 Å/K when the sample concentration was greater than 70.0 wt% (Table 4.3.2). These values are comparable to the decreasing rate for the Luzzati bilayer thickness (about -0.08 Å/K) shown in Figure 4.3.6. It is therefore reasonable to argue that in high lipid concentrations, the bilayer thickness variation surpassed the bilayer separation variation and became the only significant source of the d-spacing variation with temperature changes. This should explain the decreasing trend observed for

Table 4.3.3. Structural parameters of a 32.9 wt% cardiolipin liquid crystal at temperatures from 5 °C to 60 °C. The data were extracted from the L_α phase electron density profiles reconstructed with the line shape fitting method. T is the temperature in °C; d is the d-spacing in Å; η is the dimensionless Caillé parameter (Equation 4-13); d_B is the bilayer thickness in Å (Equation 4.2); d_S is the bilayer separation in Å; $d_{B,Luzzati} = 2\,z_H$ is the Luzzati bilayer thickness in Å; $d_{S,Luzzati}$ is the bilayer separation based on the Luzzati bilayer thickness in Å. Refer to Figure 4.3.4 for the definitions of z_H and σ_H.

T	d	η	z_H	σ_H	d_B	d_S	$d_{B,Luzzati}$	$d_{S,Luzzati}$
5	125.6	0.07060	20.5	3.0	53.0	72.6	41.0	84.6
10	124.3	0.06894	20.7	3.0	53.3	71.0	41.3	83.0
15	123.1	0.06868	20.4	3.0	52.8	70.3	40.8	82.3
20	121.9	0.06982	20.2	3.0	52.5	69.4	40.5	81.4
25	120.8	0.06737	19.9	3.0	51.8	69.0	39.8	81.0
30	119.8	0.06743	19.8	3.0	51.6	68.2	39.6	80.2
35	118.8	0.06688	19.4	3.0	50.8	68.0	38.8	80.0
40	117.9	0.06852	19.2	3.0	50.4	67.5	38.4	79.5
45	117.0	0.06886	19.0	3.0	50.0	67.0	37.9	79.1
50	116.1	0.07016	19.0	3.0	50.0	66.1	38.0	78.1
55	115.2	0.07200	18.9	3.0	49.8	65.4	37.8	77.4
60	114.5	0.07819	18.5	3.0	49.1	65.4	37.1	77.4

$(da/dT)_{C_L}$ in Figure 4.3.2 when the lipid concentration increased. However, the reason for the reversal of the trend seen in even higher lipid concentrations is unclear although the bilayer thickness variation is still expected to be the only significant source of the d-spacing change in this case.

To verify the observations in structural parameters, electron density profile reconstruction must be performed with other methods in addition to the line shape

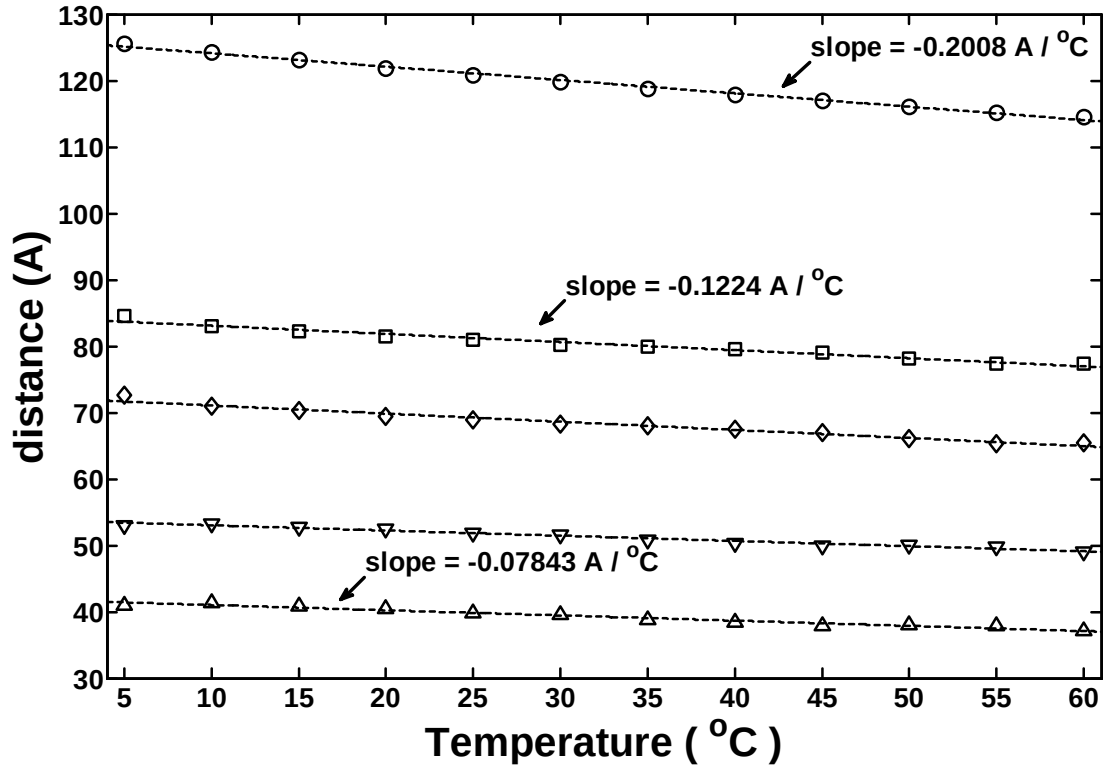

Figure 4.3.6. d-spacing, bilayer thickness and bilayer separation of the 32.9 wt% cardiolipin liquid crystal in the Lα phase as a function of temperature. Circles represent the d-spacing, downward triangles the bilayer thickness, diamonds the bilayer separation, upward triangles the Luzzati bilayer thickness, and squares the bilayer separation based on the Luzzati bilayer thickness. Slopes for the Luzzati bilayer thickness and separation are also shown.

fitting method. Because in some lipid concentrations, such as in 32.9 wt%, four X-ray scattering peaks were resolvable, we were able to reconstruct electron density profiles with the conventional peak integration method. The method is described in detail in Harper et. al. (2001). Readers are encouraged to consult the reference. In brief, electron density profile $\rho(z)$ of two lipid molecules forming the bilayer structure was modeled with four cosine functions (depending on the number of the observable scattering peaks),

$$\rho(z) = \rho_{avg} + \sum_{i=1}^{4} A_i \cos\left(\frac{2\pi i z}{d}\right), \tag{4-14}$$

with the amplitude A_i being related to the scattering intensity I_i through,

$$I_i \propto \frac{mA_i^2}{\theta}, \tag{4-15}$$

where z is the distance from the bilayer center along the bilayer normal, ρ_{avg} is the average electron density which was arbitrarily set to zero, d is the d-spacing of the L_α structure, m is the multiplicity factor and is unity for the L_α phase, and θ is an approximated Lorentz correction factor (see Section 3.2.1 for the derivation). The diffraction phases of the scattered X-rays (i.e., the signs of A_i in the centrosymmetric case, see Section 3.2.1 for the reasoning) could be determined by trial and error since the number of different combinations was only sixteen for four X-ray scattering peaks. In the case of the 32.9 wt% cardiolipin sample, where four scattering peaks could be resolved, only the diffraction phase of "+---" led to reasonable electron profiles. It should be noted that z_H values extracted from the electron density profiles reconstructed with four scattering peaks are consistently smaller than those from the reconstruction with three peaks resolvable and the fourth order peak missing (Figure 4.3.7). Reconstruction with four scattering peaks is generally considered the minimum requirement for obtaining reliable structural information, as mentioned in Section 4.3.2. It can be seen in Figure 4.3.7 that the three-peak reconstructed electron density profile exhibits more oscillations than the four-peak one does. These reflect the inaccuracy of three-peak reconstruction and are illustrated in Figure 4.3.8, in which fitting with different orders of sine functions to a square is compared. However, a consistent scaling factor of ~1.12 exists between z_H values extracted from the four-

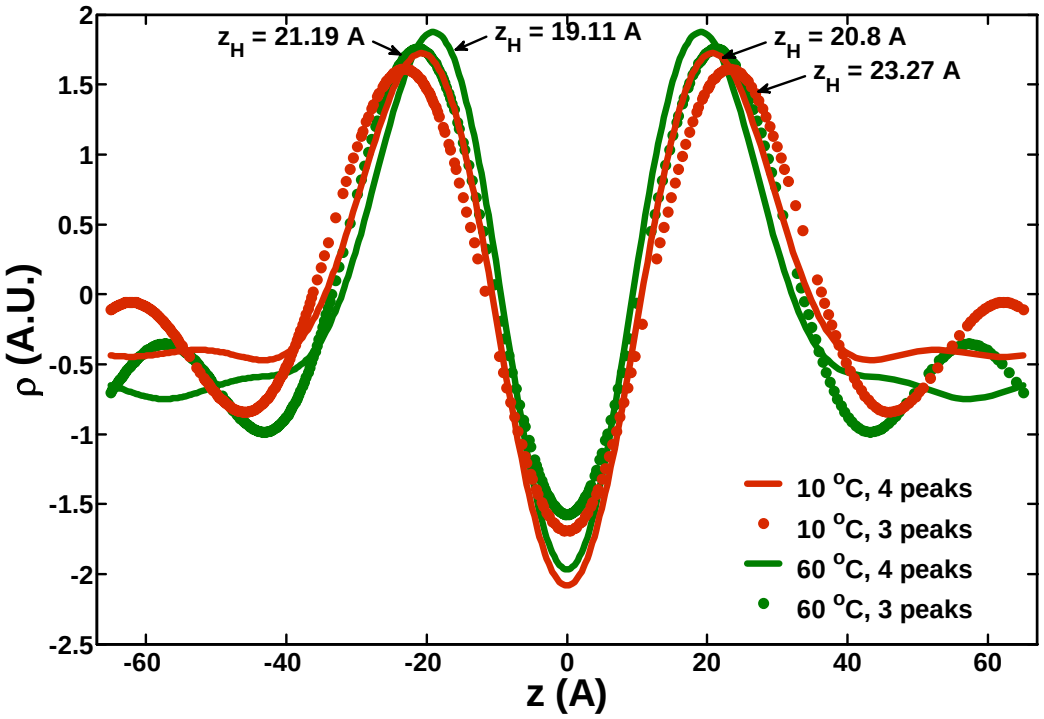

Figure 4.3.7. Electron density profile of a 32.9 wt% cardiolipin liquid crystal at 10 °C and 60 °C, reconstructed with the conventional peak integration method with four and three scattering peaks.

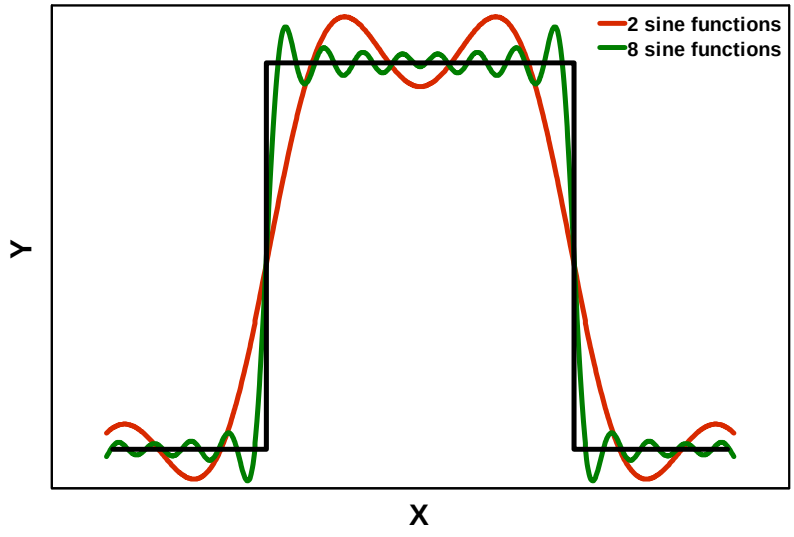

Figure 4.3.8. A square wave fitted with two or eight sine functions. The eighth order fit exhibits less noises and better represents the square wave.

peak and three-peak reconstructions. Surprisingly, this scaling factor happens to agree with the one between five- and three-peak reconstructions (with the (2,1) and (3,0) peak missing) for the POPE-water mixtures in the H_{II} phase, reported in Rappolt et. al. (2003).

Luzzati bilayer thicknesses and bilayer separations extracted from the electron density profile reconstruction with the peak integration method are shown in Table 4.3.4 and Figure 4.3.9 for a 32.9 wt% cardiolipin liquid crystal as a function of temperature. Both of the parameters are in good agreement with those from the line shape fitting method. This validates application of the line fitting method to the data presented here and confirms the observation above of the structural parameters variations with temperature. The line shape fitting method was then employed with confidence to reconstruct the electron density profiles of the L_α phase for cardiolipin-water mixtures in various lipid concentrations and temperatures. Figure 4.3.10 shows the extracted structural parameters of bilayer thickness (defined by Equation 4-2) and bilayer separation as a function of lipid fraction at chosen temperatures, corresponding to those in Figure 4.3.1. Values of those structural parameters can be found in Table 4.3.5. It can be known from Figure 4.3.10 that the d-spacing variation of the L_α phase due to sample concentration changes (Figure 4.3.1) was primarily a result of the shrinkage in the inter-bilayer water volume, because the bilayer thickness was relatively stable across the entire concentration range. Interestingly, the bilayer thickness was larger at higher lipid fractions, with a 0.039-0.124 Å expansion per percentage of concentration change. These two observations are consistent with Luzzati and Husson (1962), in which both charged and neutral lipids were studied. The latter observation also supports our reasoning in Section 4.2 to explain why the main transition temperature increased with lipid concentration because larger bilayer

thickness is presumably correlated with tighter hydrocarbon chain packing. It should also be noted that the bilayer separation went into the negative regime as the lipid concentration increased beyond some point, around 72.5 wt% to 75.0 wt% depending on the sample temperature. This might indicate that water molecules in those cases were all buried among the cardiolipin headgroups. This speculation is supported by the fact that the bilayer separation values were more negative at higher temperatures as the lipid-water interface drove further into the headgroup region due to thermally induced expansion of the headgroup surface area. As a result, the charged headgroups of cardiolipin might have directly contacted with one another in these cases. This scenario should lead to high energy penalty and induce transformation of the L_α phase to the H_{II} phase. Indeed, 72.9 wt% is the minimum concentration in which the L_α+H_{II} coexistence was observed within the temperature range studied here.

Table 4.3.4. Amplitude A_i of Equation 4-14 and structural parameters obtained with the peak integration method for a 32.9 wt% cardiolipin liquid crystal in the L_α phase at temperatures from 5 °C to 60 °C. The amplitudes were derived from the integrated peak intensities through Equation 4-15 and normalized against the third order diffraction peak amplitude. T is in °C; d, $d_{B,Luzzati}$ and $d_{S,Luzzati}$ are in Å

T	d	Amplitudes				$d_{B,Luzzati}$	$d_{S,Luzzati}$
		1	2	3	4		
5	125.6	0.16	0.91	1.0	0.55	40.6	85.0
10	124.3	0.18	0.87	1.0	0.39	41.3	83.0
15	123.1	0.22	0.89	1.0	0.51	40.0	83.1
20	121.9	0.24	0.88	1.0	0.40	40.6	81.3
25	120.8	0.27	0.84	1.0	0.46	39.36	81.5
30	119.8	0.28	0.91	1.0	0.48	39.0	80.8
35	118.8	0.29	0.90	1.0	0.45	39.0	79.8
40	117.9	0.30	0.90	1.0	0.45	38.5	79.4
45	117.0	0.32	0.91	1.0	0.47	38.2	78.8
50	116.1	0.34	0.90	1.0	0.39	38.5	77.6
55	115.2	0.35	0.92	1.0	0.46	37.7	77.5
60	114.5	0.39	0.96	1.0	0.40	38.2	76.3

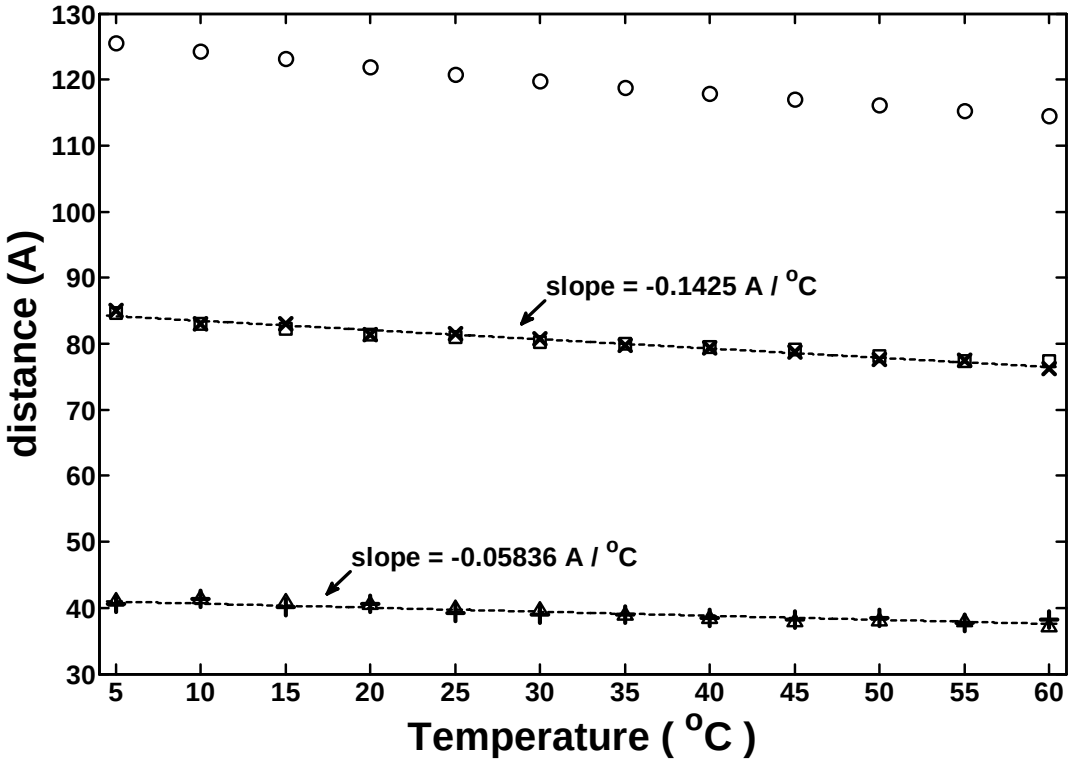

Figure 4.3.9. Comparison of the Luzzati bilayer thickness and separation of a 32.9 wt% cardiolipin liquid crystal obtained with two different electron density profile reconstruction methods. Upward triangles and plus signs are Luzzati bilayer thickness obtained with the line shape fitting method and peak integration method, respectively; squares and crosses are the bilayer separation based on the Luzzati bilayer thickness correspondingly; circles are the d-spacing. Slopes for the Luzzati bilayer thickness and separation obtained with the peak integration method are also shown.

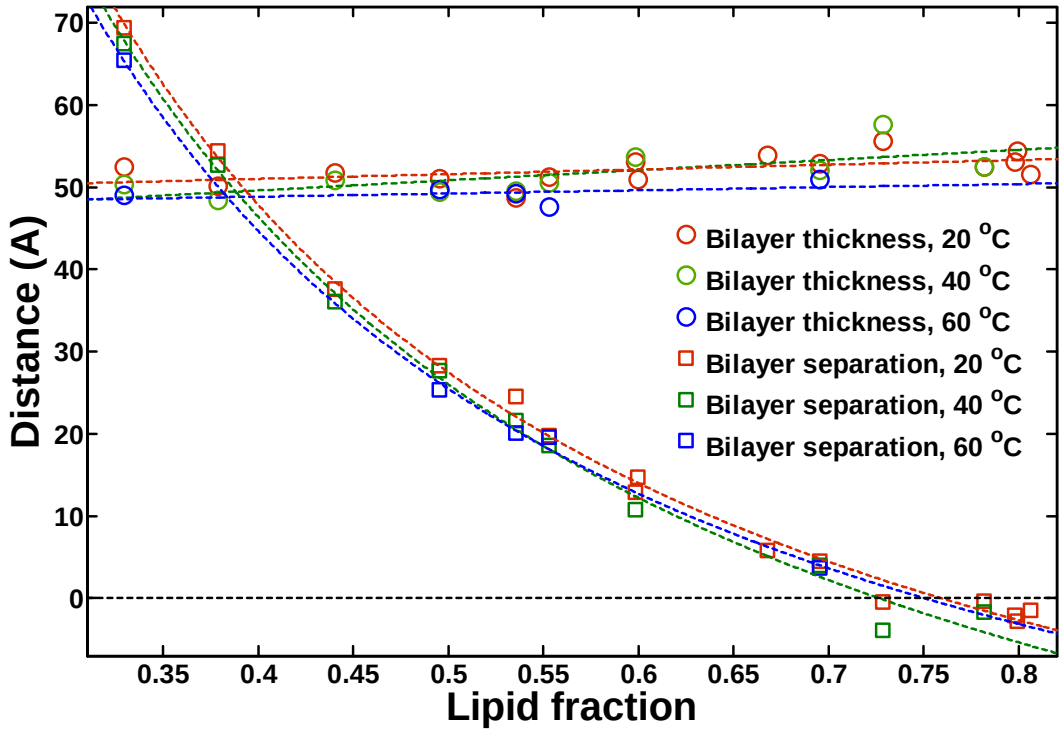

Figure 4.3.10. Bilayer thickness and separation of cardiolipin-water mixtures in the L_α phase as a function of lipid fraction at representative temperatures. Linear and power law fits were carried out for the bilayer thickness and separation, respectively. A black dashed line denotes the zero distance. The linear functions fitted to the thicknesses are $y = ax$+b with a = 5.751, b = 48.72 for 20 °C; a = 12.36, b = 44.68 for 40 °C; a = 3.859, b = 47.32 for 60 °C; the power laws fitted to the separations are $y = ax^b+c$ with a = 37.8, b = -1.043, c = -50.37 for 20 °C; a = 47.46, b = -0.9179, c = -63.6 for 40 °C; a = 37.04, b = -1.021, c = -49.66 for 60 °C.

Table 4.3.5. Structural parameters of cardiolipin liquid crystals, extracted from the electron density profiles reconstructed with the line shape fitting method. C_L is the lipid concentration; d is the d-spacing in Å; η is the dimensionless Caillé parameter (Equation 4-13); d_B is the bilayer thickness in Å (Equation 4.2); d_S is the bilayer separation in Å; $d_{B,Luzzati} = 2\,z_H$ is the Luzzati bilayer thickness in Å; $d_{S,Luzzati}$ is the bilayer separation based on the Luzzati bilayer thickness in Å. Refer to Figure 4.3.4 for the definitions of z_H and σ_H.

C_L	d	η	z_H	σ_H	d_B	d_S	$d_{B,Luzzati}$	$d_{S,Luzzati}$
				20 °C				
0.329	121.9	0.06982	20.2	3.0	52.5	69.4	40.5	81.4
0.379	104.6	0.05926	19.1	3.0	50.1	54.5	38.1	66.5
0.440	89.4	0.04730	19.9	3.0	51.8	37.6	39.7	49.7
0.495	79.4	0.03495	19.6	3.0	51.1	28.3	39.1	40.3
0.536	73.3	0.03836	18.4	3.0	48.8	24.6	36.6	36.6
0.553	71.2	0.03433	19.7	3.0	51.3	19.8	39.3	31.9
0.598	66.0	0.02517	20.3	3.1	53.1	12.9	40.7	25.3
0.600	65.7	0.04114	19.5	3.0	50.9	14.7	38.9	26.7
0.668	59.8	0.03423	20.8	3.1	54.0	5.8	41.7	18.1
0.695	57.5	0.03784	20.5	3.0	52.9	4.5	40.9	16.5
0.729	55.1	0.00491	21.7	3.1	55.5	-0.5	43.3	11.8
0.782	52.1	0.03116	20.2	3.0	52.5	-0.4	40.5	11.6
0.798	51.0	0.03096	20.5	3.0	53.1	-2.0	41.0	10.0
0.799	51.6	0.00021	21.2	3.0	54.4	-2.8	42.4	9.2
0.806	50.1	0.02028	19.9	3.0	51.6	-1.5	39.7	10.4
				40 °C				
0.329	117.9	0.06852	19.2	3.0	50.4	67.5	38.4	79.5
0.379	101.2	0.06057	18.2	3.0	48.5	52.7	36.4	64.8
0.440	86.9	0.05081	19.4	3.0	50.9	36.1	38.9	48.1
0.495	77.2	0.03470	18.7	3.0	49.5	27.7	37.5	39.7
0.536	71.1	0.03632	18.8	3.0	49.5	21.6	37.5	33.6
0.553	69.2	0.04048	19.3	3.0	50.6	18.6	38.6	30.6
0.598	64.5	0.02393	20.7	3.1	53.7	10.8	41.5	23.0
0.695	56.0	0.03150	20.0	3.0	52.1	4.0	40.0	16.0
0.729	53.7	0.00351	22.6	3.1	57.7	-3.9	45.2	8.5
0.782	50.8	0.01931	20.0	3.1	52.5	-1.7	40.0	10.9
				60 °C				
0.329	114.5	0.07819	18.5	3.0	49.1	65.4	37.1	77.4
0.495	75.1	0.03841	18.9	3.0	49.7	25.4	37.7	37.4
0.536	69.3	0.04188	18.6	3.0	49.2	20.1	37.2	32.1
0.553	67.2	0.04537	17.8	3.0	47.7	19.6	35.7	31.6
0.695	54.7	0.04247	19.5	3.0	51.0	3.7	39.0	15.7

Electron density profiles for a gel phase were also reconstructed for cardiolipin-water mixtures in selected concentrations at -20 °C (Table 4.3.6, Figure 4.3.11). Consistent with the observation in Figure 4.3.1, the bilayer separation of the gel phase was essentially unchanged when water content decreased. This fact supports our earlier claim that the gel phase was in the excess water condition even though water was limited to its liquid crystalline counterpart at higher temperatures. The bilayer separation of the gel phase was clearly shorter than 15 Å, whether the bilayer thickness defined with Equation 4-2 or the Luzzati bilayer thickness was considered. Remarkably, with the Equation 4-2 definition the bilayer separation was essentially zero for the cardiolipin sample in the gel phase at -20 °C, regardless of sample concentration. Contrary to the case of the L_α phase, in which some unstable lamellar structures converted to the hexagonal configurations, potential direct contact between the charged headgroups did not collapse the lamellar gel structure, indicating the presence of a force counteractive to the electrostatic interactions. As discussed in Section 2.2.2, the hydration force was observed to oscillate dramatically between being attractive and repulsive when the inter-surface distance was shorter than 15 Å (Israelachvili and Pashley, 1983). In close to zero inter-surface distances, otherwise repulsive hydration force was found to be attractive according to the above-cited reference. This "attractive" hydration force might account for the counterforce needed to compete with electrostatic interactions and stabilize cardiolipin in the lamellar gel structure. Nevertheless, this argument is speculative and based on a controversial experimental observation in Israelachvili and Pashley (1983). An alternative theoretical approach will be presented in the next section and its application to the gel phase will be discussed in the next chapter. It is also possible that inter-bilayer water was transferred to ice reservoirs in the sample (Gleeson et. al., 1994). WAXS on these samples could be used to detect ice.

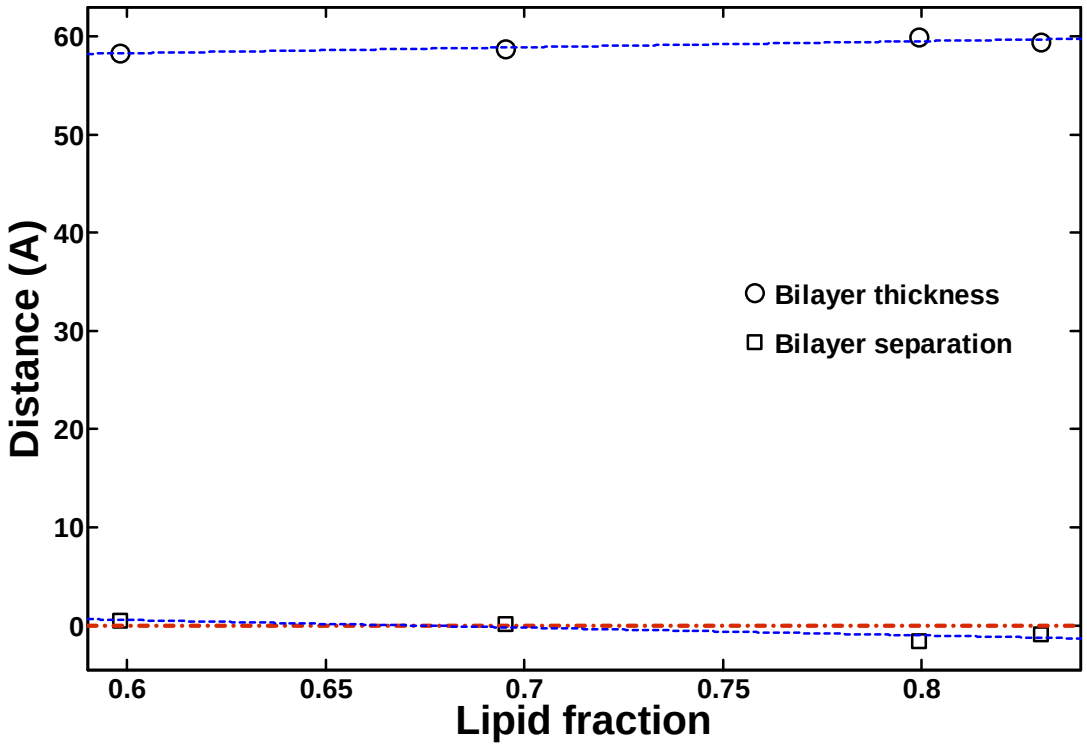

Figure 4.3.11. Bilayer thickness and separation for cardiolipin-water mixtures in a gel phase at -20 °C as a function of lipid fraction. Linear fits (blue dashed lines) are to guide the eyes. A red dash-dotted line denotes the zero distance.

Table 4.3.6. Structural parameters of cardiolipin-water mixtures at -20 °C and in the gel phase, extracted from the electron density profiles reconstructed with the line shape fitting method. C_L is in wt%; η is the dimensionless Caillé parameter; d, z_H, σ_H, d_B, d_S, $d_{B,Luzzati}$ and $d_{S,Luzzati}$ are in Å. Refer to the caption of Table4.3.5 for the definitions.

C_L	d	η	z_H	σ_H	d_B	d_S	$d_{B,Luzzati}$	$d_{S,Luzzati}$
59.8	58.8	1.945	23.3	2.9	58.3	0.4	46.6	12.2
69.5	58.9	2.139	23.3	3.0	58.7	0.2	46.6	12.3
79.9	58.4	1.683	24.0	3.0	59.9	-1.6	47.9	10.4
83.0	58.5	1.767	23.6	3.0	59.4	-0.9	47.3	11.2

4.4 The Low Temperature Lamellar-Lamellar Phase Separation Region

As the lipid concentration was within a certain range, from 55.3 wt% to 72.9 wt%, the cardiolipin-water mixtures were seen to undergo a phase separation leading to the lamellar-lamellar phase separation region at lower temperatures (the $L_{\alpha 1} + L_{\alpha 2}$ region in Figure 4.2.1). To better understand the origin of the phase separation and the nature of the two coexisting phases, we reconstructed the electron density profiles of the two phases and studied their structural parameters. It is clear that very little information can be extracted from the very limited diffraction data that was observed. The spirit of this section is to see how far one can go in trying to extract any information at all. The resultant electron density profiles should be understood in this context. In other words, the form of the electron density profiles that are derived may not be really representative of the actual bilayer profile shape, but perhaps the rate of change of distance between the peaks in these profiles, for a given set of diffraction phases, might give some information about the changes in the water spacing or bilayer thickness.

To employ the line shape fitting method outlined in Section 4.3.2 for electron density profile reconstruction, an azimuthally integrated X-ray scattering profile of two coexisting lamellar phases (Figure 4.4.1) must be deconvoluted into two separate scattering profiles for each of the phases. However, since reconstruction with the line shape fitting method relies heavily on the shape of an X-ray scattering profile, deconvolution, which inevitably leads to uncertainty in line shape (particularly in the diffuse scattering regime), will make unreliable the thereby obtained electron density profiles. Instead, we resorted to the conventional peak integration method to reconstruct electron density profiles of the two coexisting lamellar phases. While at

least four scattering peaks from samples in the L_α phase are required to obtain a reliable electron density profile reconstructed with this method, only three scattering peaks at most could be resolved unambiguously for each of the two coexisting phases. In many cases, only one scattering peak was seen. Bearing in mind the scaling factor existing between the z_H values extracted from the four- and three-peak reconstructions (Section 4.3.3), X-ray scattering profiles with three scattering peaks resolvable for each of the two coexisting phases were chosen for electron density profile reconstruction. If the ~1.12 scaling factor applies in these cases, the structural parameters obtained with the three-peak reconstruction can still yield "accurate" values after scaled with that factor.

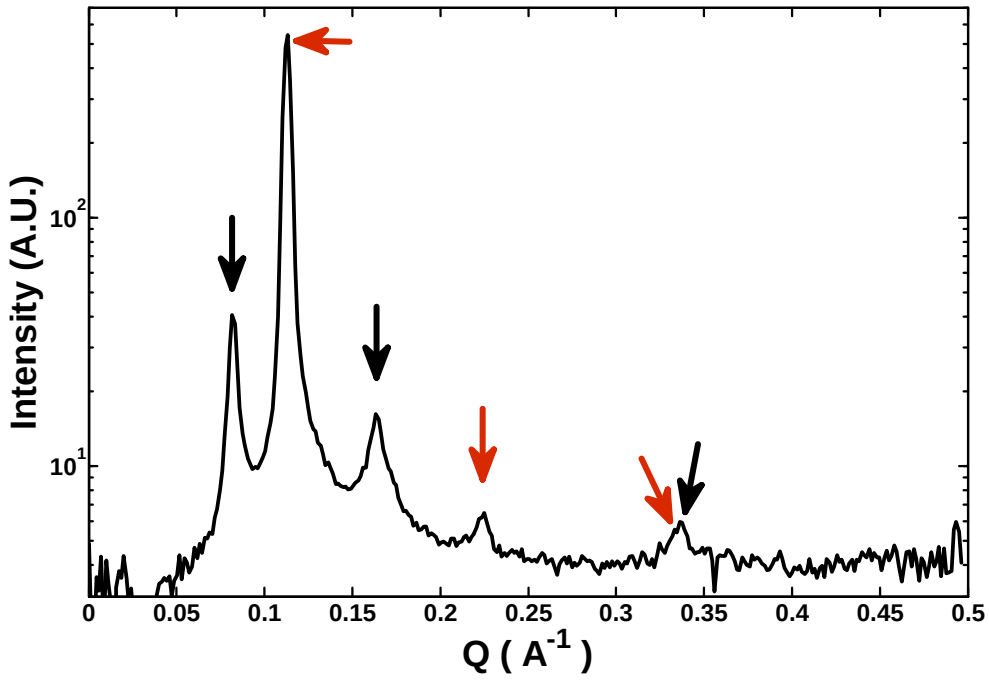

Figure 4.4.1. Azimuthally integrated X-ray scattering profile of a 69.5 wt% cardiolipin-water mixture at -5 °C. Black arrows denote the 1st, 2nd and 4th order peaks of the $L_{\alpha 1}$ phase while the 1st, 2nd and 3rd order peaks of the $L_{\alpha 2}$ phase are indicated by red arrows.

Accordingly, the X-ray scattering profile of a 69.5 wt% cardiolipin-water mixture at -5 °C was chosen for electron density profile reconstruction (Figure 4.4.1). Amplitudes of Equation 4-14 for scattering peaks of the two coexisting phases were derived from the integrated peak intensities through Equation 4-15 and are shown in Table 4.4.1. Unlike the case of the 32.9 wt% cardiolipin-water mixture presented in Section 4.3.3, determining the diffraction phases of the two coexisting lamellar phases in 69.5 wt% was not straightforward. For the $L_{\alpha 1}$ phase (the one with the larger d-spacing), both the diffraction phases of "--+" and "---" could generate reasonable electron density profiles (Figure 4.4.2a) while the diffraction phase of "--+" was the only rational choice for the $L_{\alpha 2}$ phase although the resultant electron density profile was far from ideal (Figure 4.4.2b). To solve the diffraction phase problem, electron density profiles were also reconstructed for the $L_{\alpha 1}$ phase of 66.8 wt% and 59.8 wt% cardiolipin-water mixtures at -9 °C and -14 °C, respectively, and for the $L_{\alpha 2}$ phase of a 72.9 wt% mixture at 0 °C (Table 4.4.1). As shown in Figure 4.4.3, when concentration and temperature changed, the peak, representing the phosphorous group, reconstructed for the $L_{\alpha 1}$ phase with the "---" diffraction phase became more asymmetric (Figure 4.4.3a) and deviated more from an ideal electron density profile of a lipid bilayer structure (Figure 4.3.4). On the other hand, symmetry of the peak reconstructed with the "--+" diffraction phase remained preserved, as well as the overall shape of the electron density profile (Figure 4.4.3b). This result made the diffraction phase of "--+" a preferred option for electron density profile reconstruction of the $L_{\alpha 1}$ phase. In the case of the $L_{\alpha 2}$ phase, electron density profile of a 72.9 wt% cardiolipin-water mixture, again with "--+" an only reasonable choice, exhibited a strong similarity with that of the 69.5 wt% sample, both in terms of the overall shape and peak position (Figure 4.4.4). The similarity supported adoption of the "--+" diffraction phase and validated the resultant electron density profiles.

Table 4.4.1. Amplitude A_i of Equation 4-14 and structural parameters obtained with the peak integration method for the two coexisting lamellar phases of cardiolipin-water mixtures in the lamellar-lamellar phase separation region. The amplitudes were derived from the integrated peak intensities through Equation 4-15 and normalized against the strongest amplitudes. C_L is in wt%; T is in °C; d, $d_{B,Luzzati}$ and $d_{S,Luzzati}$ are in Å. The values for $d_{B,Luzzati}$ and $d_{S,Luzzati}$ were extracted from the three-peak electron density profile reconstruction (see the text).

C_L	T	d	Amplitudes				$d_{B,Luzzati}$		$d_{S,Luzzati}$	
			1	2	3	4				
The $L_{\alpha 1}$ phase										
							--+	---	--+	---
69.5	-5	76.8	0.82	1.00	-	0.17	41.5	48.0	35.3	28.8
66.8	-9	72.8	1.00	0.98	-	0.25	39.4	48.9	33.4	23.9
59.8	-14	77.6	0.80	1.00	-	0.28	41.1	51.2	36.4	26.3
The $L_{\alpha 2}$ phase										
69.5	-5	55.7	1.00	0.16	0.14	-	42.9		12.8	
72.9	0	56.0	1.00	0.16	0.14	-	42.9		13.1	

(a)

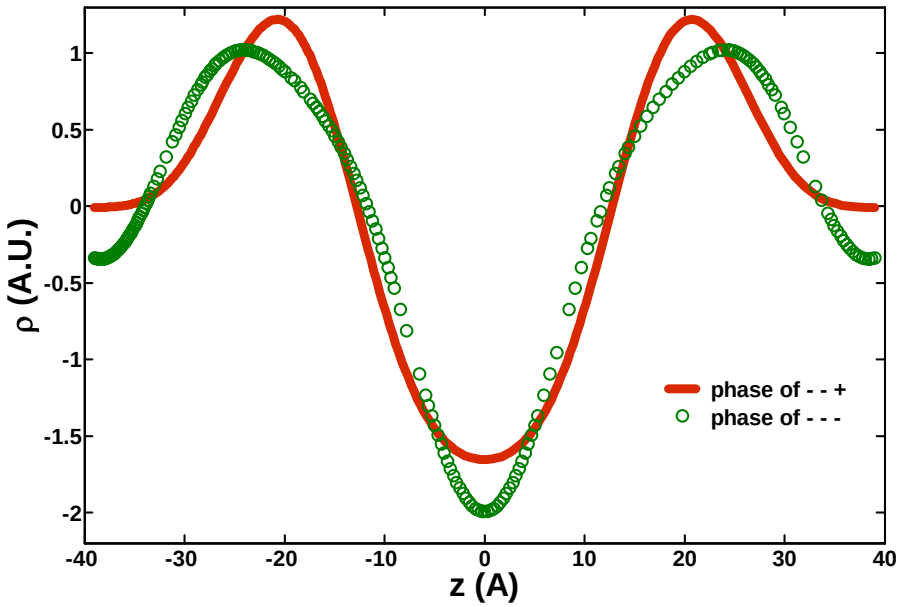

(b)

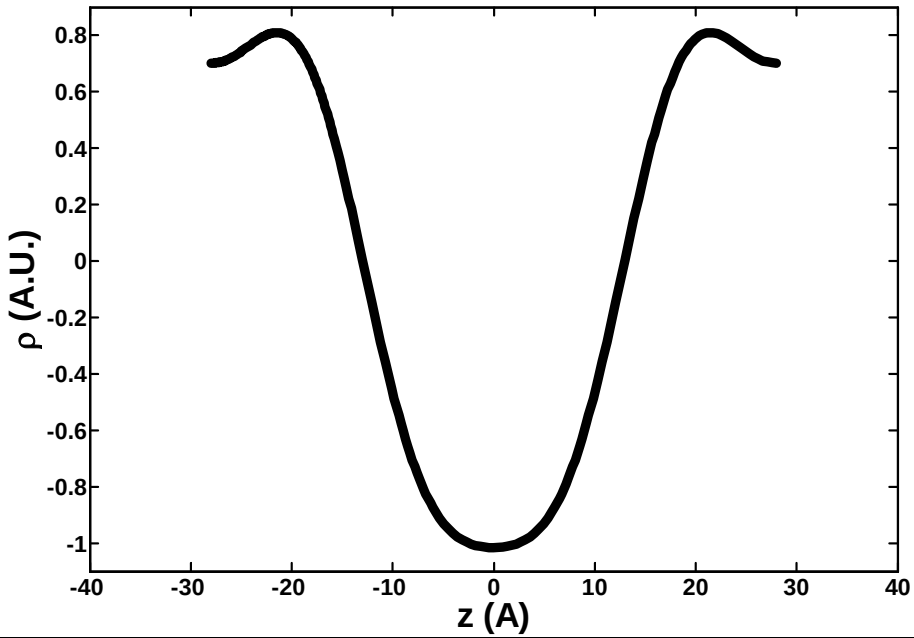

Figure 4.4.2. Electron density profiles of the $L_{\alpha 1}$ (a) and $L_{\alpha 2}$ (b) phases reconstructed with the peak integration method for a 69.5 wt% cardiolipin-water mixture at -5 °C. For the $L_{\alpha 1}$ phase, electron density profiles reconstructed with the "--+" and "---" diffraction phases are compared.

(a)

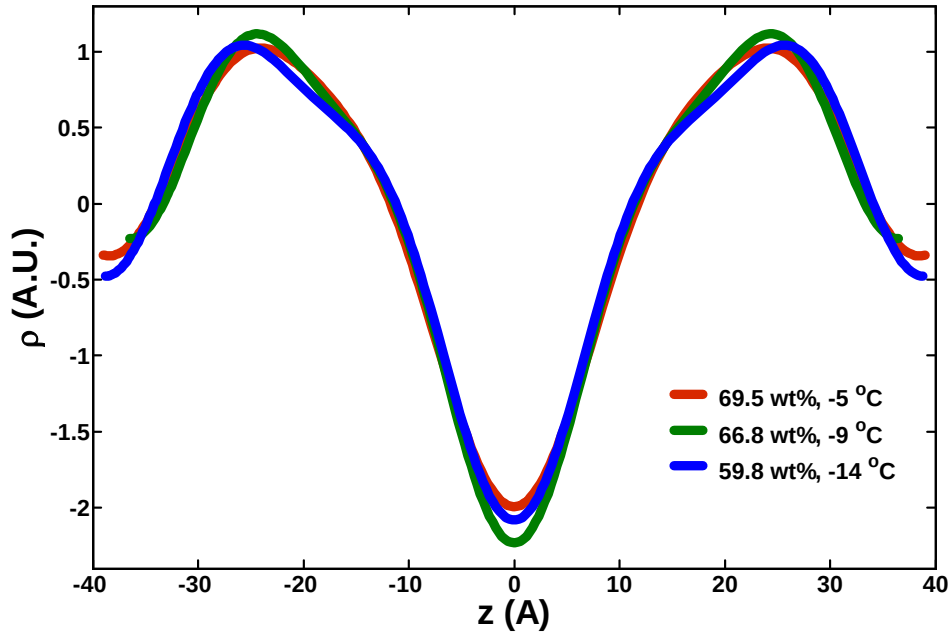

(b)

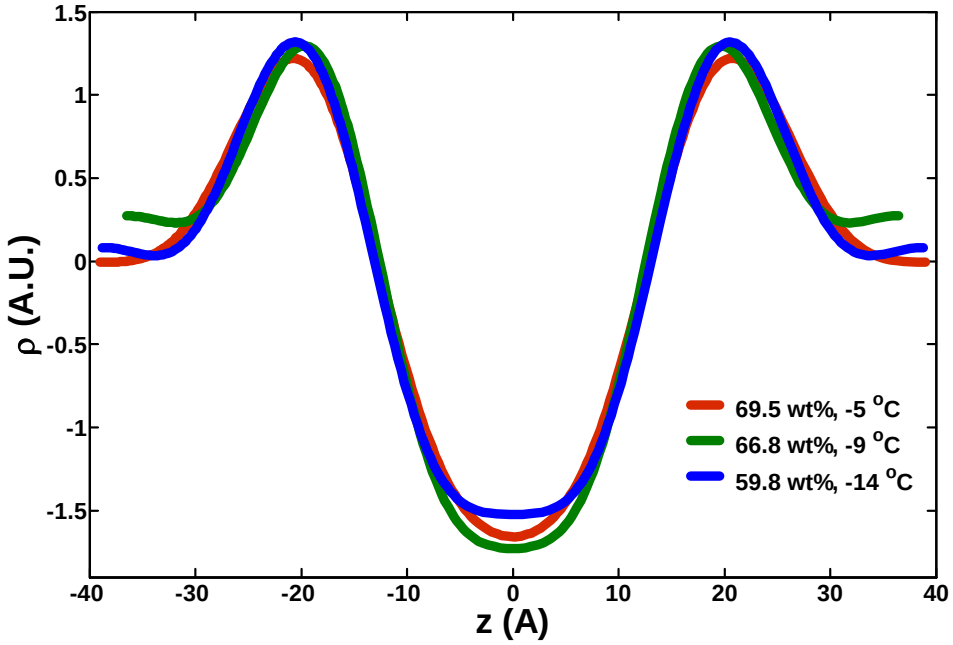

Figure 4.4.3. Comparison of the $L_{\alpha 1}$ electron density profiles based on the "---" diffraction phase (a) with those based on the "--+" diffraction phase (b) for three cardiolipin-water mixture samples at different temperatures.

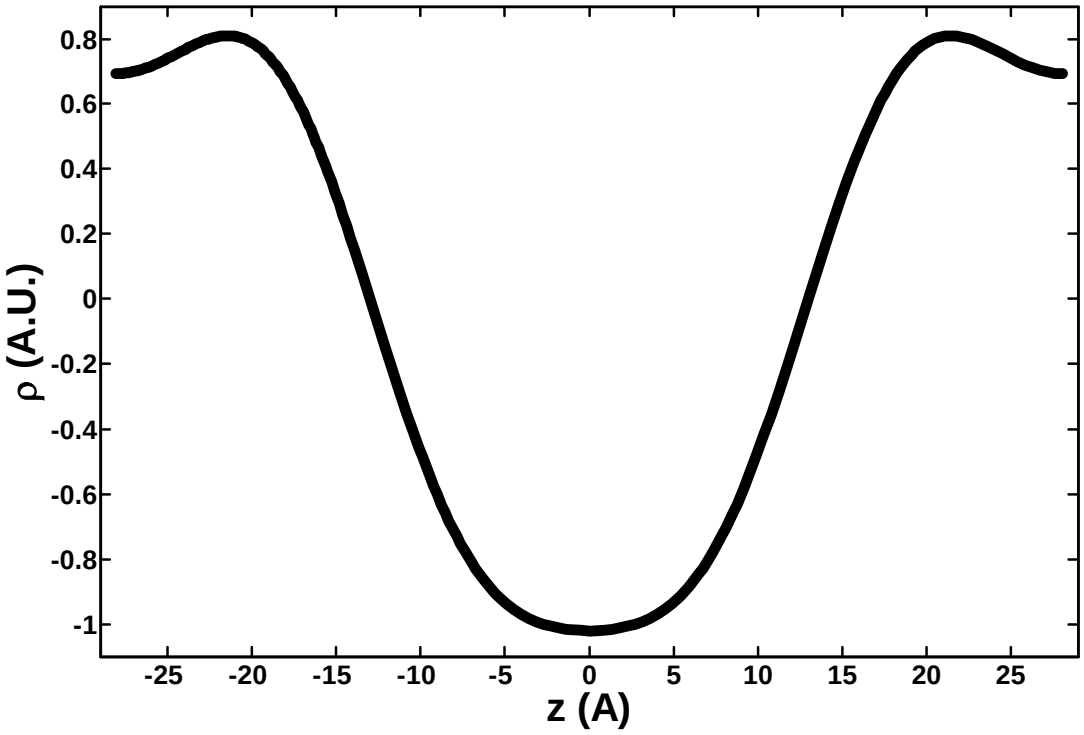

Figure 4.4.4. Electron density profile of the $L_{\alpha 2}$ phase reconstructed for a 72.9 wt% cardiolipin-water mixture at 0 °C.

To dispel any remaining uncertainty over the diffraction phases, we then turned to the structural parameters extracted from the electron density profiles. In the case of the $L_{\alpha 1}$ phase, solving for reasonable structural parameters values would also determine the correct diffraction phase because the z_H values obtained with "--+" and "---" diffraction phases are remarkably different. Since only three scattering peaks were resolved in the chosen datasets and minimally four scattering peaks were needed for obtaining a decent electron density profile, scaling the structural parameters obtained with the three-peak reconstruction might be necessary to generate accurate values. Thus, we closely examined data of the L_{α} phase electron density profile reconstructions at different temperatures reported in Harper et. al. (2001) and Rappolt et. al. (2003) to scrutinize applicability of the ~1.12 scaling factor observed in Section

4.3.3. In this analysis, selected datasets in the above-cited references and in this thesis study, where four scattering peaks were resolvable, were processed with one of the scattering peaks excluded each time. The resultant z_H values were compared with those based on the same datasets with all four scattering peaks included. As shown in Table 4.4.2, the scaling factors clearly vary with lipid identities and, within an individual dataset, even with which of the scattering peaks was omitted. In other words, the scaling factor is not independent of lipid type, liquid crystalline phase and the excluded scattering peak although the scaling factors are more or less uncorrelated with a single experimental variable (here, the temperature) for given lipids types and excluded scattering peaks. Therefore, a scaling factor is unique to a given dataset and can only be applied when an initially resolved scattering peak becomes unobservable due to, say, stronger thermal motions at high temperatures. For example, the 4th order peak of the POPE-water mixture in Rappolt et. al. (2003) became unobservable when temperature elevated to 75 °C. Based on the scaling factor obtained with our analysis (Table 4.4.2), the z_H value at that temperature could still have been determined within experimental error even when the 4th order peak was missing. This feature will also be of use when the intensity of a scattering peak cannot be evaluated unambiguously.

However, the datasets on lamellar-lamellar phase separation yielded no X-ray scattering profile with four resolvable peaks for either of the two coexisting phases at any lipid concentration and temperature. Absence of scattering peaks at sub-freezing temperatures is not likely to be due to thermal motions. It might therefore be reasonable to claim that intensities of the 3rd and 4th order peaks were intrinsically marginal for the $L_{\alpha 1}$ and $L_{\alpha 2}$ phases, respectively. We also realized from Table 4.4.2 that when the intensity of a scattering peak is relatively small, omission of that peak does not lead to substantial difference in the z_H value. Based on these two reasons, we

adopted the z_H values extracted from three-peak reconstructions for both of the coexisting phases without applying any scaling factor. The results are shown in Table 4.4.1. Readers are cautioned that the resultant z_H values might not be as accurate as those obtained with four-peak reconstruction but should still bear some precision.

Table 4.4.2. Ratios (i.e., scaling factors) of the z_H values extracted from the electron density profile reconstruction with the 1st (1), 2nd (2), 3rd (3) and 4th (4) order peaks individually excluded to those with all four peaks included. Exclusion of the strongest scattering peaks was not shown because this produced no reasonable electron density profile. The amplitudes for scattering peaks of each dataset are shown to elucidate their correlation with the scaling factors (see text).

Lipid/	*Ratio to no exclusion*				*Amplitudes*			
Temperature	1	2	3	4	1	2	3	4
Cardiolipin								
10 °C	1.01	0.89	-	1.13	0.18	0.87	1.00	0.39
60 °C	1.02	0.88	-	1.11	0.39	0.96	1.00	0.40
18:1*c*Δ9-PE*								
-4 °C	-	1.01	1.04	1.02	1.00	0.09	0.20	0.30
4 °C	-	1.01	1.04	1.01	1.00	0.09	0.21	0.29
21:0_{ch}-PE*								
55 °C	-	0.98	1.04	1.11	1.00	0.16	0.24	0.38
80 °C	-	0.98	1.04	1.21	1.00	0.16	0.19	0.33
POPE**								
30 °C	-	1.02	1.04	0.99	1.00	0.13	0.24	0.34
54 °C	-	1.02	1.04	0.98	1.00	0.17	0.25	0.31
74 °C	-	1.02	1.03	1.00	1.00	0.13	0.22	0.35

* data from Harper et. al., 2001.

** data from Rappolt et. al., 2003.

Electron density profile reconstructions carried out for 69.5 wt% and 72.9 wt% cardiolipin-water mixtures at -5 °C and 0 °C, respectively, yielded essentially identical Luzzati bilayer thickness, 42.9 Å, for the $L_{\alpha 2}$ phase (Table 4.4.1). This observation is consistent with the -10 °C curve of Figure 4.3.1a, in which d-spacing of the $L_{\alpha 2}$ phase stayed constant regardless of lipid concentration. For the $L_{\alpha 1}$ phase, close examination on the data shows that the Luzzati bilayer thickness based on the "--+" diffraction phase, 40.7±1.1 Å, appears to be more consistent with those presented in Section 4.3.3 than that based on the "---" diffraction phase, which is 49.4±1.6 Å. Also, Luzzati bilayer thickness of the $L_{\alpha 1}$ phase obtained with "--+" is thinner than that of the $L_{\alpha 2}$ phase. This result agrees with the trend seen in Figure 4.3.10, in which the bilayer thickness increases with decreasing water content (recall that $L_{\alpha 1}$ phase exhibits larger d-spacings presumably due to higher water contents). To further support adoption of the "--+" diffraction phase for the $L_{\alpha 1}$ phase and confirm "correctness" of the electron density profiles for the $L_{\alpha 2}$ phase, reconstruction with the line shape fitting method was also carried out for samples in the L_{α} phase with experimental conditions close to the phase separation region. As shown in Figure 4.4.5, immediately before the transition to the phase separation region, the d-spacing of the L_{α} phase is close to that of the $L_{\alpha 1}$ phase in 59.8 wt% and to that of the $L_{\alpha 2}$ phase in 69.5 wt% as d-spacing of the L_{α} phase shifts with lipid concentration. This similarity in the d-spacing may imply similarity in structure. Therefore, X-ray scattering profiles of 59.8 wt% and 69.5 wt% cardiolipin samples in the L_{α} phase and at -9 °C and at 0 °C respectively were employed for electron density profile reconstruction with the line shape fitting method. The extracted Luzzati bilayer thickness is 40.58 Å for 59.8 wt% and 42.58 Å for 69.5 wt%, corresponding to the $L_{\alpha 1}$ and $L_{\alpha 2}$ phases respectively. All the results presented above support adoption of the "--+" diffraction phase for the $L_{\alpha 1}$ phase and reliability of the extracted structural parameters for the both phases.

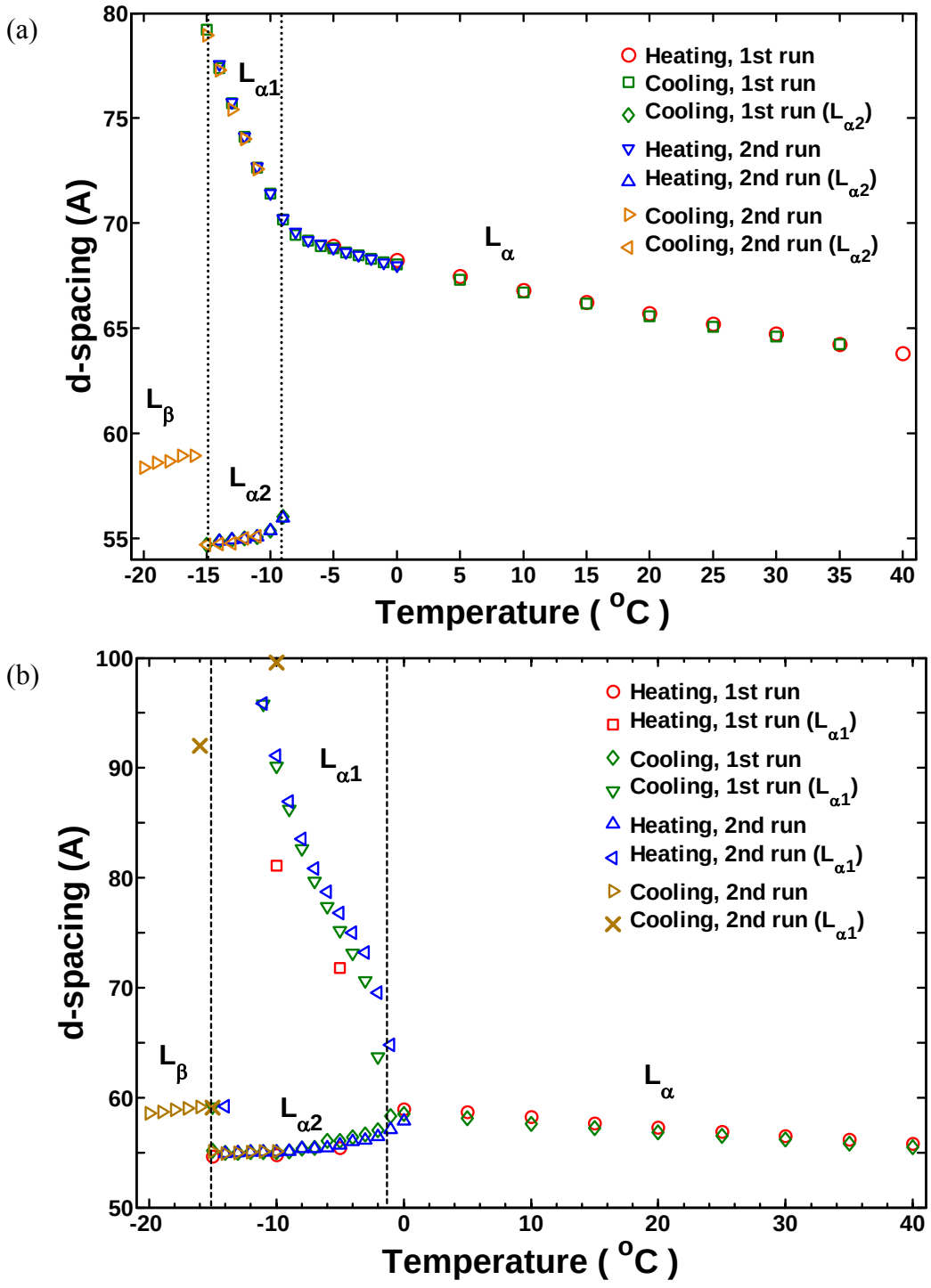

Figure 4.4.5. d-spacing of the lamellar phases as a function of temperature for 59.8 wt% (a) and 69.5 wt% (b) cardiolipin-water mixtures.

The data presented in Table 4.4.1 indicates that the observed remarkable difference in d-spacings within the lamellar-lamellar phase separation region is mainly the result of differential water distribution between the two coexisting phases, because the difference in water layer thickness (35.0±1.5 Å for the $L_{\alpha 1}$ phase versus 13.0±0.2 Å for $L_{\alpha 2}$ phase) is considerably larger than that in bilayer thickness (40.7±1.1 Å for the $L_{\alpha 1}$ phase versus 42.9 Å for the $L_{\alpha 2}$ phase). This lamellar-lamellar phase separation phenomenon is not unique to cardiolipin-water mixtures. It was also observed in another charged lipid system, surfactant didodecyldimethylammonium bromide or DDABr (Dubois et. al., 1993), and even in neural lipid systems, phospholipids PCs, when alkali ions were added to the latter (Rappolt et. al., 2001; Rappolt et. al., 1998). To our best knowledge, however, the data presented here appear to be one of few, if not the only, observations in which a one-component charged phospholipid system displays lamellar-lamellar phase separation.

The above-cited studies evoked two different mechanisms to explain a superficially identical phenomenon. In the case of neutral lipids, osmotically driven ion gradients across multilayer structures were suggested to account for the phase separation (Rappolt et. al., 2001) because ions are known to condense neural lipids (Inoko et. al., 1975; Lis et. al., 1981). On the other hand, a mechanism involving counterion mediated electrostatic "attraction" was proposed for the case of DDABr (Jho et. al., 2010; Boroudjerdi et. al., 2005; Netz, 2001). A parameter, the coupling parameter Ξ, was derived to distinguish two types of counterion distributions and correspondingly attractive/repulsive interactions between two charged surfaces,

$$\Xi \approx \frac{z^3 \sigma}{T^2}, \tag{4-16}$$

where z is counterion valence, σ is surface charge density and T is temperature. Note that Ξ is greater at higher counterion valences and lower temperatures. In the limit of $\Xi >> 1$, counterions are distributed as a flat, 2-D layer near a charged surface and are highly correlated (Figure 4.4.6). This type of counterion distribution results in net attraction between two charged surfaces and in the coexisting lamellar phase with a shorter inter-lamellar distance because repulsion between surfaces is compensated by attraction among surfaces and counterions. On the other hand, the net force between charged surfaces is repulsive and can be described by the Poisson-Boltzmann theory when $\Xi \approx 1$. This may be the case for the coexisting lamellar phase with a longer inter-lamellar distance. For our cardiolipin system, readers are reminded that even though "pure" water was used for the sample preparation, the cardiolipin-water system employed in this thesis study was never free of counterions (cardiolipin was a sodium salt as purchased) because of the need to fulfill electric neutrality. Therefore, the above-mentioned counterion-mediated attraction may apply in our system as well. Moreover, it was known that phase separation only occurred at lower temperatures and the relative amount of $L_{\alpha 2}$ phase increased with decreasing temperature (e.g., Figure 4.4.7). These two observations may be connected to the inverse quadratic relation of Ξ with temperature and further strengthen the explanation with this strong coupling approach. The fact that phase separation was observed only in a specific range of sample concentration may pose an unanswered question to this theoretical approach. Also, based on this approach, phase separation may have occurred at higher temperatures if the purchased cardiolipin was a calcium salt. An approach will be provided in the next chapter in an attempt to explain the former while still more experiments are needed to address the later and other potential questions.

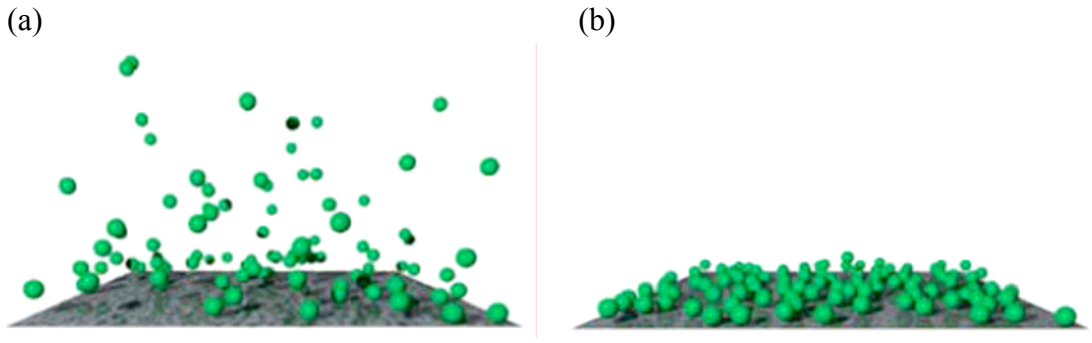

Figure 4.4.6. Snapshots of a Monte-Carlo simulation for counterion (green spheres) distributions near a charged surface when $\Xi = 1$ (a) and $\Xi >> 1$ (b). The figure is from Boroudjerdi et. al., 2005.

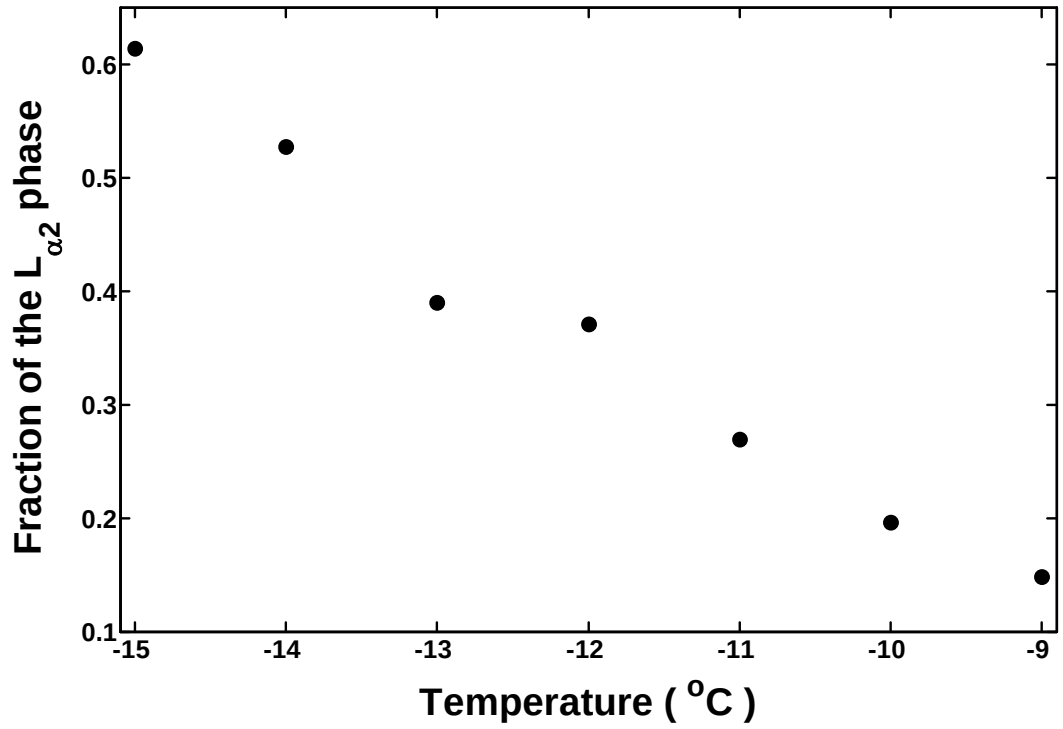

Figure 4.4.7. Fraction of the $L_{\alpha 2}$ phase in the total lamellar phases as a function of temperature for a 59.8 wt% cardiolipin-water mixture. The values were obtained by calculating integrated intensities of the first order peaks of the $L_{\alpha 1}$ and $L_{\alpha 2}$ phases.

As mentioned in Section 1.2, the physical phenomenon underlying the lipid raft model, liquid-liquid phase separation, bears a strong similarity to the phase separation observed here: both involve the coexistence of two liquid crystalline lamellar phases. However, our WAXS data could not differentiate the diffuse scattering from the L_o (as lipids rafts) phase and from the L_d (or L_α as the bulk lipid matrix) phase as having been carried out in Mills et. al. (2008a). Following the experimental protocol by Mills et. al. (2008b) may clarify whether the $L_{\alpha 1}$ and $L_{\alpha 2}$ phases observed in our cardiolipin system were actually the L_o and L_d phases speculated for the lipid raft model.

4.5 The Tiny Crystals-Cluster Phase at High Lipid Concentrations

In addition to the lamellar-lamellar phase separation region, another peculiar phenomenon observed in phase behavior of cardiolipin-water mixtures was emergence of a structure at high lipid concentrations (> ~85 wt%), which exhibited X-ray diffraction pattern consistent with clusters of tiny crystals. As shown in Figure 4.2.6, diffraction images collected from samples at this phase region displayed regular powder diffraction rings but peppered with discrete Bragg spots typical of structures with long-range periodicity, such as larger single crystals. This feature appeared to point out presence of polycrystalline structures with periodic domains larger than those usually seen in the lipid liquid crystal dispersions. However, absence of ordered structures within hydrocarbon chain region, as demonstrated by the WAXS data shown in Figure 4.5.1, indicates that the cardiolipin molecules were still in the liquid crystalline state even though they scattered crystalline-like X-ray diffraction patterns.

To explore the nature of this phase, we investigated whether the structure was in a stable equilibrium state or only a transitory one between two stable phases. For this

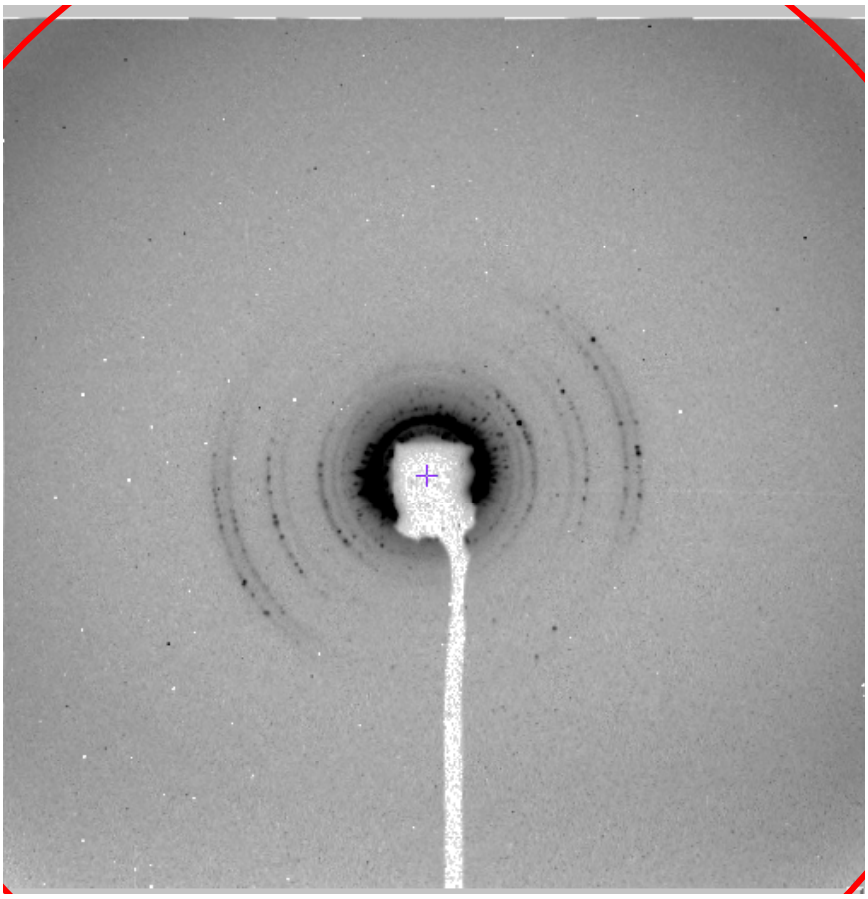

Figure 4.5.1. X-ray diffraction image of a ~87 wt% cardiolipin-water mixture in the 8th hour incubation at 35 °C. The WAXS regime covers a reciprocal space up to |Q| = 1.55 $Å^{-1}$. Red arcs mark |Q| = ~1.45 $Å^{-1}$. Compared to Figure 4.2.5a, which shows a sharp peak at 1.45 $Å^{-1}$, the current data only display a diffuse scattering peak in the corresponding region. Absence of a sharp peak in the WAXS regime suggests that this cardiolipin-water mixture was in the liquid crystalline state.

purpose, cardiolipin-water mixtures in appropriate concentrations were incubated at 30-40 °C and illuminated with X-rays in specific time intervals to record temporal evolution of the diffraction patterns. Initially, the Bragg spots were sparse and barely recognizable (Figure 4.5.2a). Powder diffraction rings still dominated the diffraction pattern. The Bragg diffraction spots were observed to multiply and enlarge gradually,

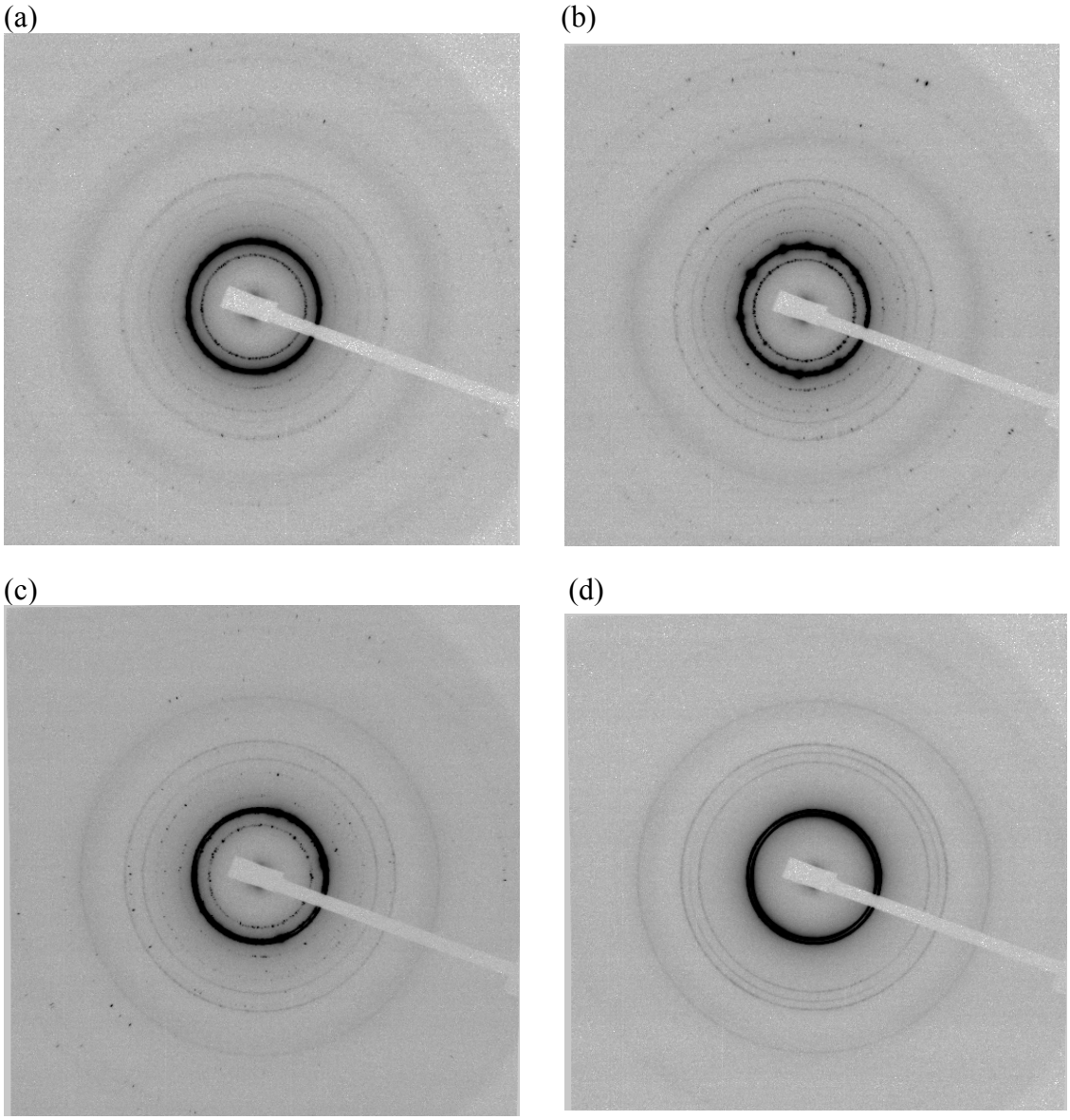

Figure 4.5.2. X-ray diffraction images of a ~86.6 wt% cardiolipin-water mixture incubated at 40 °C for 0 hr (a), 4hr (b), 14 hr (c) and 22 hr (d). See the text for the discussion on temporal evolution of the diffraction patterns.

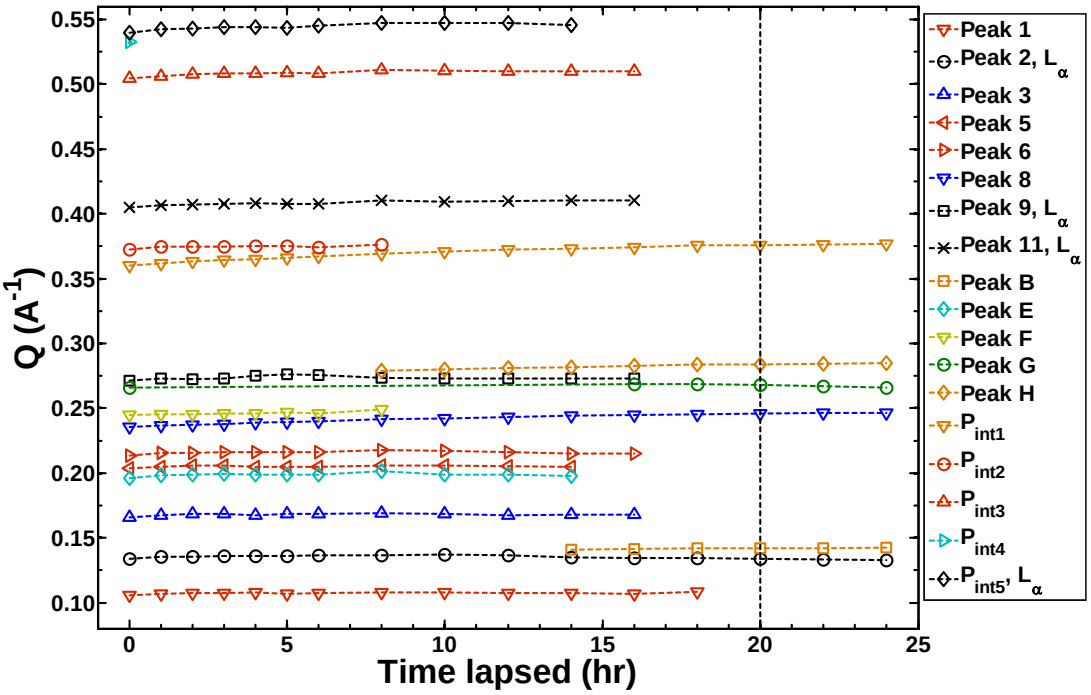

Figure 4.5.3. Peak position of each scattering peak by a ~86.6 wt% cardiolipin-water mixture as a function of incubation time at 40 °C. Peaks speculated to belong to the same family are grouped with the same color. A dashed line marks when the Bragg spots were completely undetectable.

indicating continuous growth of the tiny crystal-like domains during the incubation (Figure 4.5.2b). Surprisingly, after reaching the maximum in sharpness and discreteness, the Bragg spots became smeared and started to shrink after several hours of incubation (Figure 4.5.2c). The Bragg spots eventually disappeared altogether when the diffraction patterns returned to smooth powder diffraction rings again (Figure 4.5.2d). These diffraction peaks were spaced differentially from those observed in the beginning of the incubation and indexed as arising from the coexisting L_α and H_{II} phases. Figure 4.5.3 summarized temporal evolution of all the peaks scattered by a ~86.6 wt% cardiolipin-water mixtures. A question was prompted upon this unexpectedobservation of crystalline-like diffraction → powder diffraction transition:

(a)

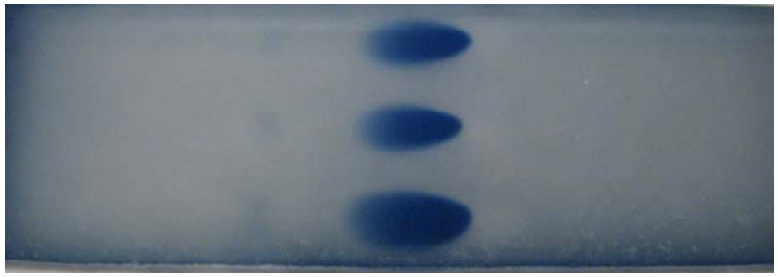

(b)

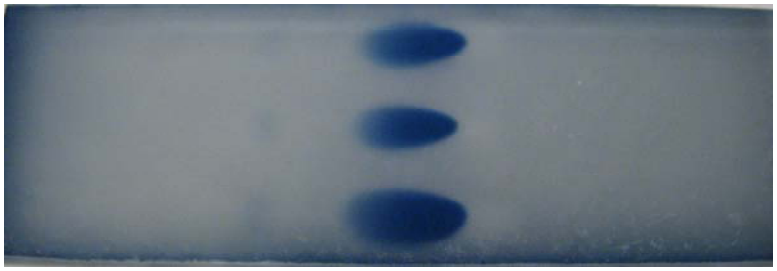

(c)

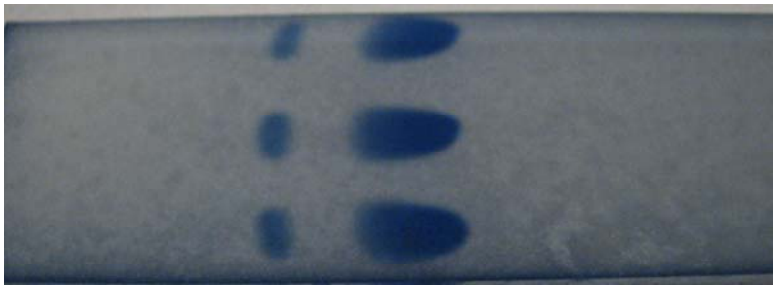

Figure 4.5.4. Thin-layer chromatography results for ~87 wt% cardiolipin-water mixtures in the different stages of incubation at 30 °C or 35 °C: (a) before incubation; (b) immediately after emergence of the crystalline-like diffraction pattern (incubation at 30 °C for 1.5 hrs); (c) after reemergence of the powder diffraction pattern (incubation at 35 °C for 18 hrs). Each row is different in the size of a sample drop used for the chromatography; 1.5 μl, 2.5 μl and 3 μl from top to bottom. (a) and (b) exhibit essentially identical patterns while in (c) the minor spots, presumably arising from the degraded cardiolipin molecules, are clearly observed.

Was this transition the result of a slow phase transition requiring a prolonged incubation at relatively higher temperatures or was it merely a product of thermal degradation (Section 3.4 details the concern over thermal degradation)? To answer this question, we carried out thin-layer chromatography for the crystalline-like samples at different stages of the incubation: before incubation, immediately after appearance of the crystalline-like diffraction pattern, and after the reemergence of the powder diffraction pattern. From the chromatography results shown in Figure 4.5.4, it is clear that forming and growing of the tiny crystal-like domains was not caused by thermal degradation. However, the results suggest that lipid thermal degradation was responsible for disappearance of tiny crystal-like domains and the return to powder diffraction patterns, even though it was not a complete breakdown as shown in Figure 3.4.1. Hence, the reemergence of powder diffraction patterns was considered as an artifact and will not be further discussed below.

From temporal evolution of the X-ray diffraction patterns demonstrated above, it was realized that the tiny-crystals cluster-like structure was apparently a stable phase at high lipid concentrations and merited further efforts to explore its structure. Therefore, we proceeded to index the X-ray scattering peaks of this structure, excluding the coexisting L_α or H_{II} phase, to determine the symmetry of its unit cell. Here, diffraction pattern of an 86.6 wt% cardiolipin-water mixture in the 5th hour of its incubation at 40 °C was taken to conduct the indexing process. Software packages from the CCP14 (Collaborative Computational Project Number 14 in Powder and Small Molecule Single Crystal Diffraction) collaboration, the *Crysfire* suite (Shirley, 1980) and *Checkcell* of the *LMGP Suite* (Laugier and Bochu), are the programs widely used to index powder diffraction peaks of small molecules and were employed here to index the scattering peaks from the cardiolipin liquid crystals. The *Crysfire* suite runs

three automatic indexing programs, *Taup* (Taupin, 1968), *Dicvol91* (Louer and Louer, 1972; Boultif and Louer, 1991) and *Treor90* (Werner et. al., 1985), against the input scattering peak positions of the cardiolipin sample to suggest the most likely unit cell symmetries along with the unit cell dimensions. Summary of the obtained unit cell suggestions and the raw scattering profile are then loaded into *Checkcell* to optimize the result. The program automatically goes through all the potential unit cell symmetries and dimensions against the experimental scattering profile to offer the best solutions.

A literature dataset reported in Shearman et. al. (2009) was first used to verify this indexing approach. Following the process described above, *Crysfire* and *Checkcell* generated a list of "estimated best solutions" to unit cell of the input X-ray scattering peaks (Table 4.5.1). Note the solutions in this list were not ordered by their suitability to data. The reported space group, $P6_3/mmc$, and unit cell dimension, $a = b = 71.5$ Å, $c = 116.5$ Å, $\alpha = \beta = 90°$, $\gamma = 120°$ for this dataset were in the estimated best solution list. Close examination might lead to the unit cell choice as reported. Combining use of these two programs would at least determine the "correct" Bravais lattice and unit cell dimension with sufficient precision for a given set of X-ray scattering peaks if one relied only on the "estimated best solutions" without manually checking each solution within. We then applied the indexing approach to our data. The preliminary unit cell suggestions by *Crysfire* are listed in Table 4.5.2. Based on these suggestions, a list of the estimated best solutions was produced by *Checkcell* (Table 4.5.3). The observed X-ray scattering profile superimposed on one of the solutions is presented in Figure 4.5.5. Careful examination to each solution concluded that the most likely unit cell symmetry and dimension were tetragonal with the space group of *P4* in the dimension of $a = b = 37.04$ Å, $c = 58.124$ Å; $\alpha = \beta = \gamma = 90°$. Table 4.5.4 compares observed and

calculated positions of the scattering peaks, based on the obtained unit cell. However, it should be noted that many diffraction orders are not seen, which makes the assignment questionable.

With 3-D periodicity and the low water contents, cardiolipin molecules in this tiny crystals cluster-like phase are speculated to arrange in inverted micellar structures, with water burying inside, within a tetragonal unit cell. This spatial arrangement may be similar to that of the *Fd3m* cubic micellar phase demonstrated in Figure 1.3.5 or of the $P6_3/mmc$ hexagonal micellar phase reported in Shearman et. al. (2009). If valid, this tetragonal micellar phase would be a new inverted micellar phase, not observed before for phospholipids, even though a micelle-like structure with a close space group, $P4_2/mmm$, has been reported for dendrimers (Ungar et. al., 2003). Nevertheless, with the number of scattering peaks observed here, we cannot make the claim with confidence. Furthermore, even if the speculation is proven true, it is still unclear why the cardiolipin-water mixtures would form domains larger than those usually observed in lipid liquid crystals. Particularly, formation of these domains prefers higher temperatures rather than lower temperatures, an apparent contradiction to conventional wisdom.

Table 4.5.1. Estimated best solutions suggested by *Checkcell* under the constraint of 0.03° angular tolerance for 2θ between the observed and calculated reflections for the hexagonal inverted micellar phase of a DOPC/DPG/Cholesterol mixture reported in Shearman et. al. (2009). Fourteen peaks were observed in this dataset. Molecular volumes are in $Å^3$; Lengths are in Å. The reported space group of $P6_3/mmc$ and unit cell dimension, $a = b = 71.5$ Å, $c = 116.5$ Å, $\alpha = \beta = 90°$, $\gamma = 120°$, are in the list

FOM	a	b	c	α	β	γ	Vol.	Syst.	Sp. Group
18.3	71.638	71.638	116.424	90	90	120	517436	HEXA	P63MC
18.3	71.638	71.638	116.424	90	90	120	517436	HEXA	P-62C
18.3	71.638	71.638	116.424	90	90	120	517436	HEXA	P63/MMC
18.3	71.638	71.638	116.424	90	90	120	517436	HEXA	P3C1
18.3	71.638	71.638	116.424	90	90	120	517436	HEXA	P-31C
18.2	71.589	71.589	116.435	90	90	120	516778	HEXA	P63MC
18.2	71.589	71.589	116.435	90	90	120	516778	HEXA	P-62C
18.2	71.589	71.589	116.435	90	90	120	516778	HEXA	P63/MMC
18.2	71.589	71.589	116.435	90	90	120	516778	HEXA	P3C1
18.2	71.589	71.589	116.435	90	90	120	516778	HEXA	P-31C
14.5	71.468	71.468	116.553	90	90	120	515556	HEXA	P63MC
14.5	71.468	71.468	116.553	90	90	120	515556	HEXA	P-62C
14.5	71.468	71.468	116.553	90	90	120	515556	HEXA	P63/MMC
14.5	71.468	71.468	116.553	90	90	120	515556	HEXA	P3C1
14.5	71.468	71.468	116.553	90	90	120	515556	HEXA	P-31C
13.6	71.595	71.595	116.296	90	90	120	516253	HEXA	P63MC
13.6	71.595	71.595	116.296	90	90	120	516253	HEXA	P-62C
13.6	71.595	71.595	116.296	90	90	120	516253	HEXA	P63/MMC
13.6	71.595	71.595	116.296	90	90	120	516253	HEXA	P3C1
13.6	71.595	71.595	116.296	90	90	120	516253	HEXA	P-31C
7.79	71.516	71.516	116.596	90	90	120	516441	HEXA	P63MC
7.79	71.516	71.516	116.596	90	90	120	516441	HEXA	P-62C
7.79	71.516	71.516	116.596	90	90	120	516441	HEXA	P63/MMC
7.79	71.516	71.516	116.596	90	90	120	516441	HEXA	P3C1
7.79	71.516	71.516	116.596	90	90	120	516441	HEXA	P-31C

Table 4.5.2. Preliminary unit cell suggestions by the *Crysfire* suite for a ~86.6 wt% cardiolipin-water mixture in the 5th hour of incubation at 40 °C. The most likely unit cell symmetries and cell dimensions are listed. Volumes are in $Å^3$; Lengths are in Å.

Merit	Pedig	Volume	a	b	c	α	β	γ
25.57	Tet__3	79744.54	37.0401	37.0401	58.1243	90	90	90
23.69	Ort__2	56555.86	26.1729	37.2102	58.0716	90	90	90
21.47	Ort__3	63355.5	29.3197	37.2102	58.0715	90	90	90
19.79	Ort__1	63371.56	29.2846	37.2653	58.0699	90	90	90
19.6	Tet__5	79871.91	37.059	37.059	58.1576	90	90	90
17.8	Mon_26	56653.47	37.057	58.252	26.249	90	88.993	90
15.3	Mon__4	57019.97	37.297	58.252	26.246	90	89.444	90
15.3	Mon_28	57019.97	37.297	58.252	26.246	90	90.556	90
15.3	Mon_27	57019.97	37.297	58.252	26.246	90	89.444	90
15.3	Mon_12	57019.97	37.297	58.252	26.246	90	89.444	90
15.3	Mon_11	57019.97	37.297	58.252	26.246	90	89.444	90
15.3	Ort__1	56644.88	58.2522	37.0509	26.2452	90	90	90
14.45	Ort__4	75261.67	26.2902	49.1083	58.2941	90	90	90
14.3	Mon__9	56998.45	37.269	58.173	26.294	90	89.028	90
14.3	Mon__2	56998.45	37.269	58.173	26.294	90	89.028	90
14.3	Mon_25	56998.45	37.269	58.173	26.294	90	89.028	90
14.3	Mon_10	56998.45	37.269	58.173	26.294	90	89.028	90
10.3	Mon_23	56283.66	37.125	58.031	26.125	90	90.039	90
10.17	Tet__1	125716	58.2687	58.2687	37.0272	90	90	90
8.7	Mon_24	56287.25	37.127	58.031	26.127	90	90.664	90
8.5	Mon_14	57032.2	37.304	58.252	26.252	90	88.72	90
8.5	Mon_13	57032.2	37.304	58.252	26.252	90	88.72	90
7.99	Tet__2	162815.6	58.2687	58.2687	47.9541	90	90	90
7.9	Mon_15	55893.14	37.134	58.031	25.944	90	91.289	90
7.6	Tet__3	338080.1	25.3989	25.3989	524.0704	90	90	90
7.6	Tet__2	338080.1	25.3989	25.3989	524.0704	90	90	90
7.6	Tet__1	338080.1	25.3989	25.3989	524.0704	90	90	90
7.09	Ort_23	36903.89	12.3413	26.1146	114.506	90	90	90
6.9	Mon_16	56180.68	37.146	58.031	26.077	90	91.914	90

Table 4.5.3. Estimated best solutions suggested by *Checkcell* under the constraint of 0.03° angular tolerance for a ~86.6 wt% cardiolipin-water mixture in the 5th hour of incubation at 40 °C. Volumes are in $Å^3$; lengths are in Å.

FOM	a	b	c	α	β	γ	Vol.	Syst.	Sp. Group
25.57	37.04	37.04	58.124	90	90	90	79745	TETR	P4
25.57	37.04	37.04	58.124	90	90	90	79745	TETR	P-4
25.57	37.04	37.04	58.124	90	90	90	79745	TETR	P4/M
25.57	37.04	37.04	58.124	90	90	90	79745	TETR	P422
25.57	37.04	37.04	58.124	90	90	90	79745	TETR	P4MM
25.57	37.04	37.04	58.124	90	90	90	79745	TETR	P-42M
25.57	37.04	37.04	58.124	90	90	90	79745	TETR	P-4M2
25.57	37.04	37.04	58.124	90	90	90	79745	TETR	P-42M
25.57	37.04	37.04	58.124	90	90	90	79745	TETR	P4/MMM
19.6	37.059	37.059	58.158	90	90	90	79872	TETR	P4
19.6	37.059	37.059	58.158	90	90	90	79872	TETR	P-4
19.6	37.059	37.059	58.158	90	90	90	79872	TETR	P4/M
19.6	37.059	37.059	58.158	90	90	90	79872	TETR	P422
19.6	37.059	37.059	58.158	90	90	90	79872	TETR	P4MM
19.6	37.059	37.059	58.158	90	90	90	79872	TETR	P-42M
19.6	37.059	37.059	58.158	90	90	90	79872	TETR	P-4M2
19.6	37.059	37.059	58.158	90	90	90	79872	TETR	P-42M
19.6	37.059	37.059	58.158	90	90	90	79872	TETR	P4/MMM

Table 4.5.4. Indexing of X-ray scattering peaks from a ~86.6 wt% cardiolipin-water mixture in the 5th hour of incubation at 40 °C. See also Figure 4.5.5. d_{obs} and d_{calc} are the observed and calculated peak positions, respectively.

Index	d_{obs}	d_{calc}
001	58.80	58.14
010	37.29	37.04
002	29.06	29.06
110	26.24	26.19
103	17.16	17.17
030	12.34	12.35

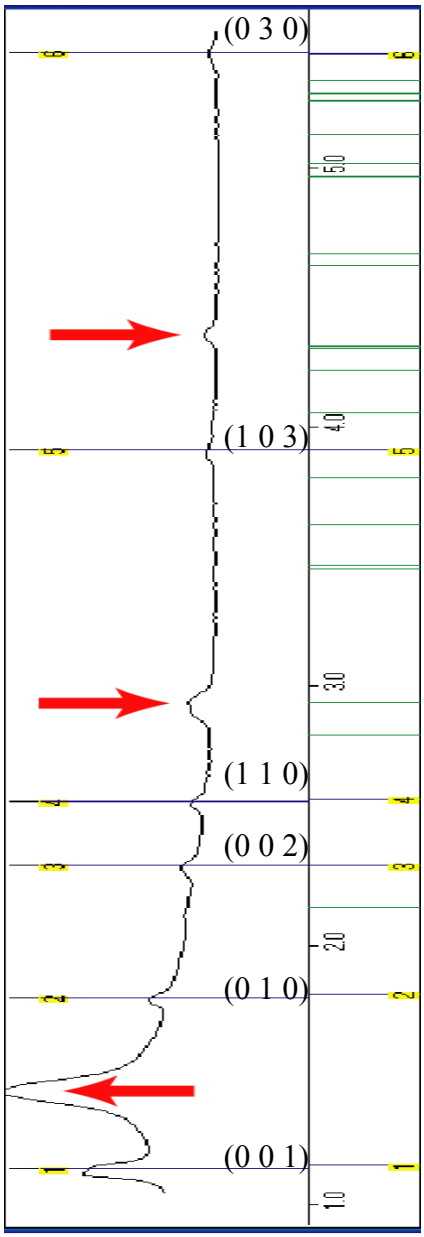

Figure 4.5.5. X-ray scattering profile of a ~86.6 wt% cardiolipin-water mixture in the 5th hour of its incubation at 40 °C, along with the calculated scattering peak positions based on the tetragonal symmetry with the space group of *P4*. Blue lines on the left and right panels indicate positions of the observed and calculated reflections respectively while green lines designate the calculated reflections that were experimentally undetectable. Arrows mark the reflections from the coexisting L_α phase. Miller index of each reflection is also shown. See also table 4.5.3.

4.6 Effects of Alkane Presence on the Cardiolipin Phase Behavior

Given the unique quadruple-hydrocarbon chain configuration of cardiolipin, a natural question raised is whether the extra hydrocarbon chains have any effect on the hydrocarbon chain packing frustration energy (see Section 2.2.3). To find out the answer, we followed the experimental method described in Kirk and Gruner (1985) and studied how releasing the packing constraint by adding alkane affected phase behavior of the cardiolipin-water mixtures. This experiment may also shed light on how the packing energy and electrostatic interactions among the charged headgroups interact with each other to determine the spatial arrangements of cardiolipin liquid crystals.

In this experiment, dodecane in 5-10 wt% of the total organic contents was mixed with cardiolipin-water mixtures. The presence of dodecane was found to significantly change phase behavior of the cardiolipin-mixtures when compared to those without dodecane. In the cardiolipin concentration of ~79 wt%, the $L_\alpha \leftrightarrow L_\alpha + H_{II}$ phase transition temperature was dramatically reduced from the previous value of 40 °C down to 5 °C in the presence of dodecane (Figure 4.6.1a). In the case of ~70 wt% cardiolipin-water mixtures, adding alkane even resulted in formation of the $L_\alpha + H_{II}$ coexistence phase, which was otherwise unobservable within the temperature range studied here (Figure 4.6.1b). Meanwhile, the lower cardiolipin concentration boundary of the $L_\alpha + H_{II}$ phase coexistence region was extended at least to ~49.8 wt% by adding dodecane, from the initial ~72.9 wt% when dodecane were not present (Figure 4.6.2). Except for favoring formation of the H_{II} phase, addition of dodecane exerted no detectable effects on phase behavior of the cardiolipin-water mixtures, at least in the two concentrations, ~79 wt% and ~70 wt%, shown above. Both phase boundaries and

unit cell dimensions of each self-assembled structure were unchanged, including those for the lamellar-lamellar phase separation and L_α-gel coexistence regions. The former may indicate that the phase separation is unrelated to hydrocarbon chain packing strain and is solely the consequence of electrostatic interactions, consistent with the conclusion drawn in Jho et. al. (2010).

Even with dodecane, the H_{II} phase still never appeared alone. Therefore, although relaxing hydrocarbon chain packing strain did energetically favor the H_{II} phase, electrostatic interactions among the headgroups might remain dominating and forced cardiolipin to adopt bilayer structures. A deeper discussion regarding interactions among elastic energies, hydrocarbon chain packing strain and electrostatic forces will be presented in Chapter 5 to understand the $L_\alpha \leftrightarrow L_\alpha + H_{II}$ phase in an energetic view.

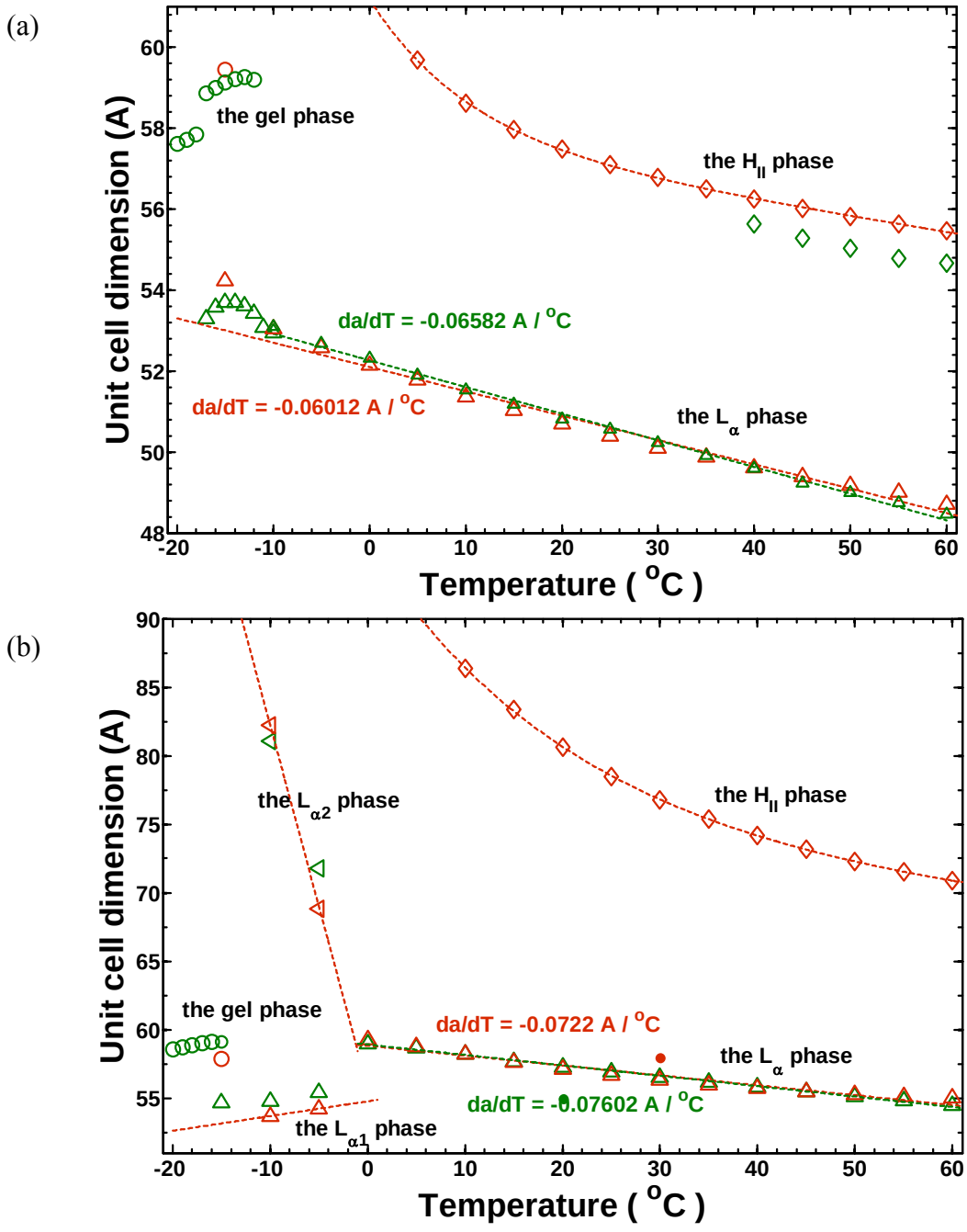

Figure 4.6.1. Unit cell dimension as a function of temperature for ~79 wt% (a) and ~70 wt% (b) cardiolipin-water mixtures with (red color symbols) and without (green color symbols) addition of dodecane. Diamonds are the H_{II} phase; Upward triangles are the L_{α} phase; circles are the gel phase.

Figure 4.6.2. Azimuthally integrated scattering profiles and X-ray scattering images (inset) of ~49 wt% cardiolipin-water mixtures without (a) and with (b) presence of dodecane. Black and red lines denote the reflections from the L_α and H_{II} phases, respectively. Even at 60 °C, the sample without dodecane was still unable to assume the H_{II} phase while 20 °C was sufficient for the sample with dodecane to form the H_{II} phase.

(a)

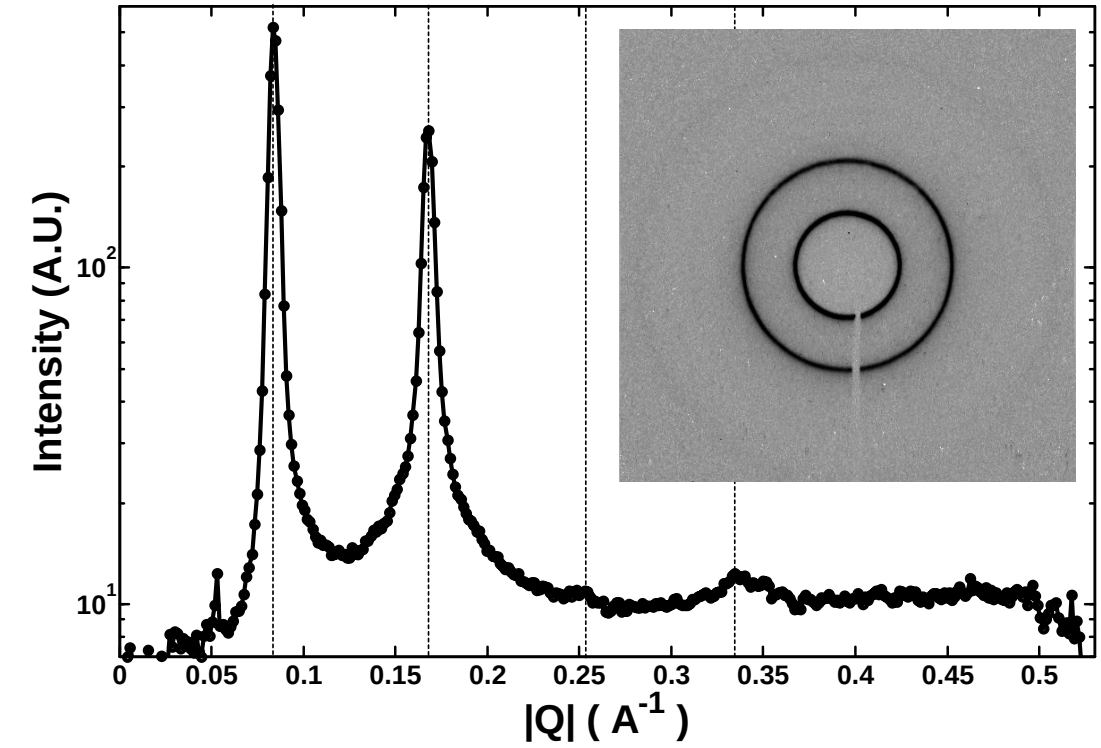
Intensity (A.U.)
10^2
10^1
0
0.05
0.1
0.15
0.2
0.25
0.3
0.35
0.4
0.45
0.5
|Q| (A^-1)

(b)

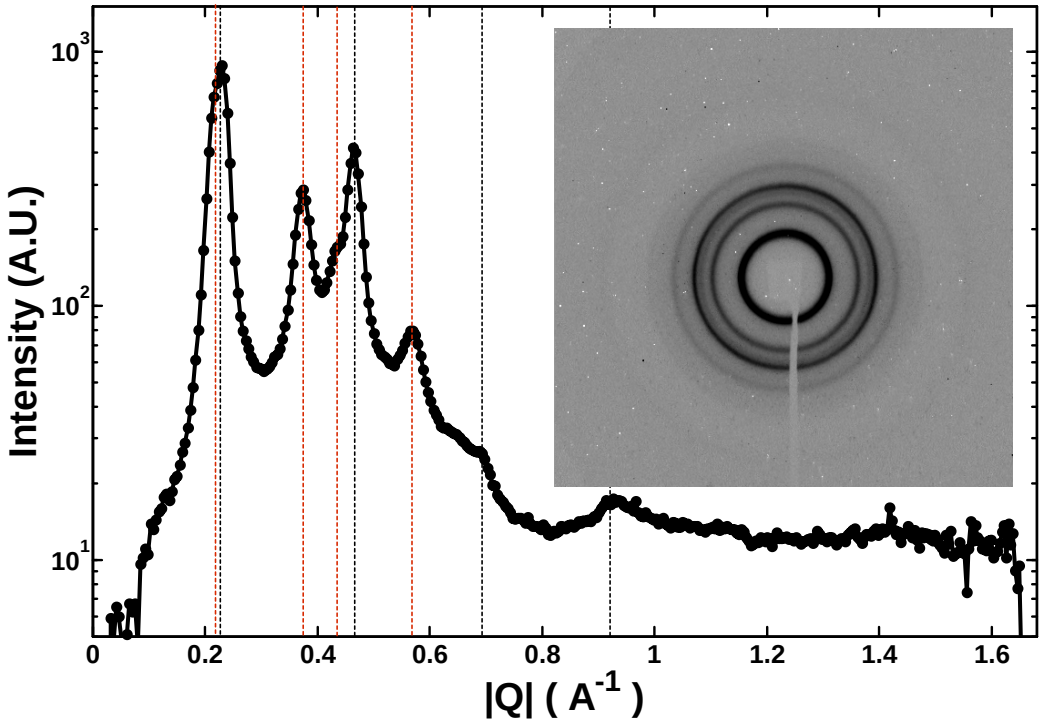
Intensity (A.U.)
10^3
10^2
10^1
0
0.2
0.4
0.6
0.8
1
1.2
1.4
1.6
|Q| (A^-1)

4.7 Summary

In this chapter, we saw cardiolipin phase behavior mapped out in temperatures from -20 °C to 60 °C and in lipid concentrations from 32.9 wt% to 85.4 wt%. We then tried to understand the phase behavior in terms of spatial arrangements of the phases. To carry out the structural study, the line-shape fitting method was employed to reconstruct electron density maps from the X-ray scattering data that would otherwise generate no structural information except the repeat distances. This reconstruction method attempted to utilize every bit of information contained in the X-ray scattering data, including shapes, positions and amplitudes of Bragg peaks and diffuse scattering. Electron density map reconstruction was also carried out with the conventional peak integration method for the few suitable data to validate the structural information obtained with the line-shape fitting method. The structural parameters obtained with the two methods matched well, confirming applicability of the line-shape fitting method.

From the structural information obtained with electron density map reconstruction, both bilayer thickness and bilayer separation were seen to decrease with increasing temperature. The former was attributed to stronger thermal motions of hydrocarbon chains at higher temperatures while the latter was explained as the result of an ever expanding headgroup surface area. Remarkably, the bilayer separation was observed to shrink faster than neutral lipids. This was speculatively attributed to the unique quadruple-hydrocarbon configuration and headgroup charges of cardiolipin. In the context of concentration variation, decrease in the bilayer separation was the main factor contributing to the decrease in d-spacing when sample concentration increased. Thickness of the water layer was even down to negative values when specific lipid

concentration and temperature were reached. Combining the observations in temperature and concentration variations, it was speculated that direct contacts of the charged headgroups, accompanying zero or negative bilayer separation, were energetically costly and led to collapse of the L_α phase in the high temperature and concentration limit. Moreover, electron density profile reconstruction carried out for the gel phase confirmed the excess water condition of the structure, even with repulsive electrostatic interactions present. Hydration "attraction" was invoked to explain the contradictory observation even though the hypothesis itself is controversial.

Electron density profiles were also reconstructed with the peak integration method for the two coexisting phases in the lamellar-lamellar phase separation region. Efforts were used to assure that reconstruction with three scattering peaks, falling short of four peaks minimally required for decent accuracy, still produce structural information with decent precision. The structural parameters showed that the two lamellar phases were in very different hydration levels. The strong-coupling approach was suggested to qualitatively explain the phenomenon. In studying another peculiar feature of the cardiolipin phase behavior, we indexed scattering peaks from the tiny crystal cluster-like phase and were led to a tetragonal unit cell with the space group of *P4*. Cardiolipin molecules were speculated to arrange in inverted micellar structures with 3-D periodicity. However, our data could not confirm the speculation with confidence. Finally, cardiolipin-dodecane-water mixtures in various cardiolipin concentrations were studied to elucidate the influence of hydrocarbon chain packing strain on a lipid with a quadruple-chain configuration. We saw formation of the H_{II} phase in an otherwise pure L_α phase region, indicating the importance of chain packing strain even

in the presence of surface charges. Implication of these experimental results will be further discussed in an energetic view in the next chapter.

CHAPTER 5

DISCUSSIONS AND CONCLUDING REMARKS

5.1 Energetics Overview

5.1.1 Structure Map

Presumably due to charged headgroups, the L_α phase is the dominant spatial configuration in cardiolipin-water mixtures when counterions and alkane are absent (Figure 4.2.1). However, in the temperature (-20 °C to 60 °C) and concentration (32.9 wt% to 85.4 wt%) ranges studied here five major phase transitions were still observed for the L_α phase: (1) $L_\alpha \leftrightarrow$ gel+water; (2) $L_\alpha \leftrightarrow L_{\alpha 1} + L_{\alpha 2}$; (3) $L_\alpha \leftrightarrow L_\alpha + H_{II}$; (4) $L_\alpha \leftrightarrow L_\alpha$+gel; (5) $L_\alpha \leftrightarrow L_\alpha$+TC. In concluding this thesis study, we will plot a "structure map" underlying these phase transitions in an effort to deduce an energetic overview to the cardiolipin phase behavior.

In Sections 4.3 and 4.4, we reconstructed electron density profiles for cardiolipin-water mixtures to extract the structural parameters. By examining the structural data presented in those two sections, one may uncover some relationships existing between the phase transitions (2)-(5) and the inter-bilayer distance d_S (following the definition in Equations 4-2 and 4-3). These relationships may be illustrated and summarized with a "structure map" as shown in Figure 5.1.1. In this structure map, phase boundaries of the transitions (2)-(5) are mapped based on temperatures and inter-bilayer distances of the L_α structures along the phase boundaries in the temperature-composition phase diagram of Figure 4.2.1. These inter-bilayer distances represent the extreme values for stable L_α configurations at different temperatures. Exceeding a certain inter-bilayer distance at a specific temperature may destabilize the L_α phase. For example, at 60 °C cardiolipin molecules can stay in an L_α structure as long as the inter-bilayer distance is

Figure 5.1.1. Structure map of cardiolipin-water mixtures. The map corresponds to the temperature-composition phase diagram shown in Figure 4.2.1 and was mapped based on sample temperatures and inter-bilayer distances of the L_α phase along phase boundaries of the phase diagram. The abscissa is the inter-bilayer distance of the "pure" L_α phase and does not necessarily reflect the distance for a coexisting lamellar structure. Circles are the L_α phase along the $L_\alpha \leftrightarrow L_\alpha + H_{II}$ phase boundary; a diamond represents the $L_\alpha \leftrightarrow L_\alpha$+TC boundary; squares are along the lamellar-lamellar phase separation boundary; triangles are along the $L_\alpha \leftrightarrow L_\alpha$+Gel phase boundary. Stars denote inter-bilayer distances of a 32.9 wt% cardiolipin-water mixture at different temperatures and imply a possible path for a temperature variation in a constant sample concentration (see the text for details). Phase boundaries backed by data are approximated with black solid lines. The speculated boundaries are denoted with dashed lines. Dashed lines with open ends reflect uncertainty regarding the boundary. A blue dashed line near the $L_\alpha \leftrightarrow L_\alpha + H_{II}$ phase boundary is a speculation for the effect of adding alkane. Note the inter-bilayer distance is higher to lower from left to right.

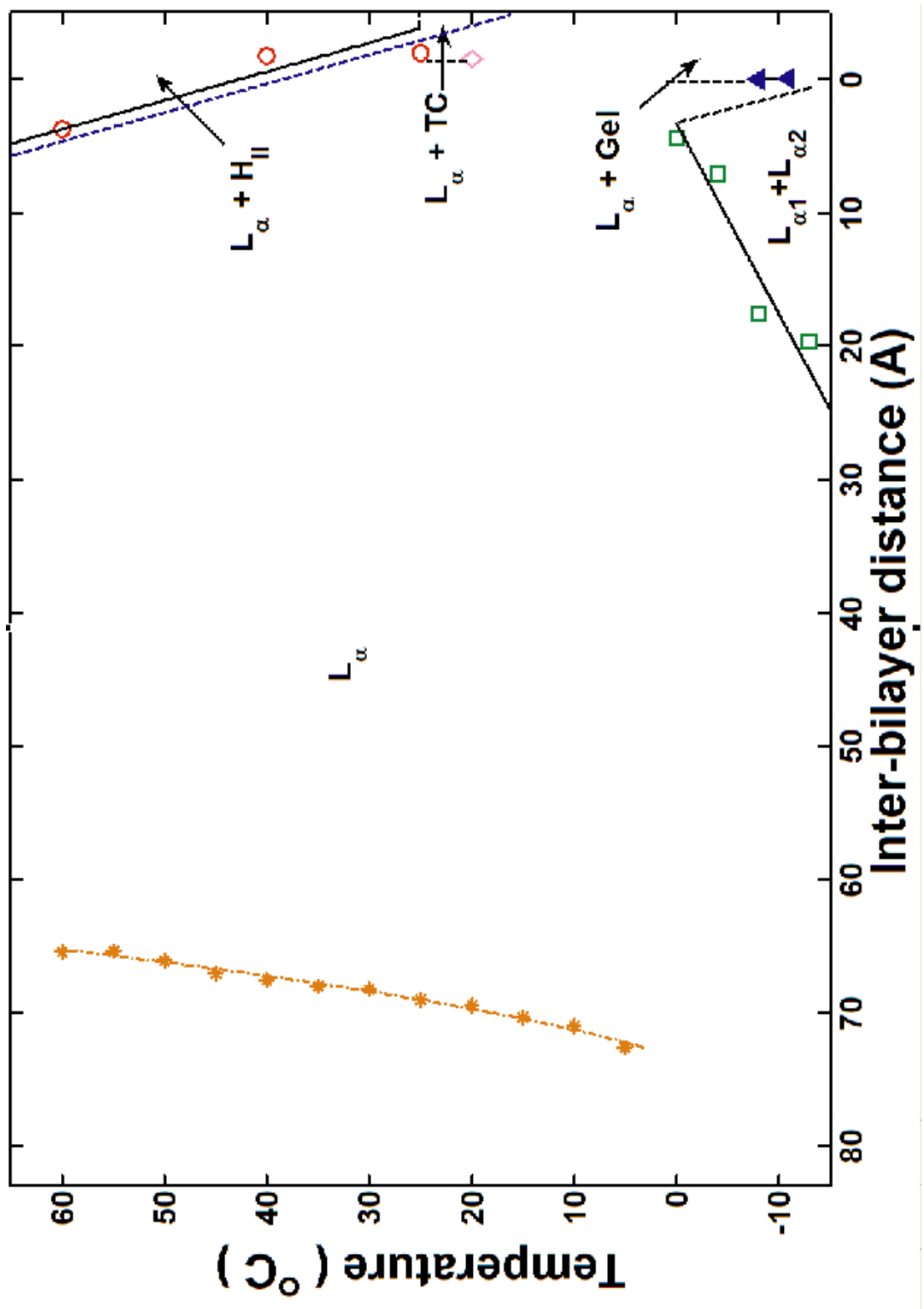
Temperature (°C)
Inter-bilayer distance (A)
L$_\alpha$
L$_\alpha$ + H$_{II}$
L$_\alpha$ + TC
L$_\alpha$ + Gel
L$_{\alpha1}$+L$_{\alpha2}$

>3.8 Å. Shortening the inter-bilayer distance by, say, removing the inter-bilayer water to below 3.8 Å would lead to the $L_\alpha \leftrightarrow L_\alpha + H_{II}$ phase transition. It is interesting to notice that all the phase transitions from the L_α phase are associated with shrinking inter-bilayer distances, even when those transitions involved no non-lamellar phase. The $L_\alpha \leftrightarrow$ gel+water transition was excluded because the main transition was more related with the bilayer thickness and more or less independent of the bilayer separation. One may find close similarity when comparing the structure map and the phase diagram. However, it should be noted that both temperature and sample concentration are factors dictating the inter-bilayer distance. The structure map is not a direct conversion of the phase diagram. An isothermal concentration variation in a phase diagram follows a straight horizontal path in the structure map while a temperature variation in a constant concentration should contour a curved path as illustrated in Figure 5.1.1 by orange star marks. It should also be noted that abscissa is the inter-bilayer distance of a "pure" L_α structure, i.e. without coexisting with another phase. When across the boundaries to the coexistence regions, values in the abscissa may not necessarily represent the inter-bilayer distances of lamellar structures. Moreover, readers are cautioned that the map is a simplification of complicated mechanisms underlying phase transitions (e.g. temperature and concentration also affect the bilayer thickness as shown in Figures 4.3.6 and 4.3.10, and consequently the phase behavior as discussed in Section 4.3.1). It serves the purpose of facilitating the following discussion, which itself is also a simplified picture.

5.1.2 $L_\alpha \leftrightarrow L_\alpha + H_{II}$ Phase Transition

As mentioned in Section 4.3, decrease in the inter-bilayer distance of the L_α phase to a near or even negative value by increasing sample concentration appears to coincide with onset of the $L_\alpha \leftrightarrow L_\alpha + H_{II}$ transition. Based on Figure 5.1.1, we may be able to explain this observation in terms of forces and interactions among lipid aggregates. Following the discussion in Section 2.3.1, forces and interactions determining phase preference in our cardiolipin system may include hydrocarbon chain packing stress, bilayer thermal undulation, inter-bilayer hydration interactions, the monolayer elastic energy, and electrostatic interactions, the last of which may be further divided into inter-bilayer repulsion and lateral repulsion within a bilayer as discussed in Section 2.2.5. Hydration interactions will not be considered here because, as discussed in Section 2.3.1, it is less significant to a lamellar-non-lamellar phase transition and may be implicitly included in the elastic energy consideration. Moreover, the discussion in Section 2.2.6 has indicated that thermal undulation is negligible unless charges on the cardiolipin headgroups are neutralized, such as by adding counterions, to result in a monolayer bending modulus of $\sim 1 k_B T$. Therefore, we will only consider the remaining three interactions in the case of the $L_\alpha \leftrightarrow L_\alpha + H_{II}$ transition.

As the inter-bilayer distance shrinks, many factors may favor formation of the H_{II} phase. Here, the most obvious one is the electrostatic inter-bilayer repulsion, arising from two approaching similarly charged surfaces. According to the double-layer theory (the first term of Equation 2-12), this repulsive force intensifies exponentially with shrinking distance between the two surfaces. It therefore is expected to be the principal driving force in destabilizing the lamellar structure. Other contributions include higher monolayer spontaneous curvatures due to diminishing headgroup

surface areas and weaker hydrocarbon chain packing stress in lower water contents (Section 4.2). On the other hand, the elastic energy/electrostatic lateral repulsion and hydrocarbon chain packing stress are interactions driving cardiolipin molecules back to the lamellar structure. Here, the elastic energy and electrostatic lateral repulsion are treated as a single factor because the former is expected to reflect effect of the latter (Section 2.2.5). Although cardiolipin molecules prefer to occupy a wedge-shaped time-averaged volume, i.e., a strong negative spontaneous curvature (see Section 2.2.4 for a discussion in the spontaneous curvature), electrostatic lateral repulsion forces the molecules to adopt a more cylindrical-like time-averaged shape as a lamellar structure. Moreover, lower water contents also lead to higher elastic energy costs for forming the H_{II} phase. This is because the monolayer curvatures ($C = 1/2R$, where R is the water core radius of a H_{II} structure) in Equation 2-14 are further away from the zero value of the spontaneous curvature, even though hydrocarbon chain packing stress decreases with reducing water core radius. Taken together, this provides a perspective on the lamellar-non-lamellar phase transition for our system, in which two types of electrostatic interactions compete with each other to determine phase preference, supplemented with effects arising from variation in hydrocarbon chain packing stress and also from some thermal-related factors when temperature is a variable.

We now turn to explaining the $L_\alpha \leftrightarrow L_\alpha + H_{II}$ transition based on Figure 5.1.1. According to Figure 5.1.1, the energy penalty associated with electrostatic inter-bilayer repulsion accumulated as the bilayer separation of cardiolipin-water mixtures shrank at a given temperature. Nevertheless, this repulsive force was still insufficient to overcome the elastic energy barrier arising from the electrostatic lateral repulsion until a certain inter-bilayer distance was reached when it was too costly to stay in the L_α phase. This threshold bilayer separation was larger at higher temperatures where

contributions from some thermal-related factors (e.g. stronger thermal motions of hydrocarbon chains lead to more wedged shapes) were significant enough to affect the overall free energy and reduced the required electrostatic inter-bilayer repulsion to compete with its lateral counterpart. Also, strength of electrostatic inter-bilayer repulsion is itself proportional to temperature (see the electrostatic double layer theory, first term of Equation 2-12). This might also contribute to decrease of the threshold with increasing temperature. Generally, the threshold bilayer separation was 0.15±2.52 Å. Any L_α structure exceeding that threshold would collapse when temperature is high enough (>20 °C according to the data presented in Chapter 4). Hydrocarbon chain packing stress was also important in this context. As shown in Section 4.6, relaxing the packing stress within cardiolipin aggregates depressed the $L_\alpha \leftrightarrow L_\alpha + H_{II}$ transition temperature considerably. In terms of the structure map, adding alkane to relax the packing strain is equivalent of shifting the $L_\alpha \leftrightarrow L_\alpha + H_{II}$ boundary of the map toward longer inter-bilayer distance or lower temperatures or both (blue dashed line in Figure 5.1.1). Nevertheless, relaxing the packing strain was still unable to generate the "pure" H_{II} phase. This suggests the supreme dominance of the electrostatic lateral repulsion in cardiolipin phase preference. Also, because the H_{II} phase is generally less hydrated than the L_α phase (Section 1.3.2; Gawrisch et. al., 1992; Gruner, 1985), the extra water dispelled during the H_{II} structures formation might be adsorbed by the coexisting L_α phase, slightly expand the inter-bilayer distance, and stabilize the L_α structures.

5.1.3 Lamellar-lamellar Phase Separation and $L_\alpha \leftrightarrow L_\alpha$+Gel Phase Transition

At the end of Section 4.4, we introduced the strong-coupling theory to explain the lamellar-lamellar phase separation phenomenon. This approach can also be described in the context of the structure map. It may work as follows: From Figures 4.2.3 and 4.4.7, it is observed that d-spacing of the $L_{\alpha 1}$ phase expanded when more $L_{\alpha 2}$ structures were formed. Moreover, even though electron density profiles in the phase separation region were reconstructed with the peak integration method (Section 4.4) and the extracted bilayer separations were based on the Luzzati definition (see Section 4.3.2), we could still obtain the bilayer separations defined with Equations 4-2 and 4-3 when considering the fact that the parameter differentiating the two definitions, σ_H, was centered at 3 Å with very small variations (Tables 4.3.3 and 4.3.5). Accordingly, we converted bilayer separation of the $L_{\alpha 2}$ phase from ~12.95 Å defined by Luzzati to ~0.95 Å defined with Equations 4-2 and 4-3, and this value was expected to vary only slightly with temperature and sample concentration based on the observations for d-spacings in Figures 4.3.1 and 4.4.5 (Figure 5.1.1 was also plotted based on this value). In other words, vast majority of the water content in the $L_{\alpha 2}$ phase was squeezed out of the inter-bilayer space during formation of the phase, regardless of temperature and sample concentration. All these observations indicate that the $L_{\alpha 1}$ phase adsorbed any extra water from the condensed $L_{\alpha 2}$ phase as would have been done by the regular L_α phase.

Back to the context of the structure map, as the inter-bilayer distance of the regular L_α phase reached a threshold value at a given low temperature, the system was unable to reduce the energy penalty by forming the H_{II} structures at low temperatures and therefore could manage to maintain the lamellar structures by resorting to the strong-

coupling interaction. This interaction stabilized the condensed $L_{\alpha 2}$ structures while simultaneously releasing the extra water to the $L_{\alpha 1}$ structures, expanding the inter-bilayer separation and consequently reducing the intensifying electrostatic inter-bilayer repulsion of the $L_{\alpha 1}$ structures as well as total free energy of the entire system. Contrary to the $L_\alpha \leftrightarrow L_\alpha + H_{II}$ transition, the inter-bilayer distance threshold for the lamellar-lamellar phase separation decreased with increasing temperature. According to Equation 4-16, the coupling parameter Ξ decreases its value quadratically with elevating temperature. Based on the correlation between the parameter and energy contribution of the strong-coupling interaction (Boroudjerdi et. al., 2005), the attraction stabilizing the $L_{\alpha 2}$ diminished at higher temperatures and therefore could be a feasible way to relax the energy penalty only when the electrostatic inter-bilayer repulsion became even stronger. All the threshold inter-bilayer distances for the phase separation at different temperatures were found to be longer than those for the $L_\alpha \leftrightarrow L_\alpha + H_{II}$ transition. This does not mean the cardiolipin lamellar structures were more intolerable to comparable electrostatic inter-bilayer repulsion at lower temperatures but only reflects that the strong-coupling interaction was capable of offering a structural configuration with a lower overall free energy than maintaining the status quo.

As the bilayer separation of the L_α phase kept shrinking, formation of the $L_{\alpha 2}$ phase could not reduce the overall free energy because there was no extra water to be squeezed out when the inter-bilayer water was drained. Without any other lower energy configuration accessible, the L_α phase could only stay in the same structure until another threshold inter-bilayer distance was reached. The strong-coupling might play a role in this case as well but instead of assisting phase separation, it might have facilitated formation of the gel phase and led to the L_α+gel coexistence phase. As

shown in Figure 4.3.11, the gel phase formed by our cardiolipin systems were in the excess water condition with an essentially zero inter-bilayer distance. Again, the strong-coupling interaction was presumed to stabilize this gel structure and, when in the L_α+gel coexistence phase, the released excess water from the gel phase was absorbed by the coexisting L_α phase to reduce the energy penalty arising from electrostatic inter-bilayer repulsion. The latter speculation is supported by an observation in which d-spacings of the L_α phase expanded more rapidly with depressing temperature in the L_α+gel coexistence region than in the pure L_α+gel region, as more gel structures were formed at lower temperatures (e.g. Figure 5.1.2). This phenomenon is similar to the relationship between the $L_{\alpha 1}$ and $L_{\alpha 2}$ phase. The threshold bilayer separation for the $L_\alpha \leftrightarrow L_\alpha$+gel transition was virtually independent of temperature and centered ~0. It appears that the L_α phase would transform to the L_α+gel phase when the inter-bilayer distance reaches zero as long as thermal motions of the hydrocarbon chains are dampened. It should be noted that the strong-coupling interaction could be swapped with the hydration "attraction" discussed in the end of Section 4.3.3 without affecting other arguments. However, readers should be reminded that the hydration attraction theory is still controversial.

5.1.4 $L_\alpha \leftrightarrow L_\alpha$+TC Phase Transition

One of the most peculiar experimental observations in this thesis study is formation of the "tiny crystals cluster-like" (TC) phase. We speculated that the cardiolipin molecules were arranged in an inverted micellar configuration in this phase (Section 4.5). In the context of the structure map, the L_α phase transformed to the L_α+TC coexistence phase when the inter-bilayer distance was sufficiently short but temperature was not high enough to induce formation of the H_{II} phase and also not low

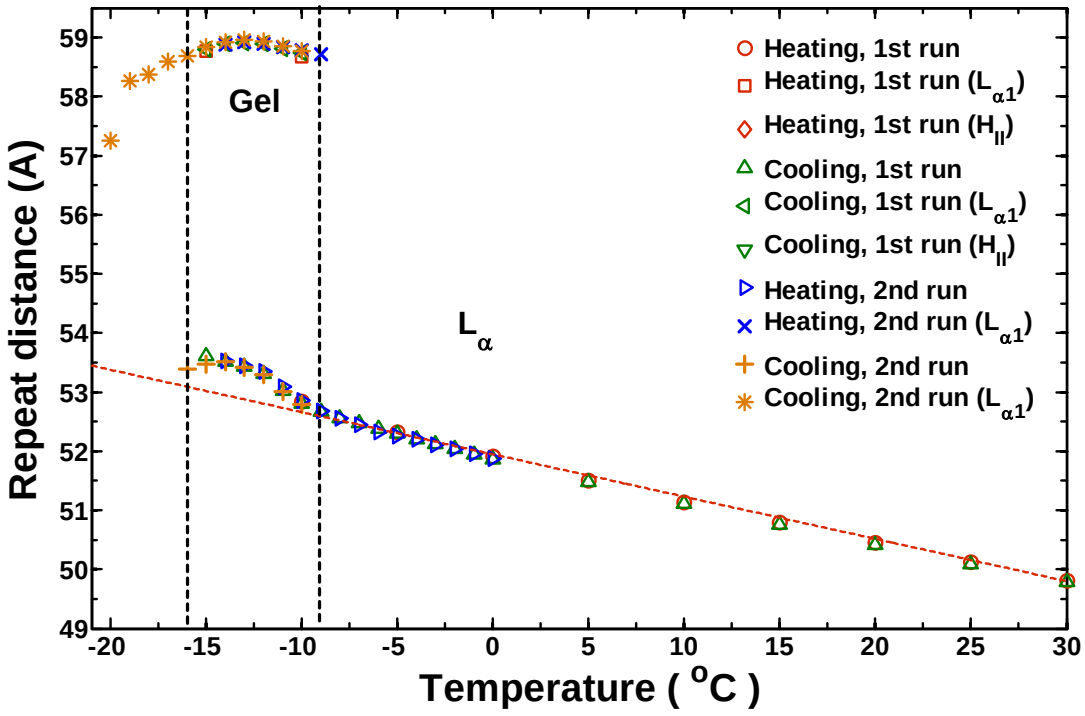

Figure 5.1.2. Repeat distances of lamellar phases as a function of temperature for an 80.6 wt% cardiolipin-water mixture. Between two vertical dashed lines is the L_α+gel coexistence region. A red dashed line is a linear fit to the L_α structures at temperatures >-9 °C, i.e. out of the coexistence region, and highlights the more rapid variation of d-spacing in the coexistence region.

enough to facilitate the lipid main transition. As a result, the system resorted to forming the TC phase to reduce the energy penalty. This might also be associated with the intermediate spontaneous curvature (relative to the charged phospholipids, DOPS and DOPA) expressed by cardiolipin, which was collectively contributed by its doubly charged headgroups and quadruple hydrocarbon chain configuration (see Section 4.2 for the phase diagram comparison). However, due to lack of more detailed structural information, we are unable to have a deeper discussion and can only speculate that the phase was an intermediate state between the H_{II} and L_α structure.

5.2 Conclusions and Future Work

The structure map of Figure 5.1.1 is motivated by reducing the mechanisms behind the observed cardiolipin phase behavior to four interactions, namely two competing electrostatic interactions, hydrocarbon chain packing stress and the strong-coupling interaction. From this approach, we notice the importance of the headgroup charges in cardiolipin phase preference. Neutralizing the surface charges by adding counterions can change cardiolipin phase behavior dramatically (Rand and Sengupta, 1972; Vasilenko et. al., 1982; Loosley-Millman et. al., 1982; Seddon et. al., 1983). From our discussion above, we may argue that the counterion-induced H_{II} structure formation is mainly carried out by decreasing electrostatic lateral repulsion while the simultaneous reduction in electrostatic inter-bilayer repulsion is counteractive to the phase transition. Similar arguments are applicable to explaining disappearance, if any, of the lamellar-lamellar phase separation and $L_\alpha \leftrightarrow L_\alpha$+gel transition in, say, cardiolipin-$CaCl_2$ mixtures. Moreover, the benefit of adopting the structure map approach is that it simplifies and generalizes the underlying mechanism of cardiolipin phase behavior. In addition to sample concentration, other experimental variables that may change the inter-bilayer distance or electrostatic inter-bilayer repulsion of the L_α structure, such as hydrostatic pressure, osmotic pressure, or counterions, might be interpreted in the context of the structure map for their effects on cardiolipin phase preference. In other words, the structure map may be a generalized type of phase diagram.

Many experimental studies can be developed based on the foundation laid with this thesis study. To strengthen the structure map perspective proposed here, corresponding experiments on cardiolipin with different chain lengths are suggested and much more extensive WAXS data is also required. Studies on cardiolipin in the

presence of various counterions or under high pressure will also be needed to further generalize this structure map approach. Another study that can be carried out is to develop the semi-quantitative approach of the structure map further into a quantitative one. This may be carried out by experimentally relating the inter-bilayer distance to the inter-bilayer electrical potential with the widely used osmotic method (e.g. Cowley et. al., 1978) and measuring the elastic energy at different temperatures (e.g. Gruner et. al., 1986). In so doing, this structure map may be transformed to an "energy map", which is more independent of sample identity or experimental approaches. Measurement of the theoretic strong-coupling interaction may also be done by correlating the inter-bilayer electrical potential with that interaction. In addition, the TC phase observed here may deserve more experimental attention to completely decipher the nature and origin of the phase.

REFERENCES

Alley, S. H.; Ces, O.; Barahona, M.; Templer, R. H. 2008. "X-ray diffraction measurement of the monolayer spontaneous curvature of dioleoylphosphatidylglycerol." Chemistry and Physics of Lipids, Volume 154, p64-67.

Als-Nielsen, J.; McMorrow, D. 2001. “Elements of Modern X-Ray Physics.” John Wiley and Sons Ltd, Chichester.

Andersen, O. S.; Koeppe, R. E. II. 2007. "Bilayer Thickness and Membrane Protein Function: An Energetic Perspective." Annual Review of Biophysics and Biomolecular Structure, Volume 36, p107-130.

Anderson, T. H.; Donaldson, S. H.; Zeng, H.; Israelachvili, J. N. 2010. "Direct Measurement of Double-Layer, van der Waals, and Polymer Depletion Attraction Forces between Supported Cationic Bilayers." Langmuir, Volume 26, p14458-14465.

Andersson, S.; Hyde, S. T.; Larsson, K.; Sven, L. 1988. “Minimal Surfaces and Structures: From Inorganic and Metal Crystals to Cell Membranes and Biopolymers.” Chemical Reviews, Volume 88, p221-242.

Attard, G. S.; Templer, R. H.; Smith, W. S.; Hunt, A. N.; Jackowski, S. 2000. "Modulation of CTP:phosphocholine cytidylyltransferase by membrane curvature elastic stress." Proceedings of the National Academy of Sciences, Volume 97, p9032-9036.

Barna, S. L.; Tate, M. W.; Gruner, S. M.; Eikenberry, E. F. 1999. "Calibration procedures for charge-coupled device x-ray detectors." Review of Scientific Instruments, Volume 70, p2927-2934.

Bartlett, D. H. 2002. "Pressure effects on in vivo microbial processes." Biochimica et Biophysica Acta, Volume 1595, p367-381.

Baumgart, T.; Hess, S. T.; Webb, W. W. 2003. "Imaging coexisting fluid domains in biomembrane models coupling curvature and line tension." Nature, Volume 425, p821-824.

Blanton, T. N.; Huang, T. C.; Toraya, H.; Hubbard, C. R.; Robie, S. B.; Louër, D.; Göbel, H. E.; Will, G.; Gilles, R.; Raftery, T. 1995. "JCPDS-International Center for Diffraction Data round robin study of silver behenate. A possible low-angle X-ray diffraction calibration standard." Powder Diffraction, Volume 10, p91-95.

Blow, D. 2002. "Outline of Crystallography for Biologists." Oxford University Press, New York.

Bogdanov, M.; Dowhan, W. 1998. "Phospholipid-assisted protein folding: phosphatidylethanolamine is required at a late step of the conformational maturation of the polytopic membrane protein lactose permease." The EMBO Journal, Volume 17, p5255-5264.

Boroudierdi, H.; Kim, Y.-W.; Naji, A.; Netz, R. R.; Schlagberger, X.; Serr, A. 2005. "Statics and dynamics of strongly charged soft matter." Physics Reports, Volume 416, p129-199.

Boultif, A.; Louër, D. 1991. "Indexing of powder diffraction patterns for low-symmetry lattices by the successive dichotomy method." Journal of Applied Crystallography, Volume 24, p987-993.

Brito, R. O.; Marques, E. F.; Gomes, P.; Araujo, M. J.; Pons, R. 2008. "Structure/Property Relationships for the Thermotropic Behavior of Lysine-Based Amphiphiles: from Hexagonal to Smectic Phases." Journal of Physical Chemistry B, Volume 112, p14877-14887.

Caffrey, M. 2008. "Crystallizing Membrane Proteins for Structure Determination: Use of Lipidic Mesophases." Annual Review of Biophysics, Volume 38, p29-51.

Chavarha, M.; Khoojinian, H.; Schulwitz, L. E. Jr.; Biswas, S. C.; Rananavare, S. B.; Hall, S. B. 2010. "Hydrophobic Surfactant Proteins Induce a Phosphatidylethanolamine to Form Cubic Phases." Biophysical Journal, Volume 98, p1549-1557.

Chen, C. S.; Mrksich, M.; Huang, S.; Whitesides, G. M.; Ingber, D. E. 1997. "Geometric Control of Cell Life and Death." Science. Volume 276, p1425-1428.

Claypool, S. M. 2009. "Cardiolipin, a critical determinant of mitochondrial carrier protein assembly and function." Biochimica et Biophysica Acta, Volume 1788, p2059-2068.

Collings, P. J. 2002. "LIQUID CRYSTALS. NATURE'S DELICATE PHASE OF MATTER." 2nd edition, Princeton University Press, Princeton.

Cowley, A. C.; Fuller, N. L.; Rand, R. P.; Parsegian, V. A. 1978. "Measurement of Repulsive Forces between Charged Phospholipid Bilayers." Biochemistry, Volume 17, p3163-3168.

Dabora, S. L.; Sheetz, M. P. 1988. "The Microtubule-Dependent Formation of a Tubulovesicular Network with Characteristics of the ER from Cultured Cell Extracts." Cell, Volume 54, p27-35.

Dahlberg, M.; Maliniak, A. 2010. "Mechanical Properties of Coarse-Grained Bilayers Formed by Cardiolipin and Zwitterionic Lipids." Journal of Chemical Theory and Computation, Volume 6, p1638-1649.

De Kruijff, B.; Cullis, P. R. 1980. "CYTOCHROME c SPECIFICALLY INDUCES NON-BILAYER STRUCTURES IN CARDIOLIPIN-CONTAINING MODEL MEMBRANES." Biochimica et Biophysica Acta, Volume 602, p477-490.

Dietrich, C.; Bagatolli, L. A.; Volovyk, Z. N.; Thompson, N. L.; Levi, M.; Jacobson, K.; Gratton, E. 2001. "Lipid Rafts Reconstituted in Model Membranes." Biophysical Journal, Volume 80, p1417-1428.

Drenth, J. 2007. “Principles of Protein X-ray Crystallography.” Springer-Verlag New York, Inc., New York.

Dubois, M.; Zemb, T.; Fuller, N.; Rand, R. P.; Parsegian, V. A. 1998. "Equation of state of a charged bilayer system: Measure of the entropy of the lamellar-lamellar transition in DDABr." Journal of Chemical Physics, Volume 108, p7855-7869.

Duesing, P. M.; Templer, R. H.; Seddon, J. M. 1997. "Quantifying Packing Frustration Energy in Inverse Lyotropic Mesophases." Langmuir, Volume 13, p351-359.

Dzyaloshinskii, I. E.; Lifshitz, E. M.; Pitaevskii, L. P. 1961. "GENERAL THEORY OF VAN DER WAALS' FORCES." Soviet Physics Uspekhi, Volume 73, p153-176.

Edidin, M. 2003. "Lipids on the frontier: a century of cell-membrane bilayers." Nature Reviews Molecular Cell Biology, Volume 4, p414-418.

Evans, E.; Needham, D. 1987. "Physical Properties of Surfactant Bilayer Membranes: Thermal Transitions, Elasticity, Rigidity, and Colloidal Interactions." Journal of Physical Chemistry, Volume 91, p4219-4228.

Farren, S. B.; Hope, M. J.; Cullis, P. R. 1983. "Polymorphic Phase Preference of Phosphatidic Acid: A ^{31}P and ^{2}H NMR Study." Biochemical and Biophysical Research Communications, Volume 111, p675-682.

Feigenson, G. W. 2009. "Phase diagrams and lipid domains in multicomponent lipid bilayer mixtures." Biochimica et Biophysica Acta, Volume 1788, p47-52.

Figueiredo Neto, A. M.; Salinas, S. R. A. 2005. “The Physics of Lyotropic Liquid Crystals. Phase Transition and Structural Properties.” Oxford University Press Inc., New York.

Ford, M. G. J.; Mills, I. G.; Peter, B. J.; Vallis, Y.; Praefcke, G. J. K.; Evans, P. R.; McMahon, H. T. 2002. "Curvature of clathrin-coated pits driven by epsin." Nature, Volume 419, p361-366.

Fuller, N.; Benatti, C. R.; Rand, R. P. 2003. "Curvature and Bending Constants for Phosphatidylserine-Containing Membranes." Biophysical Journal, Volume 85, p1667-1674.

Gawrisch, K.; Parsegian, V. A.; Hajduk, D. A.; Tate, M. W.; Gruner, S. M.; Fuller, N. L.; Rand, R. P. 1992. "Energetics of a Hexagonal-Lamellar-Hexagonal-Phase Transition Sequence in Dioleoylphosphatidylethanolamine Membranes." Biochemistry, Volume 31, p2856-2864.

Gleeson, J. T.; Shyamsunder, E.; Gruner, S. M. 1994. "Freezing and Melting Water in Lamellar Structures." Biophysical Journal, Volume 67, p706-712.

Gruner, S. M. 1985. “Intrinsic curvature hypothesis for biomembrane lipid composition: A role for nonbilayer lipids.” Proceedings of the National Academy of Sciences, Volume 82, p3665-3669.

Gruner, S. M.; Cullis, P. R.; Hope, M. J.; Tilcock, C. P. S. 1985. “LIPID POLYMORPHISM: The Molecular Basis of Nonbilayer Phases.” Annual Review of Biophysics and Biophysical Chemistry, Volume 14, p211-238.

Gruner, S. M.; Parsegian, V. A.; Rand, R. P. 1986. "Directly Measured Deformation Energy of Phospholipid H_{II} Hexagonal Phases." Faraday Discussions, Volume 81, p29-37.

Gruner, S. M.; Tate, M. W.; Kirk, G. L.; So, P. T. C.; Tuner, D. C.; Keane, D. T.; Tilcock, C. P. S.; Cullis, P. R. 1988. "X-ray Diffraction Study of the Polymorphic Behavior of N-Methylated Dioleoylphosphatidylethanolamine." Biochemistry, Volume 27, p2853-2866.

Gruner, S. M. 1989. "Stability of Lyotropic Phases with Curved Interfaces." Journal of Physical Chemistry, Volume 93, p7562-7570.

Gruner, S. M. 2005. "Nonlamellar Lipid Phases." p173-200 in "The STRUCTURE of BIOLOGICAL MEMBRANES.", Edited by Yeagle, P. L., 2nd edition, CRC Press LLC, Boca Raton.

Guinier, A. 1963. "X-ray Diffraction." Freeman, San Francisco.

Haines, T. H.; Dencher, N. A. 2002. "Cardiolipin: a proton trap for oxidative phosphorylation." FEBS Letters, Volume 528, p35-39.

Haney, E. F.; Nathoo, S.; Vogel, H. J.; Prenner, E. J. 2010. “Induction of non-lamellar lipid phases by antimicrobial peptides: a potential link to mode of action.” Chemistry and Physics of Lipids, Volume 163, p82-93.

Harper, P. E.; Mannock, D. A.; Lewis, R. N. A. H.; McElhaney, R. N.; Gruner, S. M. 2001. "X-ray Diffraction Structures of Some Phosphatidylethanolamine Lamellar and Inverted Hexagonal Phases." Biophysical Journal, Volume 81, p2693-2706.

Hauser, H.; Paltauf, F.; Shipley, G. G. 1982. "Structure and Thermotropic Behavior of Phosphatidylserine Bilayer Membranes." Biochemistry, Volume 21, p1061-1067.

Ihee, H.; Lorenc, M.; Kim, T. K.; Kong, Q. Y.; Cammarata, M.; Lee, J. H.; Bratos, S.; Wulff, M. 2005. "Ultrafast X-ray Diffraction of Transient Molecular Structures in Solution." Science, Volume 309, p1223-1227.

Inoko, Y.; Yamaguchi, T.; Furuya, K.; Mitsui, T. 1975. "EFFECTS OF CATIONS ON DIPALMITOYL PHOSPHATIDYLCHOLINE/CHOLESTEROL/WATER SYSTEMS." Biochimica et Biophysica Acta, Volume 413, p24-32.

Ipsen, J. H.; Karlstrom, G.; Mouritsen, O. G.; Wennerstrom, H.; Zuckermann, M. J. 1987. "Phase equilibria in the phosphatidylcholine-cholesterol system." Biochimica et Biophysica Acta, Volume 905, p162-172.

Israelachvili, J. N.; Pashley, R. M. 1983. "Molecular layering of water at surfaces and origin of repulsive hydration forces." Nature, Volume 306, p249-250.

Israelachvili, J. N. 1992. "INTERMOLECULAR AND SURFACE FORCES." Academic Press, London.

Israelachvili, J.; Wennerstrom, H. 1996. "Role of hydration and water structure in biological and colloidal interactions." Nature, Volume 379, p219-224.

Jacobson, K.; Mouritsen, O. G.; Anderson, R. G. W. 2007. "Lipid rafts: at a crossroad between cell biology and physics." Nature Cell Biology, Volume 9, p7-14.

Jho, Y. S.; Kim, M. W.; Safran, S. A.; Pincus, P. A. 2010. "Lamellar phase coexistence induced by electrostatic interactions." The European Physical Journal E, Volume 31, p207-214.

Jiang, Y.; Ruta, V.; Chen, J.; Lee, A.; MacKinnon, R. 2003. "The principle of gating charge movement in a voltage-dependent K^+ channel." Nature, Volume 423, p42-48.

Kaiser, H. -J.; Lingwood, D.; Levental, I.; Sampaio, J. L.; Kalvodova, L.; Rajendran, L.; Simons, K. 2009. "Order of lipid phases in model and plasma membranes." Proceedings of the National Academy of Sciences, Volume 106, p16645-16650.

Kasai, N.; Kakudo, M. 2005. "X-ray Diffraction by Macromolecules." Springer-Verlag New York, Inc., New York.

Kazimirov, A.; Smilgies, D. -M.; Shen, Q.; Xiao, X.; Hao, Q.; Fontes, E.; Bilderback, D. H.; Gruner, S. M.; Platonov, Y.; Martynov, V. V. 2006. "Multilayer X-ray optics at CHESS." Journal of Synchrotron Radiation, Volume 13, p204-210.

Keller, S. L.; Bezrukov, S. M.; Gruner, S. M.; Tate, M. W.; Vodyanoy, I.; Parsegian, V. A. 1993. "Probability of Alamethicin Conductance States Varies with Nonlamellar Tendency of Bilayer Phospholipids." Biophysical Journal, Volume 65, p23-27.

Khoo, I. -C. 2007. "Liquid Crystals." John Wiley and Sons, Inc., Hoboken.

Kirk, G. L.; Gruner, S. M.; Stein, D. L. 1984. "A Thermodynamic Model of the Lamellar to Inverse Hexagonal Phase Transition of Lipid Membrane-Water Systems." Biochemistry, Volume 23, p1093-1102.

Kirk, G. L.; Gruner, S. M. 1985. "Lyotropic effects of alkanes and headgroup composition on the L_α-H_{II} lipid liquid crystal phase transition: hydrocarbon packing *versus* intrinsic curvature." Journal de Physique, Volume 46, p761-769.

Kooijman, E. E.; Chupin, V.; Fuller, N. L.; Kozlov, M. M.; De Kruijff, B.; Burger, K. N. J.; Rand, P. R. 2005. "Spontaneous Curvature of Phosphatidic Acid and Lysophosphatidic Acid." Biochemistry, Volume 44, p2097-2102.

Koynova, R.; Caffrey, M. 2002. "An index of lipid phase diagrams." Chemistry and Physics of Lipids, Volume 115, p107-219.

Kozlov, M. M.; Leikin, S.; Rand, R. P. 1994. "Bending, Hydration and Interstitial Energies Quantitatively Account for the Hexagonal-Lamella-Hexagonal Reentrant Phase Transition in Dioleoylphosphatidylethanolamine." Biophysical Journal, Volume 67, p1603-1611.

Kozlovsky, Y.; Kozlov, M. M. 2002. "Stalk Model of Membrane Fusion: Solution of Energy Crisis." Biophysical Journal, Volume 82, p882-885.

Kulkarni, C. V.; Seddon, A. M.; Ces, O.; Templer, R. H. 2010. "Evidence that membrane curvature distorts the tertiary structure of bacteriorhodopsin." Soft Matter, Volume 6, p4339-4341.

Kurczy, M. E.; Piehowski, P. D.; Van Bell, C. T.; Heien, M. L.; Winograd, N.; Ewing, A. G. 2010. "Mass spectrometry imaging of mating *Tetrahymena* show that changes in cell morphology regulate lipid domain formation." Proceedings of the National Academy of Sciences, Volume 107, p2751-2756.

Leckband, D.; Israelachvili, J. 2001. "Intermolecular forces in biology." Quarterly Reviews of Biophysics, Volume 34, p105-267.

Lekkerkerker, H. N. W. 1989. "CONTRIBUTION OF THE ELECTRIC DOBULE LAYER TO THE CURVATURE ELASTICITY OF CHARGED AMPHIPHILIC MONOLAYERS." Physica A, Volume 159, p319-328.

Lewis, R. N. A. H.; McElhaney, R. N. 2000. “Surface Charge Markedly Attenuates the Nonlamellar Phase-Forming Propensities of Lipid Bilayer Membranes: Calorimetric and ^{31}P-Nuclear Magnetic Resonance Studies of Mixtures of Cationic, Anionic, and Zwitterionic Lipids.” Biophysical Journal, Volume 79, p1455-1464.

Lewis, R. N. A. H.; Zweytick, D.; Pabst, G.; Lohner, K.; McElhaney, R. N. 2007. "Calorimetric, X-ray Diffraction, and Spectroscopic Studies of the Thermotropic Phase Behavior and Organization of Tetramyristoyl Cardiolipin Membranes." Biophysical Journal, Volume 92, p3166-3177.

Lindblom, G.; Rilfors, L; Hauksson, J .B.; Brentel, I.; Sjölund, M.; Bergenståhl, B. 1991. "Effect of Head-Group Structure and Counterion Condensation on Phase Equilibria in Anionic Phospholipid-Water Systems Studied by ^{2}H, ^{23}Na, and ^{31}P NMR and X-ray Diffraction." Biochemistry, Volume 30, p10938-10948.

Lingwood, D.; Simons, K. 2010. "Lipid Rafts As a Membrane-Organizing Principle." Science, Volume 327, p46-50.

Lis, L. J.; Lis, W. T.; Parsegian, V. A.; Rand, P. R. 1981. "Adsorption of Divalent Cations to a Variety of Phosphatidylcholine Bilayers." Biochemistry, Volume 20, p1771-1777.

Long, S. B.; Campbell, E. B.; MacKinnon, R. 2005. "Crystal Structure of a Mammalian Voltage-Dependent *Shaker* Family K^+ Channel." Science, Volume 309, p897-902.

Loosley-Millman, M. E.; Rand, R. P.; Parsegian, V. A. 1982. "EFFECTS OF MONOVALENT ION BINDING AND SCREENING ON MEASURED ELECTROSTATIC FORCES BETWEEN CHARGED PHOSPHOLIPID BILAYERS." Biophysical Journal, Volume 40, p221-232.

Louër, P. D.; Louër, M. 1972. "Méthode d'Essais et Erreurs pour l'Indexation Automatique des Diagrammes de Poudre." Journal of Applied Crystallography, Volume 5, p271-275.

Lundbak, J. A.; Birn, P.; Tape, S. E.; Toombes, G. E. S.; Sogarrd, R.; Koeppe, R. E. II; Gruner, S. M.; Hansen, A. J.; Andersen, O. S. 2005. "Capsaicin Regulates Voltage-Dependent Sodium Channels by Altering Lipid Bilayer Elasticity." Molecular Pharmacology, Volume 68, p680-689.

Lundbak, J. A. 2006. "Regulation of membrane protein function by lipid bilayer elasticity – a single molecule technology to measure the bilayer properties experienced by an embedded protein." Journal of Physics: Condensed Matter, Volume 18, pS1305-S1344.

Lundbak, J. A.; Koeppe, R. E. II; Andersen, O. S. 2010. "Amphiphile regulation of ion channel function by changes in the bilayer spring constant." Proceedings of the National Academy of Sciences, Volume 107, p15427-15430.

Luzzati, V.; Husson, F. 1962. "THE STRUCTURE OF THE LIQUID-CRYSTALLINE PHASES OF LIPID-WATER SYSTEMS." The Journal of Cell Biology, Volume 12, p207-219.

Luzzati, V. 1997. "Biological significance of lipid polymorphism: the cubic phases." Current Opinion in Structural Biology, Volume 7, p661-668.

Malorni, W.; Giammarioli, A. M.; Garofalo, T.; Sorice, M. 2007. "Dynamics of lipid raft components during lymphocyte apoptosis: The paradigmatic role of GD3." Apoptosis, Volume 12, p941-949.

Manes, S.; Lacalle, R. A.; Gomez-Mouton, C.; Martinez-A, C. 2003. "From rafts to crafts: membrane asymmetry in moving cells." TRENDS in Immunology, Volume 24, p319-325.

Mannock, D. A.; Collins, M. D.; Kreichbaum, M.; Harper, P. E.; Gruner, S. M.; McElhaney, R. N. 2007. "The thermotropic phase behaviour and phase structure of a homologous series of racemic β-D-galactosyl dialkylglycerols studied by differential scanning calorimetry and X-ray diffraction." Chemistry and Physics of Lipids, Volume 148, p26-50.

Marcelja, S.; Radic, N. 1976. "REPULSION OF INTERFACES DUE TO BOUNDARY WATER." Chemical Physics Letters, Volume 42, p129-130.

Mariani, P.; Luzzati, V.; Delacroix, H. 1988. "Cubic Phases of Lipid-containing Systems. Structure Analysis and Biological Implications." Journal of Molecular Biology, Volume 204, p165-189.

Markin, V. S.; Kozlov, M. M.; Borovjagin, V. L. 1984. "On the theory of membrane fusion. The Stalk Mechanism." General Physiology and Biophysics, Volume 3, p361-377.

Marsh, D. 2008. "Protein modulation of lipids, and *vice-versa*, in membranes." Biochimica et Biophysica, Volume 1778, p1545-1575.

McGuiggan, P. M.; Pashley, R. M. 1988. "Forces between Mica Surfaces in Dilute Solutions of a Double-Chained Quaternary Ammonium Ion Surfactant." Journal of Colloid and Interface Science, Volume 124, p560-569.

McMahon, H. T.; Gallop, J. L. 2005. "Membrane curvature and mechanisms of dynamic cell membrane remodelling." Nature, Volume 438, p590-596.

van Meer, G.; Voelker, D. R.; Feigenson, G. W. 2008. "Membrane lipids: where they are and how they behave." Nature Reviews Molecular Cell Biology, Volume 9, p112-124.

Mileykovskaya, E.; Zhang, M.; Dowhan, W. 2005. "Cardiolipin in Energy Transducing Membranes." Biochemistry (Moscow), Volume 70, p191-196.

Millhaud, J. 2004. "New insights into water-phospholipid model membrane interactions." Biochimica et Biophysica Acta, Volume 1663, p19-51.

Mills, T. T.; Tristram-Nagle, S.; Heberle, F. A.; Morales, N. F.; Zhao, J.; Wu, J.; Toombes, G. E. S.; Nagle, J. F.; Feigenson, G. W. 2008a. "Liquid-Liquid Domains in Bilayers Detected by Wide Angle X-Ray Scattering." Biophysical Journal, Volume 95, p682-690.

Mills, T. T.; Toombes, G. E. S.; Tristram-Nagle, S.; Smilgier, D.-M.; Feigenson, G. W.; Nagle, J. F. 2008b. "Order Parameters and Areas in Fluid-Phase Oriented Lipid Membranes Using Wide Angle X-Ray Scattering." Biophysical Journal, Volume 95, p669-681.

Mitchell, D. J.; Ninham, B. W. 1989. "Curvature Elasticity of Charged Membranes." Langmuir, Volume 5, p1121-1123.

Mouritsen, O. G. 2005. "LIFE - AS A MATTER OF FAT. The Emerging Science of Lipidomics." Springer-Verlag Berlin Heidelberg, Germany.

Munro, S. 2003. "Lipid Rafts: Elusive or Illusive?" Cell, Volume 115, p377-388.

Nagle, J. F.; Tristram-Nagle, S. 2000. "Structure of lipid bilayers." Biochimica et Biophysica Acta, Volume 1469, p159-195.

Nelson, D. L.; Cox, M. M. 2005. "Lehninger PRINCIPLES OF BIOCHEMISTRY." 4th edition, W. H. Freeman and Company, New York.

Netz, R. R. 2001. "Electrostatics of counter-ions at and between planar charged walls: From Poisson-Boltzmann to the strong-coupling theory." The European Physical Journal E, Volume 5, p557-574.

Österberg, F.; Kriechbaum, M.; Polcyn, A.; Skita, V.; Tate, M. W.; So, P. T. C.; Gruner, S. M. 1994. "Pressure Induced Hydration Dynamics of Membranes." Physical Review Letters, Volume 72, p2967-2970.

Pabst, G.; Rappolt, M.; Amenitsch, H.; Laggner, P. 2000. "Structural information from multilamellar liposomes at full hydration: Fuu *q*- range fitting with high quality x-ray data." Physical Review E, Volume 62, p4000-4009.

Pabst, G.; Koschuch, R.; Pozo-Navas, B.; Rappolt, M.; Lohner, K.; Laggner, P. 2003a. "Structural analysis of weakly ordered membrane stacks." Journal of Applied Crystallography, Volume 36, p1379-1388.

Pabst, G.; Katsaras, J.; Raghunathan, V. A.; Rappolt, M. 2003b. "Structure and Interactions in the Anomalous Swelling Regime of Phospholipid Bilayers." Langmuir, Volume 19, p1716-1722.

Pabst, G. 2006. "GLOBAL PROPERTIES OF BIOMIMETIC MEMBRANES: PERSPECTIVES ON MOLECULAR FEATURES." Biophysical Review and Letters, Volume 1, p57-84.

Pan, D.; Wang, W.; Liu, W.; Yang, L.; Huang, H. W. 2006. "Chain Packing in the Inverted Hexagonal Phase of Phospholipids: A Study by X-ray Anomalous Diffraction on Bromine-labeled Chains." Journal of American Chemical Society, Volume 128, p3800-3807.

Pan, J.; Tristram-Nagle, S.; Kučerka, N.; Nagle, J. F. 2008. "Temperature Dependence of Structure, Binding Rigidity, and Bilayer Interactions of Dioleoylphospatidylcholine Bilayers." Biophysical Journal, Volume 94, p117-124.

Parthasarathy, R.; Yu, C. -H.; Groves, J. T. 2006. "Curvature-Modulated Phase Separation in Lipid Bilayer Membranes." Langmuir, Volume 22, p5095-5099.

Parthasarathy, R.; Groves, J. T. 2007. "Curvature and spatial organization in biological membranes." Soft Matter, Volume 3, p24-33.

Parton, R. G. 2003. "Caveolae - from ultrastucture to molecular mechanisms." Nature Reviews Molecular Cell Biology, Volume 4, p162-167.

Pashley, R. M.; McGuiggan, P. M.; Ninham, B. W.; Brady, J.; Evans, D. F. 1986. "Direct Measurements of Surface Forces between Bilayers of Double-Chained Quaternary Ammonium Acetate and Bromide Surfactants." Journal of Physical Chemistry, Volume 90, p1637-1642.

Pencer, J.; Jackson, A.; Kucerka, N.; Nieh, M. -P.; Katsaras, J. 2008. "The influence of curvature on membrane domains." European Biophysics Journal, Volume 37, p665-671.

Perozo, E.; Kloda, A.; Cortes, D. M.; Martinac, B. 2002. "Physical principles underlying the transduction of bilayer deformation forces during mechanosensitive channel gating." Nature Strutural Biology, Volume 9, p696-703.

Peter, B. J.; Kent. H. M.; Mills, I. G.; Vallis, Y.; Butler, P. J. G.; Evans, P. R.; McMahon, H. T. 2004. "BAR Domains as Sensors of Membrane Curvature: The Amphiphysin BAR Structure." Science, Volume 303, p495-499.

Petrache, H. I.; Gouliaev, N.; Tristram-Nagle, S.; Zhang, R.; Suter, R. M.; Nagle, J. F. 1998. "Interbilayer interactions from high-resolution x-ray scattering." Physical Review E, Volume 57, p7014-7024.

Phillips, R.; Ursell, T.; Wiggins, P.; Sens, P. 2009. "Emerging roles for lipids in shaping membrane-protein function." Nature, Volume 459, p379-385.

Pike, L. J. 2009. "The challenge of lipid rafts." Journal of Lipid Research, April Supplement, pS323-S328.

Pollack, L.; Tate, M. W.; Finnerfrock, A. C.; Kalidas, C.; Trotter, S.; Darnton, N. C.; Lurio, L.; Austin, R. H.; Batt, C. A.; Gruner, S. M.; Mochrie, S. G. J. 2001. "Time Resolved Collapse of a Folding Protein Observed with Small Angle X-ray Scattering." Physical Review Letters, Volume 86, p4962-4965.

Rand, R. P.; Sengupta, S. 1972. “CARDIOLIPIN FORMS HEXAGONAL STRUCTURES WITH DIVELENT CATIONS.” Biochimica et Biophysica Acta, Volume 255, p484-492.

Rand, R. P.; Parsegian, V. A. 1989. “Hydration forces between phospholipid bilayers.” Biochimica et Biophysica, Volume 988, p351-376.

Rand, R. P.; Fuller, N. L.; Gruner, S. M.; Parsegian, V. A. 1990. "Membrane Curvature, Lipid Segregation, and Structural Transitions for Phospholipids under Dual-Solvent Stress." Biochemistry, Volume 29, p76-87.

Rappolt, M.; Pressl, K.; Pabst, G.; Laggner, P. 1998. "L_{α}-phase separation in phosphatidylcholine-water systems induced by alkali chlorides." Biochimica et Biophysica Acta, Volume 1372, p389-393.

Rappolt, M.; Pabst, G.; Amenitsch, H.; Laggner, P. 2001. "Salt-induced phase separation in the liquid crystalline phase of phosphatidylcholines." Colloids and Surfaces A: Physicochemical and Engineering Aspects, Volume 183-185, p171-181.

Rappolt, M.; Hickel, A.; Bringezu, F.; Lohner, K. 2003. "Mechanism of the Lamllar/Inverse Hexagonal Phase Transition Examined by High Resolution X-Ray Diffraction." Biophysical Journal, Volume 84, p3111-3122.

Rasmussen, B.F.; Stock, A.M.; Ringe, D.; Petsko, G.A. 1992. “Crystalline Ribonuclease A loses Function below the Dynamical Transition at 220 K.” Nature, Volume 357, p423-p424.

Razani, B.; Lisanti, M. 2002. "The Role of Caveolae and the Caveolins in Mammalian Physiology." Reviews in Undergraduate Research, Volume 1, p44-50.

Rietveld, A.; Simons, K. 1998. "The differential miscibility of lipids as the basis for the formation of functional membrane rafts." Biochimica et Biophysica, Volume 1376, p467-479.

Roux, A.; Cuvelier, D.; Nassoy, P.; Prost, J.; Bassereau, P.; Goud, B. 2005. "Role of curvature and phase transition in lipid sorting and fission of membrane tubules." The EMBO Journal, Volume 24, p1537-1545.

Rowat, A. C.; Hansen, P. L.; Ipsen, J. H. 2004. "Experimental evidence of the electrostatic contribution to membrane bending rigidity." Europhysics Letters, Volume 67, p144-149.

Sankaram, M. B.; Powell, G. L.; Marsh, D. 1989. "Effect of acyl chain composition on salt-induced lamellar to inverted hexagonal phase transitions in cardiolipin." Biochimica et Biophysica Acta, Volume 980, p389-392.

Schlame, M.; Ren, M.; Xu, Y.; Greenberg, M. L.; Haller, I. 2005. "Molecular symmetry in mitochondrial cardiolipins." Chemistry and Physics of Lipids, Volume 138, p38-49.

Seddon, J. M.; Kaye, R. D.; Marsh, D. 1983. “INDUCTION OF THE LAMELLAR-INVERTED HEXAGONAL PHASE TRANSITION IN CARDIOLIPIN BY PROTONS AND MONOVALENT CATIONS.” Biochimica et Biophysica Acta, Volume 734, p347-352.

Seddon, J. M. 1990. “Structure of the inverted hexagonal (H_{II}) phase, and non-lamellar phase transitions of lipids.” Biochimica et Biophysica Acta, Volume 1031, p1-69.

Seddon, J. M.; Templer, R. H. 1993. “Cubic phases of self-assembled amphiphilic aggregates.” Philosophical Transaction: Physical Sciences and Engineering, Volume 344, p377-401.

Seddon, J. M.; Templer, R. H. 1995. “Polymorphism of Lipid-Water Systems.” p97-160 in “Structure and Dynamics of Membranes. From Cells to Vesicles.”, Edited by Lipowsky, R. and Sackmann, E., Volume 1A, Elsevier Science B.V., Amsterdam.

Seddon, J. M.; Robins, J.; Gulik-Krzywicki, T.; Delacroix, H. 2000. “Inverse micellar phases of phospholipids and glycolipids.” Physical Chemistry Chemical Physics, Volume 2, p4485-4493.

Shearman, G. C.; Templer, R. H., Seddon, J. M. 2006. “Inverse lyotropic phases of lipids and membrane curvature.” Journal of Physics: Condensed Matter, Volume 18, pS1105-S1124.

Shearman, G. C.; Tyler, A. I. I.; Brooks, N. J.; Templer, R. H.; Ces, O.; Law, R. V.; Seddon, J. M. 2009. “A 3-D Hexagonal Inverse Micellar Lyotropic Phase.” Journal of the American Chemical Society, Volume 131, p1678-1679.

Shearman, G.; Ces, O.; Templer, R. H. 2010. "Towards an understanding of phase transitions between inverse bicontinuous cubic lyotropic liquid crystalline phases." Soft Matter, Volume 6, p256-262.

Shirley, R. 1980. p361-382 in "Accuracy in Powder Diffraction.", Edited by Block, S.; Hubbard, C. R., Volume 567, NBS Spec. Publ.

Shyamsunder, E.; Gruner, S. M.; Tate, M. W.; Turner, D. C.; So, P. T. C.; Tilcock, C. P. S. 1988. “Observation of Inverted Cubic Phases in Hydrated Dioleoylphosphatidylethanolamine Membranes.” Biochemistry, Volume 27, p2332-2336.

Siegel, D. P. 1986a. "INVERTED MICELLAR INTERMEDIATES AND THE TRANSITIONS BETWEEN LAMELLAR, CUBIC, AND INVERTED HEXAGONAL LIPID PHASES. I. Mechanism of the $L_{\alpha} \leftrightarrow H_{II}$ phase Transitions." Biophysical Journal, Volume 49, p1155-1170.

Siegel, D. P. 1986b. "INVERTED MICELLAR INTERMEDIATES AND THE TRANSITIONS BETWEEN LAMELLAR, CUBIC, AND INVERTED HEXAGONAL LIPID PHASES. II. Implications for Membrane-Membrane Interactions and Membrane Fusion." Biophysical Journal, Volume 49, p1171-1183.

Siegel, D. P. 1993. "Energetics of Intermediate in Membrane Fusion: Comparison of Stalk and Inverted Micellar Intermediate Mechanisms." Biophysical Journal, Volume 65, p2124-2140.

Siegel, D. P. 1994. "The Mechanism of Lamellar-to-Inverted Hexagonal Phase Transitions: A Study using Temperature-Jump Cryo-Electron Microscopy." Biophysical Journal, Volume 66, p402-414.

Siegel, D. P. 1997. "The Mechanism of Lamellar-to-Inverted Hexagonal Phase Transitions in Phosphatidylethanolamine: Implications for Membrane Fusion Mechanisms." Biophysical Journal, Volume 73, p3089-3111.

Siegel, D. P.; Epand, R. M. 1997. "The Mechanism of Lamellar-to-Inverted Hexagonal Phase Transition in Phosphatidylethanolamine: Implications for Membrane fusion Mechanisms." Biophysical Journal, Volume 73, p3089-3111.

Siegel, D. P. 1999. "The Modified Stalk Mechanism of Lamellar/Inverted Phase Transitions and Its Implications for Membrane Fusion." Biophysical Journal, Volume 76, p291-313.

Siegel, D. P.; Kozlov, M. M. 2004. "The Gaussian Curvature Elastic Modulus of N-Monomethylated Dioleoylphosphatidylethanolamine: Relevance to Membrane Fusion and Lipid Phase Behavior." Biophysical Journal, Volume 87, p366-374.

Siegel, D. P.; Cherezov, V.; Greathouse, D. V.; Koeppe, R. E. II; Killian, J. A.; Caffrey, M. 2006. "Transmembrane Peptides Stabilize Inverted Cubic Phases in a Biphasic Length-Dependent Manner: Implications for Protein-Induced Membrane Fusion." Biophysical Journal, Volume 90, p200-211.

Siegel, D. P. 2008. "The Gaussian Curvature Elastic Energy of Intermediates in Membrane Fusion." Biophysical Journal, Volume 95, p5200-5215.

Siegel, D. P.; Tenchov, B. G. 2008. "Influence of the Lamellar Phase Unbinding Energy on the Relative Stability of Lamellar and Inverted Cubic Phases." Biophysical Journal, Volume 94, p3987-3995.

Siegel, D. P. 2010. "Fourth-Order Curvature Energy Model for the Stability of Bicontinuous Inverted Cubic Phases in Amphiphile-Water Systems." Langmuir, Volume 26, p8673-8683.

Simons, K.; van Meer, G. 1988. "Lipid Sorting in Epithelial Cells." Biochemistry, Volume 27, p6197-6202.

Simons, K.; Ikonen, E. 1997. "Functional rafts in cell membranes." Nature, Volume 387, p569-572.

Simons, K.; Toomre, D. 2000. "LIPID RAFTS AND SIGNAL TRANSDUCTION." Nature Reviews Molecular Cell Biology, Volume 1, p31-41.

Singer, S. J.; Nicolson, G. L. 1972. "The Fluid Mosaic Model of the Structure of Cell Membranes." Science, Volume 175, p720-731.

So, P. T. C. 1992. "HIGH PRESSURE EFFECTS ON THE MESOPHASES OF LIPID-WATER SYSTEMS." Ph.D. Thesis, Princeton University.

So, P. T. C.; Gruner, S. M.; Shyamsunder, E. 1993. “Pressure-Induced Topological Phase Transitions in Membranes.” Physical Review Letters, Volume 70, p3455-3458.

Sorre, B.; Callan-Jones, A.; Manneville, J. -B.; Nassoy, P.; Joanny, J. -F.; Prost, J.; Goud, B.; Bassereau, P. 2009. "Curvature-driven lipid sorting needs proximity to a demixing point and is aided y proteins." Proceedings of the National Academy of Sciences, Volume 106, p5622-5626.

Soubias, O.; Teague Jr., W. E.; Hines, K. G.; Mitchell, D. C.; Gawrisch, K. 2010. "Contribution of Membrane Elastic Energy to Rhodopsin Function." Biophysical Journal, Volume 99, p817-824.

Squires, A. M.; Conn, C. E.; Seddon, J. M.; Templer, R. H. 2009. "Quantitative model for the kinetics of lyotropic phase transitions involving changes in monolayer curvature." Soft Matter, Volume 5, p4773-4779.

Taheri-Araghi, S.; Ha, B. -Y. 2010. "Electrostatic Bending of Lipid Membranes: How Are Lipid and Electrostatic Properties Interrelated?" Langmuir, Volume 26, p14737-14746.

Tardieu, A.; Luzzati, V. 1973. "Structure and Polymorphism of the Hydrocarbon Chains of Lipids: A Study of Lecithin-Water Phases." Journal of Molecular Biology, Volume 75, p711-733.

Tate, M. W. 1987. "Equilibrium and Kinetic States of the L_{α}-H_{II} Phase Transition." Ph.D. Thesis, Princeton University.

Tate, M. W.; Eikenberry, E. F.; Turner, D. C.; Shyamsunder, E.; Gruner, S. M. 1991. “Nonbilayer phases of membrane lipids.” Chemistry and Physics of Lipids, Volume 57, p147-p164.

Taupin, P. D. 1968. "Une méthode générale pour I'indexations des diagrammes de poudres." Journal of Applied Crystallography, volume 1, p178-181.

Tresset, G. 2009. "The multiple faces of self-assembled lipidic systems." PMC Biophysics, Volume 2, 3.

Tristram-Nagle, S.; Nagle, J. F. 2004. "Liquid bilayers: thermodynamics, structure, fluctuations, and interactions." Chemistry and Physics of Lipids, Volume 127, p3-14.

Turner, D. C. 1990. "Structural Investigations of the Inverted Hexagonal and Inverted Cubic Phases in Lipid-Water Systems." Ph.D. Thesis, Princeton University.

Tuner, D. C.; Gruner, S. M. 1992. "X-ray Diffraction Reconstruction of the Inverted Hexagonal (H_{II}) Phase in Lipid-Water Systems." Biochemistry, Volume 31, p1340-1355.

Ungar, G.; Liu, Y.; Zheng, X.; Percec, V.; Cho, W.-D. 2003. "Giant Supramolecular Liquid Crystal Lattice." Science, Volume 299, p1208-1211.

Valiyaveetil, F. I.; Zhou, Y.; MacKinnon, R. 2002. "Lipids in the Structure, Folding, and Function of KcsA K^+ Channel." Biochemistry, Volume 41, p10771-10777.

Vasilenko, I.; De Kruijff, B.; Verkleij, A. J. 1982. "POLYMORPHIC PHASE BEHAVIOR OF CARDIOLIPIN FROM BOVINE HEART AND FROM *BACILLUS SUBTILIS* AS DETECTED BY ^{31}P-NMR AND FREEZE-FRACTURE TECHNIQUES. EFFECTS OF Ca^{2+}, Mg^{2+}, Ba^{2+} AND TEMPERATURE." Biochimica et Biophysica Acta, Volume 684, p282-286.

Veatch, S. L.; Keller, S. L. 2005. "Miscibility Phase Diagrams of Giant Vesicles Containing Sphingomyelin." Physical Review Letters, Volume 94, 148101.

Voeltz, G. K.; Prinz, W. A. 2007. "Sheets, ribbons and tubules - how organelles get their shape." Nature Reviews Molecular Cell Biology, Volume 8, p258-264.

Warren, B.E. 1969. "X-ray Diffraction." Addison-Wesley, Inc., Reading.

Werner, P.-E.; Eriksson, L.; Westdahl, M. 1985. "*TREOR*, a semi-exhaustive trial-and-error powder indexing program for all symmetries." Journal of Applied Crystallography, Volume 18, p367-370.

Winterhalter, M.; Helfrich, W. 1992. "Bending Elasticity of Electrically Charged Bilayers: Coupled Monolayers, Neutral Surfaces, and Balancing Stresses." Journal of Physical Chemistry, Volume 96, p327-330.

Wymann, M. P.; Schneiter, R. 2008. "Lipid singlling in disease." Nature Reviews Molecular Cell Biology, Volume 9, p162-176.

Yang, L; Huang, H. W. 2002. "Observation of a Membrane Fusion Intermediate Structure." Science, Volume 297, p1877-1879.

Yarar, D.; Waterman-Storer, C. M.; Schmid, S. L. 2005. "A Dynamic Actin Cytoskeleton Functions at Multiple Stages of Clathrin-mediated Endocytosis." Molecular Biology of the Cell, Volume 16, p964-975.

Yoshimura, K.; Sokabe, M. 2010. "Mechanosensitivity of ion channels based on protein-lipid interactions." Journal of the Royal Society Interface, Volume 7, pS307-S320.

Zimmerberg, J.; Kozlov, M. M. 2005. "How proteins produce cellular membrane curvature." Nature Reviews Molecular Cell Biology, Volume 7, p9-19.

Zhang, R.; Suter, R. M.; Nagle, J. F. 1994. "Theory of the structure factor of lipid bilayers." Physical Review E, Volume 50, p5047-5060.

Zhou, Y.; Raphael, R. M. 2007. "Solution pH Alters Mechanical and Electrical Properties of Phosphatidylcholine Membranes: Relation between Interfacial Electrostatics, Intramembrane Potential, and Bending Elasticity." Biophysical Journal, Volume 92, p2451-2462.

Zou, A.; Hoffmann, H., Freiberger, N.; Glatter, O. 2007. "Influence of Ionic Charges on the Bilayers of Lamellar Phases." Langmuir, Volume 23, p2977-2984.